Dynamic behaviour of electric machine stators

Pierre Millithaler

SPIM

Thèse de Doctorat

école doctorale **sciences pour l'ingénieur et microtechniques**

UFC UNIVERSITÉ DE FRANCHE-COMTÉ

Dynamic behaviour of electric machine stators

Modelling guidelines for efficient finite-element simulations and design specifications for noise reduction

Pierre Millithaler

SPIM

Thèse de Doctorat

école doctorale **sciences pour l'ingénieur et microtechniques**

UFC UNIVERSITÉ DE FRANCHE-COMTÉ

N° | X | X | X |

THÈSE présentée par

PIERRE MILLITHALER

pour obtenir le

Grade de Docteur de
l'Université de Franche-Comté

Spécialité : **mécanique - mechanical engineering**

Dynamic behaviour of electric machine stators

Modelling guidelines for efficient finite-element simulations and design specifications for noise reduction

Unités de Recherche :
Vibratec, 28 chemin du Petit Bois, BP36, 69131 ÉCULLY CEDEX, FRANCE,
Femto-ST, Département Mécanique Appliquée, UMR CNRS 6174, 24 chemin de l'épitaphe, 25000 BESANÇON, FRANCE

Soutenue publiquement le 9 octobre 2015 devant le Jury composé de :

JEAN-FRANÇOIS DEÜ	Rapporteur	Professeur au C.N.A.M., Paris
CHARLES PEZERAT	Rapporteur	Professeur à l'E.N.S.I.M., Le Mans
VINCENT LANFRANCHI	Président du jury	Professeur à l'U.T.C., Compiègne
MATHIEU CORUS	Examinateur	Docteur, E.D.F. R&D, Paris
MORVAN OUISSE	Directeur de thèse	Professeur à l'E.N.S.M.M., Besançon
NOUREDDINE BOUHADDI	Co-encadrant	Professeur à l'U.F.C., Besançon
ÉMELINE SADOULET-REBOUL	Co-encadrante	Maître de Conférences à l'U.F.C., Besançon
JEAN-BAPTISTE DUPONT	Encadrant industriel	Docteur, Chef du département Opérations à Vibratec, Écully

Acknowledgements — Remerciements

Voilà bientôt trois années écoulées depuis le début de ce projet de thèse à Vibratec. Cette aventure et toutes les choses qui y sont associées – rencontres, connaissances, résultats, ... – n'auraient pas été possibles ou aussi riches sans l'implication de certaines personnes que je souhaite remercier ici.

Tout d'abord, je remercie l'ensemble des membres du jury pour l'intérêt porté à mon travail, ainsi qu'à l'entreprise Vibratec qui a financé cette thèse CIFRE en intégralité.

Le bon déroulement de ces trois ans repose en grande partie sur quatre personnes, qui ont une place particulière dans ce projet. Je tiens à remercier chaleureusement mes encadrants Morvan Ouisse, Émeline Sadoulet-Reboul et Noureddine Bouhaddi côté Femto-S.T., ainsi que Jean-Baptiste Dupont à Vibratec, pour leur aide et leur bienveillance dans les moments les plus agréables et les plus difficiles de cette thèse. Je suis spécialement reconnaissant à Morvan pour toute son implication, sans qui cette thèse n'aurait pas même pu démarrer. Merci à vous quatre du fond du cœur !

Pour leur aide et leurs contributions diverses sur le court et sur le long terme dans tout ce projet, merci à l'entreprise Von Roll de Meyzieu et notamment à Christian Nodin pour toutes les heures qui ont été consacrées aux résines, à Vincent Placet et Frédérique Trivaudey du Femto pour les analyses DMA et les développements théoriques de calcul de structures, à Louis Humbert de BMW pour son interaction dans l'ensemble du projet, et bien sûr à Pascal Bouvet, Sylvestre Lecuru, Christian Clerc, Julien Schuh et Jean-Paul Kovalevsky de Vibratec pour leur expertise et leur sollicitude.

Sans pouvoir les citer tous, je salue également mes collègues et amis qui ont partagé mon quotidien, en l'occurrence les co-thésards du département Mec'Appli à Besançon, mes voisins doctorants du LTDS, les équipes « simu » et « manip » à Vibratec et mes homologues en CIFRE de MicrodB.

Enfin, je tiens à ne pas oublier mes parents, mon frère et la famille d'Élise, dont le support et les encouragements m'ont motivé durant ces trois années. Mes pensées les plus douces sont pour toi, Élise ; pour ton aide inestimable de chaque instant et de ta présence dans les moments heureux comme dans les épreuves, un immense merci !

Contents

List of Figures

List of Tables

INTRODUCTION

Since the first uses of electrical power in the last centuries, electricity has motivated scientists and inventors to design motorised devices for industry, agriculture, and also for transport. In spite of the rapid development of coal-fueled steam engines in the mid-19th century, the first vehicles powered with electricity were locomotives developed by the UK railway industry [2]. After the first urban tramway networks were created in Europe in the 1880's, a great number of railway devices as well as other public transportation vehicles - except for airplanes - are nowadays electric, such as trains, tramways and trolleys all over the world. As well, the automotive industry shows a growing interest for hybrid and 100%-electrical motorisations, as an alternative to conventional engines in response to oncoming price increases and shortages of fossil energies.

While the field of combustion engines benefits from a long-standing experience, designing an automotive electrical powertrain yet faces new challenges, for optimising simultaneously the effectiveness and the emission of noise. Achieving both of these goals requires a good knowledge of an electrical powertrain's mechanical behaviour. Therefore, modelling such a structure with accuracy is a key to reliable simulations in terms of structural dynamics, for which current computer performances offer a great potential through the use of the so-called *finite-element theory*.

In spite of the ever-increasing efficiency of computing tools in terms of both hardware and software, developing electric machines still requires long and costly stages based on experimental analyses on prototypes. The design uncertainties inherent to the mechanical behaviours of the so-called active parts – namely the magnetic core and and the windings – imply updating the simulation models with experimental data in order to improve the representativeness of the measurements. Consequently, the design stages of the entire manufacturing process could benefit from more effective prediction capabilities, for minimising the dependency to experimental data and thus the costs related to the prototypes and the duration of the overall development.

Combining their expertise in structural dynamics and acoustics, the company Vibratec and the institute Femto-ST Applied Mechanics Department have been involved in common R&D projects for more than five years, including simulations on electric machines. For answering the above-mentioned needs in both industrial and academic domains, this Ph.D. "*CIFRE*" programme ("*Convention industrielle de formation par la recherche*", i.e. industrial convention of research-oriented training) has been funded and hosted by Vibratec and supervised by the Femto-ST Institute, and specifically oriented towards concrete applications in projects involving structural dynamics on electric machines. The main objective this work has aimed at reaching is to improve the current modelling techniques about electric motor stators.

The present manuscript has been divided into five chapters, each corresponding to specific contributions or applications. Chapters 1 and 2 introduce the necessary theoretical

notions for the applications, as well as the state-of-the-art knowledge about the simulation and the prediction of the dynamic behaviour of an electric machine stator. Also, applied simulations including sensitivity analyses of material properties and modelling guidelines for piece connections are presented.

Chapter 3 details the developments of practical approaches for efficient finite-element simulations on laminated core structures, as well as applications on experimentally-validated modal bases of electric machine stators.

Chapter 4 deals with an experimental campaign and modelling analyses focused on the associations of windings and resins in stators.

Finally, Chapter 5 (removed from the document for confidentiality reasons) investigates modelling aspects related to the resin itself and its viscoelastic phenomena in electric motors. A comprehensive methodology of resin property optimisation is detailed for minimising the noise radiated by a switched-reluctance motor. Also, the impacts of eccentricities are investigated as part of combined electromagnetic-structural finite-element simulations.

As complements for these five parts, the appendix chapters A and B gather additional data, illustrations and the nomenclature of the common abbreviations and symbols.

1

General notions

First of all, it seems important to identify and to understand the natures of the challenges existing while attempting to model an electric machine. A comprehensive description of every aspect of each type of existing electric machines or of their functioning would be beyond the frame of this chapter, as well as a comprehensive description of every electromagnetic phenomenon engendered during its operation. Instead, this chapter will provide a general introduction to electric machines and corresponding electromagnetic notions in the two first sections. Then, the necessary theoretical background playing a part in the mechanical tools and the studies presented in this work will be described.

Several specific domains are used and combined for applying the concepts of this thesis. For enabling the readers who might not be familiar will all of them to apply every method developed or transcribed in this work, Sections 1.3 through 1.5 will introduce notions with all necessary details.

1.1/ Architecture of an electric machine

An electric motor converts electric power into mechanical power (motion), at the opposite of a generator. The different parts composing a motor are exposed in Figure 1.1; the rotor spins with the shaft while the stator is fixed. The thin air volume between the rotor and the stator is called the air gap. Although the emphasis is made on the motor itself, it can be noted that the assembly of an electric motor, an electronic conversion device and a mechanical gearbox composes an *electrical powertrain*.

As a general rule, two major classes of electric machines are distinguished according to the type of electric signal powering them: DC for direct current or AC for alternating current. The principles of the most common types of electric motors are presented briefly throughout the following paragraphs (based on the data presented in [158]), while a larger emphasis on the electromagnetic phenomena is made in Section 1.2.

DC motor

In DC machines, permanent magnets (or electromagnets) are disposed as pairs on the stator (+ and -) and produce a permanent magnetic flux. The rotor windings are fed with DC currents and therefore produce a 2-pole magnetic flux too. In order to align the two flux distributions (attraction between opposite poles and repulsion between identical

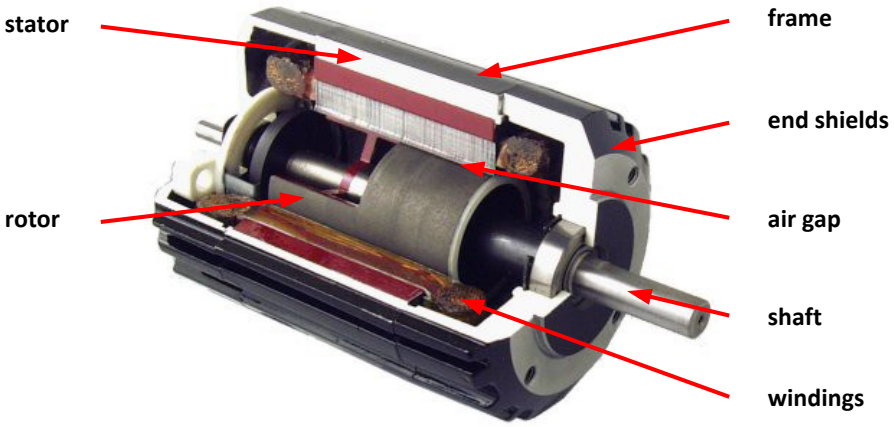

Figure 1.1 – Cutaway of an electric motor [153]

ones), forces and thus torque are applied to the rotor. As the rotor spins, new windings are fed with currents, therefore enabling a smooth and continuous rotation. An illustration of a DC motor is given in Figure 1.6, where the poles are distinguished by different colours. Although they offer a high energy output and are able to operate in an important speed range, DC machines are expensive to produce and to maintain, and are seldom used for building automobile powertrains.

AC MOTOR: SYNCHRONOUS MACHINE

One of the visible differences between DC and AC architectures lies in the stator architecture. Instead of permanent magnets, windings are disposed in the stator of an AC machine, and are fed by three-phase alternating currents. A simple illustration could be a set of three pairs of poles $(C1^+;C1^-)$, $(C2^+;C2^-)$ and $(C3^+;C3^-)$ diametrically opposed and equitably placed around the stator. The poles $C1^+$, $C2^+$ and $C3^+$ are fed with the respective currents *p1*, *p2* and *p3*, while their opposite poles $C1^-$, $C2^-$ and $C3^-$ are fed with opposite currents *-p1*, *-p2* and *-p3*, so that the currents in two successive poles are shifted by a phase $\pm 2\pi/3$. The detail of the currents is shown in Figure 1.2, where an instant T_A is marked with a dashed grey line.

As a result of this setting, while the magnitude of the magnetic field created by pole pair (respectively $\|\vec{H}_{C1}\|$, $\|\vec{H}_{C2}\|$ or $\|\vec{H}_{C3}\|$) varies sinusoidally, the resulting field $\vec{\mathbf{H}}_{\mathbf{tot}} = \vec{H}_{C1} + \vec{H}_{C2} + \vec{H}_{C3}$ applied to the rotor is of constant magnitude and rotates around the axis (thick black arrow in Figure 1.3).

Then, placing permanent magnets on the rotor creates a magnetic flux. As the stator flux rotates, torque is generated at the rotor in order to keep the two flux distributions aligned. The rotor then spins at the same speed as the stator field's, hence the name "synchronous". It can be noted that permanent magnets can be equivalently replaced by electromagnets in all kinds of motors. Synchronous machines present several assets including the easiness to pilot and to manufacture. However, they might stall if the load is too important at the rotor, or generate detrimental torque pulsations.

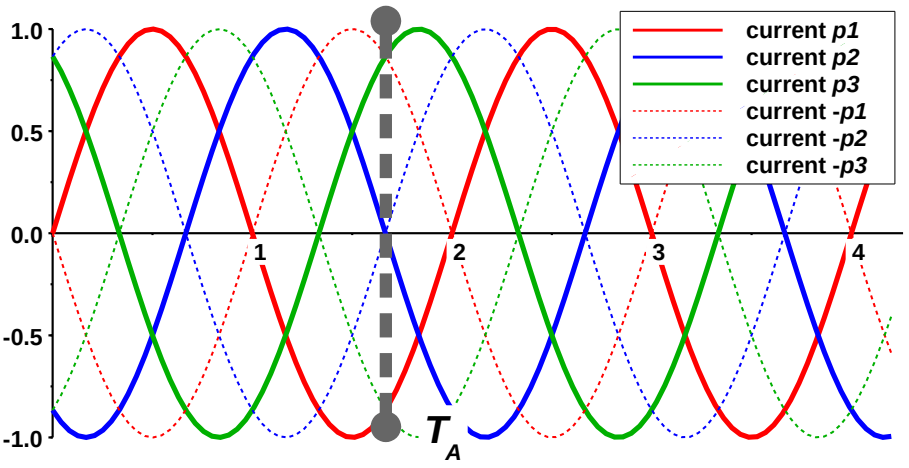

Figure 1.2 – Three-phase alternating currents

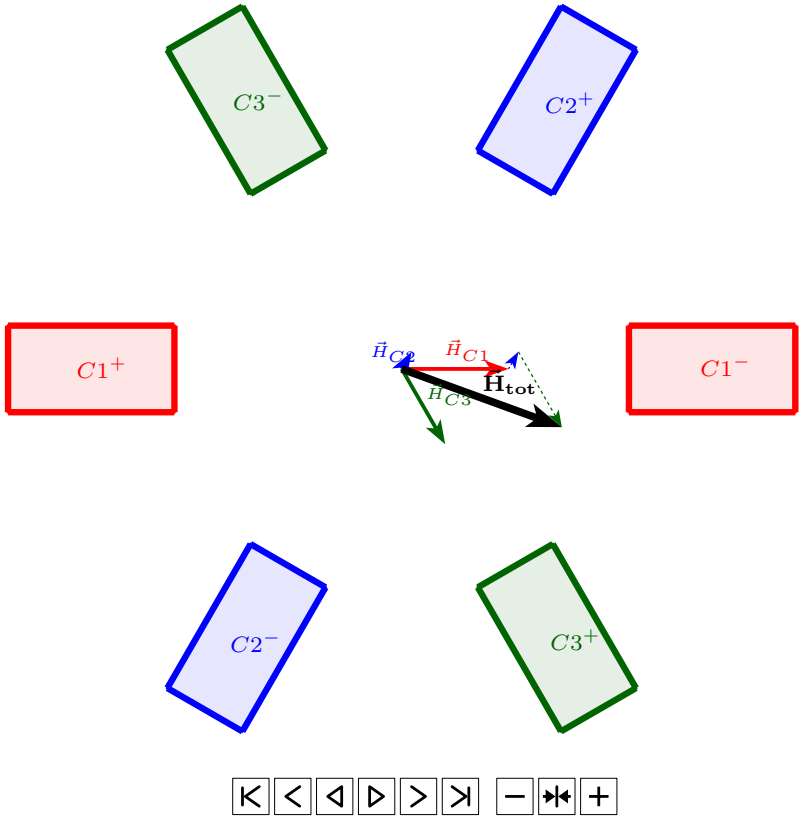

Figure 1.3 – Rotating field generation

AC MOTOR: INDUCTION MACHINE

Induction machines are driven by the same stator field as AC synchronous ones. The difference is made on the rotor, which is built from a simple homogeneous metal structure, usually referred to as a "squirrel cage" (see Figure 1.4).

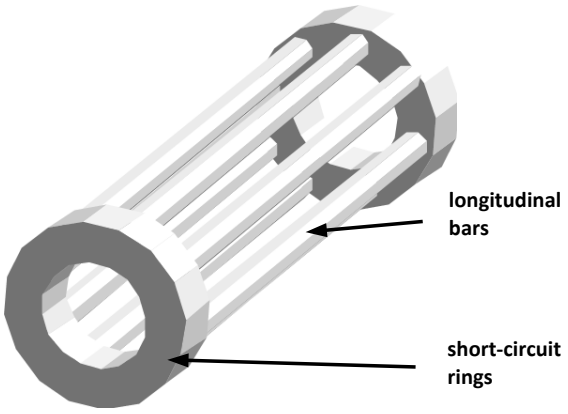

Figure 1.4 – Squirrel cage [158]

Powering the stator creates a rotating magnetic flux; as the rotor is initially immobile and generates no flux, a relative speed difference appears between the stator and the rotor flux distributions. This relative speed difference induces an electromotive force in the bars – corresponding to an electric tension –, and then to induced currents which circulate through the entire squirrel cage with the aid of the short-circuit rings. Similarly to DC machines, the currents create a magnetic flux in the rotor, and therefore a torque so that the rotor flux distribution aligns itself to the stator's. Finally, as a relative speed difference between the flux distributions is necessary to induce currents in the squirrel cage, the rotor does not spins at the same speed as the stator rotating field; this explains the use of the alternate name "asynchronous" for induction machines.

SPECIAL CASE: SWITCHED-RELUCTANCE MACHINE

The last device presented here is the so-called switched-reluctance machine, often abbreviated to SRM. Unlike standard AC machines, the rotor of a SRM is made of a single piece of ferromagnetic metal, without either windings or magnets. The stator coils are powered sequentially so that the magnetic flux circulating from the stator to the rotor creates torque while aligning the rotor teeth with the stator poles. On the illustration shown in Figure 1.5, the pair (4+;4-) is powered directly after (1+;1-): by minimising the distance in the air, the circulation of the flux (green line) creates torque, until the next pair of coils is powered instead and the rotor is spun anew.

This type of electric machine is interesting as its rotor is cheap and easy to manufacture, and has been often used for various analyses in the literature. However, due to sequentiality of the stator excitations, its functioning is likely to lead to high magnitudes of torque pulsations and important acoustic levels.

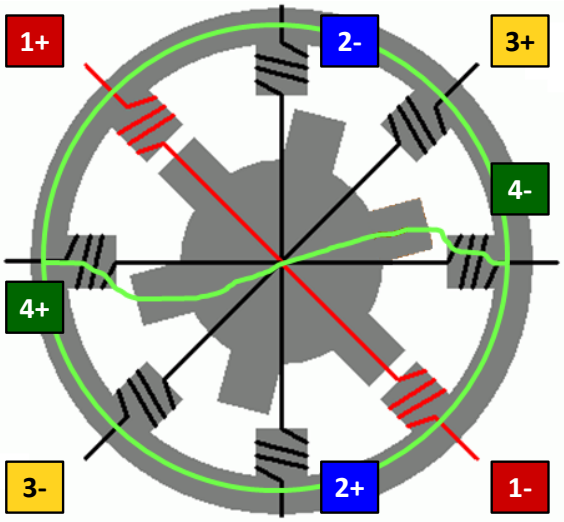

Figure 1.5 – Switched Reluctance Machine [158]

ILLUSTRATIONS OF DC, SYNCHRONOUS AND INDUCTION MACHINES

Figure 1.6 gathers illustrations of DC, synchronous and induction machines. The DC-case rotor commutations are shown with colour changes and sparks in Figure 1.6(a). The rotating magnetic field is represented in the stator for both of the AC motors 1.6(b) and 1.6(c). In the induction machine, it can be observed (with the slots) that the rotor spins at a lower speed than the induced rotor flux, which is aligned with the stator's.

1.2/ GENERATION OF ELECTROMAGNETIC EXCITATIONS

The basic introduction made in the previous section may have to be completed in order to represent with more details the generation of dynamic excitations. The part of the motor this entire thesis is focused on is the stator; this section will therefore put the spotlight on the electromagnetic phenomena occurring at the interface of the stator and the air gap. The type of machine chosen for this section is AC, the stators of which are composed of windings.

1.2.1/ MAGNETIC TORQUE

One of the main mechanical parameters that could be thought of when dealing with electrical motors is the torque, which could be also seen as a "useful" excitation. Its generation is sequenced into several steps from the original current input into the windings, including magnetomotive force, permeance and flux density at the air gap. These points are detailed in the following paragraphs.

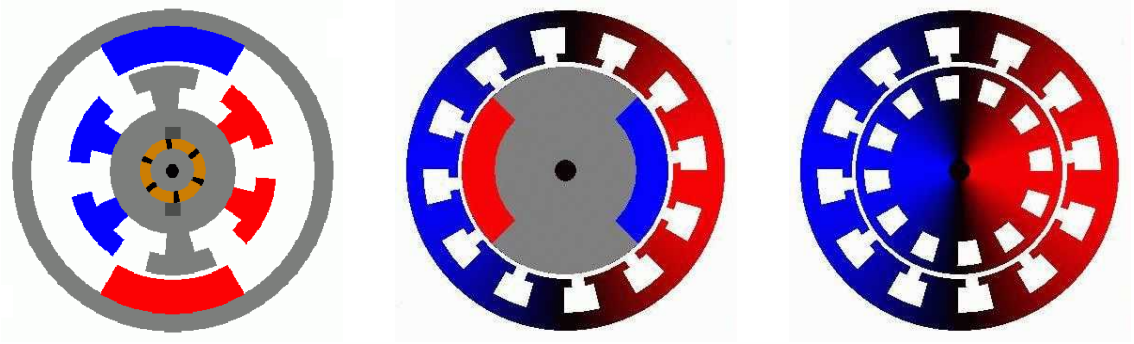

(a) DC machine (b) Synchronous machine (c) Induction machine

Figure 1.6 – Illustrations of DC, synchronous and induction machines [158]

MAGNETOMOTIVE FORCE

A coil made of n_s^w turns [i] and fed with a current I_s^w generates a magnetomotive force f^{mm} such that:

$$f^{mm} = n_s^w \cdot I_s^w \,. \tag{1.1}$$

As it can be read in Figure 1.2, the currents of poles $\{C1^+; C1^-\}$, $\{C2^+; C2^-\}$ and $\{C3^+; C3^-\}$ are respectively $\{-\sqrt{3}/2; +\sqrt{3}/2\}$, $\{0; 0\}$ and $\{+\sqrt{3}/2; -\sqrt{3}/2\}$ at the instant T_A. An illustration of the spatial distribution of magnetomotive forces MMF about the stator is given in Figure 1.7. Positive values of MMF orientate the force vectors from pole $+$ to $-$, at the opposite of negative values.

PERMEANCE

At the opposite of the reluctance $\mathcal{R}$, the permeance $\Lambda = 1/\mathcal{R}$ is the capacity to admit the magnetic flux through the air gap, and varies in function of the relative positions of stator and rotor teeth. At a given time t and stator angle α_s, the permeance per unit surface can be expressed as:

$$\lambda_a\left(t, \alpha_s\right) = \frac{\mu_{\text{air}}}{g_a\left(t, \alpha_s\right)} \,, \tag{1.2}$$

where μ_{air} is the magnetic permeability of air (often considered equal to void's permeability $\mu_0 = 4\pi \cdot 10^{-7}\ \text{N} \cdot \text{A}^{-2}$ or $\text{H} \cdot \text{m}^{-1}$) and $g_a\left(t, \alpha_s\right)$ the air gap's representative width (see Figure 1.8). A more comprehensive description of the magnetic permeance is made by [32].

FLUX DENSITY

The air-gap magnetic induction $B_a\left(t, \alpha_s\right)$ corresponds to a density of magnetic flux per unit surface (and is therefore called "flux density"), and is computed from the sum of the

i. n_s^w may be represented by a function of time and space

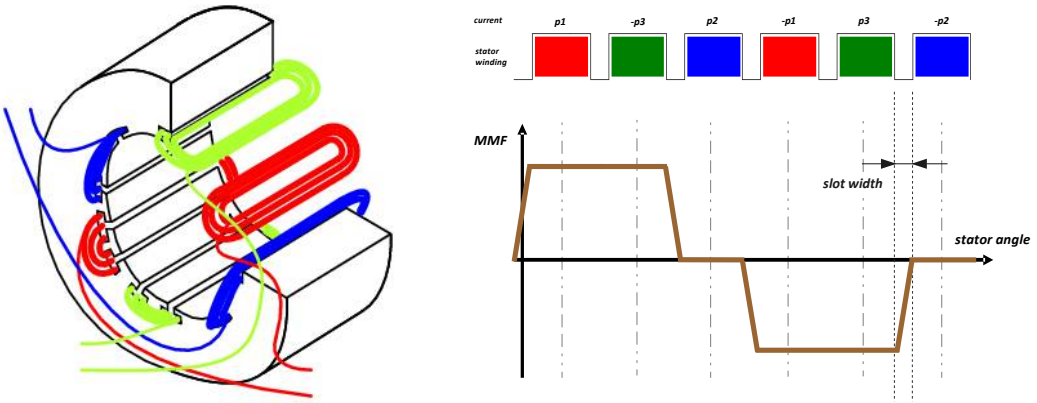

Figure 1.7 – Spatial distribution of magnetomotive force

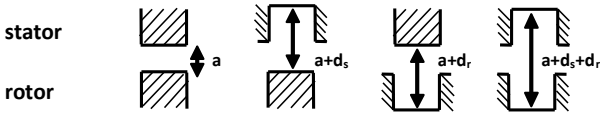

a: minimum air gap width
d_s: depth of a stator tooth
d_r: depth of a rotor tooth

Figure 1.8 – Air gap's representative width g_a in function of stator and rotor teeth's relative positions [30]

above-defined magnetomotive forces in the stator and the rotor, respectively $f_s^{mm}(t, \alpha_s)$ and $f_r^{mm}(t, \alpha_s)$ [101]:

$$B_a(t, \alpha_s) = \lambda_a(t, \alpha_s) \cdot \left[f_r^{mm}(t, \alpha_s) + f_s^{mm}(t, \alpha_s) \right] . \tag{1.3}$$

In a more general form, this expression becomes:

$$B_a(t, \alpha_s) = \frac{\mu_{\text{air}}}{g_a(t, \alpha_s)} \cdot \left[\sum_{v_r=1}^{Z_r} I_r^{\{v_r\}}(t) \cdot N_r^{\{v_r\}}(t, \alpha_s) + \sum_{v_s=1}^{\mathcal{C}_s} I_s^{\{v_r\}}(t) \cdot N_s^{\{v_r\}}(\alpha_s) \right] , \tag{1.4}$$

where r and s are the respective indices of terms referring to the rotor and the stator, Z_r the number of rotor teeth, $\mathcal{C}_s$ the number of stator phases, $I^{\{v\}}$ the current in the v-th coil and $N^{\{v\}}$ the corresponding winding function. The flux density is then directly related to the magnetic field magnitude H, by specific functions [ii] for each material. In free space though (conditions approximated in the air gap), the relation can be linearly approximated to [25]:

$$B = \mu_0 \cdot H . \tag{1.5}$$

TORQUE

Eventually, the torque applied to the rotor in the general case of an electric motor is defined by elementary contributions δT :

ii. generally non-linear, exhibiting a saturation behaviour above a certain value of H

$$\delta T = \delta\phi_s \cdot \delta\phi_r \cdot \sin(\varphi_{rs}) \ , \tag{1.6}$$

where φ_{rs} is the gap angle between the stator's and the rotor's pole axes, and $\delta\phi_s = B_s \cdot \delta A_s$ and $\delta\phi_s = B_r \cdot \delta A_r$ the flux circulations through elementary areas δA_s and δA_r, respectively. A schematic representation of flux distributions is given in Figure 1.9. Integrating the torque elementary contributions over the rotor teeth's external surfaces yields the global torque produced by the motor.

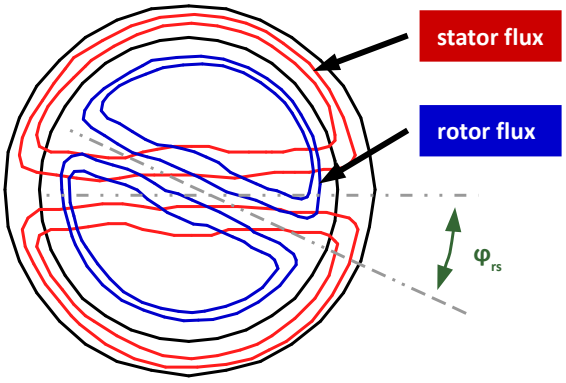

Figure 1.9 – Flux distributions

1.2.2/ SOURCES OF NOISE AND VIBRATION

The sources of vibration and noise of an electric motor are acknowledged to belong to three distinctive types [30, 90, 93, 148]:

- aerodynamic;
- mechanical;
- electromagnetic.

In a general rule, noise of aerodynamic origin is created by turbulence from the air in the motor's cooling system, and occur mostly at high speed, while mechanical sources of noise and vibration are considered negligible for electric motors in good working order. As for electromagnetic effects, they are dependent from several parameters simultaneously, such as the topologies of the poles and of the motor itself [135], and are considered as the most important sources of noise and vibrations at low frequencies (up to 10 kHz) [156]. This is why understanding these phenomena is of particular importance in the study of electric machine acoustics, and why the two other types will not be considered in this work. Amongst this, two effects are often referred to in the literature as the main sources of noise for electric machines: magnetostriction (the deformation of ferromagnetic materials due to magnetic fields) and Maxwell stresses (effects occurring at magnetic interfaces), which are detailed in Section 2.2.

A geometric comparison of magnetomotive forces and Maxwell pressure distributions has been made in [123] for a given time, and is shown in Figure 1.10. The contributions of each of the rotor's and the stator's three poles can be clearly seen with the shapes of the magnetomotive forces, as well as the stator teeths' locations and their influence on permeance.

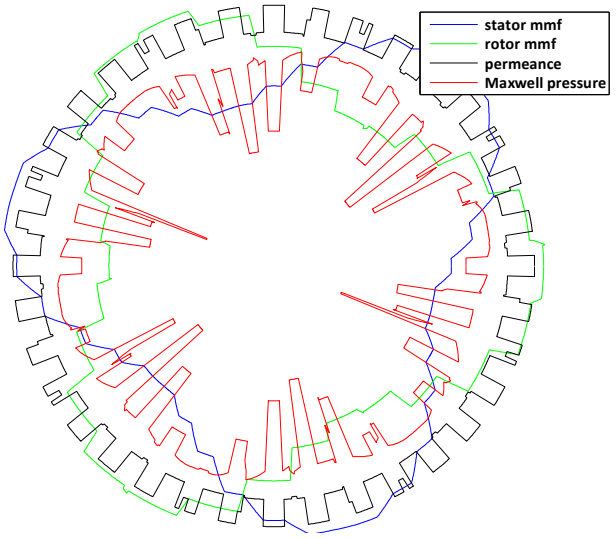

Figure 1.10 – Representation of magnetomotive forces and Maxwell pressure at a given time [123]

Although the techniques of efficient power supply currently existing enable a thorough control of the dynamic excitations generated by the input signal, this aspect has a non-negligible impact in the process of noise generation. Several works examine the influence of power supply on the creation of electromagnetic forces, such as the thorough description made in [102], presenting the so-called pulse-width modulation (PWM) in detail. As for noise generation, controlling the acoustics of electric machines stands itself for a great stake in the industry. This observation is specially important for electrically-powered transportation devices such as trains and electric cars [141], for which the acoustic impacts are crucial for sales and commercial development. In the reaction sequence illustrated in Figure 1.11, the influence of every stage on noise generation is critical.

The comprehension and the control of every electromagnetic cause of noise in an electric machine has been discussed for several decades in the literature. Although there exist several scenarios in disagreement about whether magnetostriction has a negligible influence in the noise generation process of electric motors, it has been widely acknowledged (e.g. in [50], [64], [140] and [141]) that Maxwell dynamic forces represent the main cause of vibration and noise for rotating electric machines, whereas magnetostriction is dominating in the cases of electric transformers and inductors. The present work supports this affirmation: only Maxwell pressure will be considered as dynamic excitations in the computation of responses in the next chapters.

1.2.3/ CREATION OF NOISE OF ELECTROMAGNETIC ORIGIN

The analysis and the control of noise in electric machine has recently been a topic of great interest for academic research as well as in the industry. In the case of an electric motor, the process of noise creation mainly consists in the creation of electromagnetic excitations and the mechanical response of the structure in terms of vibrations and noise emissions. Simulating this process is commonly inspired of the interactions between electromagnetic and mechanical phenomena in weak coupling (see Chapter 2), and can be divided into several steps, logically sorted as following:

1. power supply data are applied to the electromagnetic model;
2. magnetic excitations (in principle Maxwell pressure distributions) are computed from the entire electromagnetic model and projected onto the mechanical model;
3. the response of the structure is computed with the mechanical model;
4. an acoustic model enables simulating the noise generated by the structure.

This modelling process is illustrated in Figure 1.11.

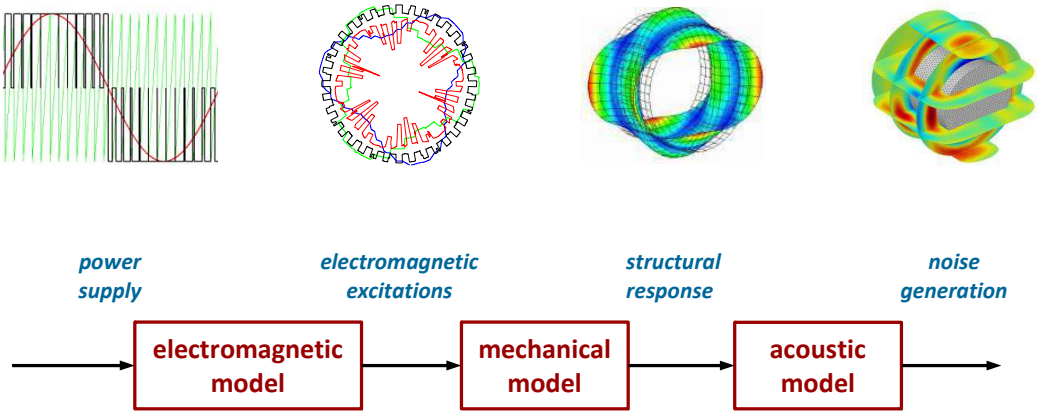

Figure 1.11 – Modelling the generation of noise in an electric machine [123, 139]

A convenient way to describe this process is to associate each model with a "transfer function". Thus, the overall transfer function and therefore the ability to simulate noise generation from power supply data is dependent from all the models: controlling the desired output requires understanding every step of the sequence. In other words, the models have all to be accurate for performing reliable noise and vibration simulations. Eventually, the main objective of this thesis is focused on the structural aspects related to electric machines, namely on simulations of vibratory behaviours.

1.3/ NOTIONS OF STRUCTURAL DYNAMICS

An important part of this work is dedicated to finite-element models. Therefore, an introduction to some theoretical notions applied to finite-element analyses is given in this section. As explained in the beginning of the chapter, the concepts presented in the remaining sections are voluntarily completed with all necessary details to enable non-specialists to apply the methods developed in the next chapters.

1.3.1/ LINEAR ELASTICITY

Some concepts about linear elasticity are introduced in this paragraph, based on the works [109] and [21]. First of all, linear elasticity refers to the fact that considered materials always behave in their elastic domain, resulting in so-called "small displacements". This assumption is valid for the entire section. Given a point M (of normal vector $\vec{n}$) on a deformable body subjected to static loading, the resulting forces at M can be expressed by

a vector $\vec{t}$. After the deformation, point M becomes M' from a displacement (u_1, u_2, u_3), with a new normal vector $\vec{n}'$ (see Figure 1.12). The default coordinate system used in this section is $(1, 2, 3)$ and is defined by the unit vectors $\vec{e}_1$, $\vec{e}_2$ and $\vec{e}_3$.

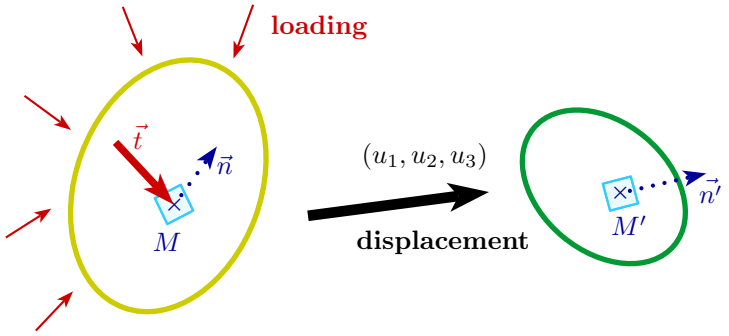

Figure 1.12 – Static displacement of point M

1.3.1.1/ ELASTICITY MATRIX

In the initial state, the loads generate a stress field of tensor $[\sigma]$ (see Figure 1.13), which can be expressed at point M on a unit volume (cube) by the relation:

$$\begin{Bmatrix} t_1 \\ t_2 \\ t_3 \end{Bmatrix} = \begin{bmatrix} \sigma_{11} & \sigma_{12} & \sigma_{13} \\ \sigma_{21} & \sigma_{22} & \sigma_{23} \\ \sigma_{31} & \sigma_{32} & \sigma_{33} \end{bmatrix} \begin{Bmatrix} n_1 \\ n_2 \\ n_3 \end{Bmatrix} . \tag{1.7}$$

The deformed state is expressed from the displacements u_i by a tensor $[\varepsilon]$ such that

$$[\varepsilon] = \begin{bmatrix} \varepsilon_{11} & \varepsilon_{12} & \varepsilon_{13} \\ \varepsilon_{21} & \varepsilon_{22} & \varepsilon_{23} \\ \varepsilon_{31} & \varepsilon_{32} & \varepsilon_{33} \end{bmatrix} , \tag{1.8}$$

whose coefficients ε_{ij} are defined by

$$\varepsilon_{ij} = \frac{1}{2}\left(\frac{\partial u_i}{\partial u_j} + \frac{\partial u_j}{\partial u_i}\right) \tag{1.9}$$

with the assumption of small displacements. In Equations (1.7) and (1.8), green terms ($i = j$) express tension-compression and red terms ($i \neq j$) shear. Also, linear elasticity implies symmetries in tensors $[\sigma]$ and $[\varepsilon]$, so that $\sigma_{ij} = \sigma_{ji}$ and $\varepsilon_{ij} = \varepsilon_{ji}$.

Another common way to express the stress and deformation fields is to use vectors $\{\sigma\}$ and $\{\varepsilon\}$ so that [iii]

iii. It can be noted that the order of the terms in these vectors is not universal, and might differ from one convention to the other.

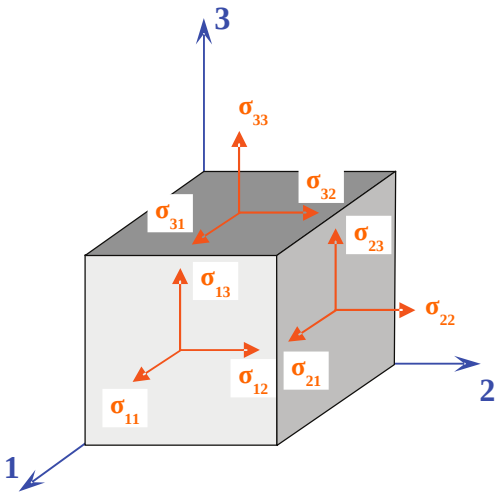

Figure 1.13 – Stress field at point M

$$\{\sigma\} = \begin{Bmatrix} \sigma_{11} \\ \sigma_{22} \\ \sigma_{33} \\ \tau_{23} \\ \tau_{31} \\ \tau_{12} \end{Bmatrix}$$

and

$$\{\varepsilon\} = \begin{Bmatrix} \varepsilon_{11} \\ \varepsilon_{22} \\ \varepsilon_{33} \\ \gamma_{23} \\ \gamma_{31} \\ \gamma_{12} \end{Bmatrix},$$

where $\tau_{ij} = \sigma_{ij}$ and $\gamma_{ij} = 2 \cdot \varepsilon_{ij}$. By the means of a fourth-order tensor $[C]$, Hooke's law links vector $\{\sigma\}$ to $\{\varepsilon\}$ by the general relation

$$\begin{Bmatrix} \sigma_{11} \\ \sigma_{22} \\ \sigma_{33} \\ \\ \sigma_{23} \\ \sigma_{13} \\ \sigma_{12} \end{Bmatrix} = \begin{bmatrix} C_{1111} & C_{1122} & C_{1133} & C_{1123} & C_{1113} & C_{1112} \\ C_{2211} & C_{2222} & C_{2233} & C_{2223} & C_{2213} & C_{2212} \\ C_{3311} & C_{3322} & C_{3333} & C_{3323} & C_{3313} & C_{3312} \\ & & & & & \\ C_{2311} & C_{2322} & C_{2333} & C_{2323} & C_{2313} & C_{2312} \\ C_{1311} & C_{1322} & C_{1333} & C_{1323} & C_{1313} & C_{1312} \\ C_{1211} & C_{1222} & C_{1233} & C_{1223} & C_{1213} & C_{1212} \end{bmatrix} \begin{Bmatrix} \varepsilon_{11} \\ \varepsilon_{22} \\ \varepsilon_{33} \\ \\ 2 \cdot \varepsilon_{23} \\ 2 \cdot \varepsilon_{13} \\ 2 \cdot \varepsilon_{12} \end{Bmatrix}, \tag{1.10}$$

where matrix $[C]$, also called *elasticity matrix*, can be reduced in linear elasticity to the form:

$$[C] = \begin{bmatrix} C_{11} & C_{12} & C_{13} & C_{14} & C_{15} & C_{16} \\ & C_{22} & C_{23} & C_{24} & C_{25} & C_{26} \\ & & C_{33} & C_{34} & C_{35} & C_{36} \\ & & & C_{44} & C_{45} & C_{46} \\ & \text{sym.} & & & C_{55} & C_{56} \\ & & & & & C_{66} \end{bmatrix} . \tag{1.11}$$

In its reverse form, Equation (1.10) defines the *compliance matrix* $[S] = [C]^{-1}$, such that:

$$\begin{Bmatrix} \varepsilon_{11} \\ \varepsilon_{22} \\ \varepsilon_{33} \\ 2 \cdot \varepsilon_{23} \\ 2 \cdot \varepsilon_{13} \\ 2 \cdot \varepsilon_{12} \end{Bmatrix} = \begin{bmatrix} S_{11} & S_{12} & S_{13} & S_{14} & S_{15} & S_{16} \\ & S_{22} & S_{23} & S_{24} & S_{25} & S_{26} \\ & & S_{33} & S_{34} & S_{35} & S_{36} \\ & & & S_{44} & S_{45} & S_{46} \\ & \text{sym.} & & & S_{55} & S_{56} \\ & & & & & S_{66} \end{bmatrix} \begin{Bmatrix} \sigma_{11} \\ \sigma_{22} \\ \sigma_{33} \\ \sigma_{23} \\ \sigma_{13} \\ \sigma_{12} \end{Bmatrix} . \tag{1.12}$$

1.3.1.2/ CHANGES OF COORDINATE SYSTEMS

Hooke's law (1.10) and the associated equations are expressed in the coordinate system – or basis – $(1, 2, 3)$ defined in the beginning of the section. Rewriting this system in another coordinate system involves changing the basis of $[C]$. The new elasticity matrix $[C']$ is then computed with

$$[C'] = [\mathcal{T}_d(\theta_d)]\,[C]\,[\mathcal{T}_d(\theta_d)]^{\mathsf{T}} , \tag{1.13}$$

where the transfer matrix $[\mathcal{T}_d(\theta_d)]$ expresses a rotation of angle θ_d about axis d. It may be observed that applying successive rotations around different axes is not equivalent if the sequence is changed [iv]. Depending on the direction considered, matrices $[\mathcal{T}_1(\theta_1)]$, $[\mathcal{T}_2(\theta_2)]$ and $[\mathcal{T}_3(\theta_3)]$ are detailed as following:

$$[\mathcal{T}_1(\theta_1)] = \begin{bmatrix} 1 & 0 & 0 & 0 & 0 & 0 \\ 0 & \cos^2(\theta_1) & \sin^2(\theta_1) & 2\cos(\theta_1)\sin(\theta_1) & 0 & 0 \\ 0 & \sin^2(\theta_1) & \cos^2(\theta_1) & -2\cos(\theta_1)\sin(\theta_1) & 0 & 0 \\ 0 & -\cos(\theta_1)\sin(\theta_1) & \cos(\theta_1)\sin(\theta_1) & \cos^2(\theta_1)-\sin^2(\theta_1) & 0 & 0 \\ 0 & 0 & 0 & 0 & \cos(\theta_1) & -\sin(\theta_1) \\ 0 & 0 & 0 & 0 & \sin(\theta_1) & \cos(\theta_1) \end{bmatrix} , \tag{1.14a}$$

$$[\mathcal{T}_2(\theta_2)] = \begin{bmatrix} \cos^2(\theta_2) & 0 & \sin^2(\theta_2) & 0 & -2\cos(\theta_2)\sin(\theta_2) & 0 \\ 0 & 1 & 0 & 0 & 0 & 0 \\ \sin^2(\theta_2) & 0 & \cos^2(\theta_2) & 0 & 2\cos(\theta_2)\sin(\theta_2) & 0 \\ 0 & 0 & 0 & \cos(\theta_2) & 0 & \sin(\theta_2) \\ \cos(\theta_2)\sin(\theta_2) & 0 & -\cos(\theta_2)\sin(\theta_2) & 0 & \cos^2(\theta_2)-\sin^2(\theta_2) & 0 \\ 0 & 0 & 0 & -\sin(\theta_2) & 0 & \cos(\theta_2) \end{bmatrix} \tag{1.14b}$$

iv. i.e. rotating around axis 1 and then around 2 is not equivalent to rotating around axis 2 and then around 1.

and

$$[\mathcal{T}_3(\theta_3)] = \begin{bmatrix} \cos^2(\theta_3) & \sin^2(\theta_3) & 0 & 0 & 0 & 2\cos(\theta_3)\sin(\theta_3) \\ \sin^2(\theta_3) & \cos^2(\theta_3) & 0 & 0 & 0 & -2\cos(\theta_3)\sin(\theta_3) \\ 0 & 0 & 1 & 0 & 0 & 0 \\ 0 & 0 & 0 & \cos(\theta_3) & -\sin(\theta_3) & 0 \\ 0 & 0 & 0 & \sin(\theta_3) & \cos(\theta_3) & 0 \\ -\cos(\theta_3)\sin(\theta_3) & \cos(\theta_3)\sin(\theta_3) & 0 & 0 & 0 & \cos^2(\theta_3)-\sin^2(\theta_3) \end{bmatrix}. \quad (1.14c)$$

1.3.1.3/ MATERIAL PROPERTIES

Defining elasticity matrices and densities for the materials of a given structure are necessary and sufficient prerequisites for many types of finite-element simulations. In its most general form (1.11), matrix $[C]$ defines an *anisotropic* or *triclinic* material with its 21 independent coefficients. Considering possible symmetries that the material properties may express reduces the complexity of matrix $[C]$ and leads to specific material denominations.

A material whose properties are symmetric with respect to a plane is called *monoclinic*. If this plane is for instance (1,2), the elasticity matrix can be reduced to the form:

$$[C^{\text{mono}}] = \begin{bmatrix} C_{11} & C_{12} & C_{13} & 0 & 0 & C_{16} \\ & C_{22} & C_{23} & 0 & 0 & C_{26} \\ & & C_{33} & 0 & 0 & C_{36} \\ & & & C_{44} & C_{45} & 0 \\ & \text{sym.} & & & C_{55} & 0 \\ & & & & & C_{66} \end{bmatrix}, \quad (1.15)$$

defined by 13 independent coefficients. If the properties have an additional symmetry plane which is perpendicular to the first [v], the material is called *orthotropic*. In this case, the elasticity matrix can be reduced to the form:

$$\left[C^{\text{ortho}}\right] = \begin{bmatrix} C_{11} & C_{12} & C_{13} & 0 & 0 & 0 \\ & C_{22} & C_{23} & 0 & 0 & 0 \\ & & C_{33} & 0 & 0 & 0 \\ & & & C_{44} & 0 & 0 \\ & \text{sym.} & & & C_{55} & 0 \\ & & & & & C_{66} \end{bmatrix}, \quad (1.16)$$

defined by 9 independent coefficients. Unlike triclinic and monoclinic properties, orthotropic materials can be defined by 9 explicit engineering constants E_i, G_{ij} and ν_{ij} (respectively Young's, shear moduli and Poisson's ratios) from the compliance matrix, such as:

[v] which is equivalent to 3 symmetry planes perpendicular to each other

$$\left[S^{\text{ortho}}\right] = \left[C^{\text{ortho}}\right]^{-1} = \begin{bmatrix} \frac{1}{E_1} & \frac{-\nu_{12}}{E_1} & \frac{-\nu_{13}}{E_1} & 0 & 0 & 0 \\ \frac{-\nu_{21}}{E_2} & \frac{1}{E_2} & \frac{-\nu_{23}}{E_2} & 0 & 0 & 0 \\ \frac{-\nu_{31}}{E_3} & \frac{-\nu_{32}}{E_3} & \frac{1}{E_3} & 0 & 0 & 0 \\ 0 & 0 & 0 & \frac{1}{G_{23}} & 0 & 0 \\ 0 & 0 & 0 & 0 & \frac{1}{G_{13}} & 0 \\ 0 & 0 & 0 & 0 & 0 & \frac{1}{G_{12}} \end{bmatrix} . \tag{1.17}$$

The symmetry of the matrix then leads to the reciprocity relation:

$$\nu_{ij} = \nu_{ji} \cdot \frac{E_i}{E_j} . \tag{1.18}$$

Orthotropic material properties can be simplified if they have a revolution symmetry around an axis. In this case, the properties are equivalent in any plane perpendicular to this axis, and the material is called *transversely isotropic*. If for instance the axis of revolution is 3, the elasticity matrix takes the form:

$$\left[C^{\text{iso-transv}}\right] = \begin{bmatrix} C_{11} & C_{12} & C_{13} & 0 & 0 & 0 \\ & C_{11} & C_{13} & 0 & 0 & 0 \\ & & C_{33} & 0 & 0 & 0 \\ & & & C_{44} & 0 & 0 \\ & \text{sym.} & & & C_{44} & 0 \\ & & & & & C_{66} \end{bmatrix} \tag{1.19}$$

where

$$C_{66} = \frac{C_{11} - C_{12}}{2} .$$

In other terms, the following relation is verified:

$$\left[C^{\text{iso-transv}}\right] = \left[\mathcal{T}_3\left(\theta_3\right)\right] \left[C^{\text{iso-transv}}\right] \left[\mathcal{T}_3\left(\theta_3\right)\right]^{\intercal} , \tag{1.20}$$

and shows the insensitivity of $\left[C^{\text{iso-transv}}\right]$ for any rotation about direction 3. Therefore, the only 5 independent engineering constants that describe the material are $E_1 = E_2$, E_3, $G_{23} = G_{13}$, $\nu_{13} = \nu_{23}$ and ν_{12}. The isotropy in plane (1,2) induced by the revolution symmetry therefore leads to:

$$G_{12} = \frac{E_1}{2 \cdot (1 + \nu_{12})} .$$

Eventually, if the properties are independent from any changes of axes or coordinate systems and therefore have no specific directions, the material is called *isotropic*. In this case, the elasticity matrix can be expressed with Lamé's coefficients λ and μ, and takes the form:

$$\left[C^{\text{iso}}\right] = \begin{bmatrix} \lambda+2\mu & \lambda & \lambda & 0 & 0 & 0 \\ & \lambda+2\mu & \lambda & 0 & 0 & 0 \\ & & \lambda+2\mu & 0 & 0 & 0 \\ & & & \mu & 0 & 0 \\ & \text{sym.} & & & \mu & 0 \\ & & & & & \mu \end{bmatrix} . \tag{1.21}$$

To put things in a nutshell, Table 1.1 summarises the simplifications of material properties between each types, and where the symbol "$\perp$" means "orthogonal".

	abbreviation	**symmetries / previous**	**symmetries / *tricl***	**independent coefficients**
triclinic	***tricl***	-	none	21
monoclinic	***mono***	***tricl*** + 1 plane	***tricl*** + 1 plane	13
orthotropic	***ortho***	***mono*** + 1 plane $\perp$	***tricl*** + 3 planes $\perp$	9 engineering constants
transversely isotropic	***iso-transv***	***ortho*** + 1 rev. axis	***tricl*** + 3 planes $\perp$ + 1 rev. axis	5 engineering constants
isotropic	***iso***	all directions identical		2 engineering constants

Table 1.1 – Summary of material simplifications

1.3.1.4/ STIFFNESS AND MASS MATRICES

For representing a given structure, a finite-element model is based on stiffness and mass matrices for the description of mechanical properties in a mathematical system. Established from the discretisation of strain energy formulations in the system, the stiffness matrix $[\mathcal{K}^e]$ of each element is defined by the expression

$$[\mathcal{K}^e] = \iiint_{\Omega^e} [\mathcal{B}^e]^{\mathsf{T}} [C] [\mathcal{B}^e] \, \mathrm{d}\Omega \, , \tag{1.22}$$

where Ω^e is the volume of the element, $\mathrm{d}\Omega$ an infinitesimal volume such that $\mathrm{d}\Omega = \mathrm{d}x\mathrm{d}y\mathrm{d}z$, $[C]$ the elasticity matrix of the element's material, and $[\mathcal{B}^e]$ a deformation interpolation matrix. As for mass properties, the element's mass matrix is derived from the system's kinetic energy. The complete definitions of stiffness and mass matrices goes beyond the frame of this study. Still, further details which are necessary for the elaboration of some methods described in the next chapters are given in Appendix A.1.

1.3.2/ EQUATIONS OF VIBRATION AND MODAL DECOMPOSITION

This paragraph elaborates on the here-above presented general notions and introduces some equations of structural dynamics, based on [15] and [113].

1.3.2.1/ FREE VIBRATIONS OF A CONSERVATIVE SYSTEM

In the case of a conservative or non-dissipative system (and therefore neglecting damping effects) and with no external loads, the dynamic behaviour of a structure composed of N degrees of freedom is described by the system [15]:

$$[\mathcal{M}]\{\ddot{q}(t)\} + [\mathcal{K}]\{q(t)\} = \{\mathbf{0}_{N,1}\} \ , \tag{1.23}$$

where $[\mathcal{M}]$ and $[\mathcal{K}]$ are the structure's mass and stiffness matrices (respectively positive-definite and positive semi-definite), and where the displacements $q(t)$ are expressed with respect to the time t, so that:

$$\ddot{q}(t) = \frac{\mathrm{d}\dot{q}}{\mathrm{d}t}(t) = \frac{\mathrm{d}^2 q}{\mathrm{d}t^2}(t) \ . \tag{1.24}$$

Looking for a solution of the form $\{q(t)\} = \{\phi\}\exp(s \cdot t)$ with $\{\phi\} \neq \{\mathbf{0}_{N,1}\}$ leads to the expression:

$$\left([\mathcal{K}] + s^2[\mathcal{M}]\right)\{\phi\} = \{\mathbf{0}_{N,1}\} \ . \tag{1.25}$$

Then, resolving Equation (1.25) yields N non-trivial, distinct solutions j (all real) with $s_j = \mathbf{i}\omega_j$:

$$\left([\mathcal{K}] - \omega_j^2[\mathcal{M}]\right)\{\phi\}_j = \{\mathbf{0}_{N,1}\} \ , \tag{1.26}$$

from which the j-th eigenvalue ω_j^2 is related to the so-called natural frequency f_j with

$$f_j = \frac{\omega_j}{2 \cdot \pi} \ . \tag{1.27}$$

Resolving the singular system (1.26) for a given eigenvalue ω_j^2 defines a mode shape (also called deformed shape) $\{\phi\}_j$ with an arbitrary proportional factor. A solution for choosing convenient proportional factors is to normalise each mode shape. This normalisation can be made to maximum unity, or with respect to the mass or stiffness matrix. This respectively corresponds to:

$$\max\{\phi\}_j = 1 \ , \tag{1.28a}$$

$$\{\phi\}_i^{\mathsf{T}}[\mathcal{M}]\{\phi\}_j = \delta_{ij} \tag{1.28b}$$

and

$$\{\phi\}_i^{\mathsf{T}}[\mathcal{K}]\{\phi\}_j = \delta_{ij} \ , \tag{1.28c}$$

where the Kronecker symbol δ_{ij} equals 1 if $i = j$ and 0 if $i \neq j$. Therefore, each mode shape $\{\phi_m\}_j$ normalised with respect to its modal mass is computed with

$$\{\phi_m\}_j = \frac{\{\phi\}_j}{\sqrt{\{\phi\}_j^\intercal [\mathcal{M}] \{\phi\}_j}} \ . \tag{1.29}$$

Associated the j-th mode shape to the corresponding natural frequency f_j constitutes the structure's j-th normal vibration mode. Eventually, the set of all modes corresponds to the system's *modal base*, and the *modal matrix* $[\phi]$ is built by concatenating the $N \times 1$ vectors $\{\phi\}_j$. Such modes describe the structure's particular abilities to be deformed: applying excitations in a way that tend to deform it in a similar way as a mode shape and near the corresponding natural frequency would create a resonance phenomenon, called "modal coincidence" (or "appropriation"). This would result in an amplification of the deformation magnitudes, and thus to possible noise, damage or undesired vibrations. Being able to predict the modal behaviour of any given structure is therefore a key issue in structural dynamics simulations. It can be noted as well that the modes of a conservative system have real values only, and are often called *normal* modes.

1.3.2.2/ VIBRATIONS OF A DAMPED SYSTEM: HYSTERETIC DAMPING

There exist several natures of damping in finite-element analyses. The two forms that are detailed in this paragraph are hysteretic and viscous damping. Considering a system in established harmonic state, the hysteretic form of damping (also referred to as "structural") is modelled with imaginary stiffness values in $[\mathcal{K}^*] = \left[\mathcal{K} + \mathbf{i}\mathcal{K}^h\right]$, such as in the following free-vibration equation [62]:

$$[\mathcal{M}] \{\ddot{q}(t)\} + [\mathcal{K}^*] \{q(t)\} = \{\mathbf{0}_{N,1}\} \ , \tag{1.30}$$

where matrix $\left[\mathcal{K}^h\right]$ represents the out-of-phase stiffness components as described in Section 1.5. The corresponding eigenvalue problem has then j distinct solutions

$$\left([\mathcal{K}^*] + \mathbf{S}_j^* [\mathcal{M}]\right) \{\phi^*\}_j = \{\mathbf{0}_{N,1}\} \ , \tag{1.31}$$

such that

$$\{\phi^*\}_j = \{\phi_R\}_j + \mathbf{i} \{\phi_I\}_j \ , \tag{1.32}$$

and where the eigenvalues $\mathbf{S}_j^* = \left(s_j^*\right)^2$ are expressed as functions of undamped circular frequencies ω_j and so-called modal loss factors η_j:

$$\mathbf{S}_j^* = -\omega_j^2 \cdot (1 + \mathbf{i}\eta_j) \ . \tag{1.33}$$

Premultiplying Equation (1.31) by the transposed conjugate $\{\phi^*\}_j^\intercal$ of $\{\phi^*\}_j$ leads to the system:

$$\mathbf{S}_j^* = -\frac{\{\phi^*\}_j^\intercal [\mathcal{K}^*] \{\phi^*\}_j}{\{\phi^*\}_j^\intercal [\mathcal{M}] \{\phi^*\}_j} \ , \tag{1.34}$$

which is decomposed into a real ($\Re$) and an imaginary ($\Im$) parts:

$$\Re\left(\mathbf{S}_j^*\right) = -\omega_j^2 \qquad \text{and} \qquad \Im\left(\mathbf{S}_j^*\right) = -\omega_j^2 \cdot \eta_j \,.$$

Finally, the damped natural frequencies $\check{f}_j$ and the modal loss factors can be expressed with the expressions [143, 62]:

$$\check{f}_j = \left| \frac{1}{2\pi} \cdot \Im\left(s_j^*\right) \right| \tag{1.35a}$$

and

$$\eta_j = \frac{\Im\left(\mathbf{S}_j^*\right)}{\Re\left(\mathbf{S}_j^*\right)} = \frac{\{\phi_R\}_j^\intercal \left[\mathcal{K}^h\right] \{\phi_R\}_j - \{\phi_I\}_j^\intercal \left[\mathcal{K}^h\right] \{\phi_I\}_j}{\{\phi_R\}_j^\intercal \left[\mathcal{K}\right] \{\phi_R\}_j - \{\phi_I\}_j^\intercal \left[\mathcal{K}\right] \{\phi_I\}_j} \,, \tag{1.35b}$$

where the sign of s_j^* is chosen arbitrarily from

$$s_j^* = \pm\sqrt{\mathbf{S}_j^*} \,.$$

If the structure's hysteretic damping coefficients are considered low (i.e. lower than 20% according to [62] and [138]), the mode shapes $\{\phi^*\}_j$ can be approximated with their real parts $\{\phi_R\}_j$. This can be computed from a normal-mode solution in a quicker way than for the complex system. In this case, Equation (1.34) can be re-written as:

$$\omega_j^2 \cdot (1 + \mathbf{i}\eta_j) = \frac{\{\phi_R\}_j^\intercal \left[\mathcal{K}\right] \{\phi_R\}_j}{\{\phi_R\}_j^\intercal \left[\mathcal{M}\right] \{\phi_R\}_j} + \mathbf{i}\frac{\{\phi_R\}_j^\intercal \left[\mathcal{K}^h\right] \{\phi_R\}_j}{\{\phi_R\}_j^\intercal \left[\mathcal{M}\right] \{\phi_R\}_j} \,, \tag{1.36}$$

from which the natural frequencies $\check{f}_j$ are reduced to their real form $f_j = \omega_j/2\pi$ with

$$\omega_j^2 = \frac{\{\phi_R\}_j^\intercal \left[\mathcal{K}\right] \{\phi_R\}_j}{\{\phi_R\}_j^\intercal \left[\mathcal{M}\right] \{\phi_R\}_j} \,. \tag{1.37}$$

Also, the expression of the modal loss factor is simplified to

$$\eta_j = \frac{\{\phi_R\}_j^\intercal \left[\mathcal{K}^h\right] \{\phi_R\}_j}{\{\phi_R\}_j^\intercal \left[\mathcal{K}\right] \{\phi_R\}_j} \,, \tag{1.38}$$

where $\{\phi_R\}_j^\intercal \left[\mathcal{K}\right] \{\phi_R\}_j$ represents the structure's total strain energy for the mode j.

1.3.2.3/ VIBRATIONS OF A DAMPED SYSTEM: VISCOUS DAMPING

The second form of damping is of viscous nature. Considering viscous damping in a matrix $[\mathcal{D}]$ and taking into account dynamic forces applied to the structure transforms Equation (1.23) into [113]:

$$\left[\mathcal{M}\right] \{\ddot{q}\,(t)\} + \left[\mathcal{D}\right] \{\dot{q}\,(t)\} + \left[\mathcal{K}\right] \{q\,(t)\} = \{\mathcal{F}\,(t)\} \,, \tag{1.39}$$

where matrix $[\mathcal{K}]$ has only real values (no hysteretic damping).

With the aid of the previously-defined modal matrix $[\phi]$ (possibly truncated to the h first modes such that $h \leq N$), generalised modal coordinates u can be computed at a given time t with:

$$\{q\} = [\phi]\{u\} \ . \tag{1.40}$$

Then, by pre-multiplying Equation (1.39) by $[\phi]^\intercal$ leads to:

$$[\phi]^\intercal [\mathcal{M}] [\phi] \{\ddot{u}\} + [\phi]^\intercal [\mathcal{D}] [\phi] \{\dot{u}\} + [\phi]^\intercal [\mathcal{K}] [\phi] \{u\} = [\phi]^\intercal \{\mathcal{F}\} \ , \tag{1.41}$$

where matrices

$$[\phi]^\intercal [\mathcal{M}] [\phi] = \begin{bmatrix} \mathfrak{m}_1 & & & 0 \\ & \mathfrak{m}_2 & & \\ & & \ddots & \\ 0 & & & \mathfrak{m}_h \end{bmatrix} \tag{1.42a}$$

and

$$[\phi]^\intercal [\mathcal{K}] [\phi] = \begin{bmatrix} \mathfrak{k}_1 & & & 0 \\ & \mathfrak{k}_2 & & \\ & & \ddots & \\ 0 & & & \mathfrak{k}_h \end{bmatrix} \tag{1.42b}$$

are diagonal. It can be noted that normalising the mode shapes with respect to the modal mass (see Equation (1.29)) in the first place leads to

$$m_j = 1 \qquad j \in [\![1, h]\!] \ ,$$

and thus to

$$[\phi]^\intercal [\mathcal{M}] [\phi] = \mathbf{I}_{h,h} = \begin{bmatrix} 1 & & & 0 \\ & 1 & & \\ & & \ddots & \\ 0 & & & 1 \end{bmatrix} \ .$$

For the matrix

$$[\phi]^\intercal [\mathcal{D}] [\phi] = \begin{bmatrix} \mathfrak{d}_1 & & & 0 \\ & \mathfrak{d}_2 & & \\ & & \ddots & \\ 0 & & & \mathfrak{d}_h \end{bmatrix}$$

to be diagonal as well, the so-called Basile's condition needs to be satisfied [113]. This requirement is fulfilled if either $[\mathcal{D}]$ can be written under the form of a proportional damping (sufficient condition), i.e. if real factors α and β can be found such that:

$$[\mathcal{D}] = \alpha [\mathcal{K}] + \beta [\mathcal{M}] \ , \tag{1.43}$$

or if Caughey's condition is verified (necessary and sufficient), as

$$[\mathcal{D}] [\mathcal{M}]^{-1} [\mathcal{K}] = [\mathcal{K}] [\mathcal{M}]^{-1} [\mathcal{D}] \ . \tag{1.44}$$

In this case, the system (1.41) can be decoupled into h equations

$$\ddot{u}_j + 2\zeta_j\omega_j\dot{u}_j + \omega_j^2 u_j = \Gamma_j \qquad j \in [\![1, h]\!] \,, \tag{1.45}$$

where for each row j,

$$\omega_j = \sqrt{\frac{\mathfrak{k}_j}{\mathfrak{m}_j}} = 2 \cdot \pi \cdot f_j \tag{1.46a}$$

is the natural circular frequency and

$$\zeta_j = \frac{\mathfrak{d}_j}{2 \cdot \sqrt{\mathfrak{m}_j \mathfrak{k}_j}} = \frac{\eta_j}{2} \tag{1.46b}$$

the modal damping ratio. Also, the modal participation factor Γ_j relative to the mode shape $\{\phi\}_j$ is defined by

$$\Gamma_j = \frac{\{\phi\}_j^\intercal \{\mathcal{F}\}}{\{\phi\}_j^\intercal [\mathcal{M}] \{\phi\}_j} = \frac{\mathfrak{F}_j}{\mathfrak{m}_j} \,, \tag{1.46c}$$

where $\mathfrak{F}_j$ and $\mathfrak{m}_j$ are the j-th mode's generalised force and modal mass, respectively.

1.3.2.4/ ENFORCED VIBRATIONS

Determining a system's enforced response corresponds to exhibiting a particular solution in Equation (1.39), for which the excitations are considered harmonic:

$$\{\mathcal{F}\} = \left\{\tilde{\mathcal{F}}\right\} \cdot \exp\left(\mathbf{i}\omega t\right) \,. \tag{1.47}$$

In this case, the particular solution is written

$$\{q\} = \{\tilde{q}\} \cdot \exp\left(\mathbf{i}\omega t\right) \,, \tag{1.48}$$

such that the so-called *direct response* is computed with

$$\{\tilde{q}\left(\omega\right)\} = \left(-\omega^2 [\mathcal{M}] + \mathbf{i}\omega [\mathcal{D}] + [\mathcal{K}]\right)^{-1} \left\{\tilde{\mathcal{F}}\right\} \,. \tag{1.49}$$

In spite of the ability to compute responses with any damping matrices, Equation (1.49) requires important computation resources if the studied system has numerous degrees of freedom. Should Basile's condition be satisfied and Equation (1.39) decoupled in the form (1.41), then the solution $\{\tilde{q}\left(\omega\right)\}$ could be written with the expression of *modal superposition response*:

$$\{\tilde{q}\left(\omega\right)\} = \sum_{j=1}^{h} \frac{\{\phi\}_j^\intercal \left\{\tilde{\mathcal{F}}\right\} \{\phi\}_j}{-\omega^2 \mathfrak{m}_j + \mathbf{i}\omega \mathfrak{d}_j + \mathfrak{k}_j} \,, \tag{1.50}$$

which is equivalent to

$$\{\tilde{q}\left(\omega\right)\} = \sum_{j=1}^{h} \frac{\{\phi\}_j^\intercal \left\{\tilde{\mathcal{F}}\right\} \{\phi\}_j}{\mathfrak{m}_j \cdot \left(-\omega^2 + 2\mathbf{i}\zeta_j\omega\omega_j + \omega_j^2\right)} \,. \tag{1.51}$$

These formulations are much quicker to compute than the matrix inversion in Equation (1.49), but are based on a truncated basis (of the h first modes) and require Basile's condition to be verified. Eventually, the effect of modal truncature can be mitigated by adding a static correction factor to Equation (1.51), also called *static residual vectors*. In its completed form, the expression becomes [134]:

$$\{\tilde{q}(\omega)\} = \sum_{j=1}^{h} \frac{\{\phi\}_j^\intercal \{\tilde{\mathcal{F}}\} \{\phi\}_j}{\mathfrak{m}_j \cdot \left(-\omega^2 + 2\mathbf{i}\zeta_j\omega\omega_j + \omega_j^2\right)} - \left(\sum_{j=1}^{h} \frac{\{\phi\}_j^\intercal \{\phi\}_j}{\mathfrak{m}_j \cdot \omega_j^2} - [\mathcal{K}]^{-1}\right) \{\tilde{\mathcal{F}}\} \ . \quad (1.52)$$

1.3.3/ COMPONENT MODE SYNTHESIS

1.3.3.1/ STATIC CONDENSATION

Several mathematical methods have been developed in order to reduce the number of DOFs in a finite-element model. One of the most common for static reduction is the so-called Guyan method, initially developed in [4] and re-used in [71]. The idea is to condensate the entire system into a limited number of DOFs where the reduced stiffness, mass, damping and force values recreate the global dynamic state. The system defined by Equation (1.39) is first treated as a static problem

$$[\mathcal{K}]\{q\} = \{\mathcal{F}\} \ . \quad (1.53)$$

A set of master-DOFs $\mathbb{M}$ is defined where the reduced system's properties are to be expressed. The set of slave-DOFs $\mathbb{S}$ is the complementary set of $\mathbb{M}$ in the global system and gathers the DOFs that will not be visible any longer in the matrices after condensation. The rows and columns are permuted in Equation (1.53) such that:

$$\begin{bmatrix} \mathcal{K}_{mm} & \mathcal{K}_{ms} \\ \mathcal{K}_{sm} & \mathcal{K}_{ss} \end{bmatrix} \begin{Bmatrix} q_m \\ q_s \end{Bmatrix} = \begin{Bmatrix} \mathcal{F}_m \\ \mathcal{F}_s \end{Bmatrix} \ , \quad (1.54)$$

where indices m and s refer to sets $\mathbb{M}$ and $\mathbb{S}$, respectively. This sub-structured system can be decomposed into

$$[\mathcal{K}_{mm}]\{q_m\} + [\mathcal{K}_{ms}]\{q_s\} = \{\mathcal{F}_m\} \quad (1.55a)$$

and

$$[\mathcal{K}_{sm}]\{q_m\} + [\mathcal{K}_{ss}]\{q_s\} = \{\mathcal{F}_s\} \ . \quad (1.55b)$$

Assuming the non-singularity of $[\mathcal{K}_{ss}]$, the slave DOF displacements can be isolated in Sub-system (1.55b)

$$\{q_s\} = [\mathcal{K}_{ss}]^{-1}\{\mathcal{F}_s\} - [\mathcal{K}_{ss}]^{-1}[\mathcal{K}_{sm}]\{q_m\} \quad (1.56)$$

and substituted into Sub-system (1.55a) so that

$$[\mathcal{K}_r]\{q_m\} = \{\mathcal{F}_r\} \ , \quad (1.57)$$

where the reduced stiffness matrix $[\mathcal{K}_r]$ and the reduced force vector $\{\mathcal{F}_r\}$ respectively stand for

$$[\mathcal{K}_r] = [\mathcal{K}_{mm}] - [\mathcal{K}_{ms}] [\mathcal{K}_{ss}]^{-1} [\mathcal{K}_{sm}] \tag{1.58a}$$

and

$$\{\mathcal{F}_r\} = \{\mathcal{F}_m\} - [\mathcal{K}_{ms}] [\mathcal{K}_{ss}]^{-1} \{\mathcal{F}_s\} \ . \tag{1.58b}$$

In terms of computation costs, this reduction is performed rather quickly by current common finite-element solvers, as the only costly operation is the inversion of matrix $[\mathcal{K}_{ss}]$. Finally, the reduction of the global System (1.39) is performed by a projection with a static transformation matrix

$$[\mathcal{W}_s] = \begin{bmatrix} \mathbf{I}_{m,m} \\ -\mathcal{K}_{ss}^{-1}\mathcal{K}_{sm} \end{bmatrix} , \tag{1.59}$$

where $[\mathbf{I}_{m,m}]$ is the $m \times m$ identity matrix. The projection is written as

$$[\mathcal{W}_s]^\intercal [\mathcal{M}] [\mathcal{W}_s] \{\ddot{q}_m\} + [\mathcal{W}_s]^\intercal [\mathcal{C}] [\mathcal{W}_s] \{\dot{q}_m\} + [\mathcal{W}_s]^\intercal [\mathcal{K}] [\mathcal{W}_s] \{q_m\} = [\mathcal{W}_s]^\intercal \{\mathcal{F}\} \ , \tag{1.60}$$

is equivalent to the reduced system

$$[\mathcal{M}_r] \{\ddot{q}_m\} + [\mathcal{C}_r] \{\dot{q}_m\} + [\mathcal{K}_r] \{q_m\} = \{\mathcal{F}_r\} \tag{1.61}$$

and defines a so-called "super-element", standing for the entire initial structure but defined by reduced matrices.

1.3.3.2/ DYNAMIC CONDENSATION

Similarly to the Guyan condensation method, one of the most common approaches for dynamic sub-structuring is the so-called "Craig-Bampton" method [6]. In this case, the global system is projected into a basis of normal modes computed after clamping the chosen master- (or interface-) DOFs. The dynamic transformation matrix $[\mathcal{W}_d]$ is defined as an enrichment of $[\mathcal{W}_s]$:

$$[\mathcal{W}_d] = \begin{bmatrix} \mathbf{I}_{m,m} & \mathbf{0}_{m,s} \\ -\mathcal{K}_{ss}^{-1}\mathcal{K}_{sm} & \phi_{ss} \end{bmatrix} , \tag{1.62}$$

where $[\mathbf{0}_{m,s}]$ is the $m \times s$ null matrix and $[\phi_{ss}]$ the modal basis at slave- (or internal-) DOFs defined by

$$\left([\mathcal{K}_{ss}] - \omega_{ss,j}^2 [\mathcal{M}_{ss}] \right) \{\phi_{ss}\}_j = \{\mathbf{0}_{s,1}\} \tag{1.63}$$

for each eigenvalue j. Eventually, norming the modal basis with unitary modal mass (see Equation (1.29)) and condensing matrices $[\mathcal{K}]$ and $[\mathcal{M}]$ with $[\mathcal{W}_d]$ leads to

$$[\mathcal{W}_d]^\intercal [\mathcal{K}] [\mathcal{W}_d] = \begin{bmatrix} \mathcal{K}_r & \mathbf{0}_{m,s} \\ \mathbf{0}_{s,m} & \Lambda_{ss} \end{bmatrix} \tag{1.64a}$$

and

$$[\mathcal{W}_d]^\intercal [\mathcal{M}] [\mathcal{W}_d] = \begin{bmatrix} \mathcal{M}_r & \mathcal{M}_{CB}^\intercal \\ \mathcal{M}_{CB} & \mathbf{I}_{s,s} \end{bmatrix} , \tag{1.64b}$$

where $[\mathcal{K}_r]$ and $[\mathcal{M}_r]$ are the statically-reduced (i.e. Guyan) matrices computed with Equation (1.61), $[\Lambda_{ss}]$ the spectral matrix corresponding to the modal basis and $[\mathcal{M}_{CB}]$ the matrix defined by

$$[\mathcal{M}_{CB}] = \left[\phi_{ss}^\intercal \left(\mathcal{M}_{sm} - \mathcal{M}_{ss}\mathcal{K}_{ss}^{-1}\mathcal{K}_{sm}\right)\right] . \tag{1.65}$$

1.4/ NOTIONS OF DETERMINISTIC MODEL UPDATING

Performing mechanical simulations does not always exactly correspond to the real behaviour of the structure. This is why updating processes are applied, in order to optimise the simulation model and improve its representativeness by minimising the discrepancies with the reference behaviour. Deterministic updating processes involve only discrete optimisation parameters (such as elastic constants), whereas stochastic processes manage probability densities instead. This section will detail some aspects of the deterministic model updating basic theory.

1.4.1/ PRINCIPLE

A common criterion used to update finite-element models is to compare two modal bases. Then, an iterative algorithm aims at adapting the parameters in order to decrease the criterion value until reaching a convergence threshold. The optimisation sequence is illustrated in Figure 1.14 and described as following:

1. computation of the initial FE model's modal basis

2. selection of updating parameters

3. measurement/computation of the reference modal basis

4. selection of updating responses

- model updating iterations:

4.1. computation of the correlation estimators

4.2. comparison with the convergence threshold

- if reached: end of the updating process
- if not reached: update FE model with stages **4.2.1.** through **4.2.4.**

4.2.1. computation of sensitivity values

4.2.2. application of changes to the FE parameters

4.2.3. computation of the new FE modal basis

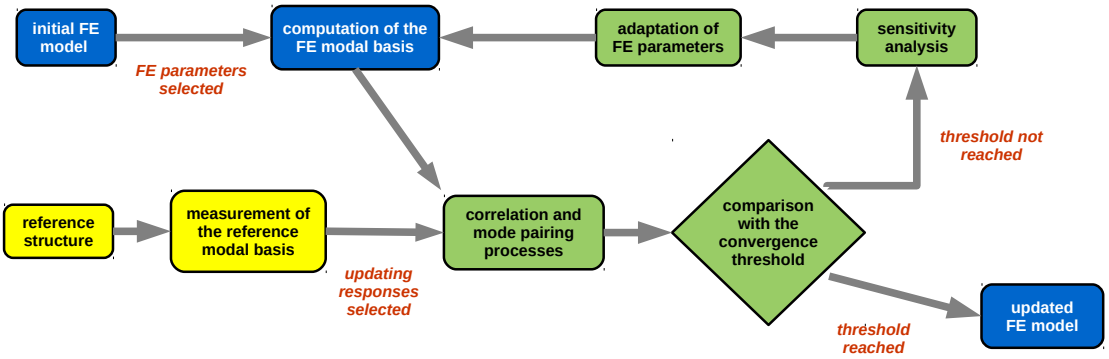

Figure 1.14 – Flowchart of a model updating process [140]

4.2.4. loop to stages **4.1.** and **4.2.**

The choice of the optimisation parameters and responses needs to be done prior to the updating iterations. The parameters are the properties of the FE model that will be updated (typically 2D-element thicknesses, elastic properties, mass densities, ...) whereas the responses are the objectives that the process will attempt to recreate with the FE modal basis (typically natural frequencies or frequency response functions). The stages **4.1.**, **4.2.1.** and **4.2.2.** (respectively the computation of correlation estimators, the sensitivity analysis and the adaptation of the FE model) stand for the core of the presented model updating algorithm and are therefore detailed throughout the following paragraphs.

1.4.2/ MODAL CORRELATION

The comparison of two modal bases can be made according to several criteria [26] and is part of model updating processes. One convenient way to estimate such modal correlation is to compare each vibration mode of the first model to each of the second. Therefore, two matrices are computed: $[\Delta f]$ and $[MAC]$, of size $M_1 \times M_2$, and where M_1 and M_2 respectively stand for the numbers of modes considered for the first and the second structures. Each component $\Delta f\left(m_{e,i}, m_{a,j}\right)$ of the matrix $[\Delta f]$ expresses the relative difference between the frequency of the first structure's i-th vibration mode $m_{1,i}$ and the second structure's j-th mode $m_{2,j}$, and is defined by the relation:

$$\Delta f\left(m_{1,i}, m_{2,j}\right) = \frac{f_{1,i} - f_{2,j}}{f_{1,i}} \,, \tag{1.66}$$

where $f_{1,i}$ et $f_{2,j}$ are the natural frequencies corresponding to the modes $m_{1,i}$ and $m_{2,j}$, respectively. In addition to this, the similarities between the shapes of the modes $m_{1,i}$ and $m_{2,j}$ (respectively called $\{\phi_{1,i}\}$ and $\{\phi_{2,j}\}$) are determined according to the so-called MAC (*Modal Assurance Criterion*), by the expression [69]:

$$MAC\left(m_{1,i}, m_{2,j}\right) = \frac{\left|\{\phi_{1,i}\}^{\mathsf{T}}\{\phi_{2,j}\}\right|^2}{\{\phi_{1,i}\}^{\mathsf{T}}\{\phi_{1,i}\}\{\phi_{2,j}\}^{\mathsf{T}}\{\phi_{2,j}\}} \,. \tag{1.67}$$

Therefore, two mode shapes are characterised by a MAC value of 0% if they are orthogonal or of 100% if identical. A perfectly updated model leads to a $[MAC]$ matrix of diagonal values at 100% and others at 0%. In practice, geometrically-coincident nodes are

associated to ensure that $\{\phi_{1,i}\}$ and $\{\phi_{2,j}\}$ have the same sizes. In the remaining paragraphs of this section, the indices "1" and "2" will refer to the reference and the updated structures, respectively.

Once the matrices $[\Delta f]$ and $[MAC]$ are computed, each mode $m_{1,i}$ is paired to the mode $m_{2,j}$ with highest MAC value. The pairs are taken into account in the correlation if their respective MAC value is above a fixed threshold, called t_{MAC}. All the other mode pairs are discarded from the correlation process. For N_{mp} mode pairs in a given correlation, the entities $\overline{|\Delta f|}$ and $\overline{MAC}$ are defined by the expressions:

$$\overline{|\Delta f|} = \frac{1}{N_{mp}} \cdot \sum_{q=1}^{N_{mp}} \left|\Delta f\left(m_{1,q}, m_{2,q}\right)\right| \tag{1.68}$$

and

$$\overline{MAC} = \frac{1}{N_{mp}} \cdot \sum_{q=1}^{N_{mp}} MAC\left(m_{1,q}, m_{2,q}\right) \ , \tag{1.69}$$

where $m_{1,q}$ and $m_{2,q}$ are the modes composing the q-th pair.

1.4.3/ SENSITIVITY ANALYSIS AND MODEL UPDATING

The sensitivity analysis aims at identifying the parameters of the FE model which have the highest influence on the selected responses. Although there exist other definitions (see e.g. [149, 150]), the $N_r \times N_p$ differential sensitivity matrix $[\mathcal{S}]$ (also referred to as the "gradient") is composed of coefficients $\mathcal{S}_{ab}$ computed from the slopes of responses r_a with respect to changes in parameter p_b:

$$\mathcal{S}_{ab} = \frac{\delta r_a}{\delta p_b} \ . \tag{1.70}$$

Selecting natural frequencies and MAC values as optimisation responses leads to non-linear relations between r_a and p_b. One of the existing practical solutions for circumventing this complexity relies on linearisation approaches, as described in [149] or in the works of [122], in order to minimise the objective function in an iterative way.

Then, the vector $\{\Delta r\} = \{r_1\} - \{r_2\}$ is built from the selected responses. For instance, choosing (e.g. lowest) $\mathfrak{A}$ natural frequencies and (e.g. highest) $\mathfrak{B}$ MAC values leads to [149]

$$\{r_1\} = \begin{Bmatrix} f_{1,1} \\ f_{1,2} \\ \vdots \\ f_{1,\mathfrak{A}} \\ MAC\left(m_{1,1}, m_{1,1}\right) = 100\% \\ MAC\left(m_{1,2}, m_{1,2}\right) = 100\% \\ \vdots \\ MAC\left(m_{1,\mathfrak{B}}, m_{1,\mathfrak{B}}\right) = 100\% \end{Bmatrix} \quad , \quad \{r_2\} = \begin{Bmatrix} f_{2,1} \\ f_{2,2} \\ \vdots \\ f_{2,\mathfrak{A}} \\ MAC\left(m_{1,1}, m_{2,1}\right) \\ MAC\left(m_{1,2}, m_{2,2}\right) \\ \vdots \\ MAC\left(m_{2,\mathfrak{B}}, m_{2,\mathfrak{B}}\right) \end{Bmatrix}$$

and

$$\{\Delta r\} = \begin{Bmatrix} f_{1,1} - f_{2,1} \\ f_{1,2} - f_{2,2} \\ \vdots \\ f_{1,\mathfrak{A}} - f_{2,\mathfrak{A}} \\ 1 - MAC\left(m_{2,1}, m_{2,1}\right) \\ 1 - MAC\left(m_{2,2}, m_{2,2}\right) \\ \vdots \\ 1 - MAC\left(m_{2,\mathfrak{B}}, m_{2,\mathfrak{B}}\right) \end{Bmatrix} .$$

The general relation

$$\{\Delta r\}_i = [\mathcal{S}]_i \{\Delta p\}_i \tag{1.71}$$

is established for the i-th iteration with $\{\Delta p\}_i = \{p\}_i - \{p\}_{i-1}$, where $\{p\}_i$ is the parameter vector to be computed at the end of the iteration (i.e. after updating) and $\{p\}_{i-1}$ the parameter vector computed in the previous iteration. Thus, pseudo-inverting $[\mathcal{S}]_i$ leads to the relative parameter changes $\{\Delta p\}_i$ with the expression

$$[\mathcal{S}]_i^{\#} \{\Delta r\}_i = \{\Delta p\}_i \ , \tag{1.72}$$

where the pseudo-inverse $[\mathcal{S}]_i^{\#}$ of $[\mathcal{S}]_i$ is defined by

$$[\mathcal{S}]_i^{\#} = \left([\mathcal{S}]_i^{\intercal} [\mathcal{S}]_i\right)^{-1} [\mathcal{S}]_i^{\intercal} \tag{1.73a}$$

if $N_r < N_p$, or

$$[\mathcal{S}]_i^{\#} = [\mathcal{S}]_i^{\intercal} \left([\mathcal{S}]_i^{\intercal} [\mathcal{S}]_i\right)^{-1} \tag{1.73b}$$

if $N_r > N_p$. In practice, other pseudo-inversion methods can be thought of (see e.g. [149, 150]) but will not be detailed here. Eventually, iterating these operations as described in Figure 1.14 completes the model updating procedure.

It can be noted that in some cases, the process fails to terminate according to the specified convergence threshold. This is why in practice, the optimisation is interrupted if either the number of iterations reaches a specified limit or if the parameter changes (values of $\{\Delta p\}_i$) fall below a given variation threshold.

1.5/ NOTIONS OF VISCOELASTICITY

Polymers such as the resins used in electric machines are usually described by viscoelastic properties [100]. A viscoelastic material is characterised by several specificities in its stress-strain behaviour, as detailed in the works of Kaliappan [100]:

- hysteresis (i.e. delay in response to enforced stresses or strains);
- creep ability (i.e. increasing strain for constant enforced stress);
- stress relaxation ability (i.e. decreasing stress for a constant enforced strain).

This section briefly introduces some knowledge about the theory of viscoelasticity.

1.5.1/ DYNAMIC-MECHANICAL PROPERTIES

The above-mentioned hysteretic specificity corresponds to an out-of-phase dynamic response of the material subjected to periodic perturbations [13, 100, 133]. For example, enforcing sinusoidal stress to a one-dimensional sample of viscoelastic material results in strain with a phase lag δ in steady state, as illustrated in Figure 1.15.

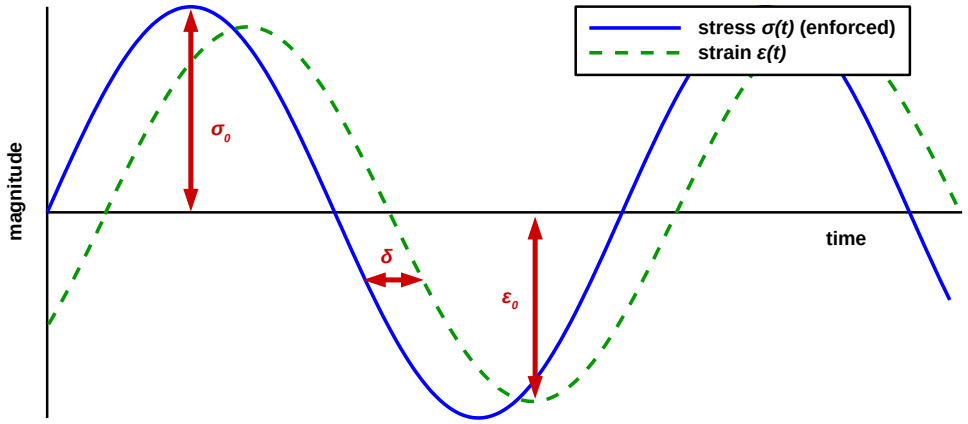

Figure 1.15 – Evolutions of stress and strain through time for a viscoelastic material [100, 152]

Therefore, the dynamic stress $\sigma(t)$ and strain $\varepsilon(t)$ can be described with the following expressions:

$$\sigma(t) = \sigma_0 \cdot \sin(\omega \cdot t + \delta) \tag{1.74}$$

and

$$\varepsilon(t) = \varepsilon_0 \cdot \sin(\omega \cdot t) \ , \tag{1.75}$$

where t is the time and ω the circular frequency. Expanding Equation (1.74) in

$$\sigma(t) = \sigma_0 \cdot \cos(\delta) \cdot \sin(\omega \cdot t) + \sigma_0 \cdot \sin(\delta) \cdot \cos(\omega \cdot t) \tag{1.76}$$

enables separating the stress's in-phase and out-of-phase terms. Then, dividing Equation (1.76) by Equation (1.75) enables introducing the moduli E' and E'' for representing the respective in-phase and out-of-phase parts as

$$E' = \frac{\sigma_0}{\varepsilon_0} \cdot \cos(\delta) \tag{1.77}$$

and

$$E'' = \frac{\sigma_0}{\varepsilon_0} \cdot \sin(\delta) \tag{1.78}$$

so that

$$\sigma(t) = \varepsilon_0 \cdot E' \cdot \sin(\omega \cdot t) + \varepsilon_0 \cdot E'' \cdot \cos(\omega \cdot t) \ . \tag{1.79}$$

Then, assimilating the in-phase part as real and the out-of-phase part as imaginary leads to a complex expression of a Young's modulus:

$$E^* = \frac{\sigma}{\varepsilon} = \frac{\sigma_0}{\varepsilon_0} \cdot (\cos(\delta) + \mathbf{i} \cdot \sin(\delta)) \ , \tag{1.80}$$

or in other terms

$$E^* = E' + \mathbf{i} \cdot E'' \ . \tag{1.81}$$

Expression (1.81) can be seen as the association of a *storage modulus* E' (describing the material's ability to store and release potential energy when subjected to deformation) and a *loss modulus* E'' (associated with the dissipation of deformation energy in heat). Finally, the ratio of E'' over E' can be seen as

$$\frac{E''}{E'} = \tan(\delta) \tag{1.82}$$

and corresponds to a mechanical damping ratio, also called *loss factor*.

1.5.2/ TEMPERATURE AND FREQUENCY

The dynamic behaviour of viscoelastic materials has been introduced as a temporal dependency in Equations (1.74) and (1.75). For the rest of this thesis, this variability will be rather seen as a dependency to the frequency f, so that $f = \omega/(2\cdot\pi)$. In addition, the dependency of viscoelastic properties to the temperature T will be also accounted for [154].

Every viscoelastic material used in this study is considered homogeneous and isotropic, and thus defined by a Young's modulus, a shear modulus and a Poisson's ratio. In this whole work, Poisson's effects are assumed independent from temperature and frequency. This assumption seems reasonable as suggested in [53], [76], [120] and [128] and judging from the small discrepancies observed in the experimental identification presented in [155]. Therefore, the complex expressions of a Young's modulus $E^*(T, f)$ is related to a complex shear modulus $G^*(T, f)$ by the linear function inspired from isotropic elasticity [18]:

$$G^*(T, f) = \frac{E^*(T, f)}{2 \cdot (1 + \nu)} \ , \tag{1.83}$$

where ν is the material's Poisson's ratio. Therefore, Equation (1.81) can be re-written in terms of shear moduli:

$$G^*(T, f) = G'(T, f) + \mathbf{i} \cdot G''(T, f) \ , \tag{1.84}$$

or in its equivalent form

$$G^*(T, f) = G'(T, f) \cdot (1 + \mathbf{i} \cdot \eta(T, f)) \ , \tag{1.85}$$

where

$$\eta = \tan(\delta) \ . \tag{1.86}$$

INTERMEDIATE CONCLUSION

This chapter has described some notions concerning electric machines, materials science and structural dynamics. The next chapter will elaborate on these bases, and detail the state-of-the-art knowledge in understanding and modelling the dynamic behaviour of electric motor stators. In addition to this, simulation analyses will be presented as pre-requisite results for the following chapters.

2

Concerning electric machine stators

In spite of the reliable experience existing for combustion engines, modelling electric motors requires understanding and predicting the influence of very specific phenomena, as explained in the previous chapter. Several research works have been published during the last two decades about the simulation of electric machines' vibratory behaviours and the design of low-noise electric motors, also referred to as "vibro-acoustically efficient". This chapter aims at exposing what the state-of-the-art is in the comprehension of the phenomena involved in the mechanical behaviour of an entire electric machine, putting an emphasis on the stator. This will be detailed throughout Sections 2.1 and 2.2, dealing with each of these aspects separately: the overall structure and the geometry of an electric machine as well as dynamic excitations. In addition to these literature reviews, other notions standing for prerequisite knowledge for the next chapters will be introduced with simulation analyses in Sections 2.3 and 2.4, respectively focusing on material property sensitivities and modelling guidelines for piece connections.

2.1 / Geometry-based phenomena

The geometries, dimensions and assemblies of the components of a stator have a great influence on its overall mechanical behaviour. Although this chapter does not focus on design guidelines for electric machines, it seems interesting to understand the technological choices that have been motivated by the research of optimum efficiency. An overview of the main usual pieces composing an electric motor has been given in Figure 1.1.

Manufacturing process of an electric machine

The way the pieces composing an electric machine are manufactured and assembled may have an important influence on its overall mechanical behaviour. Although it could not be seen as exhaustive, Van der Giet and Hameyer [107] have presented a manufacture sequence for electric machine stators:

1. the steel sheets are stacked and held under pressure;
2. the stack contour is cut by means of wire-electro discharge machining;
3. the copper windings are placed into the stator slots;

4. the stack with the windings are impregnated with insulating resin;
5. the magnetic core is pressed into a frame;
6. the housing, end-shields and rotor are assembled with the stator.

The homogeneous pieces such as frame, gearbox pinions and end-shields are generally produced by casting and machining, which will not be presented here. As their materials are usually standard metals and alloys of known properties, modelling these pieces separately is not as complex as entire structures; the assembly conditions are likely to have a strong influence on the overall dynamic behaviour.

STATOR GEOMETRY

Several studies aimed at showing the influence of a switched-reluctance machine's stator geometry on its vibratory behaviour. Pillay and Cai [44, 55] have compared four finite-element models, illustrated in Figure 2.1:

1. laminated magnetic core
2. laminated magnetic core fixed in a frame on the whole lateral surface
3. laminated magnetic core fixed in a frame with 4 keys (nodes merged)
4. stator with a ribbed frame and a terminal box

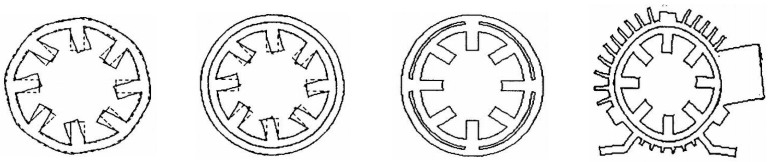

Figure 2.1 – Models of a switched-reluctance machine's stator (side views of mode shapes [55])

Some of the results of this comparison were the following:

- the yoke's and frame's thicknesses have a significant effect on the overall stator's natural frequencies;
- the frame ribs' effects can be seen as additional mass for low-frequency modes and additional stiffness for high-frequency modes.

Similarly, Cai et al. [57] have analysed the behaviours of a series of laminated stacks according to their side shapes, whereas Hong et al. [66] have looked for optimum designs of yokes and teeth in order to reduce the overall vibration magnitudes. Illustrations of these comparisons are shown in Figure 2.2 and Figure 2.3, respectively.

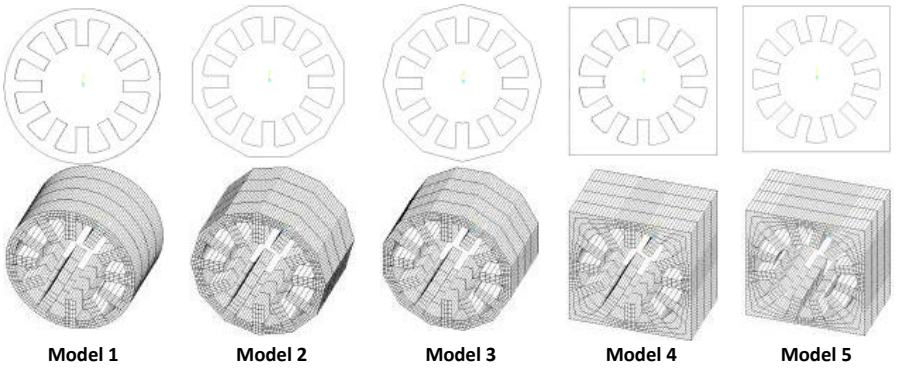

Figure 2.2 – Laminated stack shapes [57]

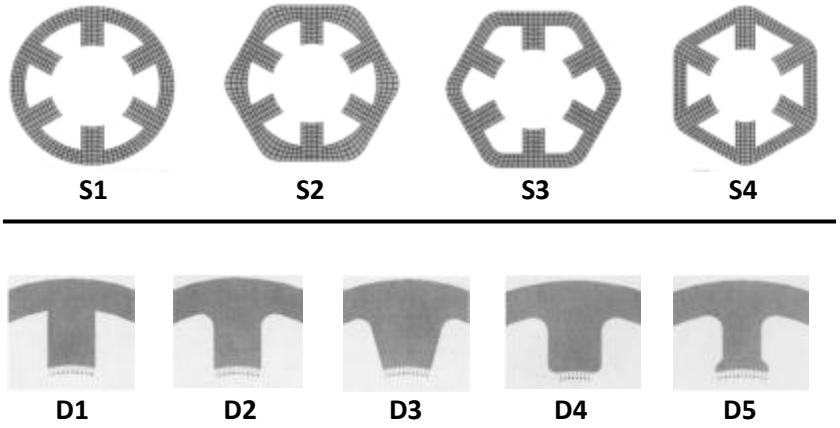

Figure 2.3 – Yoke and teeth shapes [66]

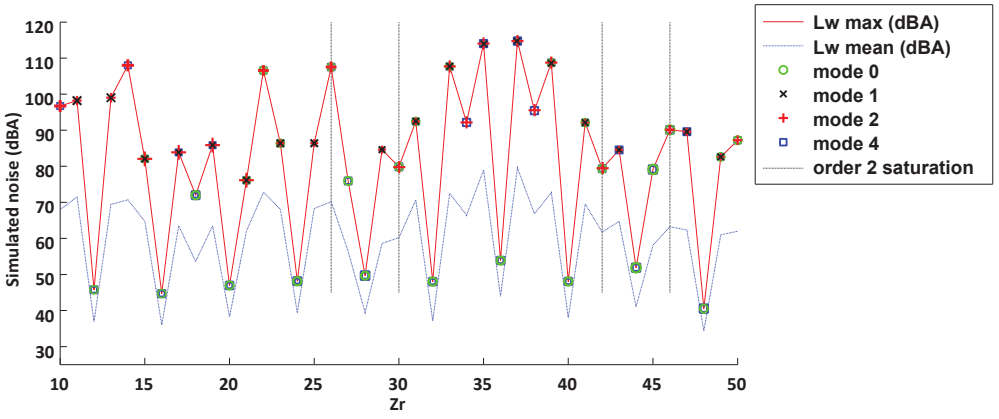

Figure 2.4 – Evolution of radiated noise with respect to Z_r and for $Z_s = 36$ [112]

In the first case, models 4 and 5 (in Figure 2.2) are considered more interesting by the authors from a vibratory point of view. Judging from their increased stiffness compared to the other models, their natural frequencies are higher (this therefore reduces the probability of coincidence between stator modes and electromagnetic excitations) and the response magnitudes are lower. In the second case (Figure 2.3), Hong et al. [66] propose the "optimum" combination S2-D3, without presenting the consequences of other choices. It seems necessary to note that such results might be difficult to apply in an industrial strategy, because of other technological constraints such as powertrain volume and mass limitations.

Number of teeth

In addition to their geometries, choosing appropriate numbers of stator and rotor teeth is a key issue for the design and the dimensioning of energy-efficient and low-noise electric motors. Garvey et al. [33] explain that stator teeth undergo both radial and tangential electromagnetic excitations. As a general rule for induction (i.e. asynchronous) machines, Le Besnerais et al. [102] indicate that the number of rotor teeth Z_r has an influence on both tooth harmonics and harmonic orders, whereas the number of stator teeth Z_s only on harmonic orders. Arkkio [31] advises not to design a rotor with an odd value for Z_r, as it would create a magnetic imbalance. Le Besnerais et al. [112] have looked for optimum $Z_r - Z_s$ combinations in order to reduce electromagnetic noise, based on the analytical design rules proposed in the Ph.D. thesis of Le Besnerais [101]. The evolution of the overall noise radiated by a machine with with $Z_s = 36$ is plotted with respect to Z_r in Figure 2.4.

As a conclusion, multiples of 4 for both Z_r and Z_s are suggested for reducing the noise radiated by the entire machine. It can be seen in Figure 2.4 that for $Z_s = 36$, multiples of 4 for Z_r generate indeed lower noise than for other values. It can be noted that this study is limited to 4-pole machines and does not account for either saturation effects or tooth-dependent structural parameters such as winding stiffness. Finally, the fact the results are bound to a specific case study implies that they are dependent from the machine's speed range and natural frequencies. They should be therefore used carefully.

Number of pole pairs

Assuming that high-pole-number electric machines have an important potential of noise generation, Cassoret et al. [129] have analysed the influence of the number of poles on the emission of electromagnetic noise. Their results show that for modes of spatial orders greater than 2 (see Appendix B.4), the magnitudes of stator vibrations for a given input power are proportional to $p^{3.588}$ (where p is the number of pole pairs), and that the stator's natural frequencies are proportional to $1/p$ [vi]. In the case of an electric machine fed by a variable-frequency converter, the authors recommend a low value of p and a low input frequency in order to reduce the emitted acoustic level. Analytic formulations enabled to compute acoustic power values with respect to a series of pole pair numbers for a given Maxwell pressure of magnitude $2,000\,\mathrm{N \cdot m^{-1}}$ and frequency 1,000 Hz. The values are

vi. There exist other dependencies for describing the evolution of natural frequencies. Other analytical expressions for the computation of stator vibrations are presented in Section 3.1.

gathered in Table 2.1, to which the analytical expressions presented in Section 3.1 can be associated.

p [−]	S [V · A]	R [cm]	L [V · A]	D^2L [cm^3]	Y_0 [nm]	Y_2 [nm]	σ [−]	S_e [cm^2]	L_{W0} [dB]	L_{W2} [dB]
1	20,000	7.03	22.1	43.69	2.3	38	0.79	156	37.4	61.7
2	10,000	8.62	13.5	40.27	5.7	375	0.82	110	43.9	80.2
4	5,000	10.57	8.3	37.12	14.3	3,682	0.87	80	50.5	98.9

p: number of pole pairs
S: motor's apparent power
R: stator teeth's inner radius
L: machine length
D: machine diameter
Y_i: magnitude of i-th order mode shape
σ: acoustic radiation factor
S_e: external vibrating area
L_{Wi}: acoustic power of i-th order mode

Table 2.1 – Radiated acoustic power with respect to p [129]

SKEWED TEETH AND SLOTS

So-called tooth harmonics are due to magnetomotive force's trapezoid-shape as well as local variation of air gap permeance while the rotor is spinning (see Figure 1.7 and Figure 1.8). An existing method for controlling such harmonics in an electric machine's generated noise spectrum is to skew the slots of the stator or the rotor, as illustrated in Figure 2.5.

Apart from its magnitude-attenuation property, skewing the rotor or the stator has a strong influence on the overall electric machine's mechanical behaviour [61, 96]. Firstly, rotor and stator teeth get into conjunction in a more localised and progressive way if either the stator or the rotor is skewed. This would tend to smooth the air-gap-width variations in the expression of flux density (1.4) (and therefore decrease the magnitudes of high-frequency terms in the excitation spectrum), but would make possible for the electromagnetic excitations to coincide with torsion modes. Secondly, the reluctant torque (and thus the corresponding additional excitation harmonics) can be reduced by skewing the structure, as it has been shown in the works of De Gersem et al. [70]. More importantly, skewed windings create axial excitations of possibly high magnitudes (especially in transient states), that non-skewed structures would not.

END-SHIELDS

It has been asserted by Fiedler [93] that for a same overall volume, small-diameter and long-length motors tend to be more silent than large-diameter and short-length ones (described by the author as "sausage" and "pan-cake"-like geometries). This has been corroborated by Garvey et al. [77], stating also that the total length is limited by the rotor's stability. Also, the works of Cai et al. [63] have shown that including windings and end-shields (also called "end-bells" or "end-plates") in the finite-element model of an assembled switched-reluctance motor was essential for the simulation of a modal basis. Their statement that the mass the windings bring to the motor tends to offset the additional

skewed stator

skewed rotor

Figure 2.5 – Skewed stator and rotor [161, 36]

stiffness from the end-shields in the computation of natural frequencies seems however invalid in the general case, and could not be backed up by their experimental analyses.

Concerning more specifically the influence of end-shields on a stator's dynamic behaviour, Anwar et al. [54] have drawn several interesting conclusions:

- Adding end-shields to a stator globally increases its natural frequencies and modifies the mode shapes.
- Although no information is given about any direction for considering it, this stiffening effect is observed to be non-uniform along the stator length. An illustration of the so-called effective stiffness is given in Figure 2.6.
- The additional stiffness depends from the ratio of stator length over external diameter, the materials and the type of connection between the pieces.

Cai et al. [63] have observed a similar stiffening effect, although their works had not exhibited any variations along the stator length.

2.2/ DYNAMIC EXCITATIONS

Simulating and controlling the electromagnetic excitations (whose origins have been introduced in Section 1.2) that electric machine stators are subjected to are vast research topics. Modelling electromagnetic phenomena has been rather well adapted to the industry, as there exist nowadays several commercial software programmes able to perform accurate simulations on relatively large structures.

As it has been outlined in Section 2.1, the electromagnetic excitations are applied to the stator at the air gap and do not have any axial component unless the stator or the rotor is skewed. Considering non-skewed machines therefore simplifies the excitations to radial and tangential parts only, and enables performing two-dimensional simulations in order to represent the entire structure. Amongst others, the works of Brudny [32], Pillay and Cai [44], Cai et al. [57] and Rainer et al. [126] tend to corroborate the facts that tangential efforts primarily take part in the creation of torque on the rotor, whereas radial efforts applied to the stator are the main cause of noise and vibration in an electric machine. On the

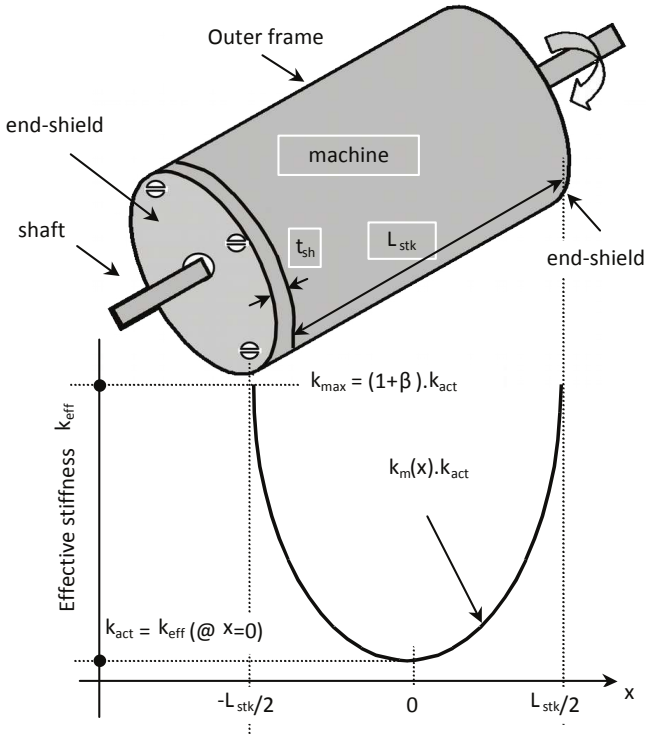

Figure 2.6 – Variation of stiffness along the stator length [54]

contrary, Humbert et al. [141] suggest not to neglect tangential efforts in noise and vibration simulations on electric machines, especially when dealing with entire powertrains. The reason for this is the fact that both components of the excitations have a similar degree of influence on the overall acoustic emission; while the impact of radial efforts is direct, the vibrations induced by tangential efforts are transmitted to the neighbouring parts of the powertrains (e.g. the gearbox) that in turn, generate noise.

Although the main objective of this document is about mechanical modelling and not electromagnetic simulations, understanding the nature of the excitations the mechanical structures are subjected to is a key stage in the computation of vibration and noise of electromagnetic origin (presented in Subsection 1.2.3). This section will present a literature review of magneto-mechanical coupling theories including magnetostrictive forces, the influence of excitation harmonics and eccentricities and existing methods of excitation processing. Also, the formulations of electromagnetic excitations used in finite-element simulations will be detailed.

2.2.1/ MAGNETO-MECHANICAL COUPLINGS

When dealing with an electric machine stator, the interface between the electromagnetic and the mechanical-structural domains is the air gap, which is therefore where the couplings have to be analysed. A relatively large number of studies have been focused on representing magneto-mechanical couplings. Amongst other existing theories, the strongly-coupled two-dimensional local approach developed by Delaere et al. [42] is based on energy minimisation in a finite-element system and aims at determining reluctance forces (i.e. related to Maxwell pressure) applied to a given structure. These forces

are intended to be applied as inputs in a mechanical harmonic solution. The main expressions are summarised as following, and further details about magneto-mechanical coupling theories can be found in [28].

The elastic energy U and magnetic energy W are defined with

$$U = \frac{1}{2} \{q\}^\intercal [\mathcal{K}] \{q\} \tag{2.1a}$$

and

$$W = \frac{1}{2} \{A\}^\intercal [\mathcal{G}] \{A\} \ , \tag{2.1b}$$

where $\{q\}$ and $\{A\}$ are the displacements and the magnetic vector potentials, and $[\mathcal{K}]$ and $[\mathcal{G}]$ the structure's elastic and magnetic stiffness matrices, respectively. The global static equation system is then constituted with the coupling matrices $[\mathfrak{C}]$ and $[\mathfrak{D}]$ such as

$$\begin{bmatrix} \mathcal{G} & \mathfrak{D} \\ \mathfrak{C} & \mathcal{K} \end{bmatrix} \begin{Bmatrix} A \\ q \end{Bmatrix} = \begin{Bmatrix} T \\ R \end{Bmatrix} \ , \tag{2.2}$$

where vectors $\{T\}$ and $\{R\}$ respectively represent the forces of magnetic and mechanical origins. Differentiating the total energy $U + W$ with respect to $\{A\}$ and $\{q\}$ then leads to the expressions of the coupling matrices:

$$[\mathfrak{D}] = \frac{1}{2} \{q\}^\intercal \frac{\partial [\mathcal{K}(A)]}{\partial \{A\}} \tag{2.3a}$$

and

$$[\mathfrak{C}] = \frac{1}{2} \{A\}^\intercal \frac{\partial [\mathcal{G}(q)]}{\partial \{q\}} \ , \tag{2.3b}$$

from what $[\mathfrak{D}]$ is recognised as the dependency of mechanical parameters towards the magnetic field (such as magnetostrictive effects, as described in Subsection 2.2.2) and $[\mathfrak{C}]$ the dependency of magnetic parameters towards the displacements.

As the authors of [42] explain that resolving the entire system (2.2) requires important computer resources, they suggest to neglect the magnetostrictive effects in the first place. This means that none of the elastic properties of the structure depend on the vector potential, and therefore $[\mathfrak{D}] = [0]$. In this case, resolving the first subsystem of Equation (2.2) yields

$$\{A\} = [\mathcal{G}]^{-1} \{T\} \ , \tag{2.4}$$

from what reluctant forces F_{rel} are computed:

$$\{F_{\text{rel}}\} = -[\mathfrak{C}] \{A\} = -\frac{1}{2} \{A\}^\intercal \frac{\partial [\mathcal{G}(q)]}{\partial \{q\}} \{A\} \ . \tag{2.5}$$

In this case, Equation (2.2) can be decoupled in

$$\begin{bmatrix} \mathcal{G} & 0 \\ 0 & \mathcal{K} \end{bmatrix} \begin{Bmatrix} A \\ q \end{Bmatrix} = \begin{Bmatrix} T \\ R + F_{\text{rel}} \end{Bmatrix} . \tag{2.6}$$

In comparison to this, Lee et al. [67] and Schlensok et al. [97] recommend to consider the magneto-mechanical coupling as weak, due to the fact that dynamic response simulations on electrical powertrains generate displacement values smaller or equal to a few micrometres at the air gap. With this assumption, matrix $[\mathcal{G}]$ is considered insensible to variations of $\{q\}$, therefore leading to $[\mathfrak{C}] = [0]$. For the applications presented in this thesis which involve electromagnetic and structural simulations performed with separate tools, both coupling assumptions are discarded: magnetostriction is considered negligible in electric motors (i.e. $[\mathfrak{D}] = [0]$, see the discussion in Subsection 2.2.2) and matrix $[\mathcal{G}]$ insensible to variations of $\{q\}$ (i.e. $[\mathfrak{C}] = [0]$). Instead, Maxwell pressure values are computed on the electromagnetic model only, whereas the structural response is determined from the projected excitation spectra.

2.2.2/ MAGNETOSTRICTIVE EFFECTS

By the principle of magnetostriction, the dimensions of ferromagnetic materials subjected to a magnetic field are altered. As it can be seen in Figure 2.7, the material tends to be expanded in the directions which are parallel to the flux lines, and contracted perpendicularly. In terms of static stress-strain equilibrium, magnetostrictive effects represent additional strains $\{\varepsilon_m\}$ in the general Hooke's law introduced in Equation (1.10). The modified expression becomes [75, 163]:

$$\{\sigma\} = [C]\left(\{\varepsilon\} - \{\varepsilon_m\}\right) , \tag{2.7}$$

where $\{\sigma\}$ is the stress tensor, $[C]$ the material's representative elasticity matrix and $\{\varepsilon\}$ the elastic strain tensor. Magnetostriction strains are generally about some micrometres per metre.

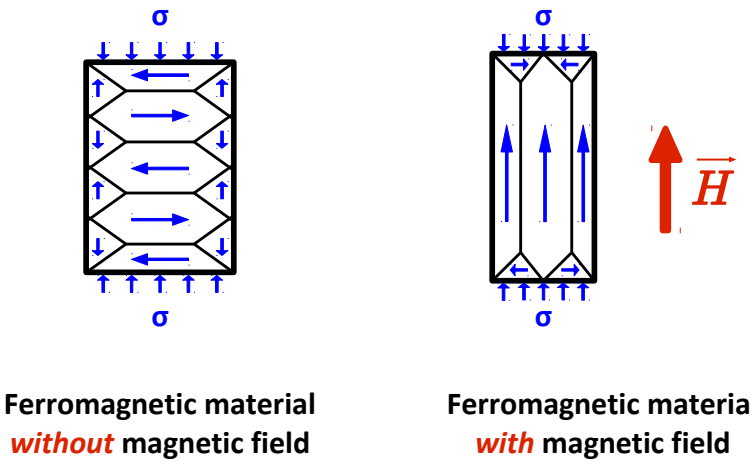

Figure 2.7 – Magnetostrictive effects

The types of devices subjected to magnetostrictive effects have been introduced in Subsection 1.2.2. Concerning electrical motors though, it has been outlined that several ar-

guments disagree on the actual responsibility of magnetostriction in the noise generation process. Whereas some (amongst others, Delaere et al. [50], Dupont et al. [140] and Humbert et al. [141]) claim that magnetostriction has negligible effects in electric machines as Maxwell pressure is the main excitation, others suggest taking the dynamic forces of magnetostrictive origin into account in any simulations. Fonteyn et al. [121] assert that magnetostrictive forces, although hard to measure in real devices, have a great responsibility in the generation of noise in asynchronous electric machines. This statement is supported by the results shown by Låftman [37] and Vijayraghavan and Krishnan [40], but is contradicted by Le Besnerais et al. [123]. As for Delaere et al. [64], their analysis of the respective effects of these phenomena in the case of an induction machine have led to the observation that magnetostriction has a negligible influence on vibration generation in comparison to Maxwell pressure.

In terms of magneto-mechanical coupling, accounting for magnetostrictive effects in Equation (2.2) is equivalent to considering $[\mathfrak{D}] \neq [0]$. Then, with the help of Equation (2.3a), Delaere et al. [42] define the vector of magnetostrictive effects $\{J_\mathrm{m}\}$ by

$$\{J_\mathrm{m}\} = -[\mathfrak{D}]\{q\} = -\frac{1}{2}\{q\}^\intercal \frac{\partial [\mathcal{K}(A)]}{\partial \{A\}}\{q\} \ , \tag{2.8}$$

where the previously-computed displacements $\{q\}$ are considered constant.

2.2.3/ MAXWELL STRESSES

Another electromagnetic effect considered here takes place at the interface of two media (1 and 2) having different magnetic permeabilities. According to the laws of transition [25] expressed at the air gap (interface air/steel, with respective permeabilities μ_0 and μ_steel), the induction vector's normal coordinate (equivalent to radial) as well as the magnetic field's tangential coordinate are both conserved (see Figure 2.8). Thus, we have:

$$B_1^r = B_2^r \tag{2.9a}$$

and

$$H_1^t = H_2^t \ , \tag{2.9b}$$

leading to the expression of the force density per unit area at the interface, the so-called Maxwell stress or pressure [25]:

$$\vec{P} = \frac{1}{\mu_0}\left(\left(\vec{n}\cdot\vec{B_2}\right)\cdot\vec{B_2} - \frac{1}{2}\left\|\vec{B_2}\right\|^2\cdot\vec{n}\right) \ , \tag{2.10}$$

that can be expressed with radial and tangential coordinates (P^r and P^t respectively), so that:

$$P^r = \frac{\left(B_2^r\right)^2 - \left(B_2^t\right)^2}{2\cdot\mu_0} \tag{2.11a}$$

and

$$P^t = \frac{B_2^r \cdot B_2^t}{\mu_0} \,. \tag{2.11b}$$

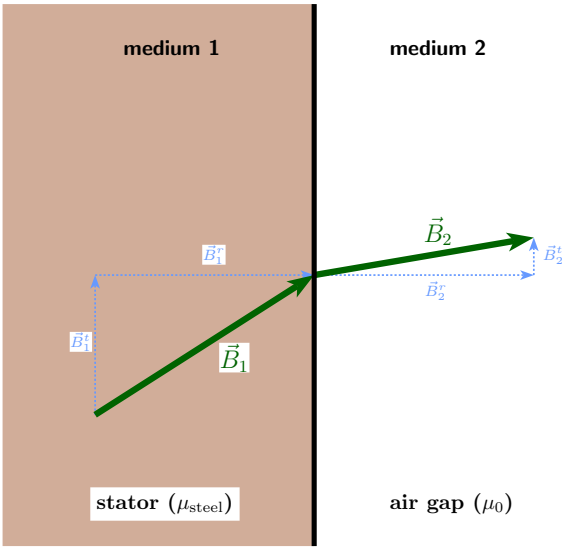

Figure 2.8 – Magnetic induction at the interface air/steel

Combining Equations (1.5) and (2.9b) and taking into account the fact that $\mu_{\text{steel}} \gg \mu_0$ [3] then leads to:

$$B_1^t \gg B_2^t \,. \tag{2.12}$$

The magnitude of the air gap's Maxwell pressure is therefore often assimilated to its radial coordinate, and:

$$P^r \approx \frac{(B_2^r)^2}{2 \cdot \mu_0} \,. \tag{2.13}$$

2.2.4/ LORENTZ FORCE

Apart from magnetostriction and Maxwell pressure, another effect can be presented while discussing the roles of electromagnetic forces in electric machine stators. If a current I travels through a conductor wire of infinitesimal length $\mathrm{d}l$ (oriented with the vector $\overrightarrow{\mathrm{d}l}$) in an external magnetic field of induction vector $\overrightarrow{B}$, Lorentz forces $\overrightarrow{\mathrm{d}F}$ are created on the wire so that:

$$\overrightarrow{\mathrm{d}F} = I \cdot \overrightarrow{\mathrm{d}l} \times \overrightarrow{B} \,. \tag{2.14}$$

In the general case of an electric machine however, magnetic induction is only observed in ferromagnetic materials whereas electric currents are only present in the wires. Assuming no flux leakage in the structure therefore implies that $\overrightarrow{B} = \overrightarrow{0}$ in the wires and $I = 0$ in the wires. Concretely, Lorentz forces are generally neglected in the analyses:

dynamic Maxwell pressures are considered instead, and the overall torque is computed by integrating tangential Maxwell pressure contributions (2.11b) over the rotor's lateral face.

2.2.5/ EXCITATION HARMONICS AND ECCENTRICITIES

Despite the fact the usual representation of the association rotor + stator is perfectly concentric, eccentricities will appear in practice when a rotor is mounted in a rotating machine [44, 97]. Other reported causes of eccentricities are variabilities in windings compositions [141] and magnetic anisotropy in the ferromagnetic materials composing an electric machine [99], but this topic will not be discussed here. Different types of eccentricities and the resulting motion of the rotor are illustrated in Figures 2.9 and 2.10.

In addition to the mechanical imbalance due to the rotor's centrifugal force in the motor, an eccentricity leads to an uneven spatial distribution of the air gap. As it has been explained in Section 1.2, air gap permeance and thus magnetic induction and Maxwell pressure are directly related to the air gap width. Therefore, there is a priori a strong influence of the eccentricity on the electromagnetic dynamic excitation spectra.

This aspect has been addressed in [102], where harmonic changes in the permeance and induction spectra (see Equations (1.2) and (1.4)) are presented. Similarly, Dupont and Lanfranchi [156] have modelled eccentricities as motor defects and analysed their influence on the noise radiated by a synchronous machine. In comparison to the excitation spectra generated by a perfect synchronous motor, it has been shown that a static eccentricity causes a modulation of ± 1 in terms of spatial order, whereas a dynamic eccentricity causes a modulation of ± 1 in terms of both engine and spatial orders.

The case of eccentric switched-reluctance machines has been analysed by various authors in the literature: the works [84], [91], [88], [114], [127], [92] and [89] all agree on the fact that static and/or dynamic eccentricities increase the magnitudes of torque harmonics. However, the influence of eccentricities on radial excitations and on Maxwell stresses' spatial orders is not frequently addressed. A complete electromagnetic/structural application on a switched-reluctance machine's finite-element model is detailed in Chapter 5.

In terms of acoustics, Schlensok et al. [97] explain that static eccentricities cause greater noise emissions than dynamic eccentricities, and should therefore be taken care of in priority. Also, the works of Tabatabaei et al. [85] have shown a direct relation between dynamic eccentricity radius and the magnitudes of excitation harmonics, and the necessity of modelling both mechanical and electromagnetic imbalances (of engine order 1) in every simulation has been outlined in [59].

2.2.6/ EXCITATION PROCESSING

To elaborate on the theory introduced in Paragraph 2.2.1, the electromagnetic excitations are in practice projected onto the finite-element structure and thus "transcribed" into adequate inputs for structural simulations. For industrial applications, several commercial finite-element solvers exist for electromagnetic (e.g. Flux™ or FEmag™) and mechanical simulations (e.g. NASTRAN™ or ANSYS™), which are able to process relatively large models in terms of DOFs.

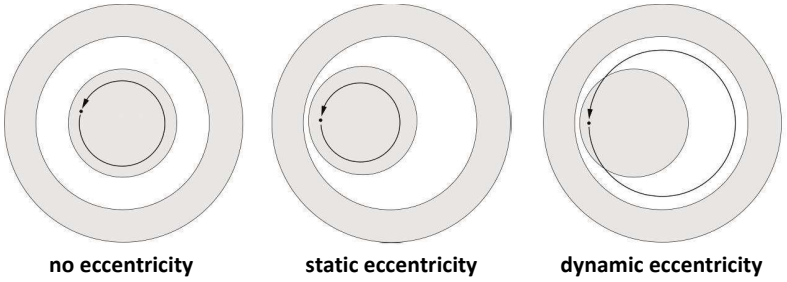

Figure 2.9 – Different types of eccentricities [97]

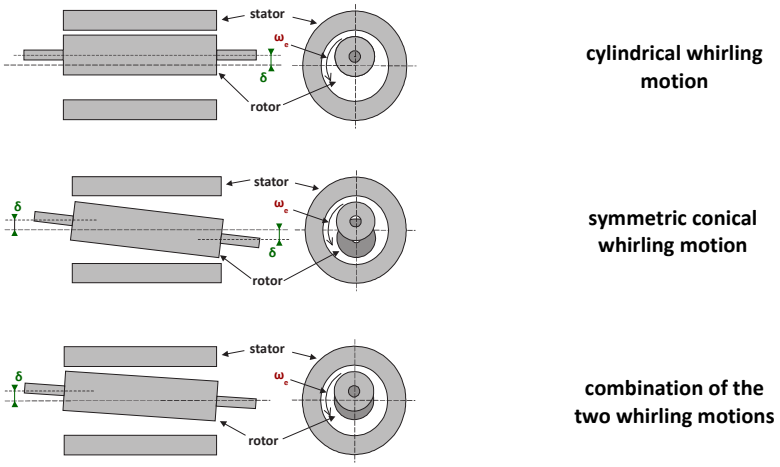

Figure 2.10 – Rotor rigid motions for dynamic eccentricity, of whirling radius δ [74]

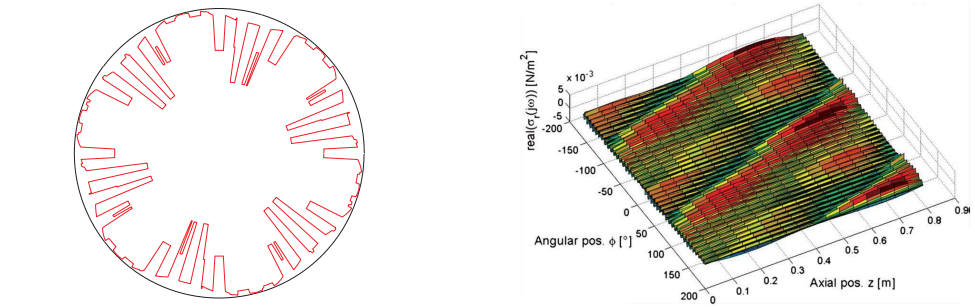

(a) Representation of Maxwell pressure for a given rotor angle [102]

(b) Interpolation of magnetic pressure at the air gap [126]

Figure 2.11 – Projection of electromagnetic excitations

As described in [144] and [157], the idea is to compute flux densities and to export Maxwell pressures (2.11a) and (2.11b) at the machine's air gap for discrete angles on the stator's inner surface (related to space) and on the rotor's outer surface (related to time by the rotation speed). Then, excitation spectra are computed and projected onto the structural mesh according to the considered engine speed or harmonic order. An illustration of projected excitations is given in Figure 2.11.

Several methods have been developed in the literature for performing these projections. An analytic analysis of magnetic excitation spectra has been made in [116], based on the previous work [108], deemed accurate by the authors. These expressions can also be associated to the analytic frequency relations developed in Section 3.1 for relatively fast vibration response computations in an entire stator.

A numerical approach has been proposed in [118], consisting in superposing the individual responses of the given structures to generic excitations after scaling them with appropriate electromagnetic-based factors. In a more industrial frame, automatised projection tools exist (e.g. in Vibratec) for linking electromagnetic simulation results to vibration and acoustic response computations on large finite-element models of electric motors.

In addition to this, some guidelines have been suggested in [97] for preparing electromagnetic finite-element simulations and representing the resulting forces, notably insisting on the necessity to model unskewed motors in two dimensions for cost-effectiveness sakes. Other examples of complete applications of vibratory/acoustic responses from electromagnetic excitations have been detailed in [136] and in [148].

2.3/ SENSITIVITIES OF MATERIAL PROPERTIES

As it has been seen so far, creating a representative finite-element model of an electric motor stator requires understanding a great deal of internal phenomena, interactions and dependencies. In addition to this, each single modelling parameter such as material properties and meshing options has an influence on the global structure's dynamic behaviour to model. Therefore, understanding these sensitivities is a key point for accurate modelling. This section, based on simulations rather than literature review, will investigate the sensitivities of a given stator's FE model with respect to material properties, and stands for prerequisite knowledge for the next chapters.

When dealing with modal simulations and finite-element model updating procedures, an important point to understand is the sensitivities of the parameters with respect to the so-called responses of the system, i.e. the reference values that the updated model should recreate. In other terms, for a given parameter p and a given response r, the sensitivity can be viewed as the rate of change of r with respect to the rate of change of p (see Subsection 1.4.3). Comparing experimental and simulated modal bases therefore suggests to evaluate the sensitivities of the finite-element model's elastic properties (parameters) with respect to the measured natural frequencies and mode shapes (responses).

2.3.1/ PARAMETERS

The stator of a switched-reluctance machine is taken as example for this section. Apart from the fact that the rotor has no windings (which makes it both robust and cheap to manufacture), this machine has the particularity of having fewer teeth at the stator and the rotor than AC electric motors. The teeth and the slots have thus a relatively large angular span: none of the windings fixed on stator teeth are in contact with their neighbours. Therefore, in order to insulate it both electrically and thermally, resin is poured over the stator. Specific for this type of electric machine architecture, this process is called "encapsulating" or "potting" [168] (more details will be given in Chapters 4 and 5).

An illustration of the magnetic core's FE model (37,688 nodes and 21,377 elements) is shown in Figure 2.12, while the model of the entire stator (115,988 nodes and 77,287 elements) is shown in Figure 2.13. The structure has been divided into several zones, each represented by a specific orthotropic material, except for the frame and the weld beads, represented by isotropic materials. The material properties are expressed in a the cylindrical coordinate system $\{r, \theta, z\}$, where z is the laminated core's stacking direction, and reference values are given in Table 2.2. The identification of representative values for these elastic properties will be presented in the next chapters. Also, the connection between the frame and the magnetic core is assumed to be perfect: the two corresponding meshes have common interface nodes in order to represent a complete cohesion over the entire contact surface.

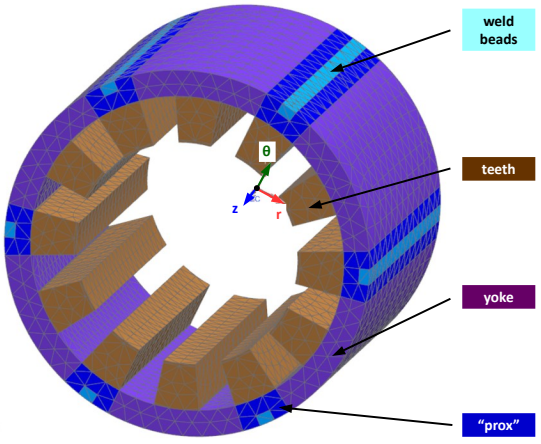

Figure 2.12 – FE model of the magnetic core

The computation of the sensitivities is assumed to be independent from the parameters' initial values. Each parameter corresponds to a distinct elastic property, whose zone is described by an index detailed in Table 2.3.

2.3.2/ SENSITIVITY COMPUTATION

There exist several ways to evaluate the sensitivity of parameters with respect to responses. Although the existing computation methods may be chosen or adapted according to specific types of finite-element models or optimisation procedures, this paragraph uses the so-called "local differential sensitivity analysis", implemented in the commercial model-updating software FEMtools™ and detailed in [149]. More details about local/global sensitivities can be found in [83].

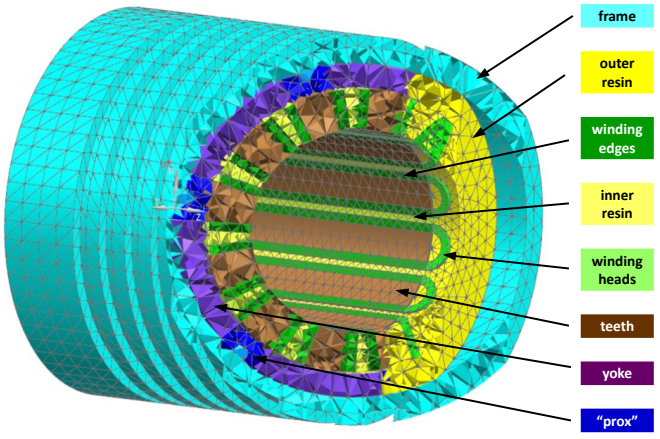

Figure 2.13 – FE model of the entire stator (cutaway)

	frame	prox	yoke	teeth	weld beads	winding edges	winding heads	inner resin	outer resin
E_r [GPa]		205	205	205		57.7	44.9	6.05	4.62
E_θ [GPa]	73.0	205	205	205	207	16.3	17.4	1.92	1.68
E_z [GPa]		157	157	157		47.6	89.9	4.81	9.43
$G_{z\theta}$ [GPa]		51.2	38.4	25.6		6.06	20.7	0.83	1.79
G_{zr} [GPa]	-	51.2	38.4	25.6	-	13.4	3.34	1.26	0.51
$G_{r\theta}$ [GPa]		82.1	61.6	41.1		20.4	13.2	2.17	1.09
$\nu_{\theta z}$ [−]		0.25	0.25	0.25		0.06	0.07	0.14	0.21
ν_{rz} [−]	0.33	0.25	0.25	0.25	0.29	0.28	0.27	0.18	0.26
$\nu_{r\theta}$ [−]		0.25	0.25	0.25		0.30	0.33	0.24	0.31
ρ [kg · m^{-3}]	2,700	7,750	7,750	7,750	7,800	7,900	7,900	2,320	2,320

Table 2.2 – Reference values of the elastic properties

Parameter index	**1**	**2**	**3**	**4**	**5**	**6**	**7**
Zone	prox	yoke	teeth	winding edges	winding heads	inner resin	outer resin

Table 2.3 – Parameter indices

Differential sensitivity coefficients are computed for given values of the parameters p_j, and are defined as slopes of the responses r_i with respect to p_j. Accounting for N responses and M parameters, the $N \times M$ sensitivity matrix $[S]$ is composed of coefficients S_{ij} defined by

$$S_{ij} = \frac{\delta r_i}{\delta p_j} \,. \tag{2.15}$$

Considering a modal basis composed of H modes, the equalities

$$\{\phi\}_a^\intercal \, [\mathcal{K}] \, \frac{\delta \, \{\phi\}_b}{\delta p_j} = \frac{\delta \, \{\phi\}_a^\intercal}{\delta p_j} \, [\mathcal{K}] \, \{\phi\}_b \tag{2.16a}$$

and

$$\{\phi\}_a^\intercal \, [\mathcal{M}] \, \frac{\delta \, \{\phi\}_b}{\delta p_j} = \frac{\delta \, \{\phi\}_a^\intercal}{\delta p_j} \, [\mathcal{M}] \, \{\phi\}_b \tag{2.16b}$$

with $a, b \leq H$ respectively describe the influence of stiffness and mass changes and enable expressing the differential sensitivity for a given natural frequency f_i with respect to a parameter p_j [149]:

$$\frac{\delta f_i}{\delta p_j} = \frac{\{\phi\}_i^\intercal \left(\dfrac{\delta \, [\mathcal{K}]}{\delta p_j} - 4 \cdot \pi^2 \cdot f_i^2 \cdot \dfrac{\delta \, [\mathcal{M}]}{\delta p_j} \right) \{\phi\}_i}{8 \cdot \pi^2 \cdot f_i \cdot \left(\{\phi\}_i^\intercal \, [\mathcal{M}] \, \{\phi\}_i \right)} \,. \tag{2.17}$$

For the structures introduced in Subsection 2.3.1, the simulated modal bases are truncated to the 16 first modes for the magnetic core and the 9 first modes for the entire stator. Sensitivities of mode shapes are not considered, although each mode is labelled in accordance to its deformed shape:

- shapes of type (a, b) correspond to "ovalisation" modes, where a stands for the *spatial order* (i.e. number of lobes along the circular section) and b the number of *nodal circles* along the length (i.e. circles of nodes having null displacement);
- label "OL,2" expresses a coupled longitudinal - (2,0) ovalisation mode;
- the other labels describe the mode shapes in full words.

More details about such mode shapes are given in Appendix B.4. The sensitivities presented in this section are computed with Equation (2.17), and therefore express the extent to which variations of the parameters induce variations of natural frequencies for the selected modes. The values are plotted in Figures 2.14 and 2.15, where the parameter indices are described in Table 2.3. In Figure 2.15, E_f and ν_f refer to E and ν of zone frame, respectively.

Several observations can be outlined from these diagrams, where references to modes or mode shapes are assimilated to the corresponding natural frequencies:

- for the magnetic core (see Figure 2.14)

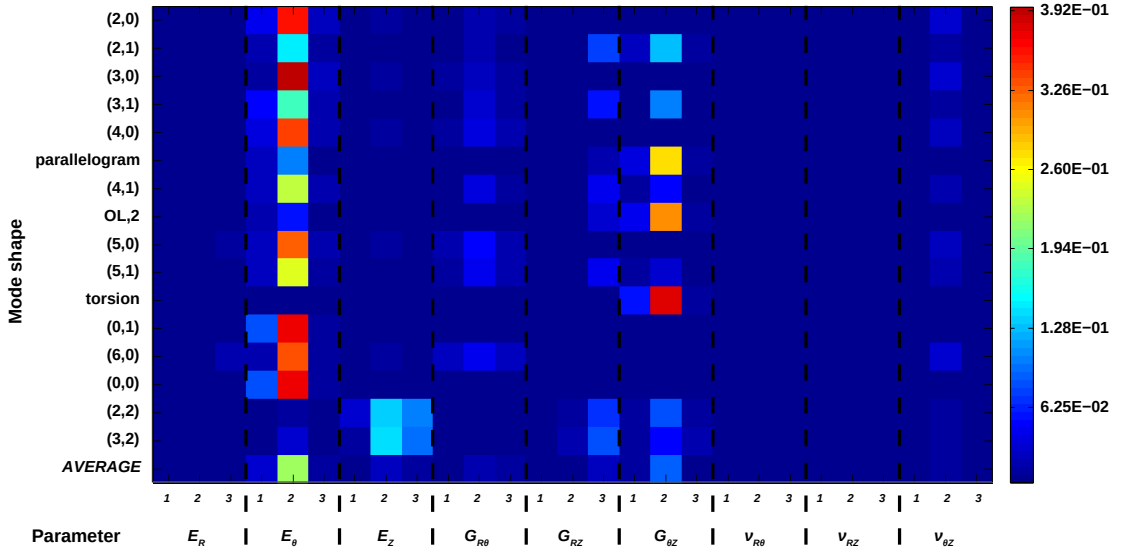

Figure 2.14 – Sensitivities of the magnetic core's elastic parameters

  - Modulus E_θ of zone yoke shows the greatest sensitivity and therefore influence on purely radial shapes, such as ($\sim$,0) ovalisation modes, as well as (0,1) and (0,0) "breathing" modes. This is consistent with the fact such modes mostly involve tension-compression deformations in direction θ in this zone.
  - To a lesser extent though still significantly, ($\sim$,1) "crossed-ovalisation" modes are sensitive to variations of the moduli E_θ and $G_{\theta z}$ of zone yoke. This can be supported by the fact such modes involve tension-compression deformations in direction θ as well as $\theta - z$ shear strains through the structure's length. Higher values of indicator a (number of lobes along the circular section) imply lower sensitivities of modulus $G_{\theta z}$ of zone yoke in comparison to modulus E_θ, as shear deformations become less significant than for lower values of a in crossed-ovalisation modes.
  - Parallelogram, "OL,2" and torsion modes are highly sensitive to $G_{\theta z}$ of zone yoke, as such modes mostly involve $\theta - z$ shear deformations through the structure's length.
  - For ($\sim$,2) modes, the moduli E_z of zones teeth and yoke show the largest, although relatively low sensitivities. This is explained by the fact theses modes tend to bend the teeth in their lengths (i.e. around direction θ); zones teeth and yoke therefore undergo tension and compression in direction z. This point is corroborated by the results in [55].
  - In average, the parameters to which the considered modes are most sensitive are moduli E_θ and $G_{\theta z}$ of the zone yoke. This point adds some details to the earlier observation in [72], where the authors noticed a significant dependency of the natural frequencies of a homogeneous isotropic SRM towards the Young's modulus.

- for the entire stator (see Figure 2.15)
  - All the considered modes show a significant sensitivity with respect to Parameter E_f (E of zone frame). This illustrates the stiffening effect the frame has over

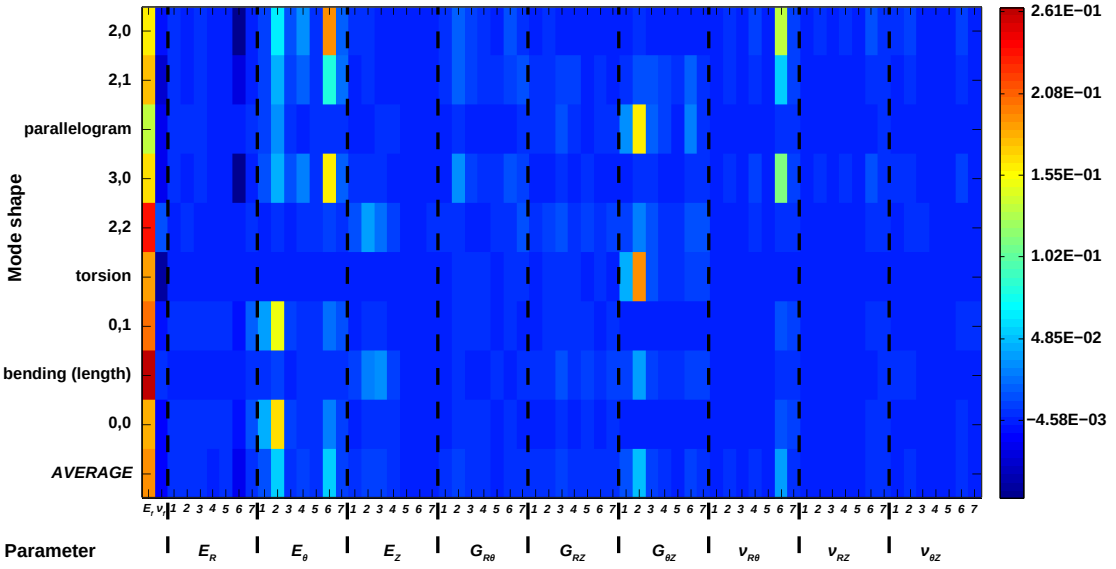

Figure 2.15 – Sensitivities of the entire stator's elastic parameters

the entire structure, but contradicts the observations in [24] for encased stacks. As an example, an increase of 50% manually applied to Parameter E_f led to increases from 6.51% to 10.41% for all of the natural frequencies considered in the correlation.

- All the modes show negligible sensitivities with respect to the windings' elastic properties. This can be explained by two facts. Firstly, the windings undergo small strains in (∼,0) ovalisation modes. And secondly, the stiffening effect of the windings on the remaining modes is negligible as their Young's and shear moduli are significantly lower than the teeth's.
- In comparison to the magnetic core without resin and windings, (2,0), (3,0) and (2,1) modes have a lower sensitivity with respect to modulus E_θ of zone yoke. Instead, they are more sensitive to variations of moduli E_θ and $\nu_{r\theta}$ of zone inner resin. This can be explained by the fact these modes induce greater strains in the resin between the teeth, as teeth and winding edges are much stiffer than the resin.
- Concerning the remaining modes, similar observations as for the magnetic core can be made: parallelogram and torsion modes are mostly sensitive to modulus $G_{\theta z}$ of zone yoke, whereas (0,1) and (0,0) "breathing" modes show greatest sensitivities towards modulus E_θ of zone yoke. This is in accordance with the conclusions in [55] and the laminated stack shapes presented in Figure 2.2.
- Apart from the frame, the parameters to which the considered modes are most sensitive in average are E_θ of zones yoke and inner resin, and $\nu_{r\theta}$ of zone inner resin to a lesser extent.

It can be concluded that natural frequencies of ovalisation modes are governed by tangential elastic properties of the zones that undergo greatest deformations. This raises the opportunity of tuning these natural frequencies in complete "potted" stators by adapting the resin properties, as will be detailed in Chapter 5.

2.4/ CONNECTION <MAGNETIC CORE - FRAME>

When performing finite-element simulations, modelling the existing boundary conditions or internal connections is generally necessary to recreate real settings, as they affect the values of the representative stiffness matrix directly. In the case of electric motor stators, some uncertainties exist for modelling the connection between the magnetic core and the frame with finite elements. The most obvious modelling guideline would be to associate both meshes by common interface nodes, representing a perfect cohesion between the two pieces. This modelling method will be referred to as "shrunk" case in the entire section. However, some manufacturing processes (e.g. heat shrinkage) do not guarantee an homogeneous cohesion over the entire contact surface. Therefore, some issues need to be addressed in order to estimate the necessity and the improvements of such details in the stator's FE model:

1. How to model this interface in order to account for possible inhomogeneous cohesion?
2. To what extent is the stator's dynamic behaviour sensitive to such changes in the FE model?
3. In other terms, is refining the FE model with an improved <magnetic core - frame> interface cost-effective?

The first subsection is a literature review of some existing notions for modelling the <magnetic core - frame> interface. At the opposite, the next two subsections will present sensitivity analyses of modelling parameters; they are based on simulations rather than literature review and stand for prerequisite knowledge for the next chapters. Finally, the last subsection will outline answering points to the above-mentioned questions and conclude on a preferred modelling guideline.

2.4.1/ CURRENT KNOWLEDGE

The necessity and the possible methods to model the <magnetic core - frame> interface in the FE model of an electric motor stator are not frequently investigated in the literature. Tang et al. [73] have confirmed the necessity of taking the existing mounting connections into account in the finite-element model of a switched-reluctance motor. In the case of an induction machine, Schlensok et al. [105] have analysed numerically the acoustic influence of a number of localised springs as a connection between the stator frame and the magnetic core (similar study in [106]). An illustration of this interface is presented in Figure 2.16.

The authors have outlined that the "shrunk" case generated the lowest noise radiation. They also introduced an optimisation procedure for the number of spring elements at the interface, while decoupling the frame's (or housing's) behaviour from the core's, therefore imposing a sufficiently low value to the springs' stiffnesses. No results about this optimisation have been presented in either [105] or [106].

Concerning the "shrunk" case, Cai and Pillay [55] have shown that the frequencies of the ovalisation modes rise monotonically with respect to the frame thickness, but are lowered if the length difference between the frame and the core is increased. On the contrary,

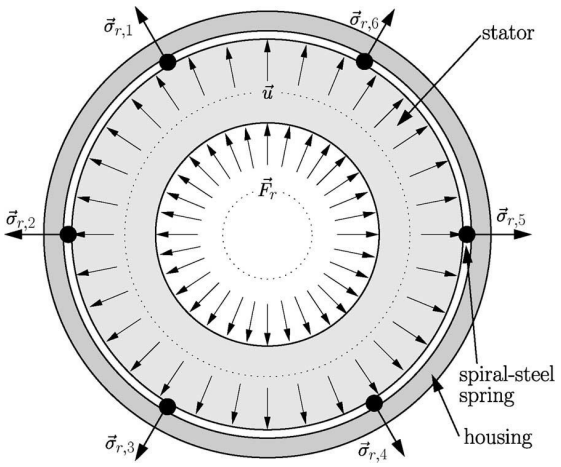

Figure 2.16 – Interface between magnetic core and frame with localised springs [105]

the same study also shows that inserting longitudinal keys between the magnetic core and the frame decouples the low-order ovalisation modes, therefore decreasing their frequencies in comparison to the "shrunk" case.

But independently from all simulation aspects, experimental analyses must justify the need to account for possible losses of contact or changes in cohesion properties at the interface in the FE model. Also, understanding where and why such changes occur could prove to be helpful (not to say necessary) in orienting the adaptation of the FE model. So far no such data have been found in the literature. In spite of the interesting notions introduced in this subsection, the questions outlined in the beginning of the section have not yet been fully answered. The next two subsections will propose simulation analyses in order to understand them better.

2.4.2/ SENSITIVITY COMPUTATION FOR LOW-ORDER OVALISATION MODES

To answer the question **1.** mentioned in the beginning of the section, the proposed improvement to the FE model consists in an additional connection mesh made of 3-D stiffness elements, replacing the initial merged nodes at the interface. The geometry of the entire stator presented in Figure 2.13 is reused in this section, where the elements related to resin and windings have been deleted and the remaining pieces remeshed with cuboid elements for convenience. A reference modal basis is computed from this initial assembly (before separating the pieces and inserting connection elements), with the first 40 modes above 1 Hz. An illustration of the finite-element model with the connection elements is given in Figure 2.17.

The interface between the frame and the magnetic core has been divided into 8 identical parts (see Figure 2.18), so that each of them is associated to a specific set of stiffness values $\{K_r, K_\theta, K_z\}$ which can be modified independently. The nodal coordinates as well as the material and stiffness properties are all expressed in the cylindrical coordinate system $\{r, \theta, z\}$, where z is the laminated core's stacking direction. The idea is to analyse the impacts of local and global variations at the interface.

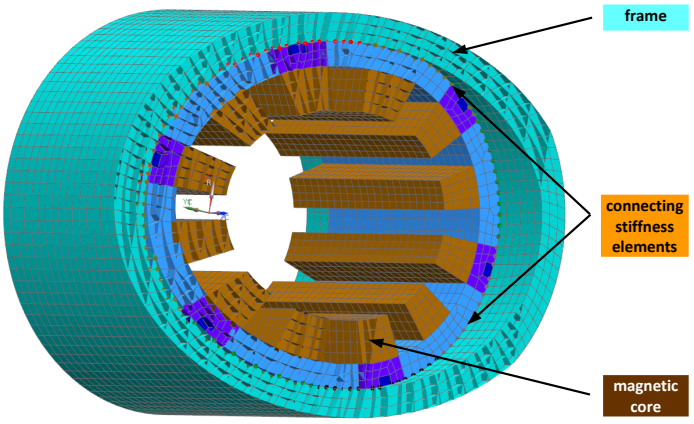

Figure 2.17 – FE model of the assembly <magnetic core + frame + connecting elements> (cutaway)

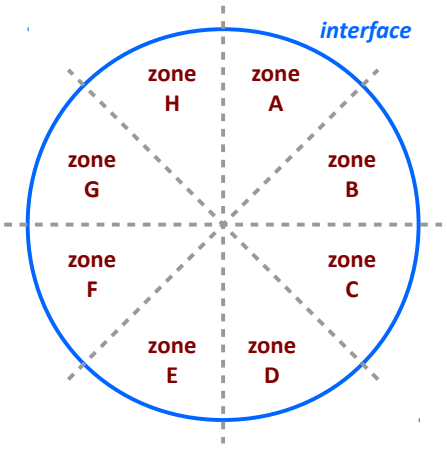

(a) Zoning of the interface

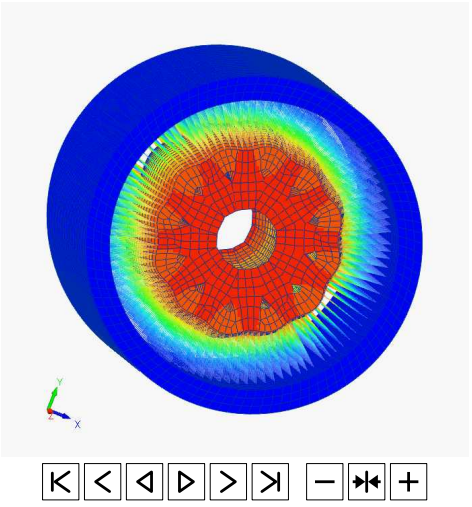

(b) Emphasis on the connecting stiffness elements

Figure 2.18 – Connecting stiffness elements

#	Parameter	Zone	#	Parameter	Zone	#	Parameter	Zone
1	K_r	A	9	K_θ	A	17	K_z	A
2	K_r	B	10	K_θ	B	18	K_z	B
3	K_r	C	11	K_θ	C	19	K_z	C
4	K_r	D	12	K_θ	D	20	K_z	D
5	K_r	E	13	K_θ	E	21	K_z	E
6	K_r	F	14	K_θ	F	22	K_z	F
7	K_r	G	15	K_θ	G	23	K_z	G
8	K_r	H	16	K_θ	H	24	K_z	H

Table 2.4 – Parameters for the connecting stiffness elements

A sensitivity analysis has been performed in order to assess the influence of connection stiffness variations on the natural frequencies of the assembly <magnetic core + frame>. As in Section 2.3, the finite-element programme FEMtools™ has been used for computing sensitivity values (see Equation (2.17)). The parameters are numbered from 1 to 24, as described in Table 2.4, and the sensitivity values for the natural frequencies of modes (2,0), (3,0), (4,0) and (0,0) are plotted in Figure 2.19. The reference values for all the parameters are $K = 10^9\,\mathrm{N}\cdot\mathrm{m}^{-1}$.

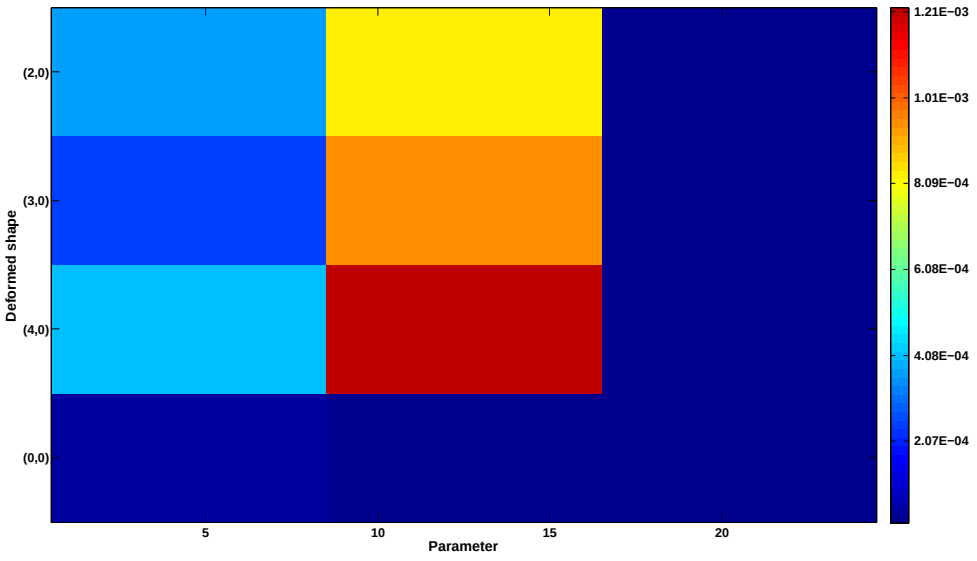

Figure 2.19 – Sensitivities of the connecting stiffness elements

Several observations can be outlined from Figure 2.19, where references to modes or mode shapes are assimilated to the corresponding natural frequencies:

- The modes (logically) have the same sensitivities towards the stiffness values of all the zones.
- The overall sensitivity values are significantly lower than those of the elastic parameters, as shown in Figures 2.14 and 2.15.
- In Figure 2.19, K_θ values have the greatest influence on the ovalisation modes, whereas sensitivities towards K_r are lower.
- K_z values have a negligible influence on the presented modes. This is consistent with the purely radial deformed shapes.
- For the given reference values, the "breathing" mode (0,0) shows negligible sensitivities towards all the parameters.

In addition to the ovalisation modes, the sensitivities of the structure's first 40 natural frequencies will be investigated in the following subsection.

2.4.3/ DESIGNS OF EXPERIMENTS ON THE FIRST 40 MODES

In addition to the above-presented analysis on ovalisation modes, designs of experiments (DOEs) based on random variations have been performed, in order to estimate the sensitivity of the 40 lowest-frequency modes of the structure. The initial value for all the stiffness elements is $10^9\,\mathrm{N}\cdot\mathrm{m}^{-1}$ in every direction.

2.4.3.1/ DOE SCENARIOS

Four DOE scenarios are distinguished:

8 zones Random values are chosen independently in each of the 8 zones (see Figure 2.18(a))

4 zones Random values are chosen independently in 4 zones ({A+B}, {C+D}, {E+F}, {G+H})

2 zones Random values are chosen independently in 2 zones ({A+B+C+D}, {E+F+G+H})

1 zone In each direction, the same values are used for all the connecting elements (all directions remain independent)

The stiffness values of all the connecting elements in a given zone are identical. Each stage is divided into the following sub-scenarios:

R: Only K_r values are modified
T: Only K_θ values are modified
Z: Only K_z values are modified
TR: K_r and K_θ values are modified
ZT: K_θ and K_z values are modified
RZ: K_r and K_z values are modified

Thus, the total number of varying parameters N_{vk} depends on the considered scenario and sub-scenario. Details are given in Table 2.5.

	R	T	Z	TR	ZT	RZ
8 zones	8	8	8	16	16	16
4 zones	4	4	4	8	8	8
2 zones	2	2	2	4	4	4
1 zone	1	1	1	2	2	2

Table 2.5 – Total number of varying parameters (N_{vk}) for each scenario

Finally, each sub-scenario is divided into 63 independent experiments, referring to indices i. In each of them and according to the restrictions of the considered sub-scenario, the value $10^{u_{ij}}\,\mathrm{N}\cdot\mathrm{m}^{-1}$ is affected to the parameter K_{ij}, where u_{ij} is a random value between 0 and 12, determined with a uniform probability density function. The other parameters keep their initial value of $10^9\,\mathrm{N}\cdot\mathrm{m}^{-1}$. A relative parameter variation indicator for the entire sub-scenario is computed with the relation:

$$\overline{|\Delta K|}_{sb} = \frac{1}{63\cdot N_{vk}}\cdot\sum_{i=1}^{63}\sum_{j=1}^{N_{vk}}\left|\log\left(\frac{K_{ij}}{10^9}\right)\right|\,, \tag{2.18}$$

where N_{vk} is the total number of varying parameters described in Table 2.5, and accounting for the modified parameters only. Then, the basis of the first 40 modes above 1 Hz is

computed for each experiment i, and compared to the reference modal basis introduced at the beginning of the section.

2.4.3.2/ DOE RESULTS

With the aid of the correlation criteria defined in Subsection 1.4.2, the modal basis computed for each sub-scenario is compared to the reference modal basis with a MAC-threshold $t_{MAC} = 0\%$ (so that all the modes are taken into account). For each sub-scenario, the global estimator $\overline{|\Delta f|}_{sb}$ is computed in order to estimate the absolute frequency discrepancy, averaged for all the corresponding 63 experiments. This estimator is computed with the following relation:

$$\overline{|\Delta f|}_{sb} = \frac{1}{63} \cdot \sum_{i=1}^{63} \overline{|\Delta f|}_i \,, \tag{2.19}$$

where $\overline{|\Delta f|}_i$ is the frequency discrepancy of the experiment i, as defined in Equation (1.68). In order to compare the results in every sub-scenario, the relative estimators $\mathfrak{v}_{sb}^{\text{rel}}$ are computed with

$$\mathfrak{v}_{sb}^{\text{rel}} = \frac{\overline{|\Delta f|}_{sb}}{\overline{|\Delta K|}_{sb}} \tag{2.20}$$

and plotted in Figure 2.20.

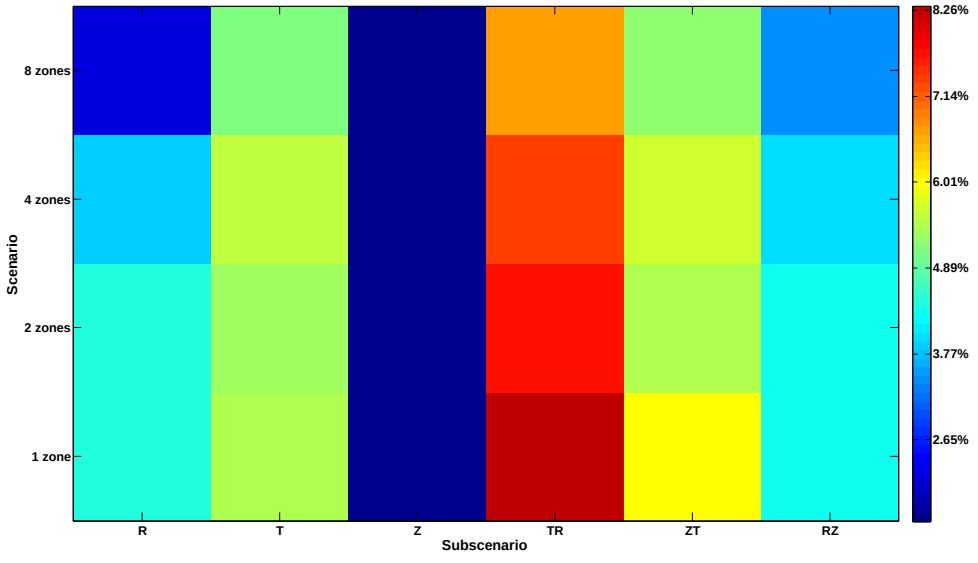

Figure 2.20 – Comparison of the DOE relative estimators $\mathfrak{v}_{sb}^{\text{rel}}$

Several observations can be made in the light of the results in Figure 2.20:

- Whereas the sensitivities towards K_z values are very small, results for sub-scenarios **R** and **T** are increasingly greater. This shows that in this mode set, shapes showing

axial, radial and tangential deformations (and thus sensitivities) represent increasing proportions, respectively.

- Results of sub-scenarios **TR**, **ZT** and **RZ** are - as expected - the sums of the corresponding respective sub-scenarios **R** , **T** and **Z**.
- The multiplicity of independent zones tends to reduce the overall sensitivities. This seems consistent with the fact that the stator's overall dynamic behaviour is less sensitive to localised than to global contact changes at the interface.

2.4.4/ MODELLING GUIDELINES

In the light of the results presented in the three last subsections, answers to the questions raised in the beginning of the section can be proposed:

1. An additional FE mesh made of 3-D stiffness elements has been proposed for modelling the interface between the stator's frame and magnetic core, substituting the merged nodes of the "shrunk" case. Zoning the interface enabled modelling possible cohesion variations as changes in contact stiffness values. In addition to being relatively light in terms of additional elements and modelling costs, this method also kept the geometrical coincidence between the interface nodes.
2. It has been shown that the ovalisation modes were significantly less sensitive to changes in connecting stiffness values than in elastic parameters. In a general rule, changes of stiffness values in axial, radial and tangential directions have an increasing impact on the stator's low-frequency modal behaviour, respectively. Also, this impact is lessened if the concerned area at the interface is reduced.
3. Finally, in spite of the relatively light changes in the FE model that modelling this interface requires, the values to affect to each of the zones' stiffness elements remain uncertain in the general case and without experimental data. Therefore, it is suggested to consider the "shrunk" case (interface nodes merged and no stiffness elements) as a default model unless experimental data require more details.

INTERMEDIATE CONCLUSION

These first two chapters have introduced some general notions about electric machines and structural dynamics, as well as state-of-the-art knowledge presented in the last two decades' literature articles. In particular, Chapter 2 has been focused on showing the influence and how to model various phenomena and parameters on the stator's dynamic behaviour.

After geometric parameters such as teeth, pole pairs, skewing and end-shields, the emphasis has been made on electromagnetic excitations, amongst which Maxwell stresses are projected onto the structural mesh in order to simulate mechanical responses. Then, two sections detailed simulation analyses about the sensitivities of the stator's modes with respect to material properties and the connection between the magnetic core and the frame. Gathering both literature reviews and newly-made simulation studies, these four sections aimed at exposing prerequisite knowledge for the next chapters. Eventually, at the opposite of this one, the following chapters will be focused on modelling specific

parts of the stator, sometimes referred to as “active parts”: the magnetic core, the windings and the resin.

3

LAMINATED STRUCTURES: FOCUS ON THE MAGNETIC CORE

As it has been introduced in Chapter 2 and illustrated in Figure 2.13, the stator of a switched-reluctance motor is composed, as a general rule, of a cylindrical frame, a laminated-steel magnetic core and fixed on it, resin-potted windings. Except for DC machines whose stators are usually not winded, the stators of synchronous and induction motors (presented in Section 1.1) are built on similar architectures. Currently, the lack of accurate or easily-implemented methods tends to rely on costly and time-consuming model-updating procedures for modelling electric machine stators. Thus, the need of developing effective modelling techniques for predicting such structures' dynamic behaviours is great [140].

As it has been outlined in the previous chapters, predicting the mechanical behaviour of entire stators requires being able to model each of the components accurately. In addition to this, the analysis detailed in Section 2.3 has shown that the stator's low-frequency modes were in average particularly sensitive to one of the magnetic core's elastic parameters. This means that the core's geometry and material properties have a strong influence on the entire stator's natural frequencies, and that understanding the behaviour of the magnetic core is essential for predicting that of an entire electric machine.

This chapter will first focus on existing analytical methods for predicting the mechanical behaviour of a laminated core. The next sections will detail the developments of practical approaches for efficient finite-element simulations of various heterogeneous structures as well as applications on experimentally-validated modal bases of electric machine stators. In addition to this, practical guidelines will be proposed for creating homogeneous models of the multi-layered magnetic core structures.

3.1/ ANALYTICAL APPROACHES

While functioning, the stator and the rotor of an electric machine undergo strong variations of magnetic field. As a result of these variations, electric "eddy" currents are induced in the ferromagnetic materials and dissipate energy by Joule effect. Despite important additional costs due to this phenomenon [79], the ferromagnetic materials are stratified and the layers are electrically insulated from each other in order to prevent energy losses and possible damage due to heat dissipation in the motor, hence the name of "laminated steel" for referring to stator and rotor core structures. Due to the fact that

the steel sheets are individually coated and stacked during the stator's or the rotor's manufacturing process (see Section 2.1), magnetic cores are also referred to as "stacks". Examples of stacks are illustrated in Figure 3.1.

(a) Individual steel sheets [167]

(b) Side view of a laminated rotor [164]

Figure 3.1 – Examples of laminated structures

Relatively numerous studies have aimed at predicting the vibratory behaviour of laminated steel structures. In addition to the observations detailed in Section 2.1, early applications to finite elements such as the series of works [20, 19, 23, 24, 22] investigated simulation approaches for modelling magnetic cores. Their observation that the frequencies of purely radial modes are independent from the stator's length has been corroborated in [55] but contradicted in [56]. In practice, current computational resources enable to observe that the stator's length has indeed negligible influence on radial modes' frequencies, using finely-meshed finite-element models. This is in agreement with the statement of [35], explaining that the vibratory behaviour of a laminated thick cylinder is dominated by that of an individual lamination. As for the assumption of orthotropic or transversely isotropic behaviour for representing overall laminated structures, it has been widely acknowledged in the literature. These points will be addressed in detail in Sections 3.2 and 3.3.

3.1.1/ ANALYTICAL COMPUTATION OF DYNAMIC RESPONSES

Based on the beam theory, analytical formulations have been proposed in the works [105], [123] and [129] for computing the dynamic responses of both induction and switched-reluctance machines. The parameters used in these expressions are the sheets' Young's modulus E_s and density ρ_s, the stator's inner radius R_i, mean yoke radius R_c, tooth length e_t, yoke width e_c and the frame's thickness e_f, as illustrated in Figure 3.2. Also, the core's stacking factor $\mathfrak{s}_\mathfrak{f}$ is defined with the assumption of a homogeneous cross-section, with the expression:

$$\mathfrak{s}_\mathfrak{f} = \frac{n_s \cdot l_s}{L_{\text{stack}}} \,, \tag{3.1}$$

where n_s is the number of steel sheets, l_s the thickness of one sheet and L_{stack} the total length of the stack.

The eigenfrequencies f_m of the purely radial modes are determined according to the spatial order m with the relations [123, 48]:

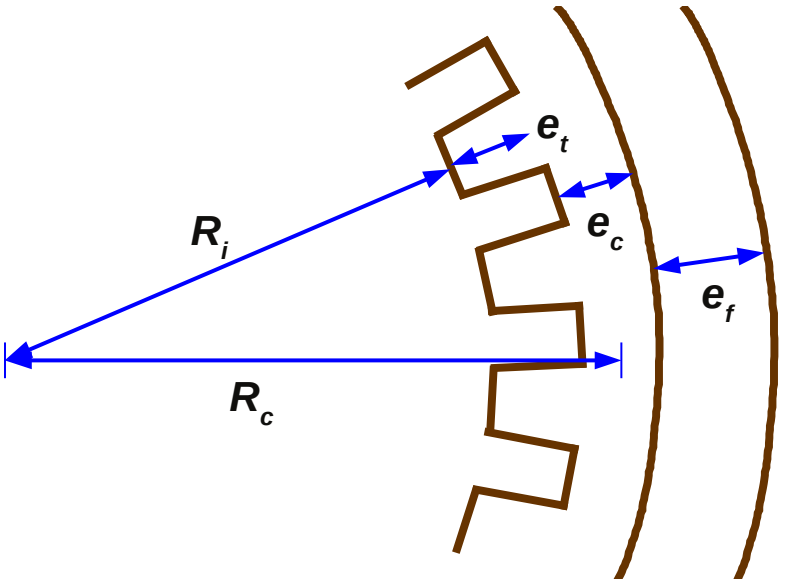

Figure 3.2 – Stator's dimensions [129, 123]

$$f_0 = \frac{1}{2 \cdot \pi \cdot a} \cdot \sqrt{\frac{E_s}{\mathfrak{s}_\mathfrak{f} \cdot \Delta_m \cdot \rho_s}} \tag{3.2a}$$

for the breathing mode $m = 0$ and

$$f_m = f_0 \cdot \frac{\alpha \cdot m \cdot \left(m^2 - 1\right)}{\sqrt{\left(m^2 + 1\right) + \alpha^2 \cdot \left(m^2 - 1\right) \cdot \left(4 \cdot m^2 + m^2 \cdot \frac{d_r}{d_m} + 3\right)}} \tag{3.2b}$$

for orders $m > 1$. a, α, d_m and d_r are the respective corrected radius factors and additional mass factors defined with

$$a = \frac{2 \cdot R_i + e_f - e_c}{2} ,$$

$$\alpha = \frac{e_c + e_f}{2\sqrt{3} \cdot a} ,$$

$$d_m = 1 + \frac{W_t + W_w}{W_f + W_y}$$

and

$$d_r = 1 + \frac{91 \cdot n_t \cdot \mathcal{A}_t \cdot e_p^3 \cdot (W_t + W_w)}{a \cdot L_{\text{stack}} \cdot e_c^3 \cdot W_t} \cdot \left(\frac{1}{3} + \frac{e_c}{2 \cdot e_t} + \left(\frac{e_c}{2 \cdot e_t}\right)^2\right) ,$$

where W_t, W_w, W_f and W_y are the total masses of teeth, windings, frame and yoke, respectively, and where n_t is the total number of teeth and $\mathcal{A}_t$ the total area of the teeth. Different expressions have been given by [56] or [137], but will not be detailed here.

Then, the response is computed by decomposing in Fourier series the radial harmonic excitation in sinusoidal contributions of complex magnitudes $P_{m,f}$, according to the spatial order m and the frequency f. The static displacements $Y^s_{m,f}$ associated to the individual contributions are defined by the relations [123]

$$Y^s_{0,f} = P_{0,f} \cdot \frac{R_i \cdot R_c}{E_s \cdot e_c} \tag{3.3a}$$

for $m = 0$ and

$$Y^s_{m,f} = P_{m,f} \cdot \frac{12 \cdot R_i \cdot R_c^3}{E_s \cdot e_c^3 \cdot (m^2 - 1)^2} \tag{3.3b}$$

for $m > 1$. Finally, dynamic displacements $Y^d_{m,f}$ are computed with

$$Y^d_{m,f} = Y^s_{m,f} \cdot \left(\left(1 - \frac{f^2}{f_m^2} \right)^2 + 4 \cdot \zeta_m^2 \cdot \frac{f^2}{f_m^2} \right)^{-1/2}, \tag{3.4}$$

where ζ_m is the damping ratio of the m-th-order mode, and where f is the excitation frequency. Determining the excitation spectra with the previously-introduced analytical expressions (1.4) and (2.11a) is thus a quick way to estimate the motor's response to electromagnetic excitations.

3.2/ MODELLING TECHNIQUES FOR LAMINATED STATOR CORES: ORTHOTROPIC HOMOGENISATION APPROACH

In spite of the benefits they represent in terms of computation costs, the above-presented analytical tools may not be reliable for complicated geometries or multi-bodied assemblies. In the case of electric motor stators, performing nowadays mechanical simulations in an industrial frame most likely requires using finite-element solvers. However, the magnetic core of a typical automotive or railway traction electric motor is composed of several hundreds of steel sheets; meshing each of the individual layers would thus lead to significantly large models and cost-prohibitive simulations, even though current computational resources enable managing increasingly bigger solutions. Therefore, an efficient way to model heterogeneous structures with reasonable numbers of DOFs is to "homogenise" the properties in the initial structure.

This section details the development of a finite-element-oriented homogenisation method and its application to a model of electric motor stator. Apart from slight changes and new material added in the following subsections, this work has been published as a full-length article in the Journal of Sound and Vibration and referenced as [166]. The bulk of the initial work has been kept identical. Also, the contents of the article have been reshaped into a conference paper, presented at the International Conference on Computational Structures Technology ("CST2014", Naples, Italy) and referenced as [160].

3.2.1/ INTRODUCTION TO 3D-HOMOGENISATION

In order to analyse a complex structure's dynamic behaviour, modelling its components may become difficult if they are numerous, small, or if some of the assembly properties are not known. This is one of the reasons why so-called "homogenisation" methods have been developed. They aim at recreating a given heterogeneous structure's behaviour by reducing the multiplicity of its components' properties, and also enable to mesh the structure independently from the sizes of the heterogeneities, that could have imposed numerous degrees of freedom in the models. Such methods are much desired for modelling composite materials, and especially for laminated structures. Kalamkarov et al. [110] have thoroughly listed and compared over 200 studies about homogenisation and have assessed the pros and cons of various analytical methods and specific applications.

For industrial projects in structural dynamics as well as academic research involving finite-element simulations on heterogeneous structures, the need of efficient techniques able to model homogeneous equivalent structures both accurately and cost-effectively is great [141]. Therefore, there is a significant interest for simple tools yielding results directly usable for common finite-element software. Motivated by the current coming-up of hybrid or 100%-electric vehicles, the development of silent devices (as well as other noise, vibration and harshness (NVH) specifications) in the automotive industry involves finite-element modelling of heterogeneous structures such as electric motor stators [140]. In this perspective, the main objective of this work is to establish a method to determine representative equivalent material properties (elasticity matrices) for laminated structures, especially for the applicability to any kind of finite-element simulation (including dynamic responses, model updating, etc.) without being limited to specific cases.

Concerning stratified materials, many applications are made under the assumption of plane stresses and strains (for instance with laminated beams or shells), for which theory predicts static and dynamic behaviours with good accuracy (e.g. [41]). In addition, there also exist exact theories and solutions describing the vibration of stratified beams and plates, such as the works [87] and [81], as well as ready-to-use 2D laminated finite elements present in several software programmes (see e.g. [65]). A finite-element-based homogenisation technique taking into account viscoelastic properties in 2D-laminates has been proposed by Koishi et al. [34]. However, some other analyses can not be simplified by such assumptions – take the case of no dimension being negligible in the model – and have to be meshed in 3D.

A short review of some existing "3D-homogenisation" methods is made in paragraphs 3.2.1.1 to 3.2.1.3, whereas a novel numerical method is detailed in paragraph 3.2.1.4. Such techniques are particularly relevant when e.g. parts of 3D finite-element models are multi-layered and need to be homogenised.

3.2.1.1/ RULE OF MIXTURES

First of all, the relations that may be the simplest for determining a homogeneous material equivalent to a heterogeneous structure, and that are used in many studies (including reference works in the field of composite materials, such as [41] and [81]), are weighted averages of the different components' elastic constants, sometimes referred to as the "rule of mixtures". The abbreviation "**WA**" (for "weighted averages") is used for referring to

this method. As shown in [81], the expressions are built from the decompositions of the structure's global stresses and strains according to each of the components.

Let us consider a laminated structure composed of N isotropic layers, stacked along the z-axis. For each layer n, the material's corresponding density ρ_n, Young's modulus E_n and Poisson's ratio ν_n are initially known, as well as its volume fraction:

$$\chi_n = \frac{V_n}{V^{\text{stack}}} \,, \tag{3.5}$$

where V_n and V^{stack} respectively stand for the layer's and the entire structure's volumes. Then, equivalent density $\tilde{\rho}$, Young's moduli $\tilde{E}_i$, shear moduli $\tilde{G}_{ij}$ and Poisson's ratios $\tilde{\nu}_{ij}$ may thus be computed with the following relations:

$$\tilde{\rho} = \sum_{n=1}^{N} \rho_n \chi_n \,, \tag{3.6}$$

$$\tilde{E}_x = \tilde{E}_y = \sum_{n=1}^{N} E_n \chi_n \,, \tag{3.7}$$

$$\tilde{E}_z = \left(\sum_{n=1}^{N} \frac{\chi_n}{E_n} \right)^{-1} \,, \tag{3.8}$$

$$\tilde{\nu}_{xy} = \sum_{n=1}^{N} \nu_n \chi_n \,, \tag{3.9}$$

$$\tilde{\nu}_{xz} = \tilde{\nu}_{yz} = \tilde{\nu}_{xy} \frac{\tilde{E}_z}{\tilde{E}_x} \,, \tag{3.10}$$

$$\tilde{G}_{xy} = \frac{\tilde{E}_x}{2 \cdot (1 + \tilde{\nu}_{xy})} \tag{3.11}$$

and

$$\tilde{G}_{xz} = \tilde{G}_{yz} = \left(\sum_{n=1}^{N} \frac{2 \cdot \chi_n \cdot (1 + \nu_n)}{E_n} \right)^{-1} \,. \tag{3.12}$$

These expressions already give a good approximation of the structure's global behaviour, at the cost of relatively simple calculations to perform. However, they might not be adapted to cases more complex than stacks of isotropic layers.

3.2.1.2/ INRIA

Begis et al. [14] have developed an analytical method (summed up and reapplied in [16]) for the determination of any structure's equivalent elasticity matrix $\left[\tilde{C}\right]$ from its components' elasticity matrices, that may even describe a triclinic behaviour, the most general material definition without any symmetries or simplifications.

For a given point on a structure, the elasticity matrix $[C]$ is defined by Hooke's law $\{\sigma\} = [C]\{\varepsilon\}$, where $\{\sigma\}$ is the stress tensor and $\{\varepsilon\}$ the strain tensor [119]. The entire linear system has been introduced in Equation (1.11), and is recalled as following:

$$\begin{Bmatrix} \sigma_{11} \\ \sigma_{22} \\ \sigma_{33} \\ \\ \sigma_{23} \\ \sigma_{13} \\ \sigma_{12} \end{Bmatrix} = \begin{bmatrix} C_{11} & C_{12} & C_{13} & C_{14} & C_{15} & C_{16} \\ & C_{22} & C_{23} & C_{24} & C_{25} & C_{26} \\ & & C_{33} & C_{34} & C_{35} & C_{36} \\ & & & & & \\ & & & C_{44} & C_{45} & C_{46} \\ & \text{sym.} & & & C_{55} & C_{56} \\ & & & & & C_{66} \end{bmatrix} \begin{Bmatrix} \varepsilon_{11} \\ \varepsilon_{22} \\ \varepsilon_{33} \\ \\ 2 \cdot \varepsilon_{23} \\ 2 \cdot \varepsilon_{13} \\ 2 \cdot \varepsilon_{12} \end{Bmatrix},$$

in which the indices 1, 2 and 3 correspond to the respective directions x, y and z in a rectangular coordinate system, or r, θ and z in a cylindrical coordinate system. In its most general definition, matrix $[C]$ is a fourth-order tensor [119], introduced in Equation (1.10) and recalled as

$$[C] = \begin{bmatrix} C_{1111} & C_{1122} & C_{1133} & C_{1123} & C_{1113} & C_{1112} \\ C_{2211} & C_{2222} & C_{2233} & C_{2223} & C_{2213} & C_{2212} \\ C_{3311} & C_{3322} & C_{3333} & C_{3323} & C_{3313} & C_{3312} \\ & & & & & \\ C_{2311} & C_{2322} & C_{2333} & C_{2323} & C_{2313} & C_{2312} \\ C_{1311} & C_{1322} & C_{1333} & C_{1323} & C_{1313} & C_{1312} \\ C_{1211} & C_{1222} & C_{1233} & C_{1223} & C_{1213} & C_{1212} \end{bmatrix}.$$

Begis et al. [16] proposed a general definition of a Y-periodic structure's equivalent elasticity matrix from an asymptotic homogenisation approach. Considering the unit cell periodically repeated in the entire structure and represented in the set of directions $y = \{y_1, y_2, y_3\}$, Y-periodic vectors $\{W^{pq}(y)\}$ need to be calculated, as solutions of

$$\frac{\partial}{\partial y_j}\left(C_{ijkh}(y) \cdot \varepsilon_{kh}\left(\{W^{pq}(y)\}\right)\right) = \frac{-\partial}{\partial y_j} C_{ijpq}(y) \tag{3.13}$$

in Y. Then, the homogenised coefficients $\tilde{C}_{ijkh}$ are computed by:

$$\tilde{C}_{ijkh} = \frac{1}{\text{vol}_Y} \int_Y \left[C_{ijkh}(y) - C_{ijpq}(y) \cdot \varepsilon_{kh}\left(\{W^{pq}(y)\}\right)\right] \mathrm{d}y\,, \tag{3.14}$$

where vol_Y is the actual volume of unit (base) cell. This approach was compared in [16] to the works [5] and [7] which addressed the same issues, and has been declared more accurate by the authors. Also, other studies were based on the same general expressions (see Equation (3.13) and Equation (3.14)) and have proposed similar analytical approaches – amongst others, the articles of Lukkassen et al. [29], Kalamkarov et al. [111], Hassan et al. [132] and Cheng et al. [147]. In spite of the appropriateness to describe periodic structures with equivalent elasticity matrices in the general case, this method may be complicated to apply due to the need of resolving condition (3.13) in the first place. This difficulty is outlined in [58], where the resolution techniques of the general expressions (3.13) and (3.14) are denoted to be "nebulous" by the authors.

However, this general homogenisation technique has been applied to laminated structures in [14], and led to "clear" expressions given for the same case as before: a structure

of N isotropic layers stacked along the z-axis. The algorithm is referred to as "**INRIA**" ("*Institut National de Recherche en Informatique et en Automatique*", i.e. french Institute for Research in Computer Science and Automation) in the entire study, and is detailed as following. Each layer's elasticity matrix $[C]_n$ is defined with Lamé's coefficients λ_n and μ_n so that

$$[C_n] = \begin{bmatrix} \lambda_n + 2\mu_n & \lambda_n & \lambda_n & 0 & 0 & 0 \\ & \lambda_n + 2\mu_n & \lambda_n & 0 & 0 & 0 \\ & & \lambda_n + 2\mu_n & 0 & 0 & 0 \\ & & & \mu_n & 0 & 0 \\ & \text{sym.} & & & \mu_n & 0 \\ & & & & & \mu_n \end{bmatrix} . \tag{3.15}$$

With the aid of the coefficients I_0, I_1, I_2 and J_0 such that

$$I_h = \sum_{n=1}^{N} \frac{(\lambda_n)^h}{\lambda_n + 2\mu_n} \cdot \chi_n \tag{3.16}$$

and

$$J_0 = \sum_{n=1}^{N} \frac{\chi_n}{\mu_n} , \tag{3.17}$$

the constants $\tilde{C}_{11}$ are computed with the global relations [14]:

$$\tilde{C}_{11} = \frac{I_1^2 - I_0 I_2}{I_0} + \sum_{n=1}^{N} (\lambda_n + 2\mu_n) \cdot \chi_n , \tag{3.18}$$

$$\tilde{C}_{22} = \tilde{C}_{11} , \tag{3.19}$$

$$\tilde{C}_{12} = \frac{I_1^2 - I_0 I_2}{I_0} + \sum_{n=1}^{N} \lambda_n \chi_n , \tag{3.20}$$

$$\tilde{C}_{13} = \tilde{C}_{23} = \frac{I_1}{I_0} , \tag{3.21}$$

$$\tilde{C}_{33} = \frac{1}{I_0} , \tag{3.22}$$

$$\tilde{C}_{44} = \tilde{C}_{55} = \frac{1}{J_0} \tag{3.23}$$

and

$$\tilde{C}_{66} = \sum_{n=1}^{N} \mu_n \chi_n . \tag{3.24}$$

The expressions, initially defined with an integration over the entire structure's thickness, have been here expressed under a discrete form. The laminated stack's equivalent elasticity matrix is therefore composed:

$$[\tilde{C}] = \begin{bmatrix} \tilde{C}_{11} & \tilde{C}_{12} & \tilde{C}_{13} & 0 & 0 & 0 \\ & \tilde{C}_{11} & \tilde{C}_{13} & 0 & 0 & 0 \\ & & \tilde{C}_{33} & 0 & 0 & 0 \\ & & & \tilde{C}_{44} & 0 & 0 \\ & \text{sym.} & & & \tilde{C}_{44} & 0 \\ & & & & & \tilde{C}_{66} \end{bmatrix} , \tag{3.25}$$

and by the way verifies the property of transverse isotropy

$$\tilde{C}_{11} = \tilde{C}_{12} + 2 \cdot \tilde{C}_{66} . \tag{3.26}$$

Identical expressions have been proposed in [68].

3.2.1.3/ PEMAT

An unreferenced homogenisation method is presented in the Ph.D. thesis of Chentouf [130]. Although he did not apply it in his thesis, the author details an algorithm for computing equivalent elastic properties for a laminated structure with N layers, using as input data the individual layers' elasticity matrices. The abbreviation "**PEMAT**" (for "permuted matrices") is used for referring to this method.

First of all, the initial elasticity matrix $[C_n]$ of each individual layer n is re-arranged into $[U_n]$ by permutation of two rows and columns in order to group the "planar" (superscript P) and "anti-planar" (superscript A) terms of $[C_n]$. For instance, if the stacking direction is 3, the rows and columns referring to indices "33" and "12" (i.e. in positions 3 and 6 in Hooke's System (1.11)) are swapped. In detail, $[U_n]$ is decomposed as

$$[U_n] = \begin{bmatrix} U_n^{PP} & U_n^{PA} \\ U_n^{AP} & U_n^{AA} \end{bmatrix} = \begin{bmatrix} C_{11} & C_{12} & C_{16} & C_{14} & C_{15} & C_{13} \\ & C_{22} & C_{26} & C_{24} & C_{25} & C_{23} \\ & & C_{66} & C_{64} & C_{65} & C_{63} \\ & & & C_{44} & C_{45} & C_{43} \\ & \text{sym.} & & & C_{55} & C_{53} \\ & & & & & C_{33} \end{bmatrix}_n \tag{3.27}$$

and verifies the initial (index i) permuted Hooke's equation

$$\begin{Bmatrix} \sigma_i^P \\ \sigma_i^A \end{Bmatrix} = \begin{bmatrix} U_n^{PP} & U_n^{PA} \\ U_n^{AP} & U_n^{AA} \end{bmatrix} \begin{Bmatrix} \varepsilon_i^P \\ \varepsilon_i^A \end{Bmatrix} . \tag{3.28}$$

In the second step, Equation (3.28) is re-arranged into

$$\begin{Bmatrix} \sigma_i^P \\ \varepsilon_i^A \end{Bmatrix} = \begin{bmatrix} V_n^{PP} & V_n^{PA} \\ V_n^{AP} & V_n^{AA} \end{bmatrix} \begin{Bmatrix} \varepsilon^P \\ \sigma^A \end{Bmatrix} , \tag{3.29}$$

where the sub-matrix $\left[U_n^{AA}\right]$ is assumed to be non-singular, and where

$$V_n^{PP} = U_n^{PP} - U_n^{PA}\left(U_n^{AA}\right)^{-1} U_n^{AP},$$
$$V_n^{PA} = U_n^{PA}\left(U_n^{AA}\right)^{-1},$$
$$V_n^{AP} = -\left(U_n^{AA}\right)^{-1} U_n^{AP}$$

and

$$V_n^{AA} = \left(U_n^{AA}\right)^{-1}.$$

Averaging matrices $[V_n]$ in Equation (3.29) over the entire stack and weighting each layer with the corresponding volume fraction χ_n yields

$$\left[\tilde{V}\right] = \begin{bmatrix} \tilde{V}^{PP} & \tilde{V}^{PA} \\ \tilde{V}^{AP} & \tilde{V}^{AA} \end{bmatrix} = \sum_{n=1}^{N} \chi_n \begin{bmatrix} V_n^{PP} & V_n^{PA} \\ V_n^{AP} & V_n^{AA} \end{bmatrix}. \tag{3.30}$$

Then, the global system

$$\begin{Bmatrix} \sigma_i^P \\ \varepsilon_i^A \end{Bmatrix} = \begin{bmatrix} \tilde{V}^{PP} & \tilde{V}^{PA} \\ \tilde{V}^{AP} & \tilde{V}^{AA} \end{bmatrix} \begin{Bmatrix} \varepsilon^P \\ \sigma^A \end{Bmatrix} \tag{3.31}$$

is re-arranged into a new equation in the form of Hooke's law:

$$\begin{Bmatrix} \sigma^P \\ \sigma^A \end{Bmatrix} = \begin{bmatrix} \tilde{Y}^{PP} & \tilde{Y}^{PA} \\ \tilde{Y}^{AP} & \tilde{Y}^{AA} \end{bmatrix} \begin{Bmatrix} \varepsilon^P \\ \varepsilon^A \end{Bmatrix}, \tag{3.32}$$

where

$$\tilde{Y}^{PP} = \tilde{V}^{PP} - \tilde{V}^{PA}\left(\tilde{V}^{AA}\right)^{-1} \tilde{V}^{AP},$$
$$\tilde{Y}^{PA} = \tilde{V}^{PA}\left(\tilde{V}^{AA}\right)^{-1},$$
$$\tilde{Y}^{AP} = -\left(\tilde{V}^{AA}\right)^{-1} \tilde{V}^{AP}$$

and

$$\tilde{Y}^{AA} = \left(\tilde{V}^{AA}\right)^{-1}.$$

Finally, the global equivalent elasticity matrix $\left[\tilde{C}\right]$ is found by permuting the same rows and columns as before in $\left[\tilde{Y}\right]$, in order to re-order Equation (3.32) into the conventional format of Hooke's law (1.11). This method is therefore not limited to isotropic layers and is able to manage triclinic materials' elasticity matrices. In the case of a stack of isotropic layers, it can be observed that the developed expressions of the equivalent coefficients $\tilde{C}_{ij}$ are identical as for method "**INRIA**".

3.2.1.4/ KPC

A numerical property identification method has been developed in the frame of this Ph.D. thesis prior to the study detailed in the next paragraphs of this section. This approach is designed for finite-element structures, and the abbreviation "**KPC**" is used for referring to it. The idea is first to extract the base cell from the initial heterogeneous structure, i.e. the cell which is periodically duplicated throughout the global structure. The application is made on a laminated stack whose base cell is composed of three layers, as illustrated in Figure 3.3. The external nodes are numbered from 1 to 8, whereas the internal nodes (at the boundaries of two elements) are numbered from 101 to 108. The global dimensions about directions x, y and z are L_x, L_y and L_z, respectively.

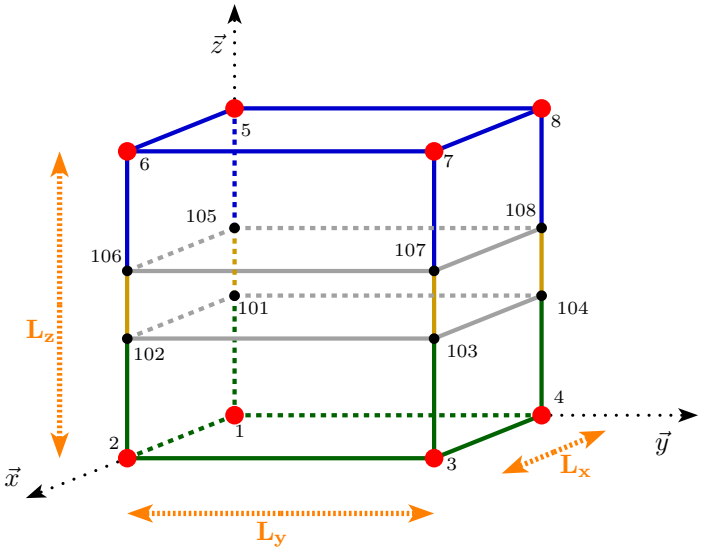

Figure 3.3 – Base cell - **KPC**

This base cell is condensed into a super-element whose master-DOFs are the translational DOFs Tx, Ty and Tz at the external nodes 1 to 8 (in red in Figure 3.3, see Paragraph 1.3.3.1 for theoretical details). The geometry described by the super-element is therefore a single 8-node element, which is characterised by the reduced 24×24 stiffness matrix $[\mathcal{K}_r]$.

The next step consists in building the stiffness matrix of a generic finite element of similar nature. With the aid of a symbolic algebra solver (such as Maxima™) and as described in Appendix A.1.1, the stiffness matrix $[\mathcal{K}^e]$ of the element is computed with Equation A.11:

$$[\mathcal{K}^e] = \det([J]) \cdot \int_{-1}^{1}\int_{-1}^{1}\int_{-1}^{1} [\mathcal{B}^e]^\intercal [C] [\mathcal{B}^e] \, \mathrm{d}\xi \mathrm{d}\eta \mathrm{d}\zeta \ .$$

For the case of a 8-node cuboid element, the interpolation function $\bar{\mathfrak{N}}_i(\xi, \eta, \zeta)$ associated to each of the reference nodes i is described by the expression

$$\bar{\mathfrak{N}}_i(\xi, \eta, \zeta) = \frac{1}{8} \cdot (1 + x_i \cdot \xi) \cdot (1 + y_i \cdot \eta) \cdot (1 + z_i \cdot \zeta) \ , \tag{3.33}$$

where x_i, y_i and z_i are the coordinates of node i. The detail of the coordinates is given in Table 3.1.

node i	x_i	y_i	z_i
1	-1	-1	-1
2	1	-1	-1
3	1	1	-1
4	-1	1	-1
5	-1	-1	1
6	1	-1	1
7	1	1	1
8	-1	1	1

Table 3.1 – Coordinates of the reference element's nodes

The global dimensions L_x, L_y and L_z are used for computing $\left[\mathcal{K}^e\left(C_{ij}\right)\right]$, leading to a 24×24 symmetric matrix whose 300 independent coefficients are linear combinations of C_{ij}. In its general form, the elasticity matrix $[C]$ is composed of 21 coefficients C_{ij} which are expressed in a vectorial form $\{C\}$. Therefore, keeping the symbolic expressions of the coefficients C_{ij} enables expressing the stiffness matrix $[\mathcal{K}^e]$ under a 300×1 vectorial form $\left\{\mathcal{K}^e\left(C_{ij}\right)\right\}$ with the relation:

$$\left\{\mathcal{K}^e\left(C_{ij}\right)\right\} = \begin{bmatrix} & & \\ & P & \\ & & \end{bmatrix} \begin{Bmatrix} C_{11} \\ C_{12} \\ \vdots \\ C_{66} \end{Bmatrix}, \tag{3.34}$$

where the transformation matrix $[P]$ is only composed of real, numerical values.

Then, computing a pseudo-inverse $\left[P^{\#}\right]$ of matrix $[P]$ (e.g. with Moore-Penrose algorithms as implemented into most common numeric solvers such as Scilab™) and pre-multiplying the vectorial form of the previously-condensed stiffness matrix $[\mathcal{K}_r]$ yields

$$\left\{\tilde{C}\right\} = \left[P^{\#}\right]\left\{\mathcal{K}_r\right\} . \tag{3.35}$$

Eventually, $\left\{\tilde{C}\right\}$ is re-arranged into the 6×6 equivalent elasticity matrix $\left[\tilde{C}\right]$.

3.2.1.5/ Discussion on the applications

The paragraphs 3.2.1.1 through 3.2.1.4 have introduced several approaches for identifying equivalent elastic properties in heterogeneous structures. Still concerning 3D models, Cecchi and Sab [98] have proposed a numerical homogenisation method for orthotropic structures based on a Reissner-Mindlin model, and applied it to brick walls. Although efficient, the algorithm nonetheless requires computing correction factors amidst the numerous computation stages and therefore seems tricky to implement.

There exist other numerical models. The works of Watt et al. [10], Kamiński and Kleiber [51], and Magalhães Dourado [80] have aimed at identifying composite structures' elastic

coefficients by the means of statistical methods, that seem complicated to use in simple, deterministic studies. As for Araújo et al. [49], they have proposed a numerical model for the identification of elastic properties of laminates, applied it to the dynamic behaviour of a stratified plate and compared the results with experimental measurements. Yet, this approach does not identify all 6 lines of Hooke's law elasticity matrix, and is therefore too restrictive to be applied to generic 3D structures.

Apart from homogenisation techniques, the recent development of several types of industrial materials and devices has motivated research in the comprehension and prediction of laminated structures' dynamic behaviours. A type of device currently under the spotlight is alternating electric machines, the stators of which are built from a multi-layered laminated structure, called the magnetic core. Amongst the studies made in this field, the works of Wang [35], Verma [20], Williams [24] or Le Besnerais [101] bring sensible notions of stator and magnetic core dynamics to the table, yet without exhibiting elastic properties or modelling techniques. As for modelling guidelines, the necessity of taking other heterogeneities such as weld beads into account in a homogenisation process of the magnetic core has, to the authors' knowledge, not yet been addressed in the literature.

As for the use of composite materials in commercial software, the implementation of 3D laminated structures is not documented or is restricted to specific non-linear or static studies. Only few works tackling homogenisation issues show the comparison of their results to those obtained with commercial software in such cases. Based on Barker's results [9] – stating that 3D-homogenisation of composite structures necessarily induces detrimental errors – Kuhlmann and Rolfes have developed their own 3D-laminated finite element [78], seemingly as accurate as MSC.MARC™'s. However, to the authors' knowledge this finite element has not yet been implemented into any software packages available on the market.

Finally, concerning experimental analyses, several approaches exist to measure the elastic behaviour of a structure. Hearmon [1] and Hayes [8] have detailed a few ways to identify a structure's entire elasticity matrix from measurements. But as this method requires several types of analysis and several types of samples, it seems very difficult to inspire an analogous application to finite-element models. This same difficulty also compromises the use of other methods, such as those developed in the articles of Pierron et al. [52] and Rikards et al. [45, 60, 82].

In this section, several types of approaches have been discussed for the application to laminated structures. Some of them are numerical or analytical/asymptotic homogenisation techniques, or deal with experimental applications, while others are based on finite-element models. The novel method proposed in this study belongs to this last category: it is based on finite elements. The emphasis is made on representative elasticity matrices, which constitute stress-strain laws for the considered materials and determine stiffness matrices for both static and dynamic analyses. The following subsections will detail its applications to simulate the dynamic behaviours of multi-layered orthotropic laminates as well as the magnetic core of an electric motor stator. The last subsection will also investigate efficient modelling techniques for FE models of electric motor stators and compare the modal simulations to experimental data from an industrial structure.

3.2.2/ DEVELOPMENT OF THE "ORTHOTROPIC" METHOD

In this subsection, a new approach aiming at determining the elastic properties of a heterogeneous structure is proposed. The equivalent material thus defined is assumed to be orthotropic (as explained in Section 3.2.1) and is characterised by nine elastic coefficients: E_x, E_y, E_z, G_{zy}, G_{zx}, G_{xy}, ν_{yz}, ν_{xz} and ν_{xy}. By the means of a limited number of static simulations and by simple processing of the corresponding displacements in the structure, all nine elastic coefficients can be computed. The definition of shear in the case of laminates can be ambiguous due to the orientation of the structure, and is therefore addressed in this work.

The study taken as an example in this section is a stack along the z-axis of three isotropic thick layers, for which the theory predicts a global transversely isotropic behaviour [119]. The structure is a cuboid <1, 2, 3, 4, 5, 6, 7, 8> composed of three 8-node solid elements, as shown in Figure 3.4. The nodes 101, 102, 103, 104, 105, 106, 107 and 108 represent the respective interfaces with their two neighbouring elements. Also, the coordinate system for the whole structure is global (i.e. rectangular unitary system) and its origin taken as node 1. The cuboid's dimensions are L_x, L_y and L_z and its faces' respective areas A_x (faces $x = 0$ and $x = 1$), A_y (faces $y = 0$ and $y = 1$) and A_z (faces $z = 0$ and $z = 1$). The descriptions of external faces is made with '$= 0$' or '$= 1$' notations (referring to the limits of the structure's volume), despite L_x, L_y and L_z.

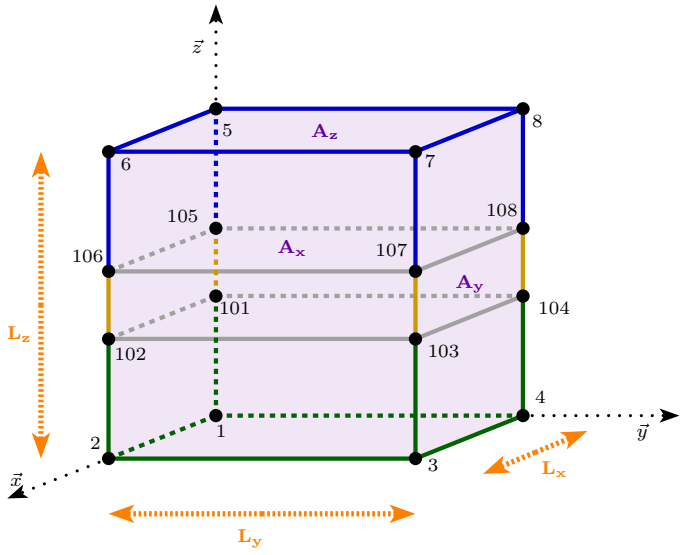

Figure 3.4 – Structure geometry

The first simulation is a pure tension along the x-axis shown in Figure 3.5: a static displacement δ_x is enforced along $-x$ to the nodes 1, 4, 5, 8, 101, 104, 105 and 108 (face $x = 0$), while the same displacement δ_x is enforced along $+x$ to the nodes 2, 3, 6, 7, 102, 103, 106 and 107 (face $x = 1$). In order to stabilise the system, plane contact constraints are applied to the faces $y = 0$ and $z = 0$.

By computing the nodal displacements $\Delta l_{x,i}$, $\Delta l_{y,i}$ and $\Delta l_{z,i}$ as well as the reaction forces $F_{x,i}$, $F_{y,i}$ and $F_{z,i}$ at every node i, the stress σ_{xx} can be found using the relation

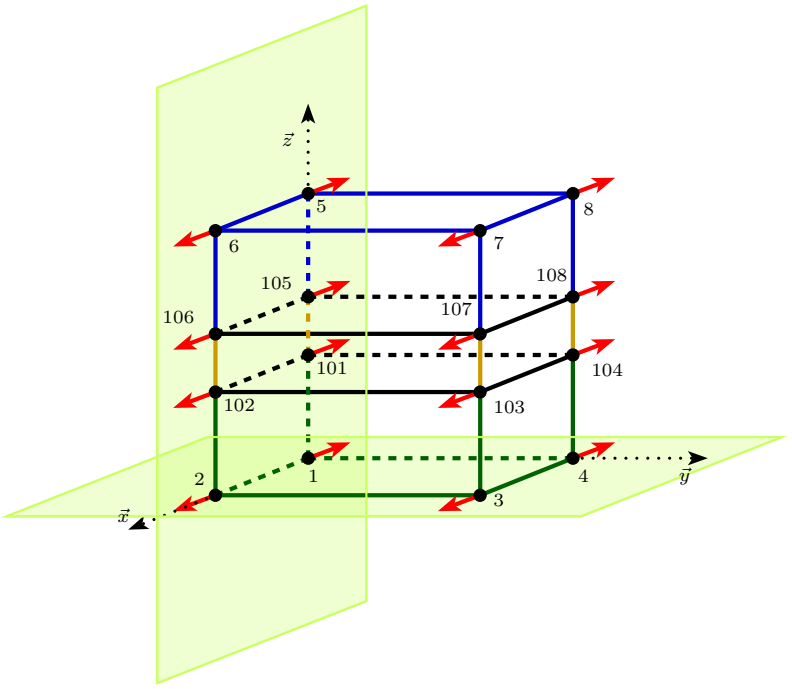

Figure 3.5 – Pure tension along x

$$\sigma_{xx} = \frac{1}{A_x} \sum_{i \in \mathcal{U}_{x1}} \frac{F_{x,i}}{2} \,, \tag{3.36}$$

where $\mathcal{U}_{x1}$ is the set of nodes located on face $x = 1$. Therefore, the Young's modulus $\tilde{E}_x$ in the x-direction may be found with [18]

$$\tilde{E}_x = \sigma_{xx} \cdot \frac{L_x}{\delta_x} \,, \tag{3.37}$$

where the ratio L_x/δ_x is related to the normal strain ε_{xx} by

$$\frac{L_x}{\delta_x} = \frac{1}{\varepsilon_{xx}} \,. \tag{3.38}$$

The Poisson's ratios $\tilde{\nu}_{xy}$ and $\tilde{\nu}_{xz}$ can then be computed with the mean displacements $\overline{\Delta l_y}^{(\mathcal{U}_{y1})}$ and $\overline{\Delta l_z}^{(\mathcal{U}_{z1})}$, such as

$$\overline{\Delta l_y}^{(\mathcal{U}_{y1})} = \frac{1}{\mathcal{B}_{y1}} \sum_{i \in \mathcal{U}_{y1}} \Delta l_{y,i} \tag{3.39}$$

and

$$\overline{\Delta l_z}^{(\mathcal{U}_{z1})} = \frac{1}{\mathcal{B}_{z1}} \sum_{i \in \mathcal{U}_{z1}} \Delta l_{z,i} \,, \tag{3.40}$$

where $\mathcal{B}_{y1}$ and $\mathcal{B}_{z1}$ respectively refer to the numbers of nodes on the faces $y = 1$ and $z = 1$ (e.g. for a stack with three layers, $\mathcal{B}_{x1} = \mathcal{B}_{y1} = 8$ and $\mathcal{B}_{z1} = 4$). This finally yields:

$$\tilde{\nu}_{xy} = \frac{-\overline{\Delta l_y}^{(\mathcal{U}_{y1})}}{2 \cdot \delta_x} \cdot \frac{L_x}{L_y} \tag{3.41}$$

and

$$\tilde{\nu}_{xz} = \frac{-\overline{\Delta l_z}^{(\mathcal{U}_{z1})}}{2 \cdot \delta_x} \cdot \frac{L_x}{L_z} \,. \tag{3.42}$$

Two similar simulations along y and z yield the global structure's remaining Young's moduli and Poisson's ratio:

$$\tilde{E}_y = \frac{L_y}{A_y \cdot \delta_y} \sum_{i \in \mathcal{U}_{y1}} \frac{F_{y,i}}{2} \,, \tag{3.43}$$

$$\tilde{E}_z = \frac{L_z}{A_z \cdot \delta_z} \sum_{i \in \mathcal{U}_{z1}} \frac{F_{z,i}}{2} \tag{3.44}$$

and

$$\tilde{\nu}_{yz} = \frac{-\overline{\Delta l_z}^{(\mathcal{U}_{z1})}}{2 \cdot \delta_y} \cdot \frac{L_y}{L_z} \,. \tag{3.45}$$

Finally, the reciprocal Poisson's ratios $\tilde{\nu}_{yx}$, $\tilde{\nu}_{zx}$ and $\tilde{\nu}_{zy}$ must verify the symmetry of the global elasticity matrix [119], such that

$$\frac{\tilde{\nu}_{ij}}{\tilde{E}_i} = \frac{\tilde{\nu}_{ji}}{\tilde{E}_j} \,. \tag{3.46}$$

The shear moduli $\tilde{G}_{zy}$, $\tilde{G}_{zx}$ and $\tilde{G}_{xy}$ may be found with shear simulations. However, some attention must be paid when defining shear in the case of non-isotropic materials and particularly for laminated composites. Although an orthotropic structure's shear moduli are often estimated without explicit consideration of either sliding or transverse shear configurations ([16, 41, 119]), it may be observed in practice that the two behaviours are not equivalent in general. This is why, in this document, the analysis separates sliding shear (illustrated in Sub-figure 3.6(a)) from transverse shear (illustrated in Sub-figure 3.6(b)) in the respective "**Ortho1**" and "**Ortho2**" scenarios. It may be noted that the identification of Young's moduli and Poisson's ratios remains identical in both scenarios.

The next paragraphs detail the determination of shear moduli by sliding shear schemes, which therefore correspond to the "**Ortho1**" scenario (see Sub-figure 3.6(a)). The simulation combines an enforced displacement δ_y applied along $-y$ at nodes 1, 2, 3, 4 (face $z = 0$), the same displacement δ_y along $+y$ at nodes 5, 6, 7, 8 (face $z = 1$) and plane contact constraints on the same faces $z = 0$ and $z = 1$ in order to generate pure shear. To stabilise the system, the T_x degree of freedom at node 1 is fixed.

The stress σ_{zy} is defined by the relation

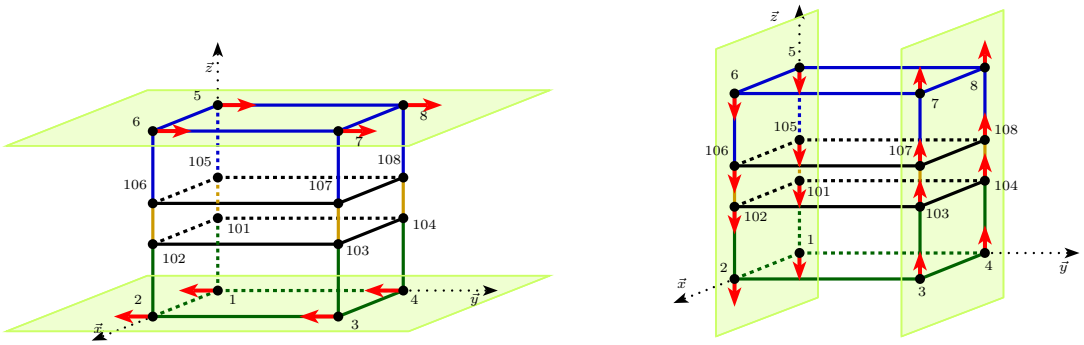

(a) Pure sliding shear $z - y$ (**Ortho1**)

(b) Pure transverse shear $y - z$ (**Ortho2**)

Figure 3.6 – Shear definitions

$$\sigma_{zy} = \frac{1}{A_z} \sum_{i \in \mathcal{U}_{z1}} \frac{F_{y,i}}{2} \,, \tag{3.47}$$

where $\mathcal{U}_{z1}$ is the set of the nodes located on the face $z = 1$. Finally, this yields the shear modulus $\tilde{G}_{zy}$ [18]:

$$\tilde{G}_{zy} = \sigma_{zy} \cdot \frac{L_z}{\delta_y} \,, \tag{3.48}$$

where the ratio L_z/δ_y is related to the shear strain ε_{zy} by

$$\frac{L_z}{\delta_y} = \frac{1}{\gamma_{zy}} = \frac{1}{2 \cdot \varepsilon_{zy}} \,. \tag{3.49}$$

The two other shear moduli are then computed in a similar way and are defined by the following expressions:

$$\tilde{G}_{zx} = \frac{L_z}{A_z \cdot \delta_x} \sum_{i \in \mathcal{U}_{z1}} \frac{F_{x,i}}{2} \tag{3.50}$$

and

$$\tilde{G}_{xy} = \frac{L_x}{A_x \cdot \delta_y} \sum_{i \in \mathcal{U}_{x1}} \frac{F_{y,i}}{2} \,. \tag{3.51}$$

3.2.3/ Comparison with other existing methods

The results of the "orthotropic" method presented in Section 3.2.2 have been compared to those obtained from some other methods that could be applied to such structures: three isotropic layers stacked along the z-axis, whose properties are gathered into Table 3.2. The structure's base cell is a 1-centimetre-long cube for which the layers are organised as following (for increasing z): titanium ($l_1 = 0.4\,\text{cm}$), polypropylene ($l_2 = 0.2\,\text{cm}$) and steel ($l_3 = 0.4\,\text{cm}$), where l_i represents the layer's thickness.

	Steel	**Polypropylene**	**Titanium**
E [GPa]	207	2.0	121
ν [−]	0.25	0.40	0.34
ρ [kg · m^{-3}]	7875	1200	4430
l [cm]	0.40	0.20	0.34

Table 3.2 – Initial stack

The other methods being compared are the homogenisation algorithms detailed in Paragraphs 3.2.1.1 through 3.2.1.4, respectively referred to as "**WA**", "**INRIA**", "**PEMAT**" and "**KPC**". A larger structure was built from this base cell, standing for a reference for comparisons. The global structure is shaped as a cuboid, has 5,024 elements, 30,144 DOFs; its dimensions along x, y and z are respectively 210 mm, 110 mm and 60 mm, so that the unit cell is reproduced periodically in every direction.

Also, a node-to-ground 3-D stiffness element is linked to each of the global cuboid's 8 outer nodes, with stiffness values of $K^{\text{ntg}} = 10^7\,\text{N} \cdot \text{m}^{-1}$ on every direction (x, y and z). The global laminated structure taken as a reference is illustrated in Figure 3.7.

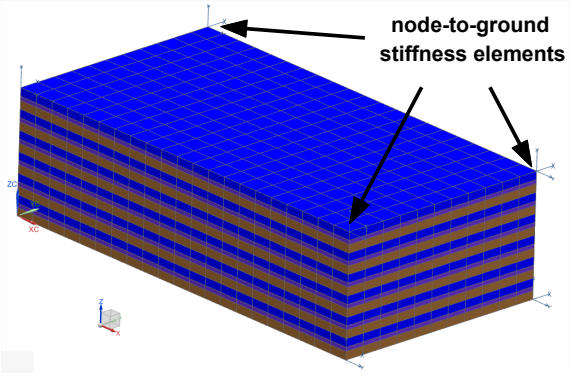

Figure 3.7 – Global laminated reference structure

The homogeneous finite-element models based on each of the equivalent materials have the same dimensions and the same total mass as the reference structure and are made of 1-centimetre-long cubic 8-node solid elements.

The elastic coefficients of the equivalent materials respectively computed with each of the methods are compared in Table 3.3. "**Ortho1**" and "**Ortho2**" refer to the scenarios developed in Section 3.2.2, and the other labels to their respective methods. As explained in Paragraph 3.2.1.3, methods "**INRIA**" and "**PEMAT**" yield equivalent results when applied to a stack of isotropic layers. Therefore, the properties computed with method "**PEMAT**" are discarded. Also, the elasticity matrix $\left[\tilde{C}^{\text{O1}}\right]$ equivalent to the material computed with method "**Ortho1**" corresponds to:

$$\left[\tilde{C}^{O1}\right] = \begin{bmatrix} 164 & 59.3 & 9.63 & 0 & 0 & 0 \\ & 164 & 9.63 & 0 & 0 & 0 \\ & & 19.4 & 0 & 0 & 0 \\ & & & 3.34 & 0 & 0 \\ & \text{sym.} & & & 3.34 & 0 \\ & & & & & 51.3 \end{bmatrix} \cdot 10^9 \,. \tag{3.52}$$

For each case, the mass matrix of the homogeneous equivalent structure is computed from the relation (3.6) (weighted averages). Apart from the reference structure, every mass matrix is therefore identical. Finally, the row "**CC**" compares the computation costs (in seconds) for each of the methods used. The finite-element solver NASTRAN™ v. 2013 is used for scenarios "**Ortho1**" and "**Ortho2**" (with a dual-core 2.5 GHz processor and 16 GB of RAM), whereas results for "**INRIA**", "**WA**" and "**KPC**" are computed with Scilab v. 5.4.1.

	Ortho1	**Ortho2**	**INRIA**	**WA**	**KPC**
$\tilde{E}_x$ [GPa]	132	132	137	132	89.0
$\tilde{E}_y$ [GPa]	132	132	137	132	89.0
$\tilde{E}_z$ [GPa]	18.7	18.7	19.0	9.50	17.6
$\tilde{G}_{zy}$ [GPa]	3.34	51.3	3.40	3.40	12.3
$\tilde{G}_{zx}$ [GPa]	3.34	51.3	3.40	3.40	12.3
$\tilde{G}_{xy}$ [GPa]	51.3	51.3	51.3	50.0	34.1
$\tilde{\nu}_{yz}$ [−]	0.326	0.326	0.313	0.023	0.144
$\tilde{\nu}_{xz}$ [−]	0.326	0.326	0.313	0.023	0.144
$\tilde{\nu}_{xy}$ [−]	0.343	0.343	0.338	0.316	0.216
$\tilde{\rho}$ $[\mathrm{kg \cdot m^{-3}}]$	5,160	5,160	5,160	5,160	5,160
CC [s]	8	8	<1	<1	<1

Table 3.3 – Comparison of elastic coefficients

It can be seen that for methods "**Ortho1**", "**Ortho2**" and "**INRIA**", Poisson's ratios have relatively similar values, whereas the differences are more important for methods "**WA**" and "**KPC**". This could be compared to the results of Chentouf [130], where it was suggested to force Poisson's ratio values to zero in all directions as a practical modelling guideline. Judging from the apparent tightness existing in the laminated stack, such an indication seems exagerated to represent the real couplings in the structure. As for the computation costs, Table 3.3 shows that they are all below 10 seconds, although they do not account for the time necessary to prepare the solutions. Independently from this preparation time, the presented method can be automatised and be adapted to any types of structures, at the cost of quick changes to perform (e.g. element thicknesses).

RESULTS

With the aid of the criteria introduced in Subsection 1.4.2, the correlation between each of the three homogeneous structures (to which the materials computed by each method

have been applied) and the reference model have been compared. To do this, the first 50 vibration modes have been computed for each case, amongst which the first 6 modes (between 413 Hz and 853 Hz) describing the "suspension" related to the node-to-ground elements have been discarded. For the reference structure, the 7$^{\text{th}}$ mode (and thus the first to be correlated) is at 3,073 Hz, while amongst all homogeneous structures, the 7$^{\text{th}}$ mode of lowest frequency is at 2,947 Hz. The paired modes for which MAC values were below 70% were discarded too. An example of paired deformed shapes between the reference structure and the homogeneous model (computed with scenario "**Ortho1**") is given in Figure 3.8. Structure (a) shows the deformation of the individual layers while structure (b) shows "flatter" boundaries due to bigger elements made of identical material properties. The two structures are paired in (c) even though the elements are of different sizes and numbers in (a) and (b).

Then, the results of the correlation are plotted in Figure 3.9 and summed up in Table 3.4 for the first 44 modes of the reference structure. For N_{mp} mode pairs in a given correlation, the expressions defining the entities $\overline{|\Delta f|}$ and $\overline{MAC}$ are recalled from Equations (1.68) and (1.69):

$$\overline{|\Delta f|} = \frac{1}{N_{mp}} \cdot \sum_{q=1}^{N_{mp}} \left|\Delta f \left(m_{1,q}, m_{2,q}\right)\right|$$

and

$$\overline{MAC} = \frac{1}{N_{mp}} \cdot \sum_{q=1}^{N_{mp}} MAC \left(m_{1,q}, m_{2,q}\right) \ ,$$

where $m_{1,q}$ and $m_{2,q}$ are the modes composing the q-th pair.

	Ortho1	**Ortho2**	**INRIA**	**WA**	**KPC**
Nb paired modes	39	20	37	30	26
$\overline{\lvert\Delta f\rvert}$ [%]	9.29	58.6	9.86	15.3	26.7
$\overline{MAC}$ [%]	93.1	83.7	93.8	89.9	89.1

Table 3.4 – Correlation of the reference structure's first 44 modes above 853 Hz

It can be clearly seen that the method "**Ortho1**" proposed in Section 3.2.2 is more accurate than the weighted averages, and of equivalent quality to "**INRIA**" in such a setting, whereas using "**Ortho2**" leads to more significant errors, especially for low-frequency modes. The discrepancies of value Δf for the mode pairs 6 to 22 of the case "**Ortho2**" can be explained by the fact the structure undergoes deformations that are related to "sliding" shear rather than "transverse" shear. To corroborate this observation, the deformed shapes of the first 9 paired modes are detailed in Figure 3.10. Although for this stacking setting, the values of $\overline{|\Delta f|}$ are all relatively high, still 39 modes of the 44 are identified by the method "**Ortho1**".

Finally, "**Ortho1**" presents a new opportunity, that none of the approaches analysed in Section 3.2.1 did. Indeed, this type of static simulation is not restrained to applications on finite-element models including distinctive elements and materials, but may also be used with structures on which no information about constitutive materials is available.

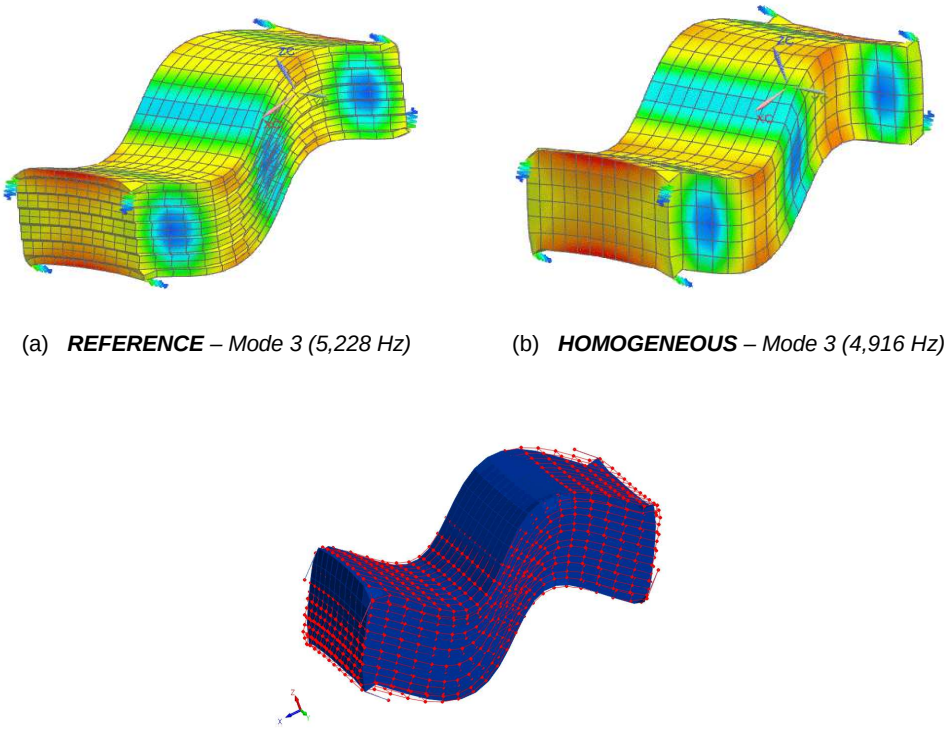

(a) ***REFERENCE*** – *Mode 3 (5,228 Hz)* (b) ***HOMOGENEOUS*** – *Mode 3 (4,916 Hz)*

(c) ***MODE PAIR 3*** – *red dots:* ***REFERENCE*** – *blue solid:* ***HOMOGENEOUS ("Ortho1")***

Figure 3.8 – Compared models' deformed shapes

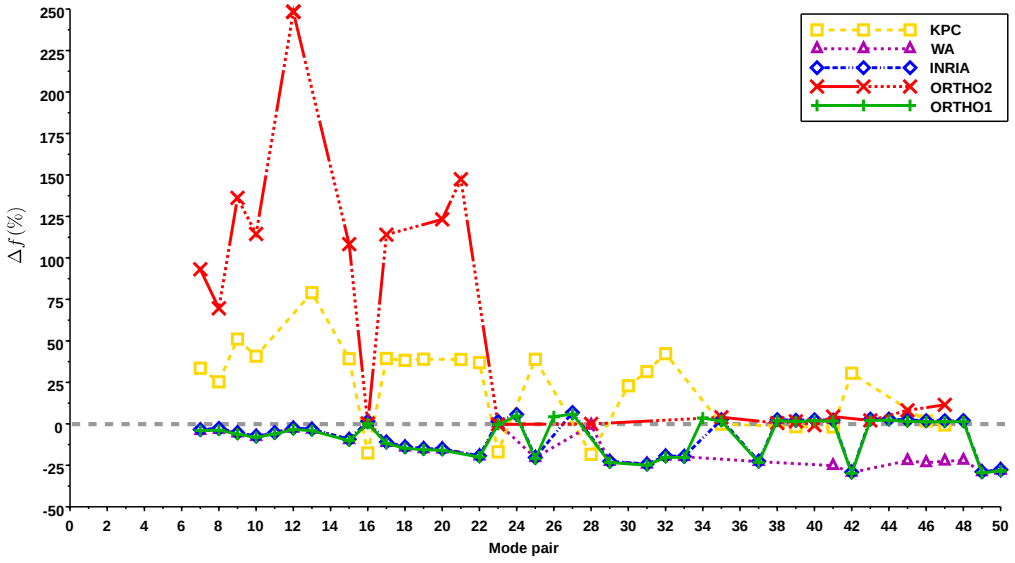

Figure 3.9 – Comparison of frequency differences with reference model ($MAC > 70\%$)

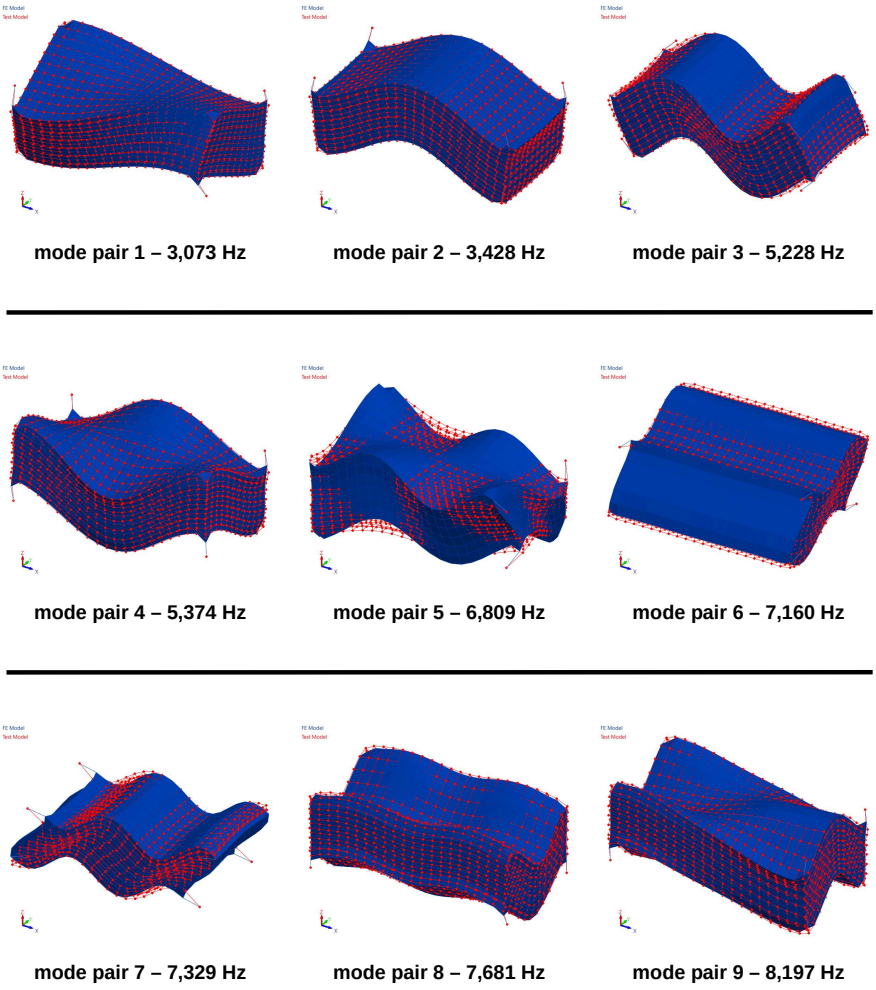

Figure 3.10 – First 9 paired modes (reference structure's natural frequencies)

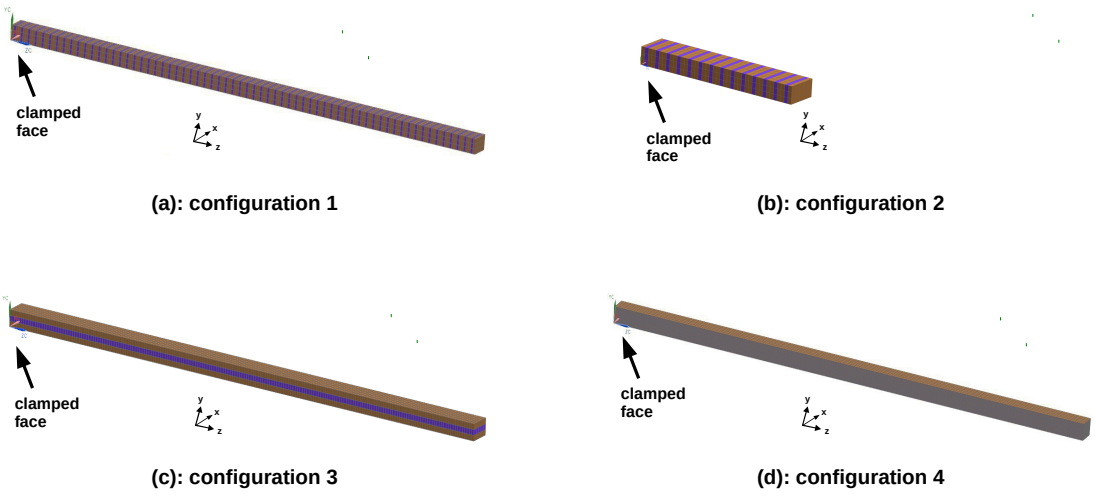

Figure 3.11 – Configurations of laminated beams

For example, a superelement whose master-nodes describe the geometry of a cuboid could be analysed with the same method, leading to the construction of an equivalent homogeneous material that would recreate the superelement's stiffness behaviour.

3.2.4/ INFLUENCE OF STACKING SETTINGS IN A BEAM

This second application aims at analysing the influence of the number of layers in a cantilever beam. For this, four FE models of laminated cantilever beams are created from the same base cell: three layers of isotropic materials, either stacked along the beam's length (models 1 and 2) or in a transverse direction (models 3 and 4). Beam 1 is composed of more layers than beam 2, but of similar thicknesses: beam 2 is shorter. To the contrary, the global dimensions of beams 3 and 4 are identical, while beam 4 is made of more layers: each of them is therefore thinner. Finally, each beam is spanned along z, and its dimensions along x and y are respectively 50 and 30 mm. The four configurations are shown in Figure 3.11, and detailed in Table 3.5.

Configuration ID	Nodes	Elements	DOFs	Stratification along	Dimension along z [mm]	Total number of layers
1	4,776	2,970	28,656	z	1,200	198
2	1,032	630	6,192	z	252	42
3	4,824	3,000	28,944	y	1,200	3
4	37,386	30,000	224,316	y	1,200	30

Table 3.5 – Details of laminated beams

The properties of the base cell are gathered in Table 3.6, in which E stands for the material's Young's modulus, ν for its Poisson's ratio and χ for the layer's volume fraction (see Equation (3.5)).

Applying the method "**Ortho1**" to this base cell yields equivalent material properties to models 1 and 2 (layers stacked along z):

$$\tilde{E}_x = \tilde{E}_y = 139\,\text{GPa}\,, \qquad \tilde{E}_z = 14.6\,\text{GPa}\,, \qquad \tilde{G}_{zy} = \tilde{G}_{zx} = 3.20\,\text{GPa}\,,$$
$$\tilde{G}_{xy} = 53.7\,\text{GPa}\,, \qquad \tilde{\nu}_{yz} = \tilde{\nu}_{xz} = 0.333 \quad \text{and} \quad \tilde{\nu}_{xy} = 0.293\,.$$

As the stacking sequences are identical in all cases, the equivalent material properties for models 3 and 4 (layers stacked along y) are defined by the same elastic constants, where indices y and z are switched.

	Steel	**Epoxy**	**Steel**
E [GPa]	207	3.0	207
ν [−]	0.25	0.37	0.25
χ [−]	1/3	1/3	1/3

Table 3.6 – Properties of the beam's base cell

Each of the four beams is associated with a homogeneous one of identical dimensions, but made of only one, equivalent material. A base of the first 72 vibration modes above 0 Hz is then computed for these 8 finite-element models. The modal bases of the initial models are compared to those of the corresponding equivalent structures using the same criteria as described in Subsection 1.4.2, with a MAC threshold at 0% for pairing the modes (so that all the modes are paired and taken into account). The results are gathered in Table 3.7.

	1	**2**	**3**	**4**
Nb paired modes	72	72	72	72
$\overline{\lvert\Delta f\rvert}$ [%]	3.19	11.1	9.51	1.38
$\overline{MAC}$ [%]	98.9	59.6	77.3	99.5

Table 3.7 – Correlation of each beam's first 72 vibration modes

Table 3.7 shows that the correlation is globally much better than for Section 3.2.3 (in which the objective was to compare the method with other existing ones). Also, the values of $\overline{|\Delta f|}$ are significantly lower for the beams with many layers (models 1 and 4) than for the others, showing that in these cases, the equivalent materials are able to recreate the initial structure's behaviour with good precision. Observing good overall correlation for models 1 and 4 and poor coefficients for models 2 and 3 is in agreement to the remark of Lukkassen et al. [29], stating that their homogenisation expression is closer to the initial, heterogeneous behaviour when the dimensions of the unit cell are small in comparison to the entire structure's.

Eventually, the homogeneous material able to recreate the initial structure's modal behaviour with the best accuracy corresponds to the case of stratification in a direction transverse to the beam's length.

3.2.5/ Electric machine stators: experimental-numerical application

Modelling the stator of an electric machine, which is generally a laminated steel stack, is a very interesting application for the studies of heterogeneous structures. Understanding the dynamic behaviour of an electric machine stator is a key issue in the prediction of the electric machine's noise and vibration simulation and prediction [141]. As outlined in Subsection 3.2.1, a stator is built from a multi-laminated magnetic core, on which windings are placed. This section will detail the simulation of a magnetic core's modal behaviour with the aid of the above-presented material property identification method, and will propose several modelling guidelines for this type of structures.

3.2.5.1/ EXPERIMENTAL DATA

The structure studied in this section is the magnetic core of a 12-tooth switched-reluctance machine (without windings or resin). It consists in 400 steel sheets of thickness 360 µm, separated from each other by 3-µm-thick varnish (epoxy) layers. Its dimensions are 154 mm (length) and 245 mm (outer diameter). By the means of a shock-hammer analysis, frequency response functions (FRF) are measured for each of the experimental mesh's 108 degrees of freedom (36 points of 3 DOFs). From these response functions, 5 purely radial vibration modes could be extracted (amongst others). These modes, sometimes referred to as "ovalisation" modes are particularly critical for the acoustic behaviour of the entire electric machine [140]; predicting them with good accuracy is therefore of particular interest. Pictures of the experimental settings are shown in Figure 3.12. This experimental modal basis stands for a reference in this section.

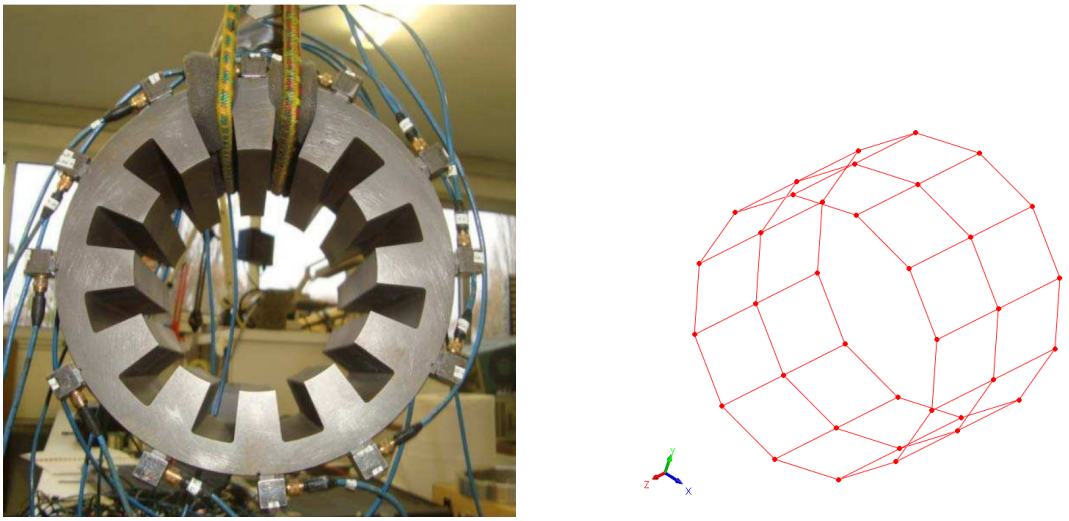

(a) FRF measurement

(b) Experimental mesh (undeformed)

Figure 3.12 – Experimental settings

3.2.5.2/ FINITE-ELEMENT MODEL

Although it may differ from one type of machine to another, the production process for this magnetic core consisted in coating steel layers with insulating varnish (in order to prevent eddy currents from taking place in the structure and therefore dissipating energy) and then simply piling them one onto the others. The stack was then placed under a press, and weld beads were applied on the lateral face while the pressure was maintained. Two examples of finite-element models representing this structure are shown in Figure 3.13.

The "initial" model details the structure as it really is: a stack of 400 isotropic steel layers separated from each other by isotropic epoxy layers, and is made of 493,164 elements and 618,426 nodes. The details of the layers is given in Table 3.8. Even with powerful computational resources, performing simulations on such a structure is time-consuming and therefore cost-prohibitive. This is why another finite-element model is generated, from the same mesh in the top face, but whose elements are extruded with the same dimensions throughout the structure's length (axis z). The new FE model is called "homogeneous" as it is made of only one homogeneous material (to be determined

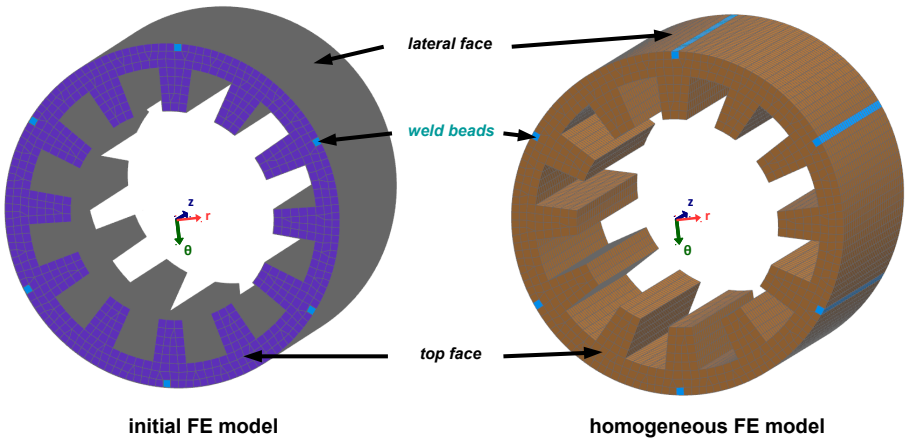

Figure 3.13 – Finite-element models of the magnetic core (axis along z)

in the following paragraphs) throughout axis z instead of the details of the layers. Its 19,158 elements and 24,768 nodes make it more appropriate than "initial" for computing modal bases. Also, due to the revolution symmetry of the structure, the finite-element models as well as the material properties are expressed in a cylindrical coordinate system of directions r, θ and z, where z is the stacking direction of the layers.

	Steel	**Epoxy**
E [GPa]	207	3.0
ν [−]	0.25	0.37
ρ [kg · m^{-3}]	7,875	1,300
l [µm]	360	3

Table 3.8 – Details of the "initial" model's layers

3.2.5.3/ MODELLING GUIDELINES

The weld beads applied on the stack's lateral face are necessary to hold the entire structure in one piece, by imposing a mechanical bond onto the whole length. In the rest of the structure, the sheets are bound together only by the varnish. The pressure applied to the stack is maintained after manufacturing near the weld beads and decreases with the distance in the rest of the structure. Although they are only a few micrometres thick and mechanical properties may vary from one varnish type to another, the local behaviour of the varnish layers and thus the interaction between the steel sheets are very likely to be dependent on the residual pressure in the stack, and therefore on the proximity to the weld beads (where the pressure is maintained) or to the free edges. This explains the necessity of dividing the entire FE model into several zones.

The analysis proposed for dividing the model efficiently is the computation of static stiffness at each of the "initial" model's top-face nodes, in order to estimate the tightness of the structure in relation to the position on the face and the distance to the weld beads. The entire model is clamped (DOFs Tr, $T\theta$ and Tz fixed as no rotations are considered on 3D elements) at the nodes on the weld beads. Displacements Δl_z (along z) are computed

in response to a 1-N static force applied along z at each node (except on the weld beads). The static stiffness values $\mathfrak{K}_z$ are then found by:

$$\mathfrak{K}_z = \frac{1}{|\Delta l_z|} \,. \tag{3.53}$$

The results are plotted in Figure 3.14.

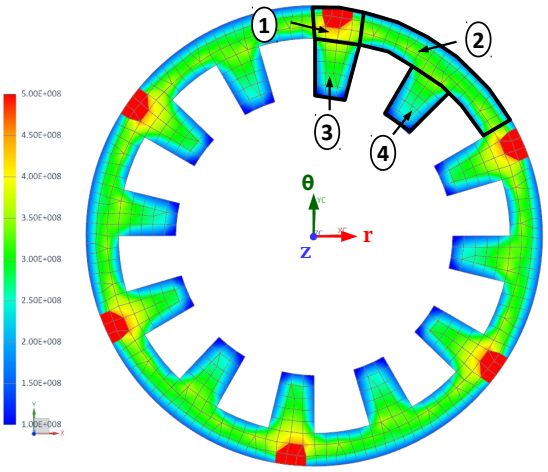

Figure 3.14 – Distribution of $\mathfrak{K}_z$ (in $\mathrm{N \cdot m^{-1}}$)

Judging from the results shown in Figure 3.14, four zones have been drawn according to the stiffness values:

1. zone "prox" (elements near the weld beads, with $1.5 \times 10^8 < \mathfrak{K}_z < 4.6 \times 10^8\,\mathrm{N \cdot m^{-1}}$);
2. zone "yoke" (with $1.3 \times 10^8 < \mathfrak{K}_z < 3.7 \times 10^8\,\mathrm{N \cdot m^{-1}}$);
3. zone "teeth-W" (elements on the teeth next to the weld beads, with $7.0 \times 10^7 < \mathfrak{K}_z < 3.8 \times 10^8\,\mathrm{N \cdot m^{-1}}$);
4. zone "teeth-Y" (elements on the teeth next to the yoke, with $6.7 \times 10^7 < \mathfrak{K}_z < 3.6 \times 10^8\,\mathrm{N \cdot m^{-1}}$).

Therefore, the "homogeneous" model should be divided into corresponding zones. It seems also relevant to associate zones 3 and 4 into one same "teeth" material definition. Finally, the finite-element model of the magnetic core which will be used for the dynamic simulations is shown in Figure 3.15, where each zone corresponds to specific material properties.

It seems important to note that the entire model is composed of 3D, solid elements, which need not necessarily be cuboidal. Although the identification method is applied to base cells made of 8-node cuboid elements (particularly convenient for modelling and homogenising stacked structures), meshing the equivalent structure remains under the control of the user: the equivalent material may be applied to any type of mesh, as long as the global geometry is kept unchanged. Therefore, the stator could have been meshed with any type of solid element (e.g. four-, five- or six-sided), even mixed, as this choice has negligible influence over the global structure's vibratory behaviour. In this case, creating the mesh with a base of six-sided elements is a good compromise between representativity and total number of DOFs.

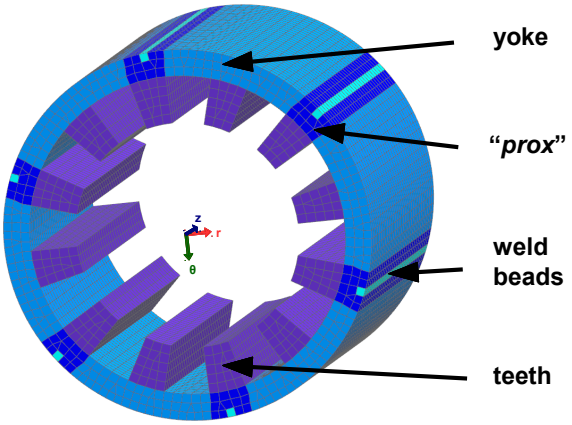

Figure 3.15 – Zoning the magnetic core's finite-element model (axis along z)

3.2.5.4/ EQUIVALENT MATERIAL PROPERTIES

The first zone under the spotlight is "*prox*", gathering the elements which are closest to the weld beads. In this zone, the proximity to the weld beads ensures the stator's tightest cohesion between the steel sheets, and implies therefore the best regularity in the successive varnish layers' thicknesses. This means that the cell <half-thick steel sheet; varnish sheet; half-thick steel sheet> is repeated regularly through the stator's length (dimension along z), with the same thicknesses everywhere. The corresponding finite-element model which will be used for material identification is therefore a 3-layered cuboid with a square base of length 400 µm, as illustrated in Figure 3.16.

Its layers' Young's moduli E, Poisson's ratios ν and thicknesses l are gathered in Table 3.9. In the whole FE model, the same density $\tilde{\rho}$ is applied to all the zones and directly taken from the measurements on the stator:

$$\tilde{\rho} = \frac{m^{\text{tot}}}{V^{\text{tot}}} = 7,750\,\text{kg}\cdot\text{m}^{-3}\,,$$

where m^{tot} and V^{tot} respectively refer to the stator's total mass and volume.

	Steel	**Epoxy**	**Steel**
E [GPa]	207	3.0	207
ν [−]	0.25	0.37	0.25
l [µm]	180	3	180

Table 3.9 – Properties of the base cell of zone "*prox*"

Applying method "**Ortho1**" to the base cell of zone "*prox*" yields an equivalent material, whose elastic constants are:

$$\tilde{E}_r^{\text{prox}} = \tilde{E}_\theta^{\text{prox}} = 205\,\text{GPa}\,, \quad \tilde{E}_z^{\text{prox}} = 157\,\text{GPa}\,, \quad \tilde{G}_{z\theta}^{\text{prox}} = \tilde{G}_{zr}^{\text{prox}} = 51.2\,\text{GPa}\,,$$
$$\tilde{G}_{r\theta}^{\text{prox}} = 82.1\,\text{GPa} \quad \text{and} \quad \tilde{\nu}_{\theta z}^{\text{prox}} = \tilde{\nu}_{rz}^{\text{prox}} = \tilde{\nu}_{r\theta}^{\text{prox}} = 0.25\,.$$

Concerning the other zones, to the authors' knowledge there does not exist any analytical or numerical method able to describe with precision the variation of the elastic properties

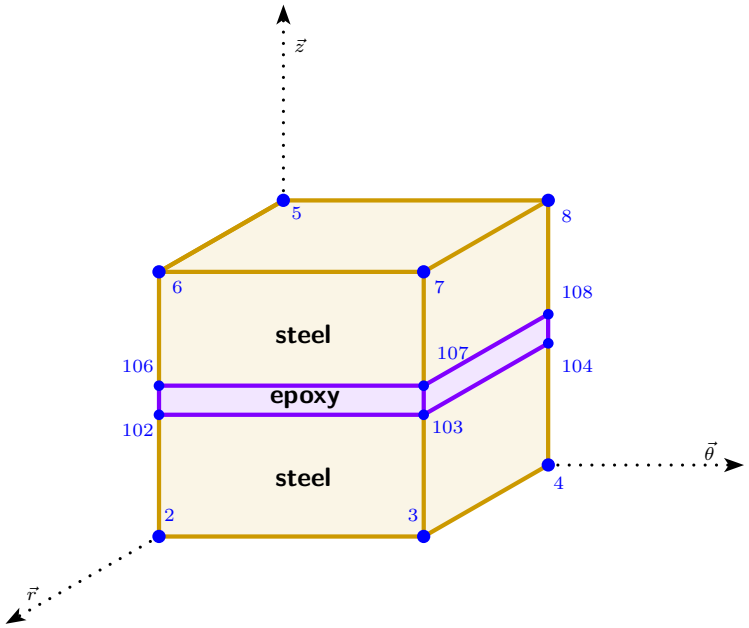

Figure 3.16 – Base cell

with the distance to the weld beads. This is why a good experience in model updating of electric machine stators is necessary to describe the behaviours of the different zones. In this case, the factors $3/4$ and $1/2$ have been applied to the shear moduli of the respective zones "yoke" and "teeth", according to their distance to the weld beads [vii]. The other coefficients remain unchanged. Eventually, the material properties are detailed in Table 3.10.

3.2.5.5/ COMPARISON WITH EXPERIMENTAL DATA

Computing the FE model's modal basis and comparing it to the experimental data with the criteria described in Subsection 1.4.2 leads to the correlation state presented in Figure 3.17 and Table 3.11, where the columns "**FEA**" and "**EMA**" respectively refer to the mode frequencies in the FE model and in the experimental modal basis. The $\overline{|\Delta f|}$ and $\overline{MAC}$ averages have been computed in the bottom row of Table 3.11 (cf. definitions in Equations (1.68) and (1.69)). Only mode pairs for which MAC values were over 60% were taken into account.

Judging from these results, it can be observed that the behaviour of the finite-element model computed with the method "**Ortho1**" is in good agreement with the measured natural frequencies, and that the model's deformed shapes correspond to the experimental ones fairly well.

The results of Table 3.11 are compared with the case "**NZ**" (no zoning: the same "***prox***" material properties applied to the whole structure), as shown in Table 3.12.

As in the previous sections, it can be seen that method "**Ortho1**" generates equivalent

vii. This choice will be validated in Section 3.3.

	prox	**yoke**	**teeth**	**weld beads**
$\tilde{E}_r$ [GPa]	205	205	205	
$\tilde{E}_\theta$ [GPa]	205	205	205	207
$\tilde{E}_z$ [GPa]	157	157	157	
$\tilde{G}_{z\theta}$ [GPa]	51.2	38.4	25.6	
$\tilde{G}_{zr}$ [GPa]	51.2	38.4	25.6	-
$\tilde{G}_{r\theta}$ [GPa]	82.1	61.6	41.1	
$\tilde{\nu}_{\theta z}$ [−]	0.25	0.25	0.25	
$\tilde{\nu}_{rz}$ [−]	0.25	0.25	0.25	0.288
$\tilde{\nu}_{r\theta}$ [−]	0.25	0.25	0.25	
$\tilde{\rho}$ $[\mathrm{kg \cdot m^{-3}}]$	7,750	7,750	7,750	7,750

Table 3.10 – Comparison of elastic coefficients

material properties that simulate the dynamic behaviour of the entire structure accurately. The necessity of zoning the model and adapting the shear coefficients according to the elements' distances to the weld beads can be clearly seen as well, as the average frequency discrepancy is increased by 68.5%. The modelling guidelines that have been proposed should be therefore followed for other geometries of magnetic core structures.

In this application especially, the initial correlations of simulated and experimental modal bases on two different electric machine stators were particularly promising for the prediction of such structures' modal behaviours. Judging from the time needed for the thorough experimental-based updating of an electric machine stator's FE model, the stakes of an accurate, initial modelling of such structures in a relatively simple and fast way are both high and numerous [139, 140].

3.2.6/ Conclusion on the orthotropic homogenisation approach

In this section, a new method for identifying equivalent material properties to laminated orthotropic structures was developed. As a necessity in order to reduce the number of degrees of freedom in the finite-element models of heterogeneous structures such as electric motor stators, the identification method enabled modelling them with equivalent representative homogeneous material properties. This new method has been applied to various domains involving multi-layered material simulations.

It has been shown that analysing laminated structures requires a "sliding shear" approach rather than a "transverse shear" one. The corresponding "**Ortho1**" approach is globally more accurate than existing reference homogenisation methods for such structures, yields good simulation results when used in an experimental-numerical application, and unlike the others, can also be applied to superelements.

An analysis of stacking settings in laminated cantilever beams has shown that the equivalent orthotropic material created with this new technique was able to recreate the initial vibratory behaviour with good precision for multi-layered structures.

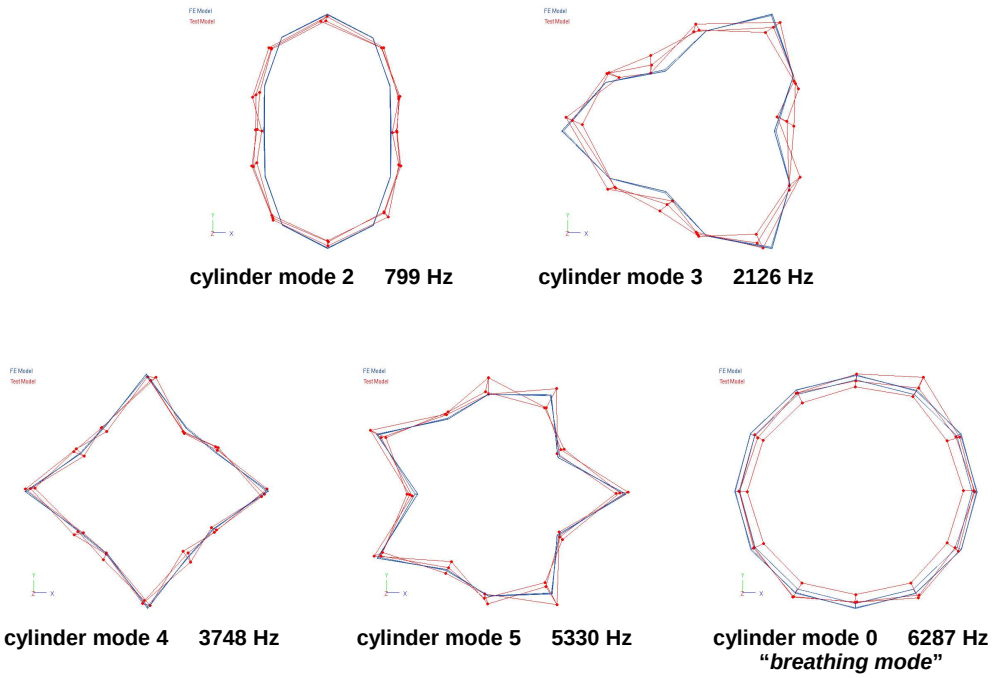

Figure 3.17 – Correlation of FE and experimental modal bases - mode shape pairs (experimental frequencies) - blue lines: simulation, red dots: measurement

Mode pair	FEA [Hz]	EMA [Hz]	Δf [%]	MAC [%]	Mode description
1	823.5	798.6	3.12	63.8	cylinder mode, order 2
2	2,179.6	2,125.5	2.55	62.3	cylinder mode, order 3
3	3,855.0	3,747.7	2.86	90.6	cylinder mode, order 4
4	5,529.3	5,330.1	3.74	82.5	cylinder mode, order 5
5	6,593.4	6,286.5	4.88	74.3	cylinder mode, order 0
Averages $\overline{\lvert\Delta f\rvert}$ ***and*** $\overline{MAC}$			***3.43***	***74.7***	

Table 3.11 – Correlations of FE and experimental modal bases

	Ortho1	NZ
$\overline{\lvert\Delta f\rvert}$ [%]	3.43	5.78
$\overline{MAC}$ [%]	74.7	74.5

Table 3.12 – Influence of zoning

Eventually, the vibratory behaviour of the magnetic core of an electric motor stator has been simulated by the means of a finite-element model with equivalent homogeneous material properties. The simulated ovalisation modes have been compared to experimental data measured on a real stator, and showed good agreement. In addition to that, the zoning guidelines proposed for finite-element models of magnetic cores have been proven efficient. It is hoped that this identification method will eventually help improve further the current knowledge about the behaviour of laminated structures and in particular of electric machine stators. Also, substituting time-consuming model updating procedures by a simple, direct method could even replace the manufacture of costly prototypes and associated measurements.

For more complicated situations however, notably in case of non-negligible preloading, or when couplings exist between tension-compression and shear in the global structure, orthotropic equivalent materials might not be accurate enough to simulate the expected behaviour of a given structure. The following section will present another method for the identification of equivalent material properties for anisotropic or triclinic structures and superelements, accounting for the influence of external perturbations such as friction and preload.

3.3/ Modelling techniques for laminated stator cores: anisotropic homogenisation approach

Initially written as a single article with two parts, the content of the previous section have been divided into two separate articles. This section details the second article, which was submitted to the Journal of Vibration and Control on July 8th, 2015 under the title "Identification of representative anisotropic material properties accounting for friction and preloading effects: contribution for structural dynamics of electric motor stators", co-authored by É. Sadoulet-Reboul, M. Ouisse, J.-B. Dupont and N. Bouhaddi. The bulk of the initial work has been kept identical. Also, the content of the article has been reshaped into conference papers, presented at the International Conference on Noise and Vibration Engineering (ISMA2014, Leuven, Belgium) and the International Conference on Dynamics of Composite Structures (DYNCOMP2015, Arles, France), respectively referenced as [159] and [165].

3.3.1/ Introduction to anisotropic homogenisation

For finite-element simulations, modelling heterogeneous structures strictly as they are in reality is sometimes both delicate and unrealistic if the heterogeneities are small or numerous: representing such models by equivalent homogeneous material properties may be a necessity in order to reduce the number of degrees of freedom in the models. In addition to this, constraints of cost-effectiveness and flexibility justify a great interest of the industry for effective methods able to recreate the dynamic behaviours of heterogeneous structures with equivalent material properties [141]. Some of the existing techniques able to determine homogeneous properties in order to model heterogeneous structures are called "homogenisation" methods.

A large number of homogenisation methods already exist in the cases of 2D, laminated, honeycomb or many other types of composite structures. A thorough review of some

of the most important ones has been made by Kalamkarov et al. in [110]. However, 3D homogenisation is relatively seldom addressed in the literature, and yet necessary to consider if attempting to model a structure when simplifications are not possible.

Millithaler et. al [166] have developed a method of 3D material property identification for multi-layered orthotropic laminates and have compared its applicability with other existing 3D homogenisation techniques (see Section 3.2). The method directly identifies the representative elastic constants $\tilde{E}_x$, $\tilde{E}_y$, $\tilde{E}_z$, $\tilde{G}_{zy}$, $\tilde{G}_{zx}$, $\tilde{G}_{xy}$, $\tilde{\nu}_{yz}$, $\tilde{\nu}_{xz}$ and $\tilde{\nu}_{xy}$ of the homogeneous equivalent material, with low-resource static simulations on the unit cell which is periodically repeated in the heterogeneous structure. Two scenarios are distinguished for the determination of equivalent shear moduli, describing either "sliding shear" or "transverse shear" conditions. Applied to dynamic analyses on several types of multi-layered structures, it has been observed that "sliding shear" was more appropriate to describe the behaviour of the laminates than "transverse shear".

There yet exists some cases in which orthotropic materials are not accurate enough to recreate the behaviour of a given structure, with yet the same necessity of using representative elasticity matrices. Unlike for orthotropic materials, identifying elastic constants such as Young's moduli, shear moduli or Poisson's ratios is not possible in the case of anisotropic, or so-called "triclinic" structures, defined by 21 independent constants [41]. In this general case, the material's 21 independent coefficients form the elasticity matrix $[C]$ in Hooke's law, as described in Equation (1.11).

Begis et al. [16] have developed a homogenisation method that can be applied to triclinic periodic structures (see Paragraph 3.2.1.2), the principles of which were taken as a reference for other techniques. Although it yields equivalent elasticity matrices, the approach requires solving analytical equations that might make them delicate to implement for finite-element analyses (difficulty reported in [58]). A different analytical formulation of elastic coefficients has been proposed by Luciano and Barbero [27]. In spite of the ability to model equivalent anisotropic material properties, the expressions of only 6 coefficients $\tilde{C}_{ij}$ amongst the elasticity matrix's 21 independent constants are detailed. Mathan and Siva Prasad [125] have developed a method of evaluation of equivalent material properties for a spiral-wound gasket and analysed its elasto-plastic behaviour. The principle is to average the stress-strain behaviour of a representative volume element over its volume by the means of independent load cases, in order to determine the equivalent compliance matrix's constants. However, the method is applied to the studied gasket only, and the structure itself is changed (angle of sealing ring) to ensure the independence of the load cases before averaging the results.

External perturbations and their influence on the behaviour of a structure have been investigated in the literature. Peillex et al. [104] successfully homogenised a model made of 10% of isotropic heterogeneities into an isotropic matrix, taking into account dynamic frictional contact conditions. By coupling their method to homogenised local friction coefficients, they were able to fairly approximate the stresses present in a heterogeneous model and their evolution through time. Smit et al. [39] as well as Yvonnet et al. [117] have tackled similar issues and taken into account possible non-linearities in their models. Yet both approaches analyse the behaviour of a non-linear, heterogeneous structure without determining any equivalent elasticity matrix, and no finite-element analyses have been performed to recreate the samples' mechanical behaviours.

In the field of laminates, Pirnat et al. [151] have developed a numerical model of a lami-

nated stack with both tangential and normal contact conditions between the layers. The 14%-error in the prediction of the natural frequencies of a laminated stack was considered good by the authors, in addition to the fact that they also updated the inter-layer contact parameters with experimental modal data. Focusing on electric machines, Kim and Kim [95] have shown experimentally that the first natural frequencies of a laminated rotor increased with the stack's pressure (i.e. preloading). Similarly, the works of Watanabe et al. [17] have outlined the fact that the natural frequencies of non-purely-radial modes on a segmented-core stator tend to increase as the clamping force increases. Dias' experimental analyses [43] have confirmed this conclusion, with the observation that purely-radial (or "ovalisation") modes were not affected by any variations of the clamping force held by the weld beads (called tie rods). However, in spite of the new opportunities they represent to the knowledge in laminated structures' vibratory behaviours, these approaches are highly dependent on experimental data or model updating procedures and do not lead to any elasticity matrices that could represent the material properties of equivalent homogeneous structures.

The influence of preloads has also been analysed in the frame of railway dynamics. The simulations performed by Wu and Thompson [47] highlighted a strong influence of preloading on the studied railway's vibrations. The measurements of Kaewunruen and Remennikov [94] on railpads led to similar observations concerning the dynamic stiffness of all types of pads.

As for industrial projects in structural dynamics, a great interest is shown for accurate and cost-efficient modelling techniques applicable to common finite-element simulations such as modal bases. In particular, the automotive industry currently focuses on new technologies such as hybrid or 100%-electric powertrains, the stators of which are built on multi-layered magnetic cores with lateral weld beads [139, 20, 24]. Performing dynamic simulations on such heterogeneous structures is however highly dependent on costly and time-consuming experimental analyses. This is why understanding and being able to predict the vibratory behaviour of a stator's laminated magnetic core without experimental data is key to performing efficient noise and vibration simulations on entire electric motors. In addition to this, Van der Giet et al. [146] reported non-linearities in the mechanical behaviour of laminated stacks, as a result of their experimental analysis on a real electric machine.

Concerning finite-element simulations, Dias [43] modelled the entire magnetic core with a single homogeneous isotropic material, based on the suggestions of [20, 24]. This choice can be contradicted in light of the results presented in Section 3.2, where the orthotropic material identification method and the modelling guidelines allowed simulating the modal behaviour of an electric motor stator with good accuracy, with an efficient zoning of the finite-element model accounting for the influence of weld beads. This work also showed that the correlation accuracy between simulated and measured ovalisation modes on a real stator would have been decreased by a relative factor of 68.5% if the finite-element model had not been zoned. The present article will elaborate on this basis and take into account friction and preload phenomena in the computation of representative anisotropic materials for improving the accuracy of dynamic simulations on the magnetic core's finite-element model.

In order to compute representative elasticity matrices for modelling heterogeneous structures, several interesting methods have been reviewed. While some of them are able to model triclinic properties in finite-element models, others deal with external pertur-

bations and their non-linear influences on the behaviours of the studied structures. To the authors' knowledge, there currently exist no approaches able to take such external perturbations into account in the definition of equivalent, linear, representative elasticity matrices. Modelling such external perturbations on a given structure generally requires performing non-linear simulations, which are in principle longer, more complicated and more restrictive (e.g. requiring special licences) than linear solutions. Approximating non-linear effects by representative linear material properties that could be used in any finite-element solution therefore offers interesting opportunities, that include analysing the influence of such effects on the material coefficients themselves, and integrating these material definitions into linear solutions such as model updating procedures.

This is why a new method is proposed, based on finite elements, modelling equivalent triclinic material properties for periodic structures and able to take into account the influence of external perturbations on the representative elasticity matrix. The following subsections will detail the development of this method, as well as various applications on finite-element models. The influence of preload on material properties will be analysed by comparing the dynamic behaviours of preloaded structures and their equivalent, homogeneous, linear finite-element models. Eventually, the magnetic core of a real electric machine stator will be modelled accounting for friction and preload effects on its teeth's steel sheets.

3.3.2/ DEVELOPMENT OF THE "TRICLINIC" METHOD

As it has been explained in Section 3.2, orthotropic material properties imply that tension-compression and shear phenomena are not coupled. For a structure subjected to external perturbations, these no-coupling assumptions may not be valid in the general case, and any linear elasticity matrix approximating its behaviour shall be therefore expressed as anisotropic, or "triclinic". The elasticity matrices computed with this new method are linear and approximate the non-linear perturbations to which the structure is subjected. The corresponding Hooke's law in the general case has been shown on Equation (1.11); in this case, the material can no longer be expressed with Young's moduli, shear moduli or Poisson's ratios [119]. Therefore, the method presented in Section 3.2, which aimed at identifying these elastic coefficients directly, is readapted for application to triclinic materials.

First of all, the prerequisite steps for this method are:

1. The zones to be modelled with equivalent, homogeneous material properties are distinguished and analysed separately;
2. For a given zone, a sample exactly recreating the periodicity of the structure as well as the external conditions (if any) is created;
3. A stiffness matrix taking into account the influence of the external perturbations is computed.

3.3.2.1/ COMPUTATION OF THE STIFFNESS MATRIX

In order to detail steps **2.** and **3.** of the sequence introduced above, a sample with two 8-node solid elements is used as an example as shown in Figure 3.18: the elements <1, 2,

3, 4, 101, 102, 103, 104> and <105, 106, 107, 108, 5, 6, 7, 8> are superimposed along the z-axis, and preloads are applied to the structure (red arrows). The two elements have to be separated if contact properties are to be taken into account (in such case, the interface nodes are doubled, although each node pair is perfectly coincident). If no contact or friction properties are modelled, the interface nodes are merged. The global cuboid's dimensions are L_x, L_y and L_z, and its faces' respective areas A_x (faces $x = 0$ and $x = 1$), A_y (faces $y = 0$ and $y = 1$) and A_z (faces $z = 0$ and $z = 1$). Also, the nodes located within an ellipse on the figure have the same coordinates. The description of external faces is simplified with '$= 0$' or '$= 1$' notations (referring to the limits of the structure's volume), in spite of the dimensions L_x, L_y and L_z.

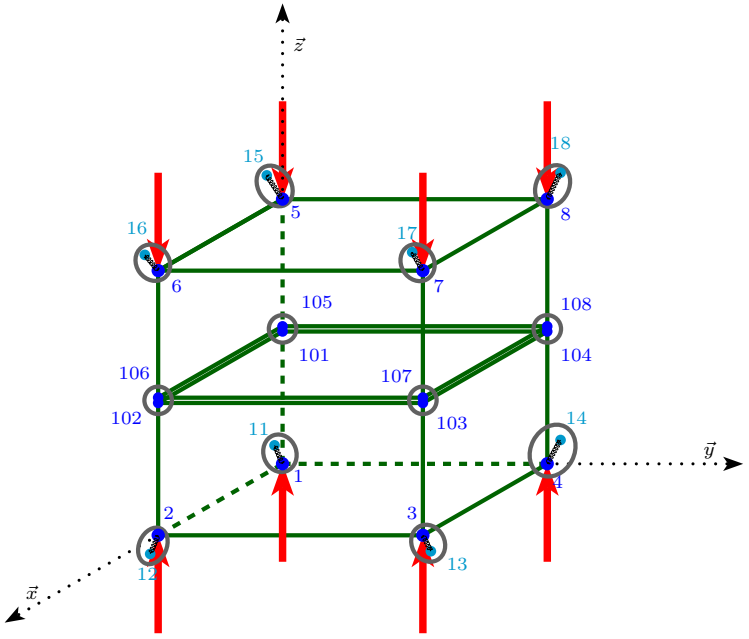

Figure 3.18 – Example of a sample under preloading

Now, for the solution to be computed, the system has to be stabilised: the outer nodes 1, 2, 3, 4, 5, 6, 7 and 8 are respectively doubled with the nodes 11, 12, 13, 14, 15, 16, 17 and 18, at the exact same coordinates. The nodes 11 through 18 are then clamped, and each pair is linked with 3D stiffness elements (this is equivalent to linking a node-to-ground 3D stiffness element to each of the structure's outer nodes 1 to 8). The numerical values of these stiffness elements have to be small enough to not perturb the entire structure's stiffness matrix values.

As an example, the stiffness matrix's diagonal components of a 1-mm-long cube made of isotropic steel ($E = 210\,\text{GPa}$ and $\nu = 0.25$) have value of $4.67 \cdot 10^7\,\text{N} \cdot \text{m}^{-1}$. In this case, using stiffness elements with a value of $1,000\,\text{N} \cdot \text{m}^{-1}$ in every direction is considered negligible compared to the stiffness matrix's values, and does not perturb the structure's overall behaviour.

For the rest of this section, $\mathcal{U}_{x0}$, $\mathcal{U}_{x1}$, $\mathcal{U}_{y0}$, $\mathcal{U}_{y1}$, $\mathcal{U}_{z0}$ and $\mathcal{U}_{z1}$ are defined as the node sets corresponding to the respective faces $x = 0$, $x = 1$, $y = 0$, $y = 1$, $z = 0$ and $z = 1$. The case of a two-layer, 8-outer-node structure is detailed in Table 3.13.

node set	face	nodes
$\mathcal{U}_{x0}$	$x = 0$	1, 2, 5, 6, 101, 102
$\mathcal{U}_{x1}$	$x = 1$	3, 4, 7, 8, 103, 104
$\mathcal{U}_{y0}$	$y = 0$	1, 4, 5, 8, 101, 104
$\mathcal{U}_{y1}$	$y = 1$	2, 3, 6, 7, 102, 103
$\mathcal{U}_{z0}$	$z = 0$	1, 2, 3, 4
$\mathcal{U}_{z1}$	$z = 1$	5, 6, 7, 8

Table 3.13 – Details on node set names in the case of a 8-outer-node structure with two layers

The prestress effects σ_0 and σ_1 are then applied to the system along the z-axis, so that

$$\sigma_0 = \frac{1}{A_z} \sum_{i \in \mathcal{U}_{z0}} F_i \tag{3.54}$$

and

$$\sigma_1 = -\frac{1}{A_z} \sum_{i \in \mathcal{U}_{z1}} F_i \ , \tag{3.55}$$

where the values F_i stand for the loadings at the nodes 1 through 8. If modelled, the contact properties are then defined according to the physics of the interface (deformable bodies, friction, etc.).

Creating the superelement with the twelve nodes 1, 2, 3, 4, 101, 102, 103, 104, 5, 6, 7 and 8 (DOFs T_x, T_y and T_z) is an efficient way to output a stiffness matrix. For instance, the ASCII-format DMIG ("Direct Matrix Input at a Grid") is a convenient way to export and reuse stiffness matrices. It seems important to emphasise that the solver used has to take into account the influence of the external perturbations over the values – if modelled – and export the corresponding stiffness matrix. In the case illustrated in Figure 3.18, the superelement created stands for a structure with two layers and four common interface nodes instead of two separate elements.

3.3.2.2/ DETERMINATION OF THE ELASTIC PROPERTIES

Unlike finite elements for which materials would be clearly defined, the stiffness matrix of a superelement does not give any direct information about the materials it stands for. The matrix may however be imported by a solver to recreate the elastic properties of an entire structure, in our case composed of two 8-node solid elements and twelve nodes (the node pairs at the interface were merged during the superelement's creation process). It is therefore possible to compute the displacements $\Delta l_{x,i}$, $\Delta l_{y,i}$ and $\Delta l_{z,i}$ as well as the reaction forces $F_{x,i}$, $F_{y,i}$ and $F_{z,i}$ at each node i.

As it has been shown, the 21 independent coefficients of an equivalent triclinic elasticity matrix $\left[\tilde{C}\right]$ have to be identified. To do this, the proposed approach consists in computing

the compliance matrix $\left[\tilde{S}\right]$ such that $\left[\tilde{S}\right] = \left[\tilde{C}\right]^{-1}$. The general relation of Hooke's law, detailed in Equation (1.11), can be reversed to express the matrix $\left[\tilde{S}\right]$:

$$\begin{Bmatrix} \varepsilon_{xx} \\ \varepsilon_{yy} \\ \varepsilon_{zz} \\ \\ 2\cdot\varepsilon_{yz} \\ 2\cdot\varepsilon_{zx} \\ 2\cdot\varepsilon_{xy} \end{Bmatrix} = \begin{bmatrix} \tilde{S}_{11} & \tilde{S}_{12} & \tilde{S}_{13} & \tilde{S}_{14} & \tilde{S}_{15} & \tilde{S}_{16} \\ & \tilde{S}_{22} & \tilde{S}_{23} & \tilde{S}_{24} & \tilde{S}_{25} & \tilde{S}_{26} \\ & & \tilde{S}_{33} & \tilde{S}_{34} & \tilde{S}_{35} & \tilde{S}_{36} \\ & & & \tilde{S}_{44} & \tilde{S}_{45} & \tilde{S}_{46} \\ & \text{sym.} & & & \tilde{S}_{55} & \tilde{S}_{56} \\ & & & & & \tilde{S}_{66} \end{bmatrix} \begin{Bmatrix} \sigma_{xx} \\ \sigma_{yy} \\ \sigma_{zz} \\ \\ \sigma_{yz} \\ \sigma_{zx} \\ \sigma_{xy} \end{Bmatrix} . \tag{3.56}$$

To calculate all the constants of $\left[\tilde{S}\right]$, the method needs six series of simulations, ie. one per component of $\{\varepsilon\}$. The first series, called xx, refers to the deformed state ε_{xx}. For better visibility, this development is made on the second series, called yy, referring to the deformed state ε_{yy}, and repeated similarly for the deformed states ε_{xx} and ε_{zz}.

The second row of Equation (3.56) is then:

$$\varepsilon_{yy} = \tilde{S}_{12}\cdot\sigma_{xx} + \tilde{S}_{22}\cdot\sigma_{yy} + \tilde{S}_{23}\cdot\sigma_{zz} + \tilde{S}_{24}\cdot\sigma_{yz} + \tilde{S}_{25}\cdot\sigma_{zx} + \tilde{S}_{26}\cdot\sigma_{xy} . \tag{3.57}$$

Thus, this series needs six independent simulations in order to identify Equation (3.57)'s six constants $\tilde{S}_{12} = \tilde{S}_{21}$, $\tilde{S}_{22}$, $\tilde{S}_{23}$, $\tilde{S}_{24}$, $\tilde{S}_{25}$ and $\tilde{S}_{26}$. This series yy corresponds to a pure tension scheme, as shown in Figure 3.19: a static displacement δ_y is enforced along $+y$ to the nodes of the face $y = 1$, whereas plane contact constraints are applied to the face $y = 0$. In other terms, the nodes of the face $y = 0$ are blocked in the direction y and left free in the directions x and z. To stabilise the system, DOFs T_x and T_z are blocked at node 1, and DOF T_z at node 2 (more details are given in Table 3.14).

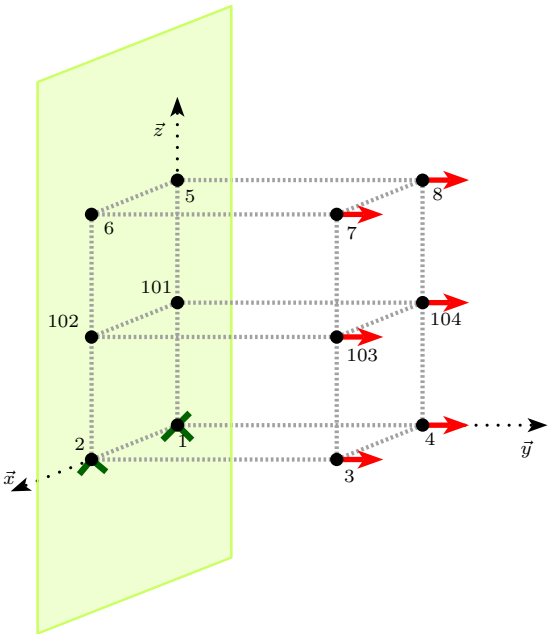

Figure 3.19 – Pure tension along y on the superelement

Then, the values of nodal reaction forces lead to the stresses $\sigma_{i,j}^{(2a)}$, where the superscript $(2a)$ refers to the first simulation of the series yy:

$$\sigma_{xx}^{(2a)} = \frac{1}{A_x} \sum_{i \in \mathcal{U}_{x1}} F_{x,i}^{(2a)} \ , \tag{3.58}$$

$$\sigma_{yy}^{(2a)} = \frac{1}{A_y} \sum_{i \in \mathcal{U}_{y1}} F_{y,i}^{(2a)} \ , \tag{3.59}$$

$$\sigma_{zz}^{(2a)} = \frac{1}{A_z} \sum_{i \in \mathcal{U}_{z1}} F_{z,i}^{(2a)} \ , \tag{3.60}$$

$$\sigma_{yz}^{(2a)} = \frac{1}{A_y} \sum_{i \in \mathcal{U}_{y1}} F_{z,i}^{(2a)} \ , \tag{3.61}$$

$$\sigma_{xz}^{(2a)} = \frac{1}{A_x} \sum_{i \in \mathcal{U}_{x1}} F_{z,i}^{(2a)} \tag{3.62}$$

and

$$\sigma_{xy}^{(2a)} = \frac{1}{A_y} \sum_{i \in \mathcal{U}_{y1}} F_{x,i}^{(2a)} \ . \tag{3.63}$$

The next five simulations of the series yy (corresponding to superscripts $(2b)$ through $(2f)$) obviously recreate the same pure tension scheme along the y-axis. The difference made between each simulation for the same series yy is in the boundary conditions of the scheme (unlike in [125]), i.e. which DOFs are blocked or set free, while enforcing the same displacements to all simulations $(2a)$ through $(2f)$. The independence between each simulation's boundary conditions must then ensure that the 6-equation system (one equation similar to (3.57) for each simulation of the series) is of rank 6. Finally, the equation system obtained is

$$\begin{Bmatrix} \varepsilon_{yy} \\ \varepsilon_{yy} \\ \varepsilon_{yy} \\ \varepsilon_{yy} \\ \varepsilon_{yy} \\ \varepsilon_{yy} \end{Bmatrix} = \begin{bmatrix} \sigma_{xx}^{(2a)} & \sigma_{yy}^{(2a)} & \sigma_{zz}^{(2a)} & \sigma_{yz}^{(2a)} & \sigma_{xz}^{(2a)} & \sigma_{xy}^{(2a)} \\ \sigma_{xx}^{(2b)} & \sigma_{yy}^{(2b)} & \sigma_{zz}^{(2b)} & \sigma_{yz}^{(2b)} & \sigma_{xz}^{(2b)} & \sigma_{xy}^{(2b)} \\ \sigma_{xx}^{(2c)} & \sigma_{yy}^{(2c)} & \sigma_{zz}^{(2c)} & \sigma_{yz}^{(2c)} & \sigma_{xz}^{(2c)} & \sigma_{xy}^{(2c)} \\ \sigma_{xx}^{(2d)} & \sigma_{yy}^{(2d)} & \sigma_{zz}^{(2d)} & \sigma_{yz}^{(2d)} & \sigma_{xz}^{(2d)} & \sigma_{xy}^{(2d)} \\ \sigma_{xx}^{(2e)} & \sigma_{yy}^{(2e)} & \sigma_{zz}^{(2e)} & \sigma_{yz}^{(2e)} & \sigma_{xz}^{(2e)} & \sigma_{xy}^{(2e)} \\ \sigma_{xx}^{(2f)} & \sigma_{yy}^{(2f)} & \sigma_{zz}^{(2f)} & \sigma_{yz}^{(2f)} & \sigma_{xz}^{(2f)} & \sigma_{xy}^{(2f)} \end{bmatrix} \begin{Bmatrix} \tilde{S}_{21} \\ \tilde{S}_{22} \\ \tilde{S}_{23} \\ \tilde{S}_{24} \\ \tilde{S}_{25} \\ \tilde{S}_{26} \end{Bmatrix} , \tag{3.64}$$

where the 6×6 matrix is referred to as $\left[\mathcal{H}^{(2)}\right]$, and where:

$$\varepsilon_{yy} = \frac{\delta_y}{L_y} \ . \tag{3.65}$$

Now, solving the system yields the six coefficients $\tilde{S}_{21} = \tilde{S}_{12}$ through $\tilde{S}_{26}$. These steps are repeated with two new simulation series (xx and zz), in order to complete the first three

rows of the compliance matrix $\left[\tilde{S}\right]$. At the same time, the symmetry of the submatrix $\left[\tilde{S}_A\right]$ must be verified, so that $\left[\tilde{S}_A\right] = \left[\tilde{S}_A\right]^\intercal$ in

$$\left[\tilde{S}\right] = \begin{bmatrix} \tilde{S}_A & \tilde{S}_B \\ - & - \end{bmatrix} . \tag{3.66}$$

The next step consists in using the symmetry of $\left[\tilde{S}\right]$ to transpose the submatrix $\left[\tilde{S}_B\right]$:

$$\left[\tilde{S}\right] = \begin{bmatrix} \tilde{S}_A & \tilde{S}_B \\ \tilde{S}_B^\intercal & - \end{bmatrix} , \tag{3.67}$$

so that computing the last three rows of $\left[\tilde{S}\right]$ only requires three simulations each instead of six. The series yz refers to the deformed state $\gamma_{yz} = 2 \cdot \varepsilon_{yz}$. The corresponding row in Equation (3.56) is then:

$$\gamma_{yz} = \tilde{S}_{14} \cdot \sigma_{xx} + \tilde{S}_{24} \cdot \sigma_{yy} + \tilde{S}_{34} \cdot \sigma_{zz} + \tilde{S}_{44} \cdot \sigma_{yz} + \tilde{S}_{45} \cdot \sigma_{zx} + \tilde{S}_{46} \cdot \sigma_{xy} . \tag{3.68}$$

In a similar way as in Section 3.2, the analysis separates sliding shear from transverse shear, in the respective "**TricI1**" and "**TricI2**" scenarios, for which the identification of the compliance matrix's first three rows yet remains identical. The following paragraphs detail the determination of the remaining compliance coefficients by transverse shear schemes (therefore corresponding to the "**TricI2**" method). The fourth series of simulations corresponds to a transverse shear scheme $y - z$, as shown in Figure 3.20: it combines an enforced displacement δ_z along $+z$ at the nodes of the face $y = 1$, and plane contact constraints on the same face $y = 1$ in order to generate pure shear. In this example also, DOFs T_x, T_y and T_z are blocked at node 1, and DOFs T_y and T_z at the other nodes of face $y = 0$.

As is the case for the previous series, Equation (3.58) through (3.63) yield the stress values needed for this simulation. Also, new boundary conditions enable creating two new independent simulations to complete this series (more details are given in Table 3.14). The system obtained is thus:

$$\begin{Bmatrix} \gamma_{yz} \\ \gamma_{yz} \\ \gamma_{yz} \end{Bmatrix} = \left[\begin{array}{ccc|ccc} \sigma_{xx}^{(4a)} & \sigma_{yy}^{(4a)} & \sigma_{zz}^{(4a)} & \sigma_{yz}^{(4a)} & \sigma_{xz}^{(4a)} & \sigma_{xy}^{(4a)} \\ \sigma_{xx}^{(4b)} & \sigma_{yy}^{(4b)} & \sigma_{zz}^{(4b)} & \sigma_{yz}^{(4b)} & \sigma_{xz}^{(4b)} & \sigma_{xy}^{(4b)} \\ \sigma_{xx}^{(4c)} & \sigma_{yy}^{(4c)} & \sigma_{zz}^{(4c)} & \sigma_{yz}^{(4c)} & \sigma_{xz}^{(4c)} & \sigma_{xy}^{(4c)} \end{array}\right] \begin{Bmatrix} \tilde{S}_{41} \\ \tilde{S}_{42} \\ \tilde{S}_{43} \\ \tilde{S}_{44} \\ \tilde{S}_{45} \\ \tilde{S}_{46} \end{Bmatrix} , \tag{3.69}$$

where the 3×6 matrix is $\left[\mathcal{H}^{(4)}\right]$, the superscripts $(4a)$, $(4b)$ and $(4c)$ refer to their corresponding simulations in the fourth series, and

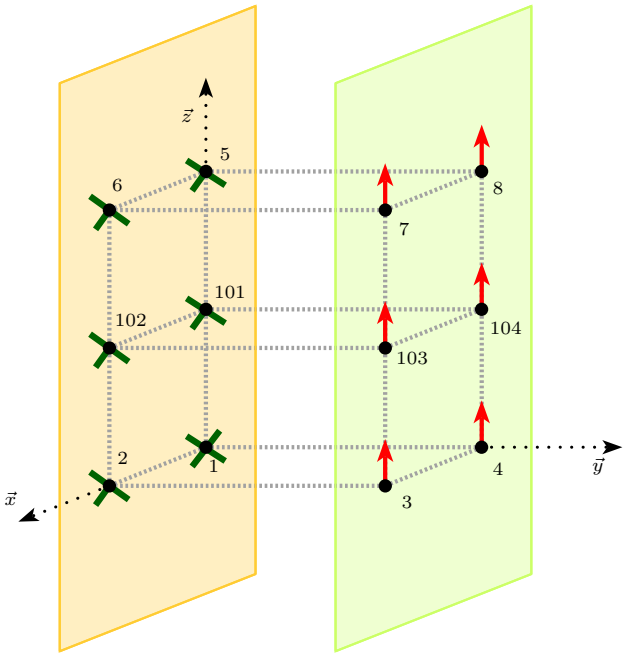

Figure 3.20 – Pure transverse shear $y - z$ on the superelement

$$\gamma_{yz} = \frac{\delta_z}{L_y} \,. \tag{3.70}$$

The matrix $\left[\mathcal{H}^{(4)}\right]$ can be divided into the two submatrices $\left[\sigma^{(4TC)}\right]$ and $\left[\sigma^{(4SR)}\right]$, respectively consisting of the terms of tension-compression and shear:

$$\left[\mathcal{H}^{(4)}\right] = \left[\sigma^{(4TC)} \quad | \quad \sigma^{(4SR)}\right] \,. \tag{3.71}$$

In detail, they stand for

$$\left[\sigma^{(4TC)}\right] = \begin{bmatrix} \sigma_{xx}^{(4a)} & \sigma_{yy}^{(4a)} & \sigma_{zz}^{(4a)} \\ \sigma_{xx}^{(4b)} & \sigma_{yy}^{(4b)} & \sigma_{zz}^{(4b)} \\ \sigma_{xx}^{(4c)} & \sigma_{yy}^{(4c)} & \sigma_{zz}^{(4c)} \end{bmatrix} \tag{3.72}$$

and

$$\left[\sigma^{(4SR)}\right] = \begin{bmatrix} \sigma_{yz}^{(4a)} & \sigma_{xz}^{(4a)} & \sigma_{xy}^{(4a)} \\ \sigma_{yz}^{(4b)} & \sigma_{xz}^{(4b)} & \sigma_{xy}^{(4b)} \\ \sigma_{yz}^{(4c)} & \sigma_{xz}^{(4c)} & \sigma_{xy}^{(4c)} \end{bmatrix} \,. \tag{3.73}$$

Knowing the values of the constants $\tilde{S}_{41}$, $\tilde{S}_{42}$ and $\tilde{S}_{43}$ through Equation (3.67) yields the vector $\left\{\gamma_{yz}^{(p)}\right\}$ such that

$$\begin{Bmatrix} \gamma_{yz}^{(p1)} \\ \gamma_{yz}^{(p2)} \\ \gamma_{yz}^{(p3)} \end{Bmatrix} = \left[\sigma^{(4TC)}\right] \begin{Bmatrix} \tilde{S}_{41} \\ \tilde{S}_{42} \\ \tilde{S}_{43} \end{Bmatrix}, \tag{3.74}$$

with the help of which the remaining unknown coefficients $\tilde{S}_{44}$, $\tilde{S}_{45}$ and $\tilde{S}_{46}$ may be computed:

$$\begin{Bmatrix} \tilde{S}_{44} \\ \tilde{S}_{45} \\ \tilde{S}_{46} \end{Bmatrix} = \left[\sigma^{(4SR)}\right]^{-1} \begin{Bmatrix} \gamma_{yz} - \gamma_{yz}^{(p1)} \\ \gamma_{yz} - \gamma_{yz}^{(p2)} \\ \gamma_{yz} - \gamma_{yz}^{(p3)} \end{Bmatrix}. \tag{3.75}$$

At last, the matrix $\left[\tilde{S}\right]$ is completed with the last two series, namely xz and xy, from which the symmetry $\tilde{S}_{ij} = \tilde{S}_{ji}$ has to be verified again. The detail of all boundary condition sets is given in Table 3.14.

3.3.3/ VALIDATION

3.3.3.1/ HOMOGENEOUS TRICLINIC SAMPLE

The method "**Tricl1**" has been first validated on a simple, homogeneous case. For this example, a cuboid 8-node element whose dimensions are $L_x = 20\,\text{mm}$, $L_y = 40\,\text{mm}$ and $L_z = 60\,\text{mm}$ was used, to which a triclinic material defined by the elasticity matrix

$$[C^{\text{exp}}] = \begin{bmatrix} 3.51 & 0.47 & 1.27 & -0.67 & -0.02 & -0.56 \\ & 13.2 & 1.03 & -0.04 & -0.07 & 0.24 \\ & & 2.97 & -0.23 & -0.59 & 0.14 \\ & & & 0.37 & 0.17 & -0.07 \\ & \text{sym.} & & & 1.09 & 0.06 \\ & & & & & 0.81 \end{bmatrix} \cdot 10^9 \tag{3.76}$$

and the associated compliance matrix

$$[S^{\text{exp}}] = \begin{bmatrix} 0.926 & -0.016 & -0.397 & 1.848 & -0.538 & 0.913 \\ & 0.079 & -0.022 & -0.041 & 0.001 & -0.034 \\ & & 0.570 & -0.649 & 0.426 & -0.454 \\ & & & 6.719 & -1.483 & 2.093 \\ & \text{sym.} & & & 1.407 & -0.678 \\ & & & & & 2.186 \end{bmatrix} \cdot 10^{-9} \tag{3.77}$$

was applied, but without any external perturbations.

		DOFs to be blocked on nodes			enforced displacements		
series	**simulation scheme**	x	y	z	x	y	z
xx	$(1a)$	$\mathcal{U}_{x0}$	1	1, 4	$\mathcal{U}_{x1}$		
	$(1b)$	$\mathcal{U}_{x0}$	$\mathcal{U}_{y0}, \mathcal{U}_{y1}$	1	$\mathcal{U}_{x1}$		
	$(1c)$	$\mathcal{U}_{x0}$	1	$\mathcal{U}_{z0}, \mathcal{U}_{z1}$	$\mathcal{U}_{x1}$		
	$(1d)$	$\mathcal{U}_{x0}$	$\mathcal{U}_{y0}, \mathcal{U}_{y1}$	$\mathcal{U}_{z0}$	$\mathcal{U}_{x1}$		
	$(1e)$	$\mathcal{U}_{x0}$	1	$\mathcal{U}_{z0}$	$\mathcal{U}_{x1}$		
	$(1f)$	$\mathcal{U}_{x0}$	$\mathcal{U}_{y0}$	1	$\mathcal{U}_{x1}$		
yy	$(2a)$	1	$\mathcal{U}_{y0}$	1, 2		$\mathcal{U}_{y1}$	
	$(2b)$	$\mathcal{U}_{x0}, \mathcal{U}_{x1}$	$\mathcal{U}_{y0}$	1		$\mathcal{U}_{y1}$	
	$(2c)$	1	$\mathcal{U}_{y0}$	$\mathcal{U}_{z0}, \mathcal{U}_{z1}$		$\mathcal{U}_{y1}$	
	$(2d)$	$\mathcal{U}_{x0}, \mathcal{U}_{x1}$	$\mathcal{U}_{y0}$	$\mathcal{U}_{z0}$		$\mathcal{U}_{y1}$	
	$(2e)$	1	$\mathcal{U}_{y0}$	$\mathcal{U}_{z0}$		$\mathcal{U}_{y1}$	
	$(2f)$	$\mathcal{U}_{x0}$	$\mathcal{U}_{y0}$	1		$\mathcal{U}_{y1}$	
zz	$(3a)$	1	1, 2	$\mathcal{U}_{z0}$			$\mathcal{U}_{z1}$
	$(3b)$	$\mathcal{U}_{x0}, \mathcal{U}_{x1}$	1	$\mathcal{U}_{z0}$			$\mathcal{U}_{z1}$
	$(3c)$	1	$\mathcal{U}_{y0}, \mathcal{U}_{y1}$	$\mathcal{U}_{z0}$			$\mathcal{U}_{z1}$
	$(3d)$	$\mathcal{U}_{x0}, \mathcal{U}_{x1}$	$\mathcal{U}_{y0}$	$\mathcal{U}_{z0}$			$\mathcal{U}_{z1}$
	$(3e)$	$\mathcal{U}_{x0}$	1	$\mathcal{U}_{z0}$			$\mathcal{U}_{z1}$
	$(3f)$	1	$\mathcal{U}_{y0}$	$\mathcal{U}_{z0}$			$\mathcal{U}_{z1}$
zy - **TricI1**	$(4a)$	1	$\mathcal{U}_{z0}$	$\mathcal{U}_{z0}, \mathcal{U}_{z1}$		$\mathcal{U}_{z1}$	
	$(4b)$	$\mathcal{U}_{x0}$	$\mathcal{U}_{z0}$	$\mathcal{U}_{z0}, \mathcal{U}_{z1}$		$\mathcal{U}_{z1}$	
	$(4c)$	$\mathcal{U}_{z0}$	$\mathcal{U}_{z0}$	$\mathcal{U}_{z0}, \mathcal{U}_{z1}$		$\mathcal{U}_{z1}$	
yz - **TricI2**	$(4a)$	1	$\mathcal{U}_{y0}, \mathcal{U}_{y1}$	$\mathcal{U}_{y0}$			$\mathcal{U}_{y1}$
	$(4b)$	$\mathcal{U}_{x0}$	$\mathcal{U}_{y0}, \mathcal{U}_{y1}$	$\mathcal{U}_{y0}$			$\mathcal{U}_{y1}$
	$(4c)$	$\mathcal{U}_{y0}$	$\mathcal{U}_{y0}, \mathcal{U}_{y1}$	$\mathcal{U}_{y0}$			$\mathcal{U}_{y1}$
zx - **TricI1**	$(5a)$	$\mathcal{U}_{z0}$	1	$\mathcal{U}_{z0}, \mathcal{U}_{z1}$	$\mathcal{U}_{z1}$		
	$(5b)$	$\mathcal{U}_{z0}$	$\mathcal{U}_{y0}$	$\mathcal{U}_{z0}, \mathcal{U}_{z1}$	$\mathcal{U}_{z1}$		
	$(5c)$	$\mathcal{U}_{z0}$	$\mathcal{U}_{z0}$	$\mathcal{U}_{z0}, \mathcal{U}_{z1}$	$\mathcal{U}_{z1}$		
xz - **TricI2**	$(5a)$	$\mathcal{U}_{x0}, \mathcal{U}_{x1}$	1	$\mathcal{U}_{x0}$			$\mathcal{U}_{x1}$
	$(5b)$	$\mathcal{U}_{x0}, \mathcal{U}_{x1}$	$\mathcal{U}_{y0}$	$\mathcal{U}_{x0}$			$\mathcal{U}_{x1}$
	$(5c)$	$\mathcal{U}_{x0}, \mathcal{U}_{x1}$	$\mathcal{U}_{x0}$	$\mathcal{U}_{x0}$			$\mathcal{U}_{x1}$
yx - **TricI1**	$(6a)$	$\mathcal{U}_{y0}$	$\mathcal{U}_{y0}, \mathcal{U}_{y1}$	1	$\mathcal{U}_{y1}$		
	$(6b)$	$\mathcal{U}_{y0}$	$\mathcal{U}_{y0}, \mathcal{U}_{y1}$	$\mathcal{U}_{z0}$	$\mathcal{U}_{y1}$		
	$(6c)$	$\mathcal{U}_{y0}$	$\mathcal{U}_{y0}, \mathcal{U}_{y1}$	$\mathcal{U}_{y0}$	$\mathcal{U}_{y1}$		
xy - **TricI2**	$(6a)$	$\mathcal{U}_{x0}, \mathcal{U}_{x1}$	$\mathcal{U}_{x0}$	1		$\mathcal{U}_{x1}$	
	$(6b)$	$\mathcal{U}_{x0}, \mathcal{U}_{x1}$	$\mathcal{U}_{x0}$	$\mathcal{U}_{z0}$		$\mathcal{U}_{x1}$	
	$(6c)$	$\mathcal{U}_{x0}, \mathcal{U}_{x1}$	$\mathcal{U}_{x0}$	$\mathcal{U}_{x0}$		$\mathcal{U}_{x1}$	

Table 3.14 – Boundary conditions for the "Triclinic" method

Given these input material properties, this application will attempt to show to what extent the elasticity matrix identified by the method corresponds to the input $[C^{\text{exp}}]$. Each simulation has been made with enforced displacements of magnitude $\delta = 1$ mm. In practice, using different values for δ in a linear solution must lead to the same results.

A linear static solution is initiated (each solution is completed within a few seconds), including output requests at all nodes in terms of displacements and reaction forces. The results of the xx-series lead to the system (3.64) (adapted to row 1 i.e. direction xx), whose numerical values are given in the following system:

$$\begin{Bmatrix} 5{\cdot}10^{-2} \\ 5{\cdot}10^{-2} \\ 5{\cdot}10^{-2} \\ 5{\cdot}10^{-2} \\ 5{\cdot}10^{-2} \\ 5{\cdot}10^{-2} \end{Bmatrix} = \begin{bmatrix} \mathbf{5.40{\cdot}10^{7}} & 0.00 & 0.00 & \boldsymbol{2.52{\cdot}10^{-7}} & 0.00 & 0.00 \\ \mathbf{9.18{\cdot}10^{7}} & \mathbf{1.89{\cdot}10^{6}} & 0.00 & 0.00 & 0.00 & \boldsymbol{-3.83{\cdot}10^{-7}} \\ \mathbf{8.39{\cdot}10^{7}} & 0.00 & \mathbf{4.46{\cdot}10^{7}} & 0.00 & \mathbf{1.85{\cdot}10^{7}} & 0.00 \\ \mathbf{1.21{\cdot}10^{8}} & \mathbf{1.00{\cdot}10^{6}} & 0.00 & \mathbf{-1.59{\cdot}10^{7}} & \mathbf{1.45{\cdot}10^{6}} & \mathbf{-3.48{\cdot}10^{7}} \\ \mathbf{5.54{\cdot}10^{7}} & 0.00 & 0.00 & 0.00 & \mathbf{2.40{\cdot}10^{6}} & \boldsymbol{-8.33} \\ \mathbf{7.59{\cdot}10^{7}} & 0.00 & 0.00 & 0.00 & 0.00 & \mathbf{-2.21{\cdot}10^{7}} \end{bmatrix} \begin{Bmatrix} \tilde{S}_{11} \\ \tilde{S}_{12} \\ \tilde{S}_{13} \\ \tilde{S}_{14} \\ \tilde{S}_{15} \\ \tilde{S}_{16} \end{Bmatrix} . \tag{3.78}$$

In this case, $\varepsilon_{xx} = 0.05$.

The 6×6 matrix $\left[\mathcal{H}^{(1)}\right]$ has a rank of 6. As it can be seen in Equation (3.78), the independence of the boundary condition sets led to a number of null or negligible values in matrix $\left[\mathcal{H}^{(1)}\right]$. This is done so that each simulation in the series involves a minimum of terms in the compliance matrix. In particular, the diagonal term $\tilde{S}_{11}$ is identified alone in the first row of $\left[\mathcal{H}^{(1)}\right]$. Solving Equation (3.78) yields the first row of the equivalent compliance matrix, as shown in Equation (3.79):

$$\begin{Bmatrix} \tilde{S}_{11} \\ \tilde{S}_{12} \\ \tilde{S}_{13} \\ \tilde{S}_{14} \\ \tilde{S}_{15} \\ \tilde{S}_{16} \end{Bmatrix} = \begin{Bmatrix} 9.262 \cdot 10^{-10} \\ -1.582 \cdot 10^{-11} \\ -3.973 \cdot 10^{-10} \\ 1.848 \cdot 10^{-9} \\ -5.376 \cdot 10^{-10} \\ 9.133 \cdot 10^{-10} \end{Bmatrix} . \tag{3.79}$$

The values found here are very close to the initial compliance matrix, including the terms of coupling between tension-compression and shear, namely $\tilde{S}_{14}$, $\tilde{S}_{15}$ and $\tilde{S}_{16}$. The maximum relative discrepancy U^{rel}_{max} is such that

$$U^{\text{rel}}_{max} = \max_{i,j} \left| \frac{\tilde{S}_{ij} - \tilde{S}^{\text{exp}}_{ij}}{\tilde{S}^{\text{exp}}_{ij}} \right| = 0.8\% \,, \tag{3.80}$$

which is very low and therefore shows that the computed results are close to the initial values. The other rows are computed in the same way. The symmetry of $\left[\tilde{S}\right]$ is confirmed, and the values match; the validation is successful for this triclinic homogeneous element. Identical results are found with method "**Tricl2**". Also, it can be noted that applying method "**KPC**" (introduced in Paragraph 3.2.1.4) in this example leads to similar, exact results.

3.3.3.2/ PRELOADED HOMOGENEOUS STRUCTURE

GLOBAL STRUCTURE

The second application of the "Triclinic" method is an analysis of a preloaded structure. The objective is to analyse the effects of the preload on the initial material's elasticity matrix, and to what extent a linear, homogeneous material could recreate the vibratory behaviour of the initial, preloaded structure. The FE model is a homogeneous cuboid of isotropic steel (Young's modulus $E = 207\,\text{GPa}$, Poisson's ratio $\nu = 0.292$ and density $\rho = 7875\,\text{kg}\cdot\text{m}^{-3}$) of respective dimensions along x, y and z of 100 mm, 70 mm and 80 mm, and has 1,008 elements and 8,034 DOFs. Tension preloads are applied along direction y to the structure. The faces $y = 0\,\text{mm}$ and $y = 70\,\text{mm}$ are subjected to static forces of respective total magnitudes $9.81 \cdot 10^6\,\text{N}$ and $-9.81 \cdot 10^6\,\text{N}$, equally distributed on the faces' nodes, so that $\pm 81.1 \cdot 10^3\,\text{N}$ is applied to each of these nodes along y. This value has been chosen to be voluntarily high to ensure observing notable effects on the responses, yet none of the yield or fracture limits are taken into account in the simulation: the material is assumed to never reach any of these limits while calculating the solutions. Therefore, the total pre-stress field σ^p_{yy} applied to the structure is:

$$\sigma^p_{yy} = 1.23 \cdot 10^{10}\,\text{N}\cdot\text{m}^{-2}\,. \tag{3.81}$$

Also, a node-to-ground 3-D stiffness element is linked to each of the global cuboid's 8 outer nodes, with stiffness values of $K^{\text{ntg}} = 1\,\text{N}\cdot\text{m}^{-1}$ on each direction x, y and z. The initial structure is illustrated in Figure 3.21.

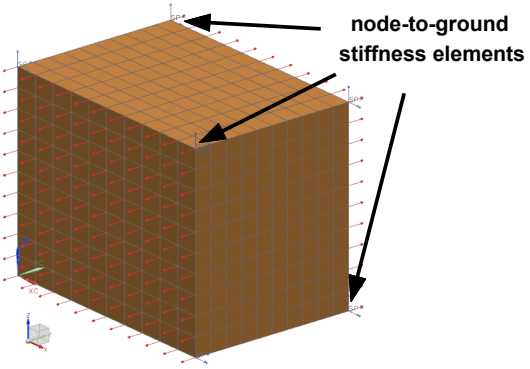

Figure 3.21 – Initial isotropic steel structure under preloading (red arrows)

EQUIVALENT MATERIAL PROPERTIES

To apply the identification method and determine equivalent material properties, a sample is created from a few elements of the structure: 3 elements along y (48 DOFs), as shown in Figure 3.22. To recreate the stress field existing in the global structure, the sample is subjected to the same pre-stress field σ^p_{yy}. To stabilise the system, a node-to-ground 3D stiffness element is linked to each of the sample's 8 outer nodes, with stiffness values of $K^{\text{ntg}} = 1\,\text{N}\cdot\text{m}^{-1}$ on each direction x, y and z.

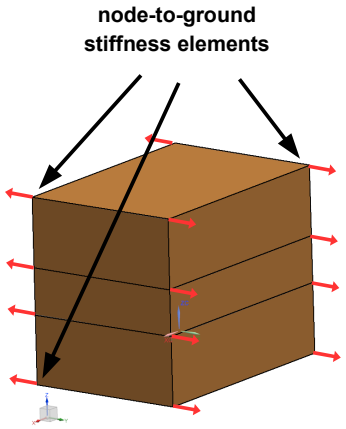

Figure 3.22 – Isotropic steel sample under preloading (red arrows)

It seems important to note that in spite of the initial structure's boundary conditions, applying the presented methods to identify equivalent materials must be made in "free" conditions, or in other words without any DOF constraints. Yet, a structure subjected to preloads needs to be stabilised, which explains the addition of node-to-ground elements to the sample (for this example, although other solutions may exist), and which is completely independent from the global structure's boundary conditions. For this material identification, the stiffness values of the node-to-ground elements have to be sufficiently high to enable computing the stiffness matrix, and as low as possible to be negligible compared to the matrix's values. In this case, it must be verified that their values after preloading are still negligible compared to the new stiffness matrix's values.

A 48×48 real and symmetric stiffness matrix is computed, accounting for the influence of the preload. By creating a new model with the sample's 16 nodes (and no elements), and importing the stiffness matrix as an external superelement, a linear static solution is initiated to apply the method according to the scenarios "**TricI1**" and "**TricI2**" presented in Section 3.3.2. Post-processing the results yields the elasticity matrices

$$\left[\tilde{C}^{\mathrm{ISO1}}\right] = \begin{bmatrix} 265 & 118 & 110 & -4.82\cdot10^{-6} & -1.66\cdot10^{-5} & -1.89\cdot10^{-6} \\ & 316 & 118 & -5.55\cdot10^{-6} & -1.69\cdot10^{-5} & 7.56\cdot10^{-6} \\ & & 264 & -1.29\cdot10^{-5} & -4.43\cdot10^{-5} & 6.54\cdot10^{-6} \\ & & & 51.2 & 8.27\cdot10^{-6} & 5.16\cdot10^{-4} \\ & \text{sym.} & & & 97.4 & 9.97\cdot10^{-1} \\ & & & & & 182 \end{bmatrix} \cdot 10^{9} \tag{3.82}$$

and

$$\left[\tilde{C}^{\mathrm{ISO2}}\right] = \begin{bmatrix} 265 & 118 & 110 & -8.39\cdot10^{-6} & -1.32\cdot10^{-5} & -8.44\cdot10^{-7} \\ & 316 & 118 & -9.64\cdot10^{-6} & -1.35\cdot10^{-5} & 3.79\cdot10^{-6} \\ & & 264 & -2.24\cdot10^{-5} & -3.52\cdot10^{-5} & 3.43\cdot10^{-6} \\ & & & 88.9 & -2.20\cdot10^{-5} & -4.07\cdot10^{-8} \\ & \text{sym.} & & & 77.4 & 0.00 \\ & & & & & 89.1 \end{bmatrix} \cdot 10^{9}\,, \tag{3.83}$$

respectively corresponding to "**TricI1**" and "**TricI2**" methods. As a reference for comparisons, the elasticity matrix corresponding to steel (without preloading) is detailed as following:

$$\left[C^{\mathrm{stl}}\right] = \begin{bmatrix} 273 & 125 & 125 & 0 & 0 & 0 \\ & 273 & 125 & 0 & 0 & 0 \\ & & 273 & 0 & 0 & 0 \\ & & & 80.1 & 0 & 0 \\ & \text{sym.} & & & 80.1 & 0 \\ & & & & & 80.1 \end{bmatrix} \cdot 10^{9} \tag{3.84}$$

In order to compare it with these results, the method "**Ortho1**" developed in Section 3.2 (intended to be applied to orthotropic laminated structures) has been applied to the same superelement (computed from the isotropic steel sample under preloading), and yielded the following elastic coefficients:

$$\begin{array}{lll} \tilde{E}_x = 201\,\mathrm{GPa}\,, & \tilde{E}_y = 242\,\mathrm{GPa}\,, & \tilde{E}_z = 201\,\mathrm{GPa}\,, \\ \tilde{G}_{zy} = 116\,\mathrm{GPa}\,, & \tilde{G}_{zx} = 49.5\,\mathrm{GPa}\,, & \tilde{G}_{xy} = 89.1\,\mathrm{GPa}\,, \\ \tilde{\nu}_{yz} = 0.313\,, & \tilde{\nu}_{xz} = 0.298 \quad \text{and} & \tilde{\nu}_{xy} = 0.259\,. \end{array}$$

Judging from the values of the matrices, the following observations can be made:

- While $\left[C^{\mathrm{stl}}\right]$ has a shape inherent to isotropic properties, this is not the case of $\left[\tilde{C}^{\mathrm{ISO1}}\right]$ and $\left[\tilde{C}^{\mathrm{ISO2}}\right]$: the preloading effects have altered the initial material's isotropy;

- Relatively low terms of coupling between tension-compression and shear have been determined by the two scenarios "**TricI1**" and "**TricI2**";
- In both matrices $\left[\tilde{C}^{\text{ISO1}}\right]$ and $\left[\tilde{C}^{\text{ISO2}}\right]$, the tension preloading along y resulted in an increase of the coefficient $\tilde{C}_{22}$ from its value in $\left[C^{\text{stl}}\right]$, which is the diagonal term of Hooke's law in direction yy. This is consistent with the expected stiffening effect from tension preloading [12].

Two equivalent homogeneous structures are then computed, with the same dimensions and the same density as the initial model.

MODAL CORRELATION ANALYSIS

To evaluate the capacity of the equivalent material properties to recreate the behaviour of the preloaded structure, a state of modal correlation is calculated. To perform this, modal bases of the first 200 vibration modes are computed for the structures detailed in Table 3.15. The first 6 modes, describing the "suspension" related to the node-to-ground elements (all below 14 Hz), have been discarded. Compared to this, the lowest 7$^{\text{th}}$ mode frequency amongst all the structures (and thus first to be correlated) is at 14,5 Hz.

Structure	Basis name
Steel (initial)	**Init**
Steel (under preloads)	**PrId**
Homogeneous (scenario "**TricI1**")	**TricI1**
Homogeneous (scenario "**TricI2**")	**TricI2**
Homogeneous (method "**Ortho1**")	**Ortho1**

Table 3.15 – Definition of the modal bases

The criteria defining the correlation consist in comparing each vibration mode of the first model to each of the second, and have been introduced in Paragraph (1.4.2). The pairs of modes for which MAC values are highest are assembled, and are taken into account if the MAC values are above a fixed threshold. All the other mode pairs are discarded from the correlation process. For the correlation, the reference modal basis is "**PrId**", to which the other bases are compared. The MAC-threshold is fixed at 0% for pairing the modes (so that all the modes are paired and taken into account). The results of the correlation are gathered in Table 3.16. For N_{pm} mode pairs in a given correlation, the entities $\overline{|\Delta f|}$ and $\overline{MAC}$ are defined by the expressions (1.68) and (1.69).

	Init	**TricI1**	**TricI2**	**Ortho1**
Nb paired modes	194	194	194	194
$\overline{\lvert\Delta f\rvert}$ [%]	3.85	7.64	1.40	6.25
$\overline{MAC}$ [%]	72.0	42.6	90.3	48.5

Table 3.16 – Correlation of the first 194 modes above 3,000 Hz

The results given in Table 3.16 can be summarised as below:

- Both natural frequencies and deformed shapes are affected by the application of preloads, as the figures of column "**Init**" show;
- Scenario "**Tricl2**" is capable of recreating the behaviour of the structure under preloads with good accuracy, while method "**Tricl1**" is much less efficient in this setting.
- In spite of the similarities of the shapes of $\left[\tilde{C}^{\mathrm{ISO1}}\right]$ and $\left[\tilde{C}^{\mathrm{ISO2}}\right]$ with that of an orthotropic material's elasticity matrix (for which no tension-compression/shear and shear/shear coupling terms exist), it can be clearly seen that using the "**Ortho1**" method is not adapted to such a setting.

3.3.3.3/ PRELOADED LAMINATED STRUCTURE

GLOBAL STRUCTURE

For the last validation case, the same structure as in Subsection 3.2.3 has been analysed: a laminated cuboid of 5,024 elements, 30,144 DOFs and respective dimensions along x, y and z of 210 mm, 110 mm and 60 mm. The stack's base cell is composed of 3 isotropic layers, the properties of which have been detailed in Table 3.2, and is oriented along z. For each layer, E is the Young's modulus, ν the Poisson's ratio, ρ the density and l the thickness. Also, the volume fraction χ_n of layer n is defined with Equation (3.5).

In this case, the structure is subjected to tension preloads along the stacking direction (z). The total loads on the top and bottom faces are respectively $13.2 \cdot 10^7$ N and $-13.2 \cdot 10^7$ N, equally distributed on the faces' nodes, so that $\pm 500 \cdot 10^3$ N is applied along z to each of these nodes. As before, this value has been chosen to be voluntarily high to ensure observing notable effects on the responses, yet none of the yield or fracture limits are taken into account in the simulation: the material is assumed to never reach any of these limits while calculating the solutions. Also, no contact conditions are taken into account between the different layers: the structure is assumed to experience no delamination. Similarly to the corresponding structure in Subsection 3.2.3, a node-to-ground 3D stiffness element is linked to each of the global cuboid's 8 outer nodes, with stiffness values of $K^{\mathrm{ntg}} = 1 \cdot 10^7\,\mathrm{N} \cdot \mathrm{m}^{-1}$ on each direction x, y and z. The global structure taken as reference is illustrated in Figure 3.23.

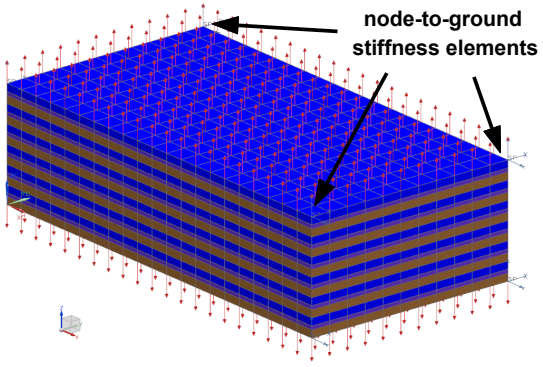

Figure 3.23 – Global laminated structure under preloading (red arrows)

EQUIVALENT MATERIAL PROPERTIES

To apply the material homogenisation approach and determine an equivalent material, a sample is created from a few elements of the structure. In this application, the sample consists of the 3-layered base cell (48 DOFs) of which the entire model is composed, and is illustrated in Figure 3.24. To recreate the stress field existing in the global structure, the sample's 8 outer nodes are subjected to the same nodal loads ($\pm 500 \cdot 10^3$ N per node), as the thicknesses of the base cell layers are identical in the sample and in the global structure. To stabilise the system, a node-to-ground 3D stiffness element is linked to each of the sample's 8 outer nodes, with stiffness values of $K^{\text{ntg}} = 1\,\text{N} \cdot \text{m}^{-1}$ on every direction x, y and z.

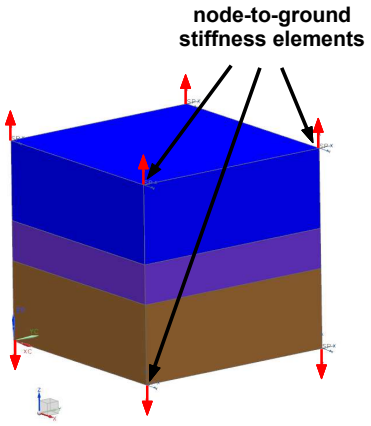

Figure 3.24 – Base cell under preloading (red arrows)

As before, the addition of node-to-ground elements to the sample is necessary to stabilise the system, and yet independent from the initial, global structure. Again, the stiffness values of the node-to-ground elements are negligible in comparison to the sample's stiffness matrix's.

A 48×48 stiffness matrix is computed (which is real and symmetric) and takes into account the influence of the preload. By creating a new model with the sample's 16 nodes (and no elements), and importing the stiffness matrix as an external superelement, a linear static solution is initiated to apply the methods "**TricI1**" and "**TricI2**" presented in Section 3.3.2. Post-processing the results yields the elasticity matrices

$$\left[C^{\text{LMT1}}\right] = \begin{bmatrix} 146 & 52.2 & 36.1 & -2.16 & -2.03 & -0.207 \\ & 146 & 36.1 & -2.16 & -2.03 & -0.207 \\ & & 110 & -6.61 & -6.21 & -0.635 \\ & & & 30.2 & 0.416 & 1.68 \\ & \text{sym.} & & & 30.1 & 1.33 \\ & & & & & 47.6 \end{bmatrix} \cdot 10^9 \tag{3.85}$$

and

$$\left[C^{\mathrm{LMT2}}\right] = \begin{bmatrix} 147 & 52.6 & 37.2 & -4.89 & -4.60 & -1.02 \\ & 147 & 37.2 & -4.89 & -4.60 & -1.02 \\ & & 114 & -15.0 & -14.1 & -3.14 \\ & & & 66.5 & 2.87 & 7.65 \\ & \text{sym.} & & & 66.2 & 7.28 \\ & & & & & 49.1 \end{bmatrix} \cdot 10^9 \ , \tag{3.86}$$

respectively corresponding to "**TriclI**" and "**TriclI2**" methods. Associated to them, the matrix $\left[\tilde{C}^{\mathrm{O1}}\right]$ composed of the elastic moduli determined in Section 3.3.2 (see Equation (3.52), for the case of an orthotropic material without external perturbations) is recalled in the following equation:

$$\left[\tilde{C}^{\mathrm{O1}}\right] = \begin{bmatrix} 164 & 59.3 & 9.63 & 0 & 0 & 0 \\ & 164 & 9.63 & 0 & 0 & 0 \\ & & 19.4 & 0 & 0 & 0 \\ & & & 3.34 & 0 & 0 \\ & \text{sym.} & & & 3.34 & 0 \\ & & & & & 51.3 \end{bmatrix} \cdot 10^9 \ .$$

Judging from the values of the matrices, several observations can be made:

- Non-negligible terms of coupling between tension-compression and shear have been determined by the two methods "**TriclI**" and "**TriclI2**";
- The matrices $\left[C^{\mathrm{LMT1}}\right]$ and $\left[C^{\mathrm{LMT2}}\right]$ are both positive definite (their eigenvalues are all strictly positive), which is a necessary condition for a system to be stable [119];
- In both matrices $\left[C^{\mathrm{LMT1}}\right]$ and $\left[C^{\mathrm{LMT2}}\right]$, the tension preloading along z resulted in an increase of the coefficients $\tilde{C}_{33}$, $\tilde{C}_{44}$ and $\tilde{C}_{55}$ from their values in $\left[\tilde{C}^{\mathrm{O1}}\right]$, which are the diagonal terms of Hooke's law in each direction involving z (respectively zz, yz and xz). This is consistent with the expected stiffening effect from tension preloading [12];
- In both matrices $\left[C^{\mathrm{LMT1}}\right]$ and $\left[C^{\mathrm{LMT2}}\right]$, the directions x and y have similar coefficients, which shows that the laminated structure has in this case an equivalent behaviour in planes normal to the stacking direction;
- In $\left[C^{\mathrm{LMT2}}\right]$, the absolute values involving shear in directions yz and xz are significantly greater than in $\left[C^{\mathrm{LMT1}}\right]$, which is similar to the comparison between the "**Ortho2**" and "**Ortho1**" cases in Section 3.2.

The homogeneous structure to which the equivalent material of each method is applied has the same dimensions and the same total mass as the reference cuboid, and is made of 1-centimetre-long cubic, 8-node, solid elements. Therefore, the equivalent density $\tilde{\rho}$ is calculated by the relation of weighted average (3.6).

As a density value and an elasticity matrix fully define a material for the computation of a real modal basis, two equivalent homogeneous structures are computed. For each of them, the dimensions are identical to the reference matrix's, but one-centimetre-long cubic elements replace the three-layered base-cells that were homogenised.

The only remaining parameters to calculate are the equivalent node-to-ground stiffness values, which have been affected by the application of the preloads. This stage is essential in the validation since their initial values ($K^{\text{ntg}} = 1 \cdot 10^7\,\text{N} \cdot \text{m}^{-1}$) are not negligible compared to the global stiffness matrix's values, unlike those of the sample taken for the property identification or the application in the previous section (where the value was $1\,\text{N} \cdot \text{m}^{-1}$). The equivalent values of the node-to-ground elements after preloading are computed from the stiffness matrix of the global structure under preloads. The idea is to select a corner node, to which a node-to-ground stiffness element is linked, and to extract the values involving both its neighbouring nodes (except for the node at the interface of two different materials) and itself. As an example, the corner node 1 and its direct neighbours 2 and 4 are selected (see Figure 3.25).

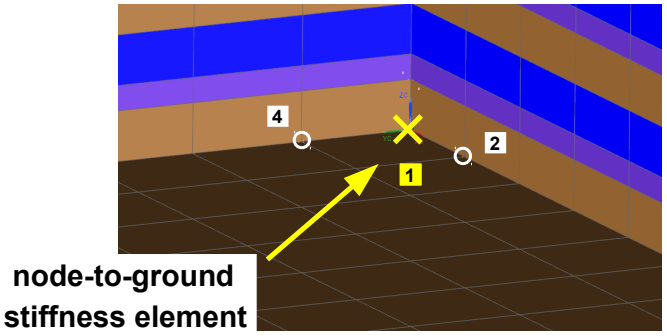

Figure 3.25 – Corner node and direct neighbours

When assembling the stiffness matrices of different elements in a system, the values corresponding to identical DOFs present on several elements are added [15]. As nodes 2 and 4 are each linked to two elements having identical stiffness matrices (same dimensions and material), the diagonal values in the global stiffness matrix $\mathcal{K}^f$ of the free system (without either node-to-ground stiffness elements or boundary conditions) verify the equations:

$$\left.\begin{aligned} 2 \times \mathcal{K}^f_{1x:1x} &= \mathcal{K}^f_{2x:2x} \\ &= \mathcal{K}^f_{4x:4x} \end{aligned}\right\}, \tag{3.87}$$

$$\left.\begin{aligned} 2 \times \mathcal{K}^f_{1y:1y} &= \mathcal{K}^f_{2y:2y} \\ &= \mathcal{K}^f_{4y:4y} \end{aligned}\right\} \tag{3.88}$$

and

$$\left.\begin{aligned} 2 \times \mathcal{K}^f_{1z:1z} &= \mathcal{K}^f_{2z:2z} \\ &= \mathcal{K}^f_{4z:4z} \end{aligned}\right\}, \tag{3.89}$$

in which the indices $nd : nd$ refer to the component of row 'nd' and of column 'nd' in matrix $\mathcal{K}^f$, and where n and d respectively stand for the node number and the direction. When a node-to-ground element of stiffness values K^{ntg}_x, K^{ntg}_y and K^{ntg}_z is linked to node 1, the equations become:

$$\left.\begin{aligned} 2 \times \left(\mathcal{K}^f_{1x:1x} - K^{\text{ntg}}_x\right) &= \mathcal{K}^f_{2x:2x} \\ &= \mathcal{K}^f_{4x:4x} \end{aligned}\right\}, \tag{3.90}$$

$$\left.\begin{aligned} 2 \times \left(\mathcal{K}^f_{1y:1y} - K^{\text{ntg}}_y\right) &= \mathcal{K}^f_{2y:2y} \\ &= \mathcal{K}^f_{4y:4y} \end{aligned}\right\} , \tag{3.91}$$

and

$$\left.\begin{aligned} 2 \times \left(\mathcal{K}^f_{1z:1z} - K^{\text{ntg}}_z\right) &= \mathcal{K}^f_{2z:2z} \\ &= \mathcal{K}^f_{4z:4z} \end{aligned}\right\} . \tag{3.92}$$

In the case of a preloaded structure, a way of computing equivalent stiffness values K^{LMT}_x, K^{LMT}_y and K^{LMT}_z for the node-to-ground elements is by averages. Therefore, from the preloaded system's global stiffness matrix $\mathcal{K}^p$, we have:

$$K^{\text{LMT}}_x = \mathcal{K}^p_{1x:1x} - \frac{\mathcal{K}^p_{2x:2x} + \mathcal{K}^p_{4x:4x}}{4} , \tag{3.93}$$

$$K^{\text{LMT}}_y = \mathcal{K}^p_{1y:1y} - \frac{\mathcal{K}^p_{2y:2y} + \mathcal{K}^p_{4y:4y}}{4} \tag{3.94}$$

and

$$K^{\text{LMT}}_z = \mathcal{K}^p_{1z:1z} - \frac{\mathcal{K}^p_{2z:2z} + \mathcal{K}^p_{4z:4z}}{4} , \tag{3.95}$$

where $\mathcal{K}^p$ is the stiffness matrix of the global system under preloads. For the system studied, the final values are:

$$K^{\text{LMT}}_x = 20.4 \cdot 10^6 \,\text{N} \cdot \text{m}^{-1} ,$$
$$K^{\text{LMT}}_y = 19.4 \cdot 10^6 \,\text{N} \cdot \text{m}^{-1}$$

and

$$K^{\text{LMT}}_z = 120 \cdot 10^6 \,\text{N} \cdot \text{m}^{-1} .$$

This shows that the influence of the preloads affects the structure in a similar way along the directions x and y, and that the equivalent suspension stiffness values are significantly greater than the original ones ($K^{\text{ntg}} = 10.0 \cdot 10^6 \,\text{N} \cdot \text{m}^{-1}$).

MODAL CORRELATION ANALYSIS

To evaluate the capacity of the equivalent material to recreate the behaviour of the preloaded structure, the modal correlations between the models are analysed. To perform this, modal bases of the first 50 modes are computed for the structures detailed in Table 3.17. The first 6 modes, describing the "suspension" related to the node-to-ground elements (all below 2,500 Hz), have been discarded.

For the correlation, the reference modal basis is "**Prld**", to which the other bases are compared. The paired modes for which MAC values are below 70% are discarded. The results

Structure	Suspension stiffness $[\cdot 10^6\,\mathrm{N\,m^{-1}}]$			Basis name
	K_x^{LMT}	K_y^{LMT}	K_z^{LMT}	
Laminated (initial)	10.0	10.0	10.0	**Init**
Laminated (under preloads)	10.0	10.0	10.0	**Prld**
Homogeneous (scenario "**Tricl1**")	20.4	19.4	120	**Tricl1**
Homogeneous (scenario "**Tricl2**")	20.4	19.4	120	**Tricl2**

Table 3.17 – Definition of the modal bases

of the correlation are gathered in Table 3.18, where $\overline{|\Delta f|}$ corresponds to the average of the frequency differences' absolute values, and $\overline{MAC}$ the mean MAC value of the paired modes.

	Init	**Tricl1**	**Tricl2**
Nb paired modes	23	36	17
$\overline{\lvert\Delta f\rvert}$ [%]	38.0	12.1	14.7
$\overline{MAC}$ [%]	90.3	87.5	88.1

Table 3.18 – Correlation of the first 44 modes above 2,500 Hz

The results given in Table 3.18 can be summarised as below:

- Both natural frequencies and deformed shapes have been affected by the application of preloads, as the figures of column "**Init**" show;
- In spite of the important behaviour difference induced by the application of the preloads, method "**Tricl1**" is capable of identifying 36 of the 44 modes;
- However, the material from method "**Tricl2**" is not efficient to simulate the behaviour of the initial structure under preloading, as only 17 of the 44 modes are identified.

As in Section 3.2, it can be said that recreating the lower-frequency modes of laminated structures with homogeneous equivalent material properties requires identifying them with sliding shear simulations instead of transverse shear. On the contrary, the results of the analysis in Paragraph 3.3.3.2 show that identifying equivalent material properties for a continuous structure is much more accurate with transverse shear simulations.

3.3.4/ Electric machine stators: finite-element modelling accounting for frictional effects

3.3.4.1/ Finite-element model

The ability of an electric machine stator's finite-element model with orthotropic material properties to simulate the modal behaviour of the corresponding real structure has been

shown in Section 3.2, along with modelling guidelines that led to zoning the model. The same stator is considered in this section, and consists in a stack of several hundreds of steel sheets separated from each other by varnish. During its manufacturing process, weld beads are applied on the lateral side of the stack, while the magnetic core is placed under a press. When the pressure is released, the stack is held in one piece by the weld beads, while in the rest of the structure, the only bond between the sheets is the varnish. This is a source of heterogeneities in the behaviour of the entire structure. Therefore, the finite-element model of the magnetic core has been divided into several zones according to the distance to the weld beads, with specific material properties associated to each of the zones. The same model as in Section 3.2 is used in this section (see Figure 3.15). It is made of 19,158 elements and 24,768 nodes (expressed in a cylindrical coordinate system of directions r, θ and z) for 12 teeth, its dimensions are 154 mm (length) and 245 mm (outer diameter). The sheets are stacked along the z-axis.

3.3.4.2/ EQUIVALENT MATERIAL PROPERTIES

The present analysis focuses on the interaction between the steel sheets and the possibility to take such effects into account in the equivalent material properties. Because of their proximity to the weld beads, the zone "prox" is assumed to experience no friction effects between the layers. Therefore, this zone is associated to the same orthotropic material as in Subsection 3.2.5.

On the contrary, friction effects between the steel sheets are modelled in the epoxy layers for the zones "yoke" and "teeth". Compressive preload is taken into account in order to model the residual pressure remaining after the manufacturing process, and is assumed to be homogeneous in each zone. The unit (or base) cell periodically repeated in this zone is thus a set of four 8-node solid elements superimposed along the z-axis. The base cell is illustrated in Figure 3.26, and the stacking sequence is detailed in Table 3.19.

material	thickness [µm]	nodes	transition
steel	180	**1, 2, 3, 4, 11, 12, 13, 14**	common nodes
epoxy	1.5	**11, 12, 13, 14,** *201, 202, 203, 204*	*interface*
epoxy	1.5	*205, 206, 207, 208,* **15, 16, 17, 18**	*interface* common nodes
steel	180	**15, 16, 17, 18, 5, 6, 7, 8**	

Table 3.19 – Stacking sequence - base cell

The entire base cell is composed of 24 nodes and thus 72 DOFs. The idea is to identify equivalent material properties from a superelement in which the master-nodes describe the glued elements (nodes 1 to 18 - written in bold in Table 3.19) and the slave-nodes the interface (nodes 201 to 208 - in italic). The definition of "master" and "slave" DOFs are given in Subsection 1.3.3. The pairs of interface nodes have the same coordinates. To stabilise the system, a node-to-ground 3D stiffness element is linked to each of the outer

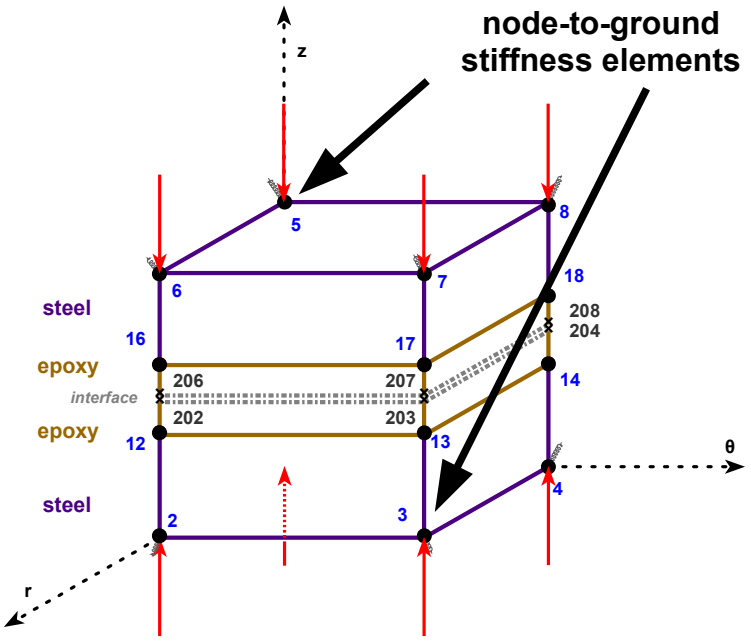

Figure 3.26 – Base cell - zones "prox" and "teeth"

nodes 1, 2, 3, 4, 5, 6, 7 and 8, with stiffness values of $K^{\text{ntg}} = 1\,\text{N}\cdot\text{m}^{-1}$ on every direction r, θ and z.

To the authors' knowledge, there are currently no data available concerning either prestress values on a magnetic core's tooth or friction between two steel sheets. In this application, the initial load applied to the stator during its production is equivalent to a mass of 2,500 kg (i.e. $\approx$ 25 kN), and therefore corresponds to a compressive prestress of $1.52\cdot10^{6}\,\text{N}\cdot\text{m}^{-2}$ along the z-axis.

In order to evaluate the distribution of residual stresses in the different zones of the stator, the static stiffness values computed in Subsection 3.2.5 are taken as references. The mean values were $3.0\cdot10^{8}\,\text{N}\cdot\text{m}^{-1}$ in zone "prox", $2.5\cdot10^{8}\,\text{N}\cdot\text{m}^{-1}$ in zone "yoke" (i.e. 83% of zone "prox") and $1.3\cdot10^{8}\,\text{N}\cdot\text{m}^{-1}$ in zone "teeth" (i.e. 43% of zone "prox"). Using the same factors to represent the distribution of prestresses, a compression of $1.27\cdot10^{6}\,\text{N}\cdot\text{m}^{-2}$ is applied on zone "yoke" and $6.58\cdot10^{6}\,\text{N}\cdot\text{m}^{-2}$ on zone "teeth". Apart from this prestress, the identification of equivalent properties is made in the same way and with the same base cell for both zones. The contact properties are described by a Coulomb dry friction with a coefficient $\mu = 0.9$, and occur at the interface described previously.

A 72×72 real symmetric stiffness matrix is computed and takes into account the influence of the preload and friction. Reducing it with the "Craig-Bampton" method (widely used in FE simulations and detailed in Subsection 1.3.3) with master-nodes 1 to 18 yields a new stiffness matrix (real, symmetric and of size 48×48). By creating a new model with the 16 master-nodes (and no elements) and importing the reduced stiffness matrix as an external superelement, a linear static solution is initiated to apply the method "**Tricl1**" presented in Section 3.3.2 (sliding shear scenario). Post-processing the results yields the elasticity matrices

$$\left[\tilde{C}^{\text{yoke}}\right] = \begin{bmatrix} 227 & 65 & 29 & 6\cdot10^{-4} & -1\cdot10^{-5} & 2\cdot10^{-8} \\ & 227 & 29 & 6\cdot10^{-4} & -1\cdot10^{-5} & 5\cdot10^{-8} \\ & & 90 & 2\cdot10^{-3} & -4\cdot10^{-5} & 1\cdot10^{-8} \\ & & & 45 & 3\cdot10^{-3} & 4\cdot10^{-1} \\ & \text{sym.} & & & 45 & 4\cdot10^{-1} \\ & & & & & 78.1 \end{bmatrix} \cdot 10^9 \tag{3.96}$$

and

$$\left[\tilde{C}^{\text{teeth}}\right] = \begin{bmatrix} 233 & 69 & 43 & 2\cdot10^{-7} & -2\cdot10^{-7} & 3\cdot10^{-8} \\ & 233 & 44 & 2\cdot10^{-7} & -2\cdot10^{-7} & 1\cdot10^{-8} \\ & & 14 & 2\cdot10^{-7} & -2\cdot10^{-7} & 2\cdot10^{-8} \\ & & & 3.3 & 2\cdot10^{-4} & 1\cdot10^{-1} \\ & \text{sym.} & & & 3.3 & 1\cdot10^{-1} \\ & & & & & 55 \end{bmatrix} \cdot 10^9 \,. \tag{3.97}$$

Judging from the values of matrices $\left[\tilde{C}^{\text{yoke}}\right]$ and $\left[\tilde{C}^{\text{teeth}}\right]$, several observations can be made:

- non-negligible inter-shear coupling terms have been determined for both zones, as well as non-negligible tension-shear coupling terms for zone "yoke";
- in rows 4 and 5 of both matrices, the diagonal terms correspond to the equivalent sliding shear stiffness values in directions $\theta - z$ and $r - z$;
- in both matrices, the rows relative to series rr and $\theta\theta$ (as well as θz and rz) have similar values. Globally, this expresses the fact that directions r and θ are equivalent, which is consistent with the apparent symmetry of the base cell;
- compared to the material properties of homogeneous isotropic steel (see Equation (3.84)), the diagonal values of both matrices $\left[\tilde{C}^{\text{yoke}}\right]$ and $\left[\tilde{C}^{\text{teeth}}\right]$ are lower than in matrix $\left[C^{\text{stl}}\right]$, especially for rows 4 and 5. This seems consistent with the fact the base cells are subjected to friction instead of being glued elements (with common nodes);
- compared to each other, the diagonal values of rows 4, 5 and 6 are higher in zone "yoke" than in zone "teeth". This indicates that the tightening effect due to prestress is more notable in the yoke's shear properties than in the teeth's.

As for zone "prox", the material properties are kept identical as in Subsection 3.2.5: $\tilde{E}_r = \tilde{E}_\theta = 205\,\text{GPa}$, $\tilde{E}_z = 157\,\text{GPa}$, $\tilde{G}_{z\theta} = \tilde{G}_{zr} = 51.2\,\text{GPa}$, $\tilde{G}_{r\theta} = 82.1\,\text{GPa}$, and $\tilde{\nu}_{\theta z} = \tilde{\nu}_{rz} = \tilde{\nu}_{r\theta} = 0.25$. The weld beads are modelled with isotropic steel, such as $E = 207\,\text{GPa}$ and $\nu = 0.29$. The same density $7,750\,\text{kg}\cdot\text{m}^{-3}$ is applied to the entire structure.

3.3.4.3/ COMPARISON WITH EXPERIMENTAL DATA

A modal basis is simulated in real domain between 0 and 10,000 Hz from the entire magnetic core's finite-element model. This simulated modal basis is compared with a set of 5 purely radial modes (same experimental modal basis as in Subsection 3.2.5), extracted from frequency response functions measured with an impact hammer on the magnetic core of a real stator. These modes are sometimes referred to as "cylinder" or "ovalisation" modes, and are critical for the acoustic behaviour of the entire stator [140]; being able to predict them accurately is thus of particular interest. The experimental settings are shown in Figure 3.12. The experimental mesh is composed of 108 degrees of freedom (36 points of 3 DOFs).

The comparison of the simulated and experimental modal bases is presented in Table 3.20, where the columns "**FEA**" and "**EMA**" respectively refer to the mode frequencies in the FE model and in the experimental modal basis. The deformed shapes of the ovalisation modes are identical as in Figure 3.17. The $\overline{|\Delta f|}$ and $\overline{MAC}$ averages have been computed with Equation (1.68) and (1.69) and shown in the bottom row of Table 3.20. Also, the results of Table 3.20 (called "**Ortho1 + Tricl1**") are compared with "**Ortho1**" averages, as shown in Table 3.21.

Mode pair	**FEA [Hz]**	**EMA [Hz]**	Δf [%]	MAC [%]	**Mode description**
1	818.6	798.6	2.5	64	cylinder mode, order 2
2	2,172.9	2,125.5	2.23	61.7	cylinder mode, order 3
3	3,847.4	3,747.7	2.66	89.1	cylinder mode, order 4
4	5,471.4	5,330.1	2.65	69.1	cylinder mode, order 5
5	6,543.8	6,286.5	4.09	75.5	cylinder mode, order 0
Averages $\overline{\lvert\Delta f\rvert}$ ***and*** $\overline{MAC}$			***2.83***	***71.9***	

Table 3.20 – Correlations of FE and experimental modal basis

In Table 3.21, the 17% relative decrease of $\overline{|\Delta f|}$ and only 4% relative decrease of $\overline{MAC}$ show a significant improvement in the simulation accuracy of the above-presented ovalisation modes, of particular importance regarding electric motor acoustics [140]. This tends to compensate the complexity increase due to replacing explicit orthotropic elastic constants by a fully-defined elasticity matrix for the zone "teeth", although the identification method can be automatised with low-resource computer algorithms, and the computation costs for any FE simulations remain unchanged regardless of the type of materials.

	Ortho1	**Ortho1 + Tricl1**
$\overline{\lvert\Delta f\rvert}$ [%]	3.43	2.83
$\overline{MAC}$ [%]	74.7	71.9

Table 3.21 – Accuracy improvement

3.3.5/ SPECIFICITIES OF THE METHODS

Several details about the properties of the method presented above have to be added. For both the "orthotropic" and "triclinic" methods, creating a sample whose global geometry is not a cuboid highly complicates the establishment of the solution. Indeed, if one of the element's faces is not a perfect rectangle (for instance if one of its angles differs from 90°), the reaction forces computed on neighbouring faces will be misused. This tendency is particularly important for the identification of orthotropic and isotropic materials in unknown structures. For similar reasons, using the "triclinic" method on homogeneous, orthotropic structures may lead to fewer variables than equations while computing the matrix $\mathcal{H}$ (see Equation (3.64)), and therefore to a rank lower than 6. In such cases, pseudo-inverting $\mathcal{H}$ may retrieve the expected values, including null ones.

The elements' geometric properties have another influence on the method. In the case of heterogeneous structures, for instance a laminated composite made of isotropic layers, the elastic constants E, G and ν vary discontinuously in the stacking direction, thus implying heterogeneities and discontinuities in the computed reaction forces. Indeed, while applying the "triclinic" method to a stack made of isotropic layers without external perturbations, the simulations of the series xx generate important and uneven reaction forces at the nodes constrained with plane contacts on faces $y = 0$ and $z = 0$, because of the layers' different materials. This comes out as non-negligible coupling terms between tension-compression and shear, and therefore contradicts the assumption of orthotropy due to the system's symmetries ([119, 16]). This is why a laminated structure presenting a priori no coupling between tension-compression and shear needs to be analysed with the "orthotropic" method presented in Section 3.2. In practice, applying a single pure tension simulation to a cuboid structure would confirm the existence of non-null coupling terms between tension-compression and shear in the equivalent material, and would therefore suggest using either the "orthotropic" or the "triclinic" methods.

Eventually, the last point concerns the ability of both the "orthotropic" and "triclinic" methods to be applied to superelements. In a structure to be reduced into a superelement and taken as sample for material identification, it must be clear that none of the slave DOFs may be located on external surfaces, or correspond to any of the simulations' constrained DOFs (as listed in Table 3.14). Otherwise, the boundary conditions have to be taken into account before reducing the structure, which therefore requires as many independent superelements as independent simulation schemes. All other nodes, not located on external faces, may be taken as slave DOFs and reduced, without hindering the identification process.

The "Triclinic" method can be summarised in the following sequence:

1. Zoning;

2. Creation of a representative cuboid sample in a chosen zone;
3. Application of the corresponding external perturbations;
4. Computation of the preloaded sample's stiffness matrix;
5. Determination of the superelement's equivalent compliance matrix.
   a) Computation of the first three rows;
   b) Transposition of the submatrix of coupling between tension-compression and shear;
   c) Calculation of the remaining three rows.

3.3.6/ Conclusion on the anisotropic homogenisation approach

This section has proposed a new method of equivalent material identification based on finite-element simulations for general anisotropic models. With the aid of the approach developed in this section, equivalent material properties for a continuous anisotropic model, a continuous structure subjected to preloading and a preloaded laminated stack have been exhibited. As a result, it has been shown that anisotropic materials can be identified with little derivation on continuous structures if no external perturbations are applied. The other analyses have shown that preloading effects alter the initial symmetries in the material properties on a 3D isotropic model, and induce couplings between tension-compression and shear in the equivalent material properties of a multi-layered laminated stack. It has been observed that under preloads, anisotropic continuous structures require transverse shear simulations, whereas sliding shear identification scenarios are more accurate for recreating the behaviour of laminated models. This observation is identical to the conclusion of Section 3.2.

Also, the modal behaviour of an electric motor stator's laminated magnetic core has been simulated with equivalent anisotropic material properties that accounted for the friction behaviour under compression preloads between steel sheets in the teeth and the yoke. Low-frequency ovalisation modes have been computed and showed good accuracy in comparison to experimental data from a real stator. An accuracy improvement has been also observed in comparison to orthotropic properties. This new identification method raises hopes to improve the current prediction capacities to perform noise and vibration simulations on multi-layered magnetic cores, without needing to rely on experimental data from costly prototypes and time-consuming model updating procedures. The ability of this new method to be applied to superelements, and therefore estimate the influence of external perturbations on the material properties, presents a "conversion" opportunity from stiffness matrices to elasticity matrices.

Intermediate conclusion

This chapter has presented and compared several elastic property identification methods that have been applied to the finite-element models of various heterogeneous and externally-perturbed structures. It has been shown that the ability of an equivalent material property set to recreate the dynamic behaviour of the corresponding initial structure is affected by the definition of shear chosen for the identification and the existence of

couplings between tension-compression and shear. As a result, laminated structures require "sliding shear" identification scenarios, whereas pre-stressed homogeneous bodies are best modelled by "transverse shear" moduli. The analyses showed that subjecting a body to tension pre-loads induced either orthotropy if the initial structure was homogeneous and isotropic, or anisotropy for the laminated stack.

Applied on the laminated magnetic core of a switched-reluctance machine stator, the "Orthotropic" method led to a satisfying 3.43% average discrepancy in the simulation of critical ovalisation modes. Considering compression preloads and friction between the sheets of the magnetic core enabled decreasing this average discrepancy to 2.83%. It can not be denied that the complexity of implementation is increased when replacing the presented "Orthotropic" by the "Triclinic" approach in the case of the electric machine stator. However, the ability to identify equivalent material properties to superelements or heterogeneous structures subjected to external perturbations offers interesting perspectives for further academic or industrial applications. The next chapters will bring the other active parts under the spotlight (windings and resin) and will associate experimental analyses to simulation approaches.

4

WINDINGS AND INSULATING RESINS: EXPERIMENTAL ANALYSES AND APPLICATION TO FINITE-ELEMENT MODELS

As it has been introduced in Chapter 1, winding coils are generally placed on the stators of AC machines and on the rotors of DC machines. A coil consists in a winding of a current-conducting wire (typically copper) that is impregnated with resin in order to ensure an electric insulation as well as a mechanical bond. Due to this heterogeneity, modelling windings with finite-elements requires homogenisation methods such as those presented in Chapter 3. In addition to this difficulty, the existing knowledge on the contact conditions between the windings and the magnetic core is somehow limited. To put things in a nutshell, performing mechanical simulations on the finite-element model of an electric machine stator including the magnetic core, the windings and the resin is currently a real challenge.

This chapter will focus on the existing knowledge about the modelling techniques of electric machine windings including insulating resin. The first section will detail the state-of-the-art of the current knowledge about the dynamic behaviour of windings, whereas the next sections will detail an experimental campaign and a modelling analysis on stator samples with windings and resin. While Section 4.1 focuses on windings alone or included in complete stators, a more specific emphasis on the resin alone will be made in Chapter 5.

4.1/ CURRENT KNOWLEDGE ABOUT WINDINGS

Due to the wires that compose it, a coil tends to be characterised by a uni-directional behaviour and a relatively low bending stiffness. In a typical AC machine stator, the coils are winded into several slots [61]: some parts are held between the stator teeth whereas others make the connections at the external faces of the machine. Therefore, it seems consistent to consider that the wires will not behave identically in or out of the stator slots. Based on simulations of stresses resulting from electromagnetic excitations in stator windings, Lin and Arkkio [103] have shown that stresses and strains were not homogeneously distributed in the windings, contradicting earlier observations in [38]

but confirming the hypothesis of behaviour difference. Consequently, one of the first modelling guidelines that is suggested in this chapter is to distinguish the two winding zones "in slots" and "out of slots".

As for the terminologies, "end windings" are commonly used for referring to the zone "out of slots", whereas references to the other zones seem more confusing in the literature (e.g. "stator bars" in [145]). For convenience in further applications in this thesis and as suggested in Section 2.3, the alternative terminologies "winding heads" for "end windings" and "winding edges" for "stator bars" will be preferred. An illustration of this choice is shown in Figure 4.1.

Several published works have investigated finite-element modelling possibilities for representing windings. First of all, Lin et al. [124] have reported major complexities for describing the dynamic behaviours of winding heads, and thus recommended to use finely-meshed three-dimensional models only, as illustrated in Figure 4.2. In a similar way, the detailed winding meshes of the case study presented by Chentouf et al. [131] were divided into several zones throughout the stator length. Each of the zones were represented by orthotropic material properties and needed to be updated with experimental data. However, in these two examples the large numbers of DOFs and the necessity to update the models with experimental measurements result in important computation costs. Theoretical explanations about model updating are given in Section 1.4.

At the opposite, Cai et al. [63] considered that the coils were tightly fixed on the poles but did not bring additional stiffness to the magnetic core, and suggested to model the windings as additional mass and damping only. Applying this suggestion and considering the geometry of a wire turn (see Figure 4.3), Tang et al. [72, 86] have proposed the following analytical formulation of the density ρ_{wp} of a winded pole (tooth):

$$\rho_{wp} = \frac{m_{\text{tooth}} + m_{\text{coil}}}{V_{\text{tooth}}} \,, \tag{4.1}$$

where V_{tooth} is the volume of a tooth, m_{tooth} its mass and m_{coil} the mass of the coil. In detail, these values are defined by

$$V_{\text{tooth}} = L_{\text{stack}} \cdot W_{\text{tooth}} \cdot H_{\text{tooth}} \,, \tag{4.2a}$$

$$m_{\text{tooth}} = \rho_{\text{stack}} \cdot \mathfrak{s}_{\mathfrak{f}} \cdot V_{\text{tooth}} \tag{4.2b}$$

and

$$m_{\text{coil}} = N_t \cdot \left(\rho_{\text{coil}} \cdot (\pi \cdot W_{\text{tooth}} + 2 \cdot L_{\text{stack}}) \cdot \left(\pi \cdot \left(\frac{d_{\text{wire}}}{2} \right)^2 \right) \right) \,, \tag{4.2c}$$

where L_{stack}, W_{tooth} and H_{tooth} are respectively the length, the width and the height of the tooth, ρ_{stack} and ρ_{coil} are the respective densities of the stack and the coil, $\mathfrak{s}_{\mathfrak{f}}$ is the stacking factor as defined in Equation (3.1), N_t is the number of wire turns in the coil and d_{wire} the diameter of the wire. Once ρ_{wp} is computed, the authors suggest to apply the value to the stator teeth without adding elements for modelling the coils.

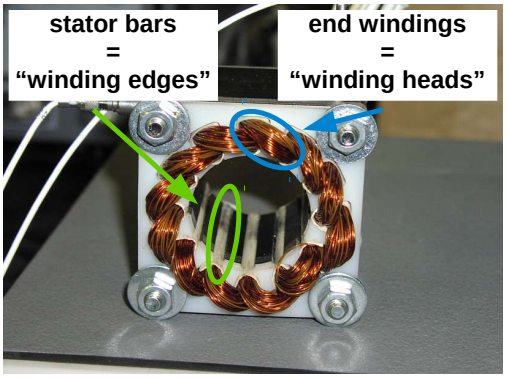

Figure 4.1 – Picture of a winded stator [72]

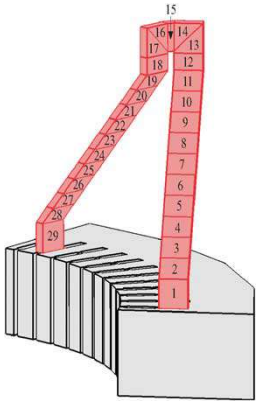

(a) Finite-element meshing of a single wire [103]

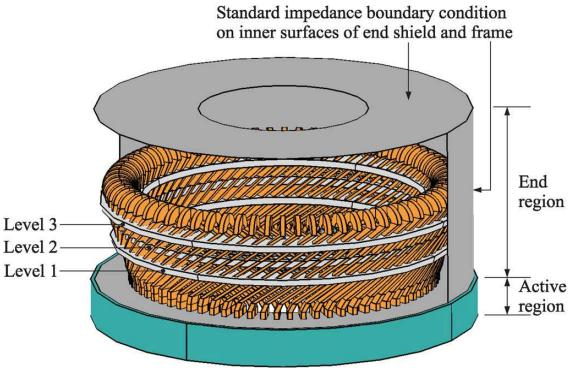

(b) Detailed geometries of winding heads [124]

Figure 4.2 – Geometries of winding heads

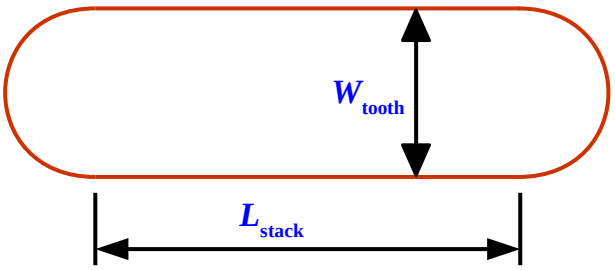

Figure 4.3 – Geometry of a single wire turn [86]

An original modelling approach has been proposed by Schlegl et al. [145]. Focusing on the windings, they suggest to mesh the coils in 3D, replace the rest of the structure with stiffness elements and update the model with experimental measurements (see Figure 4.4). Although this alternative model reduces the computation costs significantly in comparison to the models presented in [124] and [131], this approach can not be integrated into any simulations on entire stators as the other parts are replaced by equivalent stiffness elements. Moreover, the need to update the model limits the possibilities to use this approach in design stages.

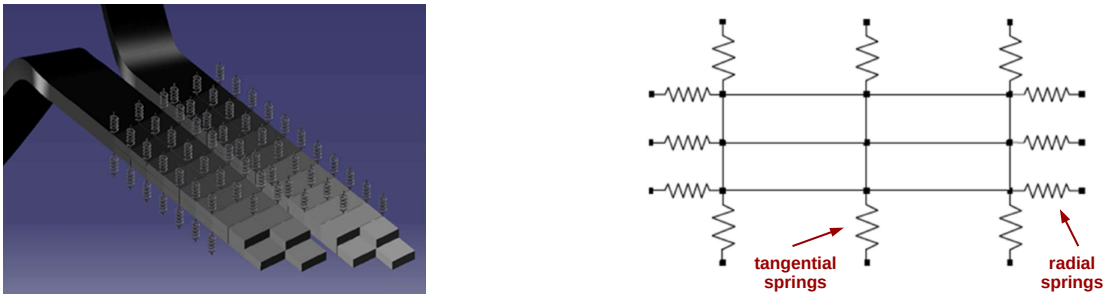

(a) 3D view of the model

(b) Cross-sectional view

Figure 4.4 – Model of stator windings [145]

As for Ji et al. [142], they pretend that representing winding heads with equivalent homogeneous properties is not accurate enough for being reliable. Instead, they propose to use a hybrid electronic model that can not be integrated to finite-element simulations. In conclusion, the only reasonable approach presented in this section that does not require updating finite-element models is the mass density computation detailed in [86]. As a consequence, the need of developing robust methods for modelling windings as parts of entire stators (and thus assembled with resin) is great, and has been outlined in [140]. Therefore, the next sections will describe an experimental analysis on real stator samples with windings and adaptation investigations to finite-element modelling. With the aid of experimental modal data, representative finite-element models will be sought for representing windings in an electric machine. Finally, the dependency of the elastic properties towards temperature changes will be investigated.

4.2/ EXPERIMENTAL ANALYSES

As part of this Ph.D. programme, a vast experimental campaign has been organised for analysing the effects of windings and insulating resin in the dynamic behaviour of a stator. The expected result is to understand how to generate reliable models of entire electric machines. To do this, the experimental process consists in manufacturing two-toothed samples of a real stator core, fix copper windings on the teeth and insert insulating resin in the entire structure. Several sorts of industrial resins are selected according to the types of electric machines they are usually used for as well as their respective viscoelastic properties.

The following subsections will describe all the stages of the experimental process: the design of steel samples, the production of the windings, the application of the resins and

the dynamic measurements.

4.2.1/ STEEL SAMPLES

Eight samples of homogeneous steel have been milled by the company Pi-Méca (Saint-Vit, France), as illustrated in Figure 4.5. A detailed draft of the sample is given in Appendix A.2. Homogeneous steel has been preferred to laminated steel so that the uncertainties related to the core's heterogeneity do not interfere with this study.

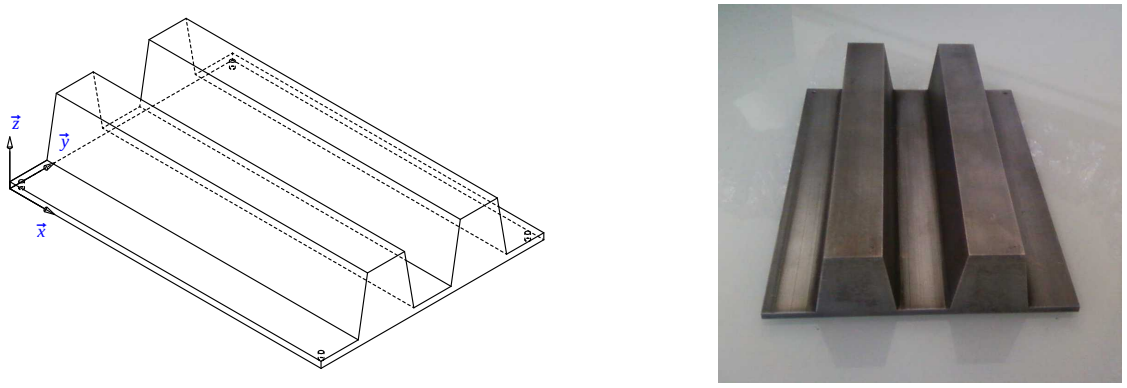

(a) Sketch of the sample

(b) Picture of the steel sample

Figure 4.5 – Core sample

The geometry is derived from the switched-reluctance motor stator presented in Sections 2.3, 3.2 and 3.3, although the yoke width has been altered to ensure that the frequencies of bending modes are sufficiently low to afford convenient measurements on the sample.

4.2.2/ PRODUCTION OF WINDINGS

Altogether, sixteen winding coils were required as each of the eight steel samples were composed of two teeth. Six industrial coils from the initial stator were provided, whereas the remaining ten were produced by hand. For this, enamelled copper wires of $2.50 \times 1.25\,\text{mm}$ cross-section were provided by the company APX (Sarrians, France) and winded about a tooth pattern so that each of the coils had an identical mass of 440 g. As it can be seen in Figure 4.6, the hand-made windings are in contact while industrial coils are clearly separated.

Following some of the results shown in Section 4.1, the windings are assumed to have a negligible stiffness effect on the stator core, hence small discrepancies induced by the different mass distribution between hand-made and industrial coils. The validity of this assumption is to be tested in the following sections.

(a) Industrial windings

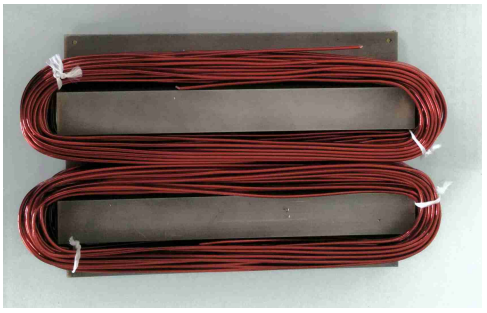

(b) Hand-made windings

Figure 4.6 – Windings on sample teeth

(a) Distributed AC motor windings

(b) On-tooth SRM windings

Figure 4.7 – AC vs. SRM stator architectures [169, 170]

name	winding type	application family	resin reference
P1	hand-made	encapsulation	15225
P2	hand-made	encapsulation	15244
P3	hand-made	encapsulation	15350 NA
P4	hand-made	encapsulation	15350 FL
P5	industrial	impregnation	3630 XLE
P6	industrial	impregnation	3630 VPI
P7	hand-made	impregnation	3630 HIR
P63	industrial	encapsulation	15350 NA

Table 4.1 – Details of the experimental cases

4.2.3/ RESIN APPLICATIONS

Once the windings are placed on the sample teeth, the last operation before the measurements is the application of resin. The nature of the resin as well as the application process depends from the type of electric machine. Whereas an AC (alternating-current) machine's stator has numerous, thin teeth, an SRM's (switched-reluctance machine's) is composed of fewer and wider teeth and slots (see Figure 4.7). Therefore, this difference requires adapted resin settings for each motor type; while in the former case, windings are *impregnated*, the latter stator is entirely *potted* (or *encapsulated*) with resin [162]. In this chapter, these different types are referred to as "application families".

The company Von Roll (Meyzieu, France) is experienced in the design and the application of insulating resins in electric machines. Thanks to their involvement in this project, seven different resins were applied to the samples. The experimental cases are labelled "P1" to "P7" with an additional "P63", as described in Table 4.1. Note that cases P3 and P63 are encapsulated with the same resin.

An illustration of each application process is given in Figure 4.8: at the opposite of sample P2, for which the resin is poured over until filling the cast entirely (encapsulation), sample P7 is plunged into a resin container and then hung for drip-drying (impregnation). The encapsulation/potting process involves placing the sample and its cast in vacuum in order to ensure that no air remains in the resin and between the wires. The samples are then baked according to the resin specifications and cooled at room temperature. In the end of the process, the resin takes a solid shape. The volume occupied by the resin in either potted or impregnated samples can be compared in the detailed views presented in Figure 4.9. Pictures of all the eight studied samples are gathered in Figure 4.10.

(a) Resin potting / encapsulation (sample P2)

(b) Resin impregnation (sample P7)

Figure 4.8 – Resin application processes for encapsulation and impregnation (at Von Roll)

4.2.4/ DYNAMIC MEASUREMENTS

Once cooled, each sample is analysed in turn. Beginning with P1, the sample is equipped with 11 tri-axial accelerometers, labelled between 1101 and 1123 as shown in Figure 4.11.

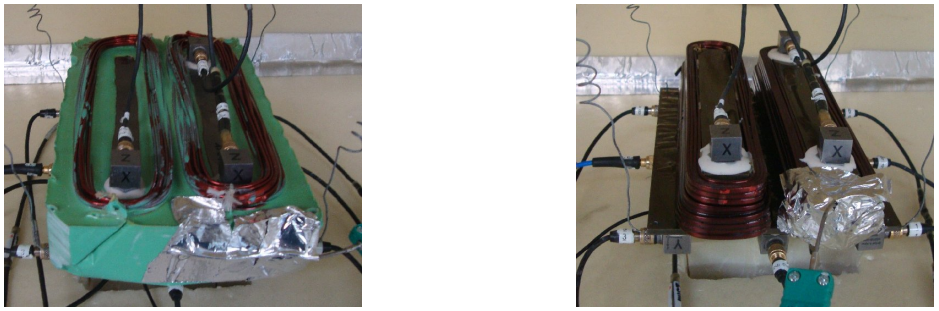

(a) Sample P2 (b) Sample P5

Figure 4.9 – Detailed views of samples P2 and P5

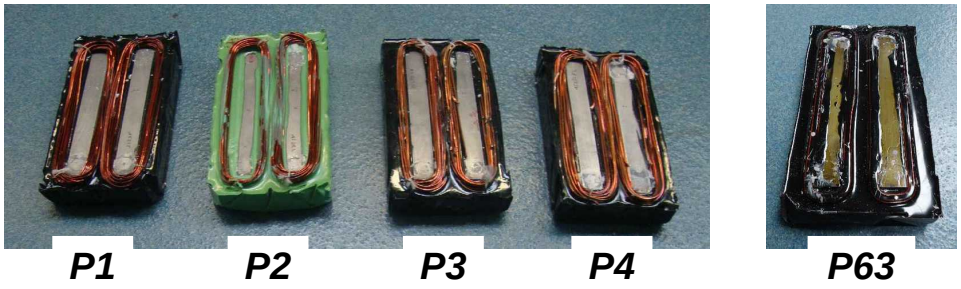

Figure 4.10 – Completed samples

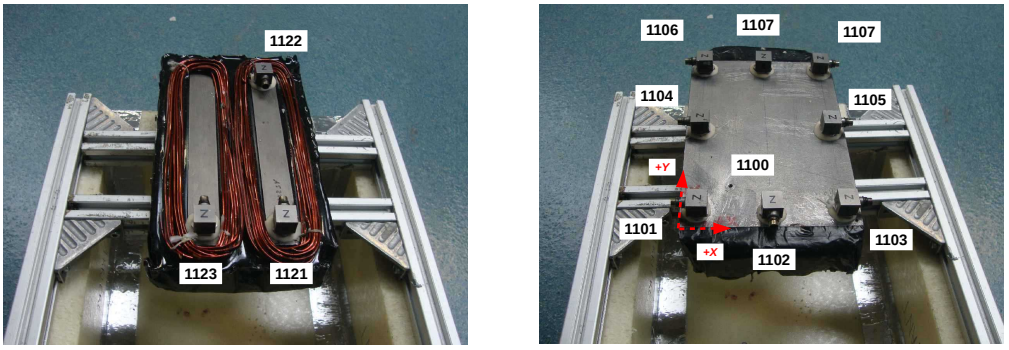

(a) Top face (b) Bottom face

Figure 4.11 – Accelerometer positioning (sample P1)

Point 1100 refers to the excitation. This geometry is identical for all the samples, and is detailed in Table 4.2. In particular, the coordinate system used for the measurements is rectangular and has its origin at the steel corner near point 1101. As shown in Subfigure 4.11(b), the axes $+X$ and $+Y$ are defined by the shorter and longer edges of the bottom face, respectively, and the axis $+Z$ is oriented from the top to the bottom face.

label	**X** [mm]	**Y** [mm]	**Z** [mm]
1121	32.5	10	-29.4
1122	75	10	-29.4
1123	32.5	144	-29.4

top face

label	**X** [mm]	**Y** [mm]	**Z** [mm]
1100	25	30	0
1101	10	10	0
1102	55	10	0
1103	100	10	0
1104	10	77	0
1105	100	77	0
1106	10	144	0
1107	55	144	0
1108	100	144	0

bottom face

Table 4.2 – Accelerometer coordinates

The first objective is to measure frequency response functions (FRFs) at every point 1101 to 1123 and every translational DOF Tx, Ty and Tz in response of an excitation at point 1100 and about DOF $-Tz$. This measurement is done at room temperature (25°C) after suspending the sample with soft springs in a box made with thermally-insulating foam. Amongst other possible techniques, the excitation is made with an electrodynamic shaker. This choice is explained by the fact the samples are suspected to exhibit a nonlinear dynamic behaviour; applying a purely sinusoidal excitation and controlling the input force magnitude ensures a better repeatability than e.g. impact hammers between all the measurements and all the samples. Response functions are measured by sweeping the interval [500; 10,000 Hz] with the excitation frequency (which takes 90 seconds). Pictures of the measurement environment are shown in Figure 4.12, while other details about the acquisition equipment are given in Subsection 4.2.5.

A 36-channel analyser is used, mainly for processing the data from the accelerometers and sending them to the computer, but also for piloting the shaker's frequency via a voltage amplifier. Then, the force applied to the sample is measured by a load cell (see Figure 4.13) via a charge amplifier and enables the closed-loop control of the shaker by enforcing a constant 0.5 N force magnitude. The shaker is placed under the sample and outside the insulation box. The load cell is screwed in the bottom face at point 1100 and a steel rod of diameter 0.8 mm is used for linking the shaker to the sample, so that the chucks are distant of approximately 2 cm.

Once all the 33 FRFs are stored, a modal basis is extracted with the aid of the module PolyMAX™ of the software suite LMS.TestLab™. This stage is performed by spotting the acceleration maxima in the FRFs and defining the relevant ones as modes. In the end, a complex modal basis is built.

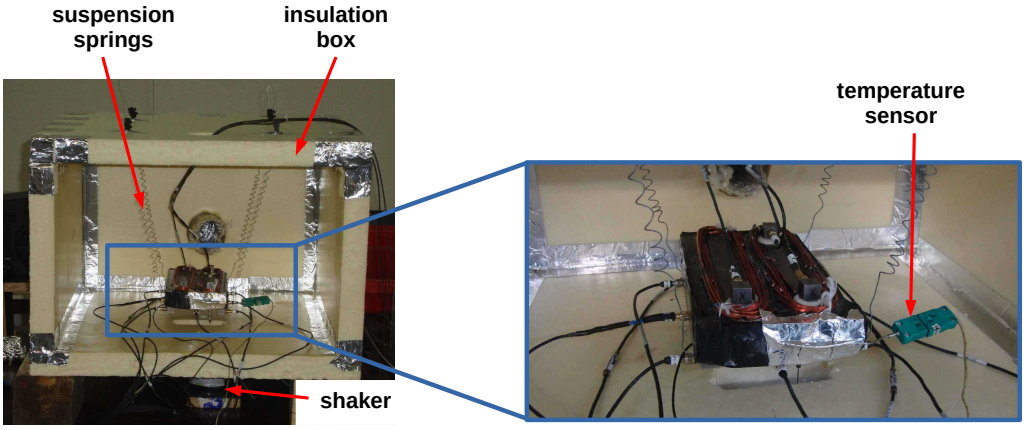

Figure 4.12 – Measurement environment (sample P1)

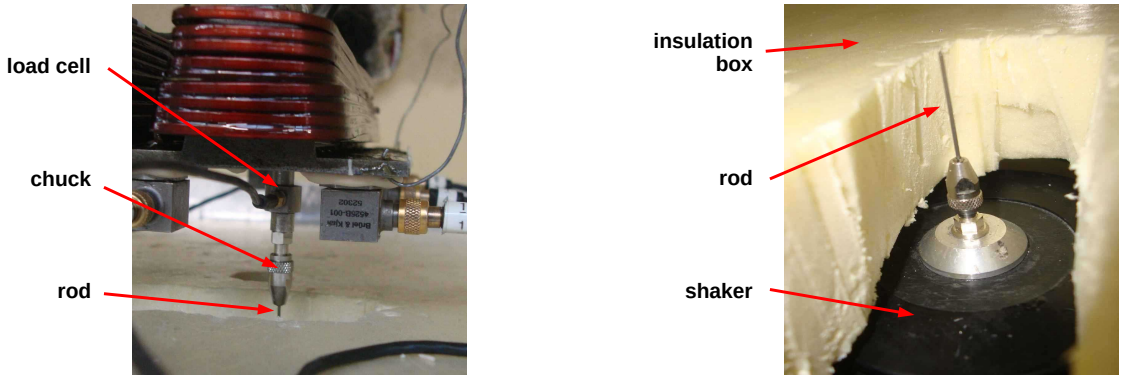

(a) Load cell (b) Shaker

Figure 4.13 – Harmonic excitation on sample P6

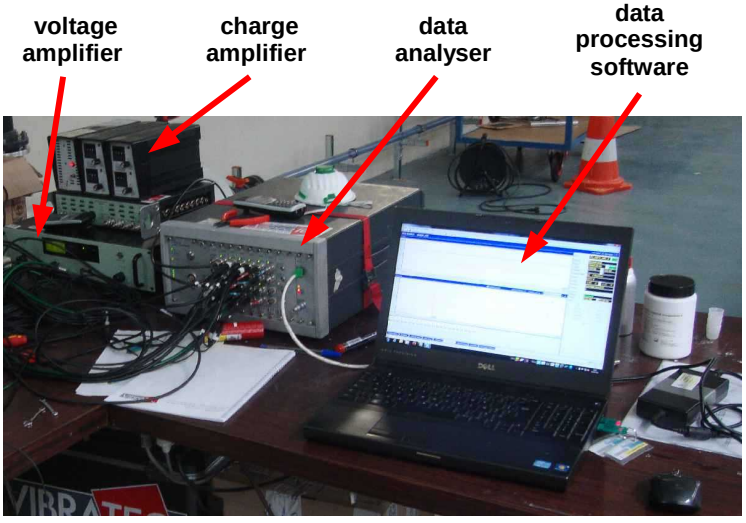

Figure 4.14 – Acquisition equipment

For convenience when comparing it with simulation results, the modal basis is expressed in the real domain according to the following rules (default in LMS.TestLab™):

- complex magnitudes are kept identical;
- complex phases $\varphi \in]-\pi; 0]$ are fixed at $\varphi = {}^{-\pi}/_{2}$;
- complex phases $\varphi \in]0; +\pi]$ are fixed at $\varphi = {}^{+\pi}/_{2}$.

The samples are then heated up to 90°C in an oven so that the measurement process is repeated between 80°C and 25°C with decreasing steps of 5°C. By closing the insulation box, the temperature variations are minimised during each frequency sweep.

4.2.5/ ACQUISITION EQUIPMENT

The acquisition equipment that was used for performing the above-presented measurement is presented in Figure 4.14 and detailed throughout the following points:

- **accelerometers:** B&K™ 4525 B001 (6 grammes each)
- **voltage amplifier:** B&K™ S/N 2317620
- **charge amplifier:** ENDEVCO™ Σ104
- **shaker:** B&K™ 4N S/N 2317620
- **data analyser:** LMS.TestLab™ S/N 42042606
- **data processing software:** LMS.TestLab™ v. 12A

4.3/ FINITE-ELEMENT MODELS OF WINDINGS AND RESIN

Considering the modal bases described in Section 4.2 as references, the possibilities and the limits to simulate the modal behaviour of each sample with finite-element models are investigated. As it has been outlined earlier, the main difficulties lie in modelling the windings and the resin accurately and being able to adapt the models to the considered case, namely to the specific resin type or to temperature- and frequency-dependent properties. After a brief description of the critical mode pairs to focus on, this section analyses the representativeness of different modelling approaches at a fixed temperature, and then focuses on the variabilities of the model properties with respect to temperature changes.

4.3.1/ CRITICAL MODES

Amongst all the modes extracted from the experimental FRFs, some are of particular significance regarding the global stator's behaviour. Four modes of the sample family "potted" and three of the family "impregnated" are considered critical due to the global natures of their shapes (and not localised). These experimental modes are associated to the corresponding simulated modes by the means of the correlation criteria described in Subsection 1.4.2. The mode pairs are labelled according to the average experimental natural frequency amongst the samples of a same family, with "PT" referring to "potted" and "PG" to "impregnated". Each mode pair is shown in complete and reduced views in the respective Figures 4.15 and 4.16.

Concerning the complete stator's dynamic behaviour, mode pairs PT4 and PG1 are specifically representative of the ovalisation modes. Therefore, a particular emphasis is put on these modes. Additional details about these modal bases are given in Appendix A.4.

Although it can not be evidently illustrated in this manuscript, it seems important to outline that the experimental analyses on potted samples with hand-made windings (ie. P1, P2, P3 and P4) globally yielded few modes with neat deformed shapes. While PT1 (torsion) modes could be distinguished without doubt at the sight of their shapes, PT4 could hardly ever be extracted from the FRFs. At the opposite, each modal basis of samples P5, P6 and P63 included a PG1-like (respectively PT4-) mode. This point will be discussed further in Paragraph 4.3.2.1 and Subsection 4.3.4.

As for sample P7, no modes could be extracted due to the FRF curves' overall too poor quality. Although the measurements were performed in similar conditions as the other samples, the response curves showed great numbers of maxima. Compared to the critical modes described in Figure 4.16, the deformed shapes extracted at these maxima led to too low MAC values to be considered meaningful and reliable for further analyses. The suspected reasons for these poor-quality measurements are the numerous contacts and free wire sections originating from the hand-made windings where the impregnating resin does not guarantee cohesion between all the wires. Therefore, sample P7 has been discarded from the next stages of this study.

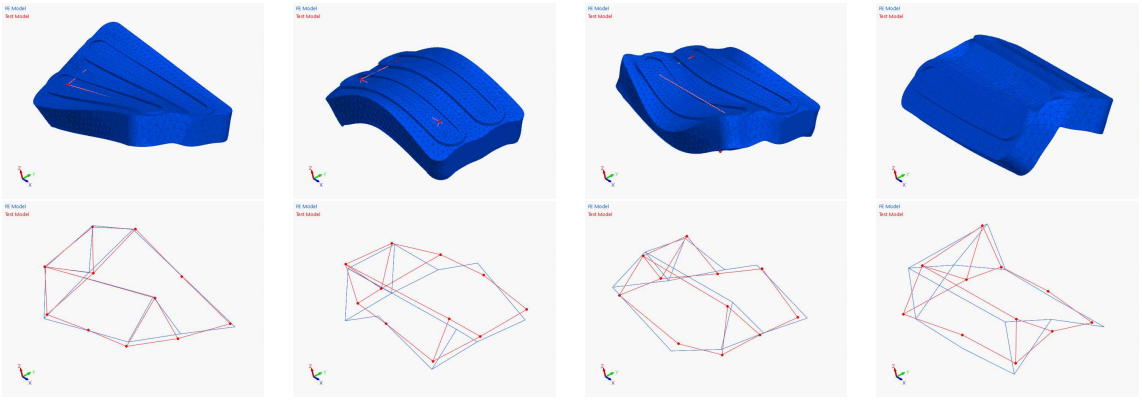

PT1 at $\approx 2,500$ Hz **PT2** at $\approx 4,000$ Hz **PT3** at $\approx 5,500$ Hz **PT4** at $\approx 5,900$ Hz

Figure 4.15 – Critical modes - potted samples

4.3.2/ General modelling guidelines

This subsection aims at comparing the representativeness of possible finite-element modelling modelling techniques for the presented samples, based on simulation-measurement modal correlations. The temperature is fixed at 25°C. Each model is based on the two-toothed steel core, as shown in Figure 4.17 on which the accelerometers are represented with 6-gramme lumped mass elements. Except for the cases FEM T3, FEM T4, FEM G1 and FEM G2 (see details in Appendix A.5), the material properties of the core and the lumped masses are not altered.

The comparison consists in 21 cases involving 10 FE models for potted samples and 11 models for impregnated samples. As this analysis focuses on modelling techniques more

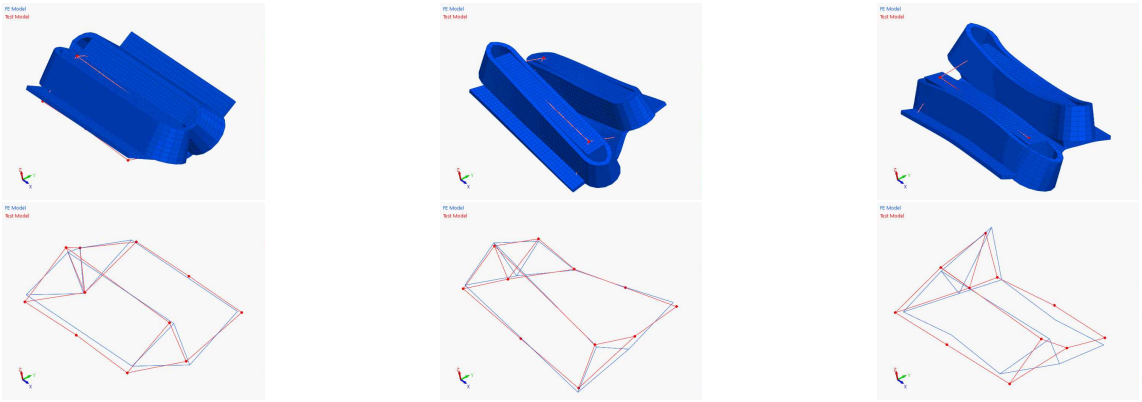

PG1 at $\approx 650\,\text{Hz}$ **PG2** at $\approx 1,400\,\text{Hz}$ **PG3** at $\approx 3,100\,\text{Hz}$

Figure 4.16 – Critical modes - impregnated samples

than on resin properties, the only considered samples are P1 (potted) and P5 (impregnated), and the results are generalised for the corresponding families. The sample P63 is discarded from this comparison due to the important changes related to the winding types. This case will be addressed in Subsection 4.3.4.

The principle is to correlate an initial simulated modal basis (computed from generic material properties) with the corresponding experimental modal basis. Then, the FE model is updated according to the method described in Section 1.4, where the parameters consist in a specific set of material properties. In this study, the comparison criteria are the final frequency discrepancy $\overline{|\Delta f|}$ defined in Equation (1.68) and the number of mode pairs N_{mp} above the MAC threshold $\text{t}_{MAC} = 40\%$. The software used for performing finite-element model updating is DDS FEMtools™.

STABILITY

Performing updating procedures on models which are composed of equivalent meshes for representing entire pieces might require specific elastic properties that would not be representative of any real material. In such case, the variations induced by the updating iterations may be important and cause instability in the system. Therefore, some explanations are given in the following paragraphs, as well as a correction technique developed in order to stabilise the updated material definitions.

One of the necessary conditions to perform a finite-element simulation in an elastic structure is the stability of the system: the transition of an equilibrium state to a deformed state requires a positive input of energy [21]. In terms of material properties, this is equivalent to having only strictly positive eigenvalues in the elasticity and compliance matrices $[C]$ and $[S]$, whose definitions have been introduced in Chapters 1 and 3. In principle, material properties corresponding to natural elements such as metals are initially stable (e.g. $E > 0$ and $|\nu| < 0.5$ for isotropic materials). However, properties identified by mathematical processes such as model updating or optimisation procedures might cause instability due to one ore more negative eigenvalues in matrix $[C]$. This can be observed for example while performing unconstrained model updating on Poisson's ratios while Young's or shear moduli are kept unchanged.

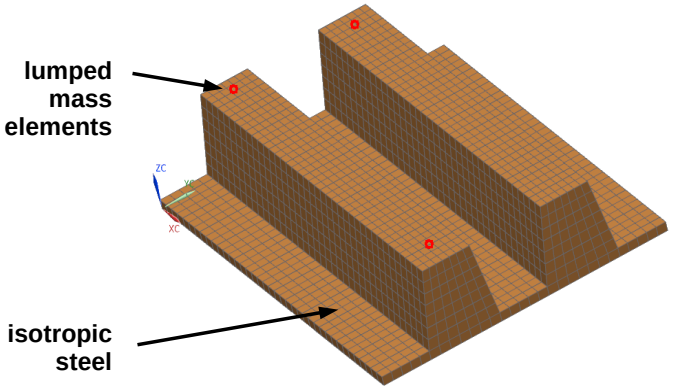

Figure 4.17 – FE model of the steel core

Considering the initial elasticity matrix $[C]$ real and diagonalisable, there exists an invertible matrix $[P]$ such that

$$[C] = [P]\,[\Lambda]\,[P]^{-1}\ , \tag{4.3}$$

where the spectral matrix $[\Lambda]$ is real and diagonal. The solution proposed in this study for guaranteeing the positivity of each of an elasticity matrix's eigenvalues is to recompute an elasticity matrix $\left[C^b\right]$ from

$$\left[C^b\right] = \left([C]^2\right)^{1/2} = \left([P]\,[\Lambda]^2\,[P]^{-1}\right)^{1/2}\ , \tag{4.4}$$

where $[\Lambda]^2$ only has strictly positive values. If $[C]$ is initially stable, then $\left[C^b\right] = [C]$.

This stabilisation process has been suggested to be added in the development of the commercial model-updating software FEMtools™. As performing it only requires low computer resources, stabilising the updated elasticity matrices with Equation (4.4) after each updating cycle would be an efficient way to ensure a proper physical meaning to the updated material properties. In addition to that, this could enable updating anisotropic material's coefficients independently, for what versions prior to 3.7.2 (2014) were limited to global factor scaling. The development team of FEMtools™ has shown an interest to adding this new feature to their next versions.

Definitions of the updated parameters

Amongst all the studied FE models, the most relevant ones for the current analysis have been selected and shown in Figures 4.18 to 4.21, where labels "G" and "T" refer to the "potted" and "impregnated" families, respectively. The detail of all the tested modelling possibilities is given in Appendix A.5. The available updating parameters are listed in white on a green background in the figures, where **TK** is the thickness, **NSM** the non-structural mass and **RHO** the density. The labels **ISO** and **ORTHO** refer to the respective elastic parameter sets $\{E, \nu\}$ and $\{E_x, E_y, E_z, G_{yz}, G_{zx}, G_{xy}\}$, and **KXYZ** to the values $\{K_x, K_y, K_z\}$ of stiffness elements. Note that the structure is meshed with either tetrahedral or cuboid elements, which has negligible influence on its dynamic behaviour. A case

specifying "all" updating parameters actually considers only the parameters defined in the corresponding figure. Also, a 2-D coating mesh shares the associated solid body's nodes. The main observations are summed up and adapted to modelling guidelines in paragraphs 4.3.2.1 and 4.3.2.2.

Specificities:

- all 3D
- teeth adjacent to the winding edges (no resin between them)

Updating parameters:

- all

Results:

- $N_{mp} = 3$ and $\overline{|\Delta f|} = 0.12\%$

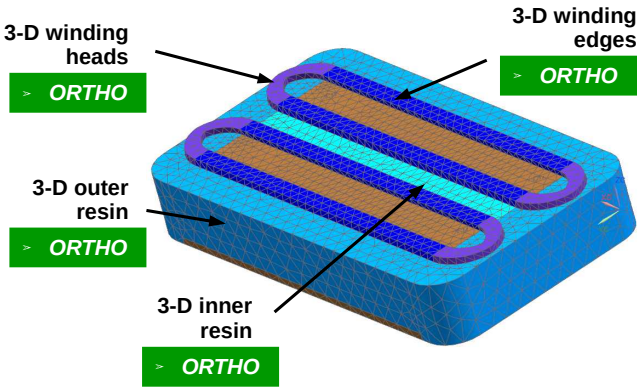

Figure 4.18 – FEM T9 - "potted" family

Specificities:

- each zone is characterised by a single set of elastic properties (e.g. winding heads and neighbouring resin)
- representative densities conserved as in FEM T9 (not updated)

Updating parameters:

- all

Results:

- $N_{mp} = 3$ and $\overline{|\Delta f|} = 0.4\%$

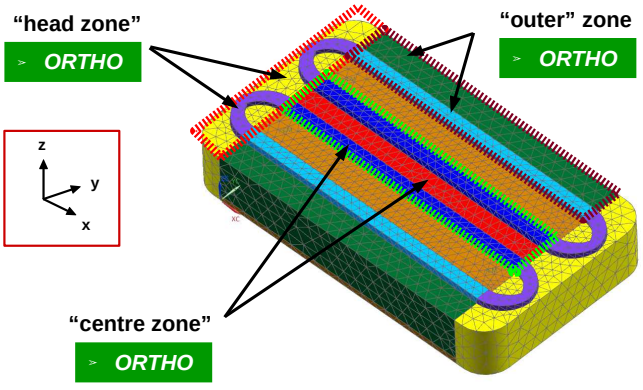

Figure 4.19 – FEM T10 - "potted" family

Specificities:
- the meshes of winding edges and teeth are separated with a 3-D mesh

Updating parameters:
- all

Results:
- $N_{mp} = 3$ and $\overline{|\Delta f|} = 0.39\%$

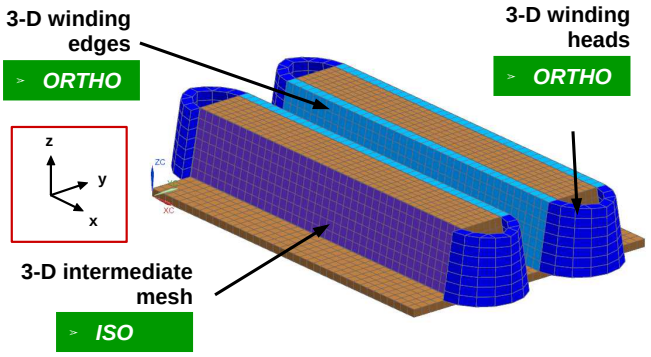

Figure 4.20 – FEM G9 (adapted view) - "impregnated" family

Specificities:
- same as FEM G9

Updating parameters:
- all
- constraint: constant total winding mass

Results:
- $N_{mp} = 3$ and $\overline{|\Delta f|} = 0.10\%$

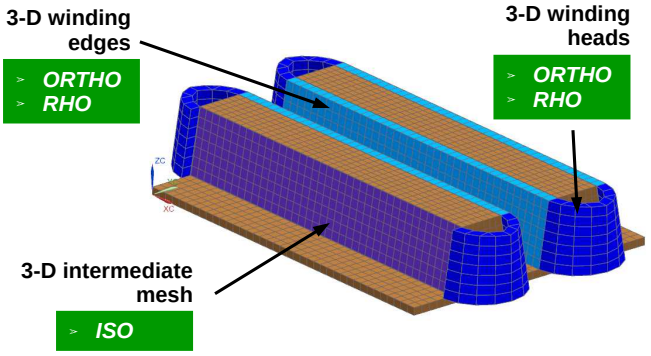

Figure 4.21 – FEM G10 (adapted view) - "impregnated" family

4.3.2.1/ COMMENTS AND RESULTS FOR POTTED SAMPLES (EXCEPT P63)

As it has been explained in Subsection 4.3.1, many of the modes extracted for the samples P1, P2, P3 and P4 were associated to deformed shapes of poor cleanness, which led to overall low MAC values in the updating processes' correlation stages. Specifically focused on the mode PT1 (i.e. ensuring lowest frequency discrepancy for this mode during the updating process), the comparison of the proposed configurations brought the models FEM T9 and FEM T10 under the spotlight as they showed the lowest average values $\overline{\Delta f}$.

The two models differ by their definitions of the windings-resin interaction. For FEM T9, the windings and the resin are considered having a clear interface, modelled by elastic property changes. On the contrary, FEM T10 represents a combined homogeneous behaviour for modelling loose windings and resin between the copper wires, where only the initial mass distributions are conserved.

The modelling guidelines for potted samples with hand-made windings resulting from this analysis are listed as following:

- the resin and the windings need to be modelled by representative volumes and masses instead of equivalent coating meshes or tooth properties;
- considering loose windings with inter-penetrated resin requires representing homogeneous orthotropic zones instead of both windings and resin volumes.

4.3.2.2/ COMMENTS AND RESULTS FOR IMPREGNATED SAMPLES

Benefiting from overall clean experimental mode shapes for samples P5 and P6, almost all the proposed configurations of impregnated samples enabled to recreate Figure 4.16's three outlined critical modes after updating. However, the localisation of the resin and thus its influence on the sample's behaviour is trickier to determine. Specifically focused on the mode PG1, the models FEM G9 and FEM G10 show the lowest $\overline{\Delta f}$ values after updating.

In the light of the presented results, the following modelling guidelines are proposed for impregnated samples:

- the windings should be represented by three-dimensional orthotropic meshes;
- the winding heads need to be included with representative geometry instead of an equivalent coating mesh;
- the total mass of the windings has to be respected;
- the meshes should not be merged to the tooth edges (i.e. no tight contact);
- the resin ought to be modelled with three-dimensional elements between the teeth and the windings.

Eventually, representing windings with detailed individual wires has been tested in none of the considered FE models due to the large number of DOFs this choice would have led to. The good accuracy of the selected four updated models compared to the experimental modal bases confirms the validity of homogeneous representative volumes, and thus suggests adding this modelling guideline to the lists of both families.

The possibility to model windings with equivalent elastic properties computed with Chapter 3's identification methods could also be discussed here:

- The fact that some of the windings are home-made complicates the identification of a representative unit cell to express the periodicity in the structure.
- The research of effective modelling guidelines in both subsections 4.3.2 and 4.3.3 involve model updating procedures that need to be performed independently of the initial elastic property values.
- Identifying equivalent elastic properties would require validation from experimental data on the windings alone, which has not been tested in this thesis. Other remarks about the dependencies of the stator's modes to the windings' properties are given in Subsection 2.3.2.

4.3.3/ TEMPERATURE DEPENDENCY

After selecting representative models, the variability of the material properties is analysed with respect to temperature. This stage is relevant as the motor temperature varies while functioning, and the material properties of the polymers used as resins show notable dependencies towards temperature and time. The principle of this study is the same as in Subsection 4.3.2: for each temperature and each sample, the selected FE model is updated with the corresponding experimental modal basis. For minimising variations, the updated material properties for a given temperature are considered as initial parameter values for the next temperature step. Also, for samples P5 and P6, the material properties of the windings are considered constant: only the resin properties are updated with respect to temperature changes.

For each sample family, two FE models have been selected in Subsection 4.3.2. This subsection however focuses on only one of them, namely FEM T10 (elastic zones) for samples P1, P2, P3 and P4, and FEM G9 (identical densities in winding heads and edges) for samples P5 and P6. This choice is made for a better representativeness of real conditions [viii]; the corresponding illustrations are recalled in Figure 4.22 with the appropriate direction indications. The relative evolution curves of the updated parameters with respect to temperature are plotted in Figures 4.23 to 4.32, on pages 141 to 144. The evolutions are expressed as relative ratios in comparison to the initial values at 25°C (detailed as "init" in the legends).

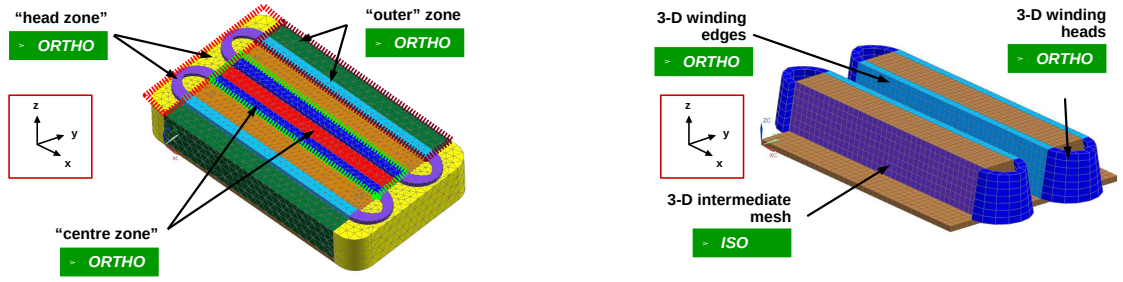

(a) For samples P1, P2, P3 and P4

(b) For samples P5 and P6

Figure 4.22 – Selected FE models

For each sample, the objective is to identify the relation between the parameter variations and the evolution of the corresponding resin's storage modulus. Therefore, the evolution of the corresponding resin's storage modulus is added to each case in comparison to the simulated values. However, the experimental data describing the resin's properties (see Appendix A.3) are only available at 1 Hz, which has to be taken into account as the polymers have a frequency-dependent behaviour. Therefore, anticipating from the studies detailed in Chapter 5, the behaviour of every resin is extrapolated at 1,000 Hz (in order to approximate the critical modes' frequencies) with the aid of the expression:

$$\log\left(f_{\eta\_max}\right) = 0.4054 \cdot T_0 - 32.316\ ,$$

viii. The second samples have been also considered for this study but showed poorer updating possibilities at higher temperatures, and are therefore discarded for the rest of this chapter.

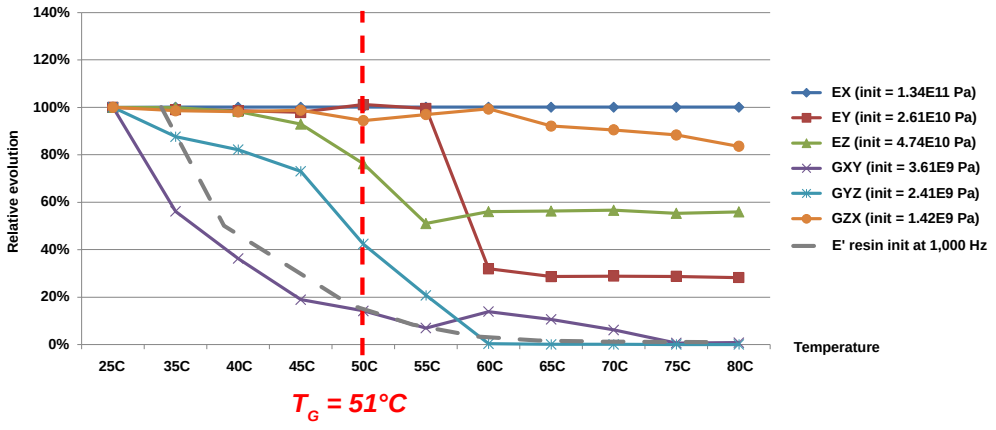

Figure 4.23 – Evolution curves of updated material properties for sample P1 (centre zone)

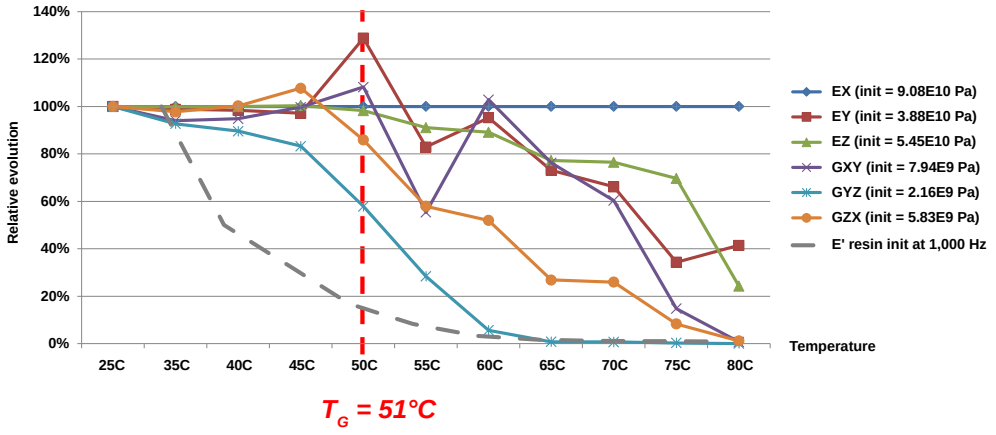

Figure 4.24 – Evolution curves of updated material properties for sample P1 (head zone)

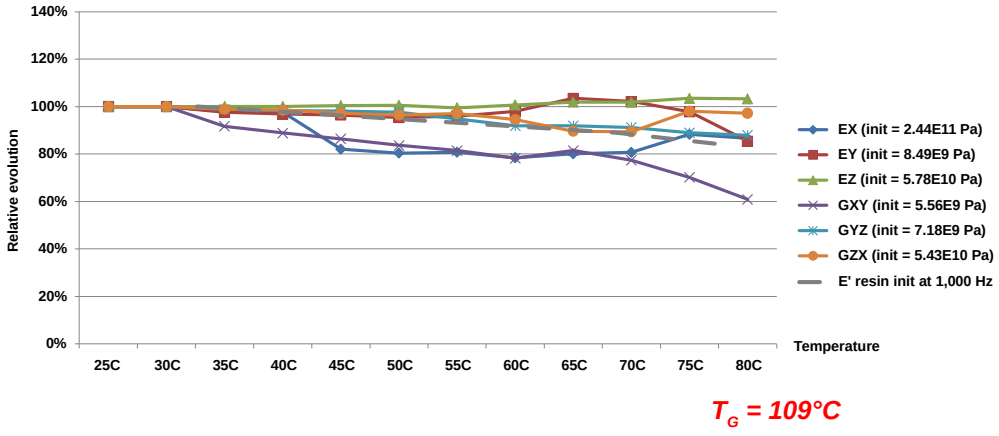

Figure 4.25 – Evolution curves of updated material properties for sample P2 (centre zone)

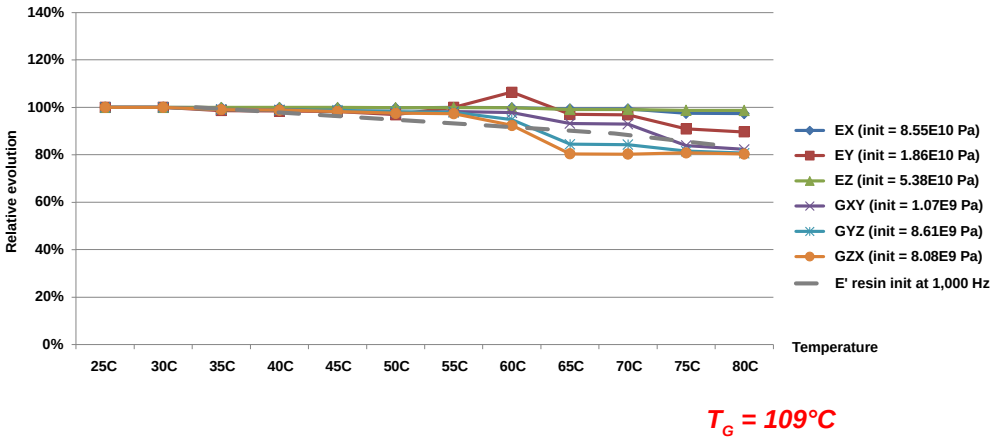

Figure 4.26 – Evolution curves of updated material properties for sample P2 (head zone)

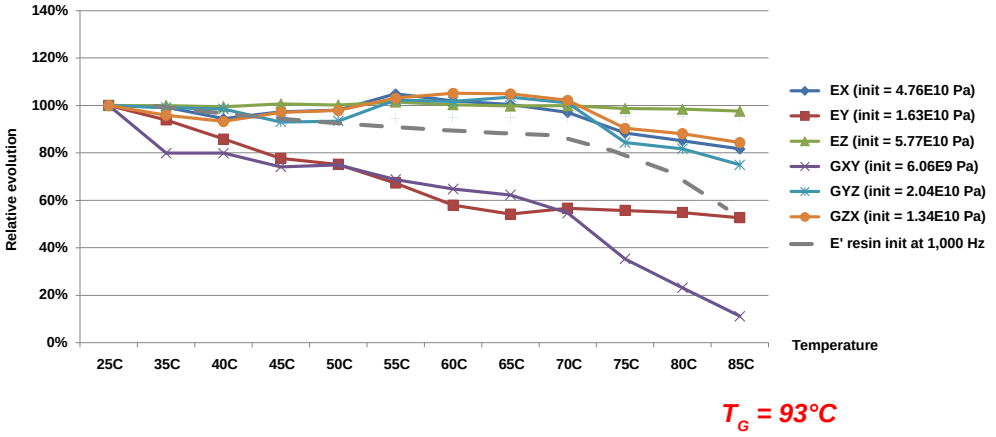

Figure 4.27 – Evolution curves of updated material properties for sample P3 (centre zone)

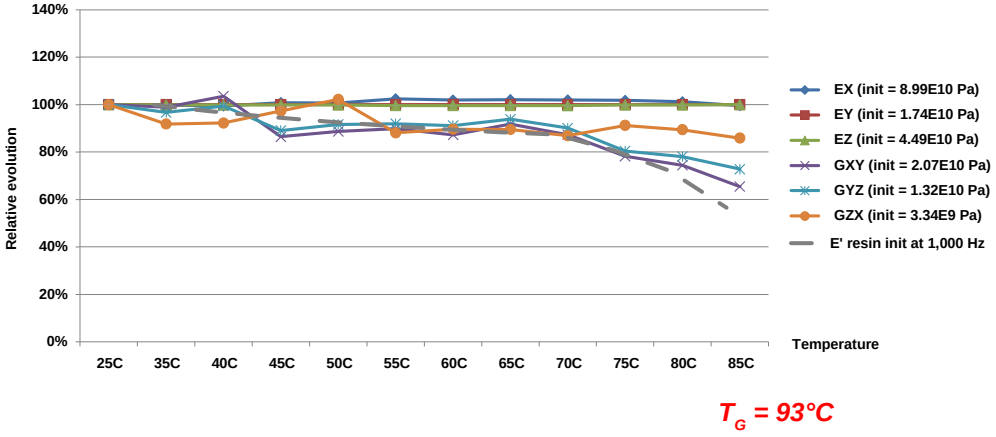

Figure 4.28 – Evolution curves of updated material properties for sample P3 (head zone)

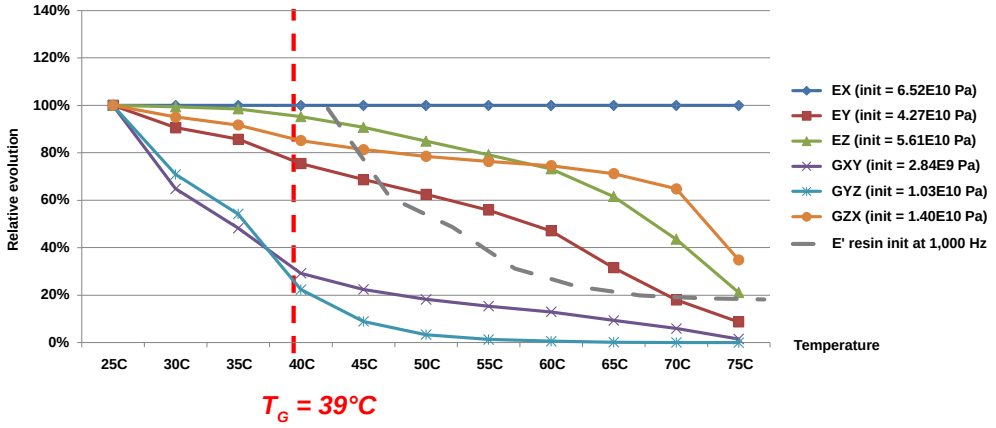

Figure 4.29 – Evolution curves of updated material properties for sample P4 (centre zone)

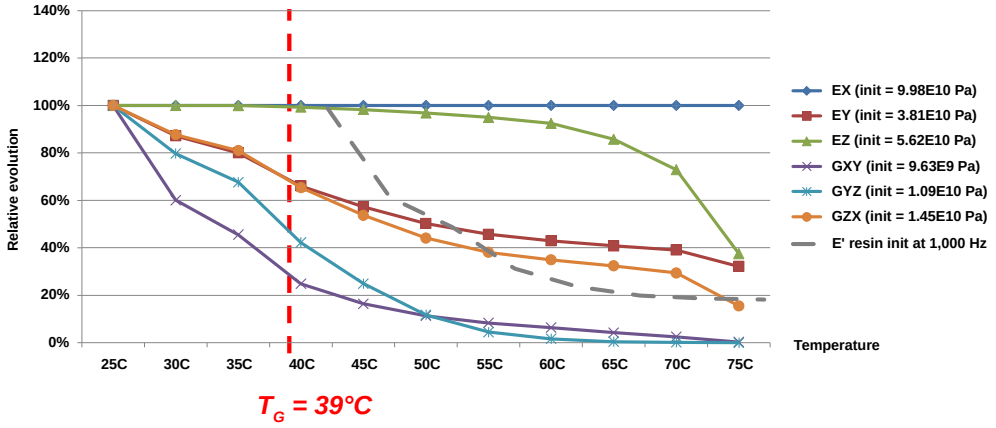

Figure 4.30 – Evolution curves of updated material properties for sample P4 (head zone)

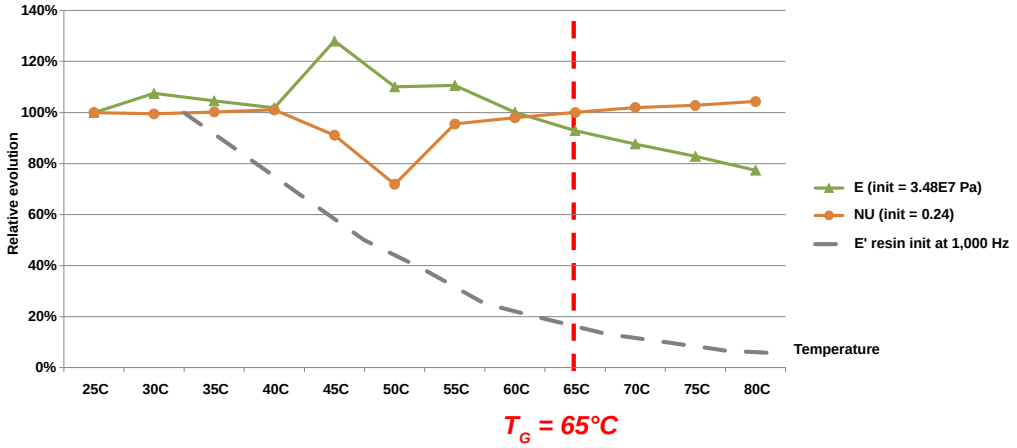

Figure 4.31 – Evolution curves of updated material properties for sample P5

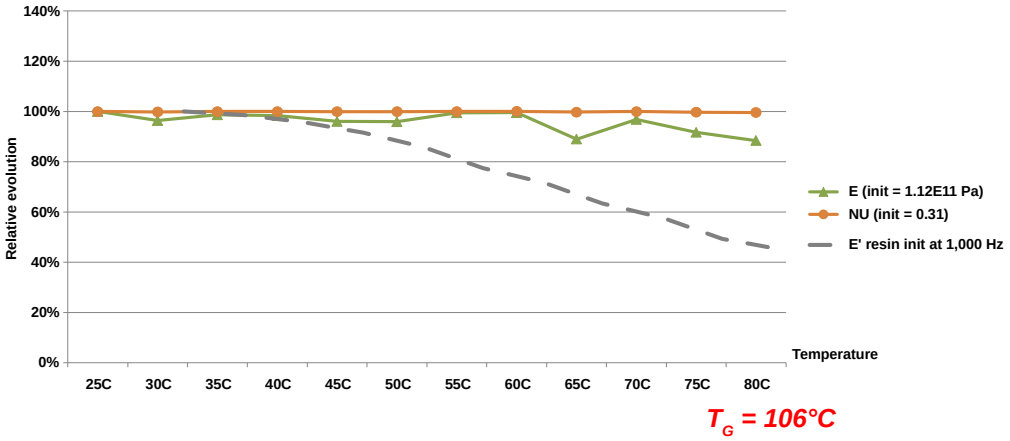

Figure 4.32 – Evolution curves of updated material properties for sample P6

where f_{η_max} and T_0 characterise the resin at a specific frequency and temperature, respectively. Considering a frequency shift from 1 Hz to 1,000 Hz leads to

$$\log(1,000) - \log(1) = (0.4054 \cdot T_{1,000} - 32.316) - (0.4054 \cdot T_1 - 32.316) \ ,$$

which is equivalent to the temperature shift

$$T_{1,000} - T_1 = \frac{\log(1,000) - \log(1)}{0.4054} \approx +7.4°\text{C}.$$

Translating the temperature evolutions measured at 1 Hz by +7.4°C thus gives a more accurate idea of the resin's behaviour at 1,000 Hz. The corresponding corrected evolutions of the resin's elasticity modulus are plotted in dashed grey curves for each case. Eventually, the elastic parameters of the "outer zone" are not shown for the cases P1 to P4 (though they are still updated), as they have no equivalent in the global stator structure.

As it can be observed in the evolution curves associated to samples P1 and P5, some updated values happen to increase while the temperature increases, although the Young's modulus value of every resin exhibits an opposite behaviour. For sample P1, this is explained by the fact that the natures of the paired modes are not identical at all temperature steps. Some parameters are updated according to the influence they have on the paired natural frequencies (see Subsection 1.4.3): if a given mode is not paired at the next temperature step (e.g. too low MAC value or too poor quality to be extracted from measurement data), then the sensitivity values can vary importantly, and thus explain the different updated parameters.

The explanation of the changes observed for P5 is somehow different. Analysing the experimental FRFs from which the modes have been extracted shows the dependency of PG1 mode's frequency (see Figure 4.16) towards temperature. As it can be seen in Figure 4.33, zooming on the corresponding acceleration peak in the FRF curves exhibits two distinct maxima (approximately distant from 100 Hz) whose magnitudes change with respect to the temperature. At low temperatures, the lower-frequency maximum is significantly higher than the other (hence the term of "main" mode in Figure 4.33), and vice-versa. At some points even, there is only one maximum visible. Therefore, even though

both modes are extracted whenever possible (and always show MAC values near 100% when compared to each other), the updating process selects only one of them to pair it with its simulated equivalent. This phenomenon is actually the cause of the abrupt parameter variations observed in Figure 4.31 for the sample P5, as the paired mode changes between 40°C and 45°C.

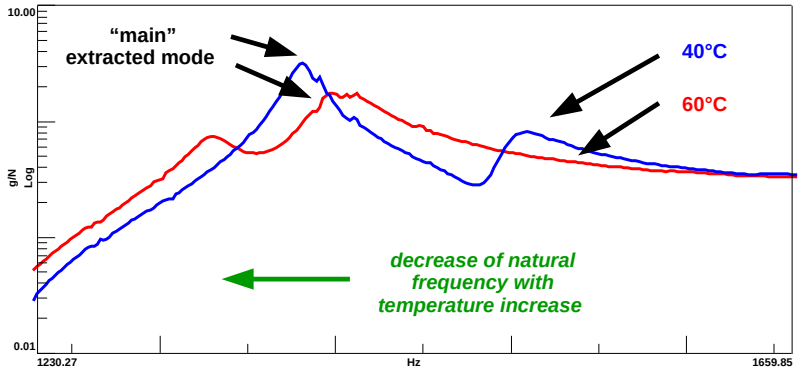

Figure 4.33 – Temperature-dependency of the first torsion mode, for sample P5

4.3.3.1/ COMMENTS AND RESULTS

The analysis presented in this subsection has outlined some interesting results. They are listed as following.

- Figures 4.23 to 4.32 clearly show that the resin's elastic properties and their variations with respect to temperature have a non-negligible influence on the samples' modal behaviours.
- This influence is significantly higher for potted samples than for impregnated samples, as the shapes of the parameter changes for samples P1 to P4 are globally in better agreement with the resin's variations than for P5 and P6.
- In particular, the most important variations are observed on the samples for which the resin's glass-transition temperature is within the temperature range [25°C; 80°C] (P1, P4 and P5), whereas the other samples (P2, P3 and P6) exhibit relatively low parameter variations.
- The parameter variations are difficultly explained by the resin's behaviour for samples P5 and P6, although the final correlation values after updating the corresponding FE models were as satisfactory as for the other samples.
- For the "potted" samples P1 to P4, parameters GXY and GYZ (associated to the shear moduli of same names) show the greatest variations. This is explained by the fact that mode PT1 is particularly sensitive to these two parameters: as the associated natural frequency varies, so do these parameters. This observation can be compared to the remarks of Subsection 2.3.2, outlining that the entire stator's torsion mode was sensitive to $G_{\theta z}$. For the presented samples, the equivalent parameter is G_{xy}, which thus shows an agreement between the two studies.

4.3.4/ SPECIAL CASE: SAMPLE P63

Although some interesting temperature-depending tendencies were observed for the samples P1 to P4, it can not be denied that predicting the evolutions of the equivalent elastic parameters from only the resin's storage modulus measurements is a tricky task. Noticing that hand-made windings are actually in contact from one tooth to the other raises the questions of the existence and the influence of a possible stiffening effect of the copper wires on the samples' mechanical behaviour. As it has been explained in previous sections, this stiffening effect is commonly assumed negligible and therefore suggests to account only for the copper's mass in finite-element simulations. At the light of the results from Subsections 4.3.2 and 4.3.3, this assumption is now tested with the analysis on the last sample, P63. This sample is the one whose geometry is closest to the complete stator's.

Figures 4.6 and 4.10 show that unlike the other potted samples, the windings are clearly separated in P63. Repeating the operations detailed in Subsections 4.3.2 for sample P63 leads to the optimum FE model illustrated in Figure 4.34, with which all 4 critical modes are paired after updating, for an average frequency discrepancy $\overline{\Delta f} = 0.24\%$ at room temperature.

Unlike for the other potted samples, the experimental analyses on P63 yielded good-quality extracted modes and most interestingly clean deformed shapes for the bending mode PT4 (see Figure 4.15). Although the masses and resin properties are identical in both samples P3 and P63, the torsion mode PT1 and bending mode PT4 have been measured in average (for all temperatures) at 8% and 11% lower frequencies in P63 than in P3. This is a first indicator of stiffness changes induced by the two winding types.

The new FE model illustrated in Figure 4.34 most simply represents the sample as it is, with one single isotropic material for all the resin. The material properties at 25°C are detailed in Table 4.3. It can be noted that although updated, the value of the resin's representative Young's modulus is identical to that of experimental measurements performed on this resin (see Chapter 5 for details).

The temperature analysis presented in Subsection 4.3.3 is reapplied on sample P63, where only the resin's representative Young's modulus is updated through temperature changes. The resulting relative evolution curve is shown in Figure 4.35. As before, the relative evolution measured for the corresponding real resin (see Appendix A.3) is expressed at 1,000 Hz by a temperature shift of $+7.4$°C, and is plotted as a dashed grey curve.

As it can be seen in the figure, the evolution curves relative to simulated and measured data are in fair agreement. This confirms the validity of the proposed FE model for this sample and also shows that the winding properties can be considered as temperature-independent. Therefore, applying the relative changes measured on the sample (at 1 Hz) to the resin's Young's modulus of the FE model is, for this case, fairly predictive for simulating the global sample's dynamic behaviour.

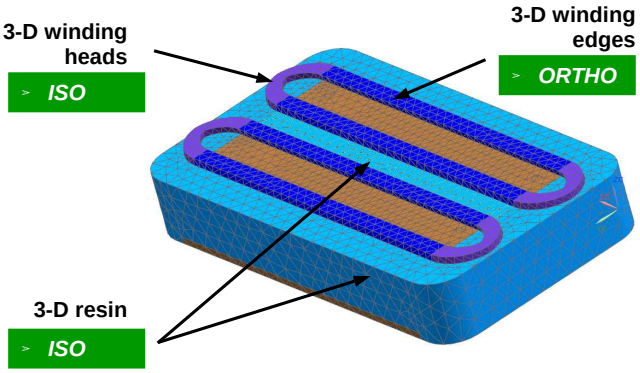

Figure 4.34 – FEM T11

	teeth	resin	winding heads	winding edges
$\tilde{E}_x$ [GPa]	200	4.02	101	96.8
$\tilde{E}_y$ [GPa]				122
$\tilde{E}_z$ [GPa]				105
$\tilde{G}_{zy}$ [GPa]	-	-	-	35.9
$\tilde{G}_{zx}$ [GPa]				61.3
$\tilde{G}_{xy}$ [GPa]				86.5
$\tilde{\nu}_{yz}$ [−]	0.24	0.33	0.30	0.30
$\tilde{\nu}_{xz}$ [−]				0.28
$\tilde{\nu}_{xy}$ [−]				0.30
$\tilde{\rho}$ [kg m^{-3}]	7,770	2,050	4,700	4,700

Table 4.3 – Material properties of sample P63 at 25°C

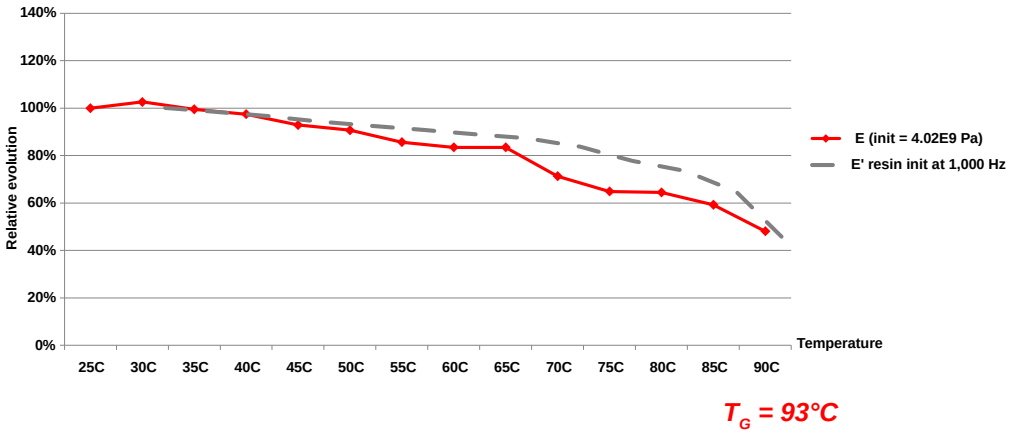

Figure 4.35 – Evolution curves of updated material properties for sample P63

As this sample is the most representative of the entire stator's geometry, preferring FEM T11 for performing FE simulations needs to be included in the previous modelling guidelines:

- for modelling the stator of a real switched-reluctance machine, the windings ought to be modelled with three-dimensional homogeneous meshes with a similar geometry as the real ones;
- the resin needs to be modelled as close as possible from the real conditions, in this case with a single isotropic material for all the zones;
- the windings can be considered as temperature-independent;
- the relative evolution of the resin's storage modulus measured at 1 Hz can be used to predict the value of the resin's representative Young's modulus in the FE model.

INTERMEDIATE CONCLUSION

This chapter has presented an experimental campaign on eight stator samples with windings and resin, and has investigated the possibilities of modelling them with modal finite-element simulations and take into account the influence of temperature variations. Distinguishing two families of electric machine technologies, namely with "potted" or "impregnated" stators, this study has first selected appropriate models amongst a series of possible choices, and has then analysed the evolutions of modelling parameters with respect to temperature changes in the samples by the means of model updating procedures. Resulting from these sections, guidelines have been proposed for improving modelling techniques of entire stators including windings and resin, with a particular emphasis on encapsulated switched-reluctance machines.

The main modelling guidelines are recalled hereafter:

- the windings should be represented with equivalent homogeneous material properties instead of detailed meshes of the wires;
- discarding pieces (e.g. windings) from the model and representing them with equivalent properties such as additional coating elements has been proven detrimental to the overall accuracy;
- the mass of each piece needs to be integrally modelled;
- the windings can be considered as temperature-independent;
- in a nutshell, establishing a representative FE mesh of an entire stator ought to be done as close as possible from the pieces' real geometries, including one single zone of isotropic material for representing the potting resin. The values of the corresponding Young's modulus can be predicted from the relative evolution of the resin's storage modulus with respect to temperature.

This chapter has also shown that the samples composed of hand-made windings yielded a significantly poorer quality in the experimental modal analyses. Especially, the bending mode most representative of the entire stator's ovalisation behaviour was only exploitable when measured on samples with industrial windings. This observation therefore invalidates the assumption that the windings' only contribution in the global stator's

behaviour was of mass, and suggests to consider both stiffness and mass effects in FE simulations.

The analyses on impregnated samples have also led to several major modelling guidelines. However, associating on-tooth (i.e. SRM-like) windings with impregnation is rarely applied in the industry at the moment but may be rapidly expanding with the current interest for segmented stators which require this kind of combination. For thinly-toothed stators such as standard asynchronous AC machines though, this knowledge could be strengthened by further studies on adapted samples.

Property evolutions of each resin have been used as reference curves in comparison to the updated parameters in the temperature analyses. The transposition proposed in order to approximate the behaviour at 1,000 Hz instead of 1 Hz can be discussed as the temperature shift factor is associated to only one of the considered resins. However, this approach has reduced the possible discrepancies to the resin's real behaviour and has enabled sensible observations and the suggestion of important guidelines on the most representative sample. Determining shift factors adapted to each of the other resins would require experimental and numerical applications as described in Chapter 5, but goes beyond the frame of this study.

Eventually, the fact that the resin's frequency- and temperature-dependent tendency is responsible for important changes in the behaviour of the studied assemblies suggests to put an emphasis on viscoelastic phenomena. Chapter 5 will detail a comprehensive analysis on the resin properties and a concrete application for noise reduction in electric machines. This chapter has been placed in the appendices for confidentiality reasons.

5

Viscoelastic phenomena in electric motors: finite-element modelling approaches and noise-reduction capacities

This entire chapter has been removed from the initial document for confidentiality reasons.

CONCLUSIONS

Funded by the company Vibratec and supervised by the Femto-S.T. Institute, this thesis has been focused on the mechanical behaviour of electric machines. In particular, the main objective was to develop efficient modelling techniques for performing finite-element simulations on electric motor stators. To achieve this, the work has been divided into five chapters, whose main contributions are summarised hereafter.

While the first chapter introduced the necessary theoretical notions for the applications, the content of the second chapter concerned the state-of-the-art knowledge about the simulation and the prediction of the dynamic behaviour of an electric machine stator. Various assumptions and practical notions have been presented. In addition, sensitivity analyses have been performed on the elastic parameters of a stator's finite-element model, and outlined that the critical cylinder modes were particularly sensitive to the equivalent material properties of the resin between the teeth and the magnetic core's yoke. Also, the impacts of stiffness changes in the connection between the frame and the magnetic core of an electric motor stator have been investigated, and suggested to adopt a simple, merged interface for best representativeness without experimental data.

Focused on the magnetic cores only, the third chapter detailed the development of two methods of equivalent material property identification applied for multi-layered laminated structures subjected to pre-stress and friction. Most importantly, this chapter showed that the ability of an equivalent material property set to recreate the dynamic behaviour of the initial heterogeneous structure is affected by the definition of shear and the existence of couplings between tension-compression and shear. While laminated structures require "sliding shear" identification scenarios, pre-stressed homogeneous bodies are best modelled with "transverse shear" moduli. The effectiveness of the developed "Orthotropic" method has been compared to reference numerical homogenisation results from the literature. Without need of time-consuming updating procedures, the direct applications to a concrete magnetic core's finite-element model led to a satisfying accuracy in the simulation of critical ovalisation modes when compared to experimental modal data measured on an industrial structure.

Specifically oriented towards windings and insulating resins, the fourth chapter dealt with thorough experimental analyses on core samples and the determination of sensible guidelines for representative finite-element models. With a distinction of two major families of electric machines, appropriate finite-element models have been selected, with the aid of which the evolutions of modelling parameters have been analysed with respect to temperature changes. Amongst other guidelines, the resin can be modelled in the entire stator with the properties measured from a single polymer rod. The value of the corresponding Young's modulus can be predicted from the relative evolution of the resin's storage modulus with respect to temperature.

At last, concentrated on the resin's viscoelastic behaviour, the fifth chapter (removed from

the document for confidentiality reasons) presented a comprehensive methodology for the computation of optimised properties in order to minimise the noise emitted by a complete electric machine. The combination of viscoelastic property tuning with representative electromagnetic and structural finite-element simulations enabled to decrease up to 10 dB of the peak radiated power values in a switched-reluctance motor. In further steps, including static and dynamic eccentricities in the motor showed a substantial enrichment of the electromagnetic excitation spectra, which led to significantly strengthened overall noise emissions. Although the same viscoelastic property tuning as for the motor without eccentricities allowed to mitigate this detrimental acoustic level increase, this study outlined the necessity to prevent eccentricities from occurring in electric machines.

Main modelling guidelines

Based on the results presented in all five chapters, the main guidelines for creating accurate finite-element models of electric machine stators are summarised hereafter:

- Without specific experimental need to tell otherwise, the frame and the magnetic core ought to be modelled with merged interface nodes. This choice seems the best compromise between the uncertainties about the phenomena occurring at the interface and the computation costs related to the number of degrees of freedom in the model.
- Under rough assumptions such as modelling the magnetic core with a single zone, numerical and/or analytical methods such as "PEMAT" or the well-known "rule of mixtures" (see Subsection 3.2.1) are fastest to apply as they do not require post-processing the results.
- However, none are capable of accounting for external perturbations and specific zoning of the structure. For such requirements, using either the "Ortho" or "Aniso" method proposed in Chapter 3 would be more appropriate. Judging from the relatively slight efforts required with current finite-element meshing programmes for this option, zoning the structure and determining orthotropic material properties as explained in Section 3.2 seems to be the best compromise between representativeness and time needed for the preparation of the simulations.
- As for the magnetic core, the windings should be represented with equivalent homogeneous material properties instead of detailed meshes of the wires. Both stiffness and mass properties in the windings have influence on the stator's overall behaviour.
- Each piece and its integral mass need to be modelled in the stator.
- Finally, for performing a dynamic response simulation involving viscoelastic materials such as resins, two cases can be distinguished:
  - In the considered frequency/temperature range, the variations of the material properties are assumed negligible. In this case, the materials can be modelled with non-viscoelastic properties (i.e. frequency- and temperature-independent), and the response can be computed with modal superposition algorithms.

– In the considered frequency/temperature range, the variations of the material properties are assumed significant. In this case, the materials have to be modelled with frequency- and temperature-dependent properties, and the response needs be computed with direct resolution systems only. Although more accurate than the former one, this case may require a considerably longer time to be solved if no pseudo-modal solutions (see the corresponding discussion in Chapter 5) are adopted.

FUTURE PROSPECTS

Finally, this work presents opportunities for further applications. One of most direct application that could be thought of is a faster and more efficient design of new electric motor and vehicle models. Indeed, the new methods presented in this thesis could alleviate the current needs of experimental data for predicting the dynamic behaviour of a design model accurately. The necessity of manufacturing costly and numerous prototypes could be reduced with more accurate simulations in the design stages of a new machine. In addition to this, the capacity to create accurate models of electric machine stators enables sensible optimisation procedures in the early design stages; combining optimised geometries (e.g. adapted volume for better integration in a car body), electromagnetic performances (e.g. modified tooth shapes for smoothing magnetic flux variations during the rotor's rotation), power supply strategies (e.g. enhanced PWM) and manufacturing processes (e.g. cost reductions) could be assets for producing affordable, reliable, energy-efficient and acoustically attractive machines.

The applied simulations detailed in this thesis could benefit from further experimental analyses such as testing optimised resins in complete stator structures. In particular, it would be interesting to manufacture an "optimised" switched-reluctance machine with the resin properties determined in Chapter 5 and compare experimentally its acoustic emissions with those of the initial device. Possibly, analysing the influence of motor defects other than eccentricities (e.g. rotor misalignment) with both simulations and measurements could help proposing new design guidelines for optimised performances.

Eventually, amongst other currently fast-growing technologies, segmented stators present interesting manufacturing assets, and are composed of several parts with on-tooth windings. Combining these manufacturing assets with the low costs related to switched-reluctance machines' architectures and an acoustically-optimised design with adapted resin properties could lead to affordable and robust technologies for future 100%-electric vehicles such as cars, trains or even airplanes. In a more long-term perspective, future developments and improvements in the domain of composite structures could benefit from more effective modelling tools for three-dimensional heterogeneous structures.

Appendices

A

ADDITIONAL DATA

This appendix chapter gathers some additional data that were not presented in the document's main matter.

A.1/ DEFINITIONS OF STIFFNESS AND MASS MATRICES

Some notions related to elasticity matrix definitions have been defined in Subsection 1.3.1. The relations used to compute a structure's global stiffness and mass matrices are introduced in this section. The entire theory is not to be detailed; more information can be found in [115, 11], on which this section is based. Also, as the details are given for the three-dimensional case, it can be adapted to any type of elements by discarding undesired dimension(s) in the equations and taking into account the contributions of possible additional phenomena (such as bending stiffness).

A.1.1/ STIFFNESS MATRICES

Considering a finite element composed of n DOFs and k nodes, the stiffness matrix $[\mathcal{K}^e]$ (the superscript e refers to this single element) is defined from the principle of virtual works by

$$[\mathcal{K}^e] = \iiint_{\Omega^e} [\mathcal{B}^e]^\intercal \, [C] \, [\mathcal{B}^e] \, \mathrm{d}\Omega \, , \tag{A.1}$$

where Ω^e is the volume of the element, $\mathrm{d}\Omega$ an infinitesimal volume such that $\mathrm{d}\Omega = \mathrm{d}x\mathrm{d}y\mathrm{d}z$, $[C]$ the elasticity matrix of the element's material, and $[\mathcal{B}^e]$ the deformation interpolation matrix which links the deformation tensor to the nodal displacements (u_i, v_i, w_i) with the relation

$$\begin{Bmatrix} \varepsilon_{xx} \\ \varepsilon_{yy} \\ \varepsilon_{zz} \\ 2 \cdot \varepsilon_{yz} \\ 2 \cdot \varepsilon_{zx} \\ 2 \cdot \varepsilon_{xy} \end{Bmatrix} = [\mathcal{B}^e] \begin{Bmatrix} u_1 \\ v_1 \\ w_1 \\ \vdots \\ u_k \\ v_k \\ w_k \end{Bmatrix} . \tag{A.2}$$

The computation of matrix $[\mathcal{K}^e]$ and all the unknown terms in Equation (A.1) is explained hereafter. The displacement field $\{u, v, w\}$ in the element can be described by means of interpolation functions $\mathfrak{N}(x, y, z)$ so that:

$$u(x, y, z) = \sum_{i=1}^{k} \mathfrak{N}_i(x, y, z) \cdot u_i \,, \tag{A.3a}$$

$$v(x, y, z) = \sum_{i=1}^{k} \mathfrak{N}_i(x, y, z) \cdot v_i \tag{A.3b}$$

and

$$z(x, y, z) = \sum_{i=1}^{k} \mathfrak{N}_i(x, y, z) \cdot z_i \,, \tag{A.3c}$$

or in a vectorial form

$$\begin{Bmatrix} u(x, y, z) \\ v(x, y, z) \\ w(x, y, z) \end{Bmatrix} = [\mathcal{N}^e] \begin{Bmatrix} u_1 \\ v_1 \\ w_1 \\ \vdots \\ u_k \\ v_k \\ w_k \end{Bmatrix} \,, \tag{A.4}$$

where u_i, v_i and w_i are the respective displacements on directions x, y and z at node i. The matrix $[\mathcal{N}^e]$ thus associates the interpolation functions to the corresponding displacements. As such functions $\mathfrak{N}_i$ are not straightforward to exhibit in the general case, a reference element composed of n DOFs and k nodes is considered, and the space variables ξ, η and ζ are used to describe the behaviour of the reference element. The reference nodes have for coordinates either -1 or $+1$ in each direction. Then, the k reference interpolation functions $\bar{\mathfrak{N}}_i$ are obtained from Lagrange polynomials, so that $\bar{\mathfrak{N}}_i(\xi, \eta, \zeta) = 1$ at node i and 0 elsewhere. Also, the fact the element is isoparametric enables using identical functions $\mathfrak{N}_i$ and $\bar{\mathfrak{N}}_i$ for each node i. Then, any point of coordinates (x, y, z) on the real element can be associated to a point on the reference element by the transformation expressions

$$x(\xi, \eta, \zeta) = \sum_{i=1}^{k} \bar{\mathfrak{N}}_i(\xi, \eta, \zeta) \cdot x_i \,, \tag{A.5a}$$

$$y(\xi, \eta, \zeta) = \sum_{i=1}^{k} \bar{\mathfrak{N}}_i(\xi, \eta, \zeta) \cdot y_i \tag{A.5b}$$

and

$$z(\xi, \eta, \zeta) = \sum_{i=1}^{k} \bar{\mathfrak{N}}_i(\xi, \eta, \zeta) \cdot z_i \,, \tag{A.5c}$$

where x_i, y_i and z_i are the coordinates of the real nodes and $\bar{\mathfrak{N}}_i$ the interpolation functions of the reference element. The displacement field (u, v, w) in the real element is defined by the same expressions, with respect to variables ξ, η and ζ and from nodal displacements u_i, v_i and w_i. In a vectorial form, this is equivalent to:

$$\begin{Bmatrix} u(\xi,\eta,\zeta) \\ v(\xi,\eta,\zeta) \\ w(\xi,\eta,\zeta) \end{Bmatrix} = \left[\mathcal{N}^e\right] \begin{Bmatrix} u_1 \\ v_1 \\ w_1 \\ \vdots \\ u_k \\ v_k \\ w_k \end{Bmatrix} . \tag{A.6}$$

Then, the deformation interpolation matrix $[\mathcal{B}^e]$ of Equation (A.2) has to be composed from the relations defining strain values ε_{ij}:

$$\varepsilon_{xx}(\xi,\eta,\zeta) = \frac{\partial u}{\partial x}(\xi,\eta,\zeta) = \sum_{i=1}^{k} \frac{\partial \bar{\mathfrak{N}}_i}{\partial x}(\xi,\eta,\zeta) \cdot u_i \ , \tag{A.7a}$$

and omitting the variable dependencies,

$$\varepsilon_{yy} = \frac{\partial v}{\partial y} = \sum_{i=1}^{k} \frac{\partial \bar{\mathfrak{N}}_i}{\partial y} \cdot v_i \ , \tag{A.7b}$$

$$\varepsilon_{zz} = \frac{\partial w}{\partial z} = \sum_{i=1}^{k} \frac{\partial \bar{\mathfrak{N}}_i}{\partial z} \cdot w_i \ , \tag{A.7c}$$

$$2 \cdot \varepsilon_{yz} = \frac{\partial v}{\partial z} + \frac{\partial w}{\partial y} = \sum_{i=1}^{k} \left(\frac{\partial \bar{\mathfrak{N}}_i}{\partial z} \cdot v_i + \frac{\partial \bar{\mathfrak{N}}_i}{\partial y} \cdot w_i \right) \ , \tag{A.7d}$$

$$2 \cdot \varepsilon_{zx} = \frac{\partial w}{\partial x} + \frac{\partial u}{\partial z} = \sum_{i=1}^{k} \left(\frac{\partial \bar{\mathfrak{N}}_i}{\partial x} \cdot w_i + \frac{\partial \bar{\mathfrak{N}}_i}{\partial z} \cdot u_i \right) \tag{A.7e}$$

and

$$2 \cdot \varepsilon_{xy} = \frac{\partial u}{\partial y} + \frac{\partial v}{\partial x} = \sum_{i=1}^{k} \left(\frac{\partial \bar{\mathfrak{N}}_i}{\partial y} \cdot u_i + \frac{\partial \bar{\mathfrak{N}}_i}{\partial x} \cdot v_i \right) \ . \tag{A.7f}$$

However, the displacements and thus the reference interpolation functions have to be expressed with respect to variables x, y and z for the derivatives to be computed in Equations (A.7a) to (A.7f). This is why a jacobian matrix $[J]$ is used to change variables from (ξ, η, ζ) to (x, y, z), such that:

$$\begin{Bmatrix} \frac{\partial \bar{\mathfrak{N}}_i}{\partial \xi} \\ \frac{\partial \bar{\mathfrak{N}}_i}{\partial \eta} \\ \frac{\partial \bar{\mathfrak{N}}_i}{\partial \zeta} \end{Bmatrix} = [J] \begin{Bmatrix} \frac{\partial \bar{\mathfrak{N}}_i}{\partial x} \\ \frac{\partial \bar{\mathfrak{N}}_i}{\partial y} \\ \frac{\partial \bar{\mathfrak{N}}_i}{\partial z} \end{Bmatrix} , \tag{A.8}$$

and where the values in

$$[J] = \begin{bmatrix} \frac{\partial x}{\partial \xi} & \frac{\partial y}{\partial \xi} & \frac{\partial z}{\partial \xi} \\ \frac{\partial x}{\partial \eta} & \frac{\partial y}{\partial \eta} & \frac{\partial z}{\partial \eta} \\ \frac{\partial x}{\partial \zeta} & \frac{\partial y}{\partial \zeta} & \frac{\partial z}{\partial \zeta} \end{bmatrix} \tag{A.9}$$

are computed from Equations (A.5a) to (A.5c). It seems interesting to note that the terms in $[J]$ only depend from the coordinates of the real element, and that its determinant does not equal 0 unless the real element is distorted [ix]. Then, reversing System (A.8) yields:

$$\begin{Bmatrix} \frac{\partial \bar{\mathfrak{N}}_i}{\partial x} \\ \frac{\partial \bar{\mathfrak{N}}_i}{\partial y} \\ \frac{\partial \bar{\mathfrak{N}}_i}{\partial z} \end{Bmatrix} = [J]^{-1} \begin{Bmatrix} \frac{\partial \bar{\mathfrak{N}}_i}{\partial \xi} \\ \frac{\partial \bar{\mathfrak{N}}_i}{\partial \eta} \\ \frac{\partial \bar{\mathfrak{N}}_i}{\partial \zeta} \end{Bmatrix} , \tag{A.10}$$

from what matrix $[\mathcal{B}^e]$ can be computed entirely.

Eventually, the stiffness matrix $[\mathcal{K}^e]$ of the real element, previously introduced in Equation (A.1), can be now computed from the reference element, such that:

$$[\mathcal{K}^e] = \det([J]) \cdot \int_{-1}^{1} \int_{-1}^{1} \int_{-1}^{1} [\mathcal{B}^e]^\intercal [C] [\mathcal{B}^e] \, \mathrm{d}\xi \mathrm{d}\eta \mathrm{d}\zeta \, . \tag{A.11}$$

For an N-DOF structure composed of Q elements, the assembly process starts by creating Q matrices of size $N \times N$, called $[\mathcal{K}^g]_i$. Each of them is filled with the values of the corresponding element stiffness matrix $[\mathcal{K}^e]_i$ (placed in $[\mathcal{K}^g]_i$ according to the global DOFs), and 0 elsewhere. The structure's global stiffness matrix $[\mathcal{K}]$ is then assembled by:

$$[\mathcal{K}] = \sum_{i=1}^{Q} [\mathcal{K}^g]_i \, . \tag{A.12}$$

ix. Geometric criteria exist for finite-element solvers, but will not be detailed here.

A.1.2/ MASS MATRICES

Defining mass matrices is simpler. The equation defining the mass matrix $[\mathcal{M}^e]$ of the same element is

$$[\mathcal{M}^e] = \det([J]) \cdot \rho \cdot \int_{-1}^{1}\int_{-1}^{1}\int_{-1}^{1} \left[\bar{\mathcal{N}}^e\right]^{\mathsf{T}} \left[\bar{\mathcal{N}}^e\right] \mathrm{d}\xi \mathrm{d}\eta \mathrm{d}\zeta \,, \tag{A.13}$$

where the interpolation matrix $\left[\bar{\mathcal{N}}^e\right]$ has been introduced in Equation (A.6), and where ρ represents the element's density. The assembly process for computing the global mass matrix $[\mathcal{M}]$ is identical as for $[\mathcal{K}]$.

A.2/ DRAFT OF THE HOMOGENEOUS STEEL STATOR SAMPLE

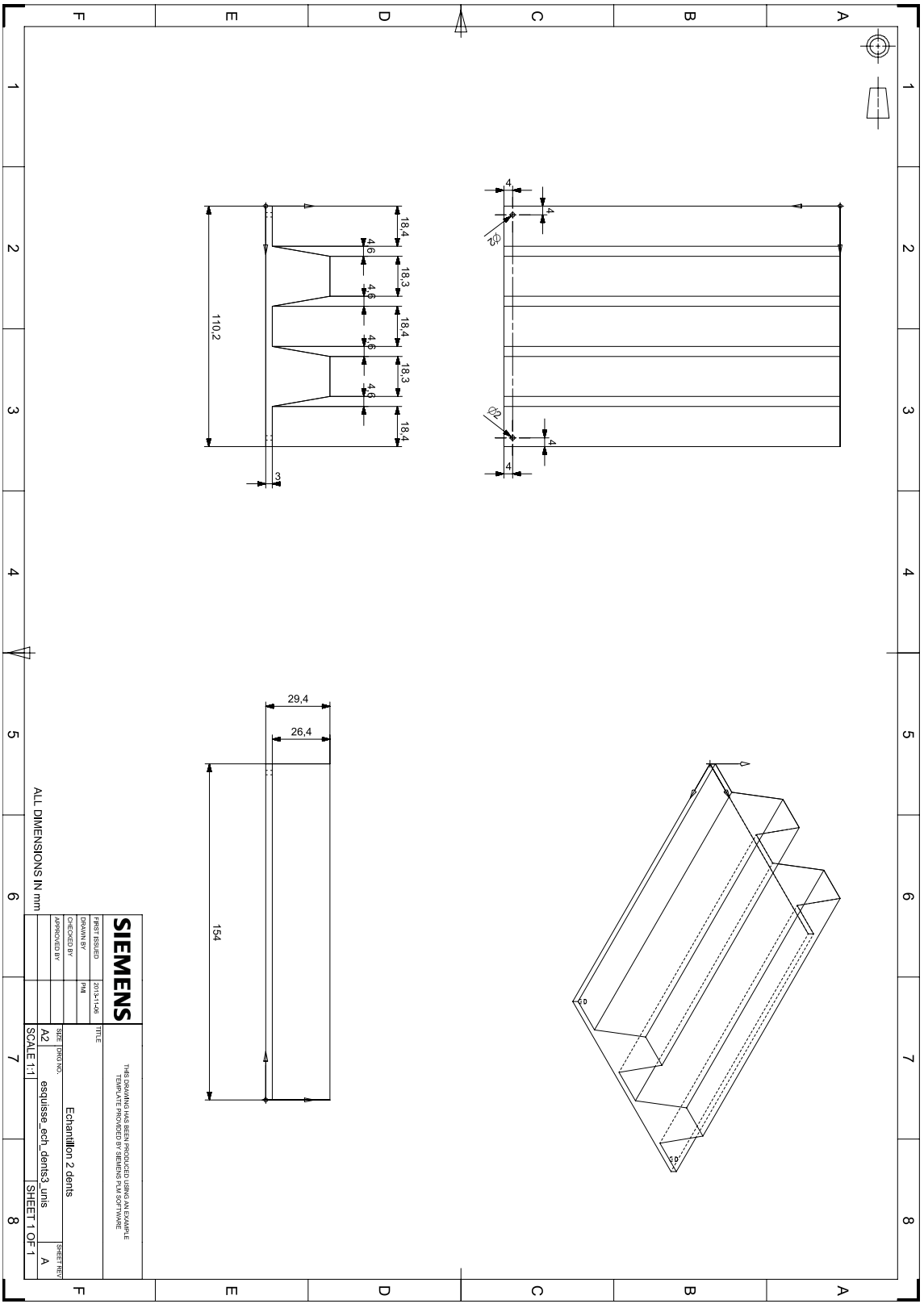

A.3/ DMA CURVES OF INITIAL VON ROLL'S RESIN SAMPLES

The viscoelastic properties of the resins used in Section 4.2's experimental analyses have been measured for an excitation frequency of 1 Hz by the means of a Dynamic Mechanical Analyser (DMA) at Von Roll Company (Meyzieu, France). The experimental curves are associated to their respective design references and to the resin labels defined in Section 4.2, and are shown in Subsections A.3.1 and A.3.2. On each curve, the so-called "Modulus" is related to the material's Young's modulus by a constant factor.

A.3.1/ PROPERTIES OF THE RESINS USED FOR SAMPLES P1 TO P4

P3 - ref. 15350 NA

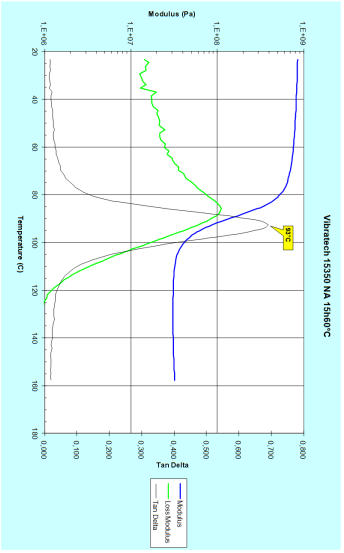

P1 - ref. 15225

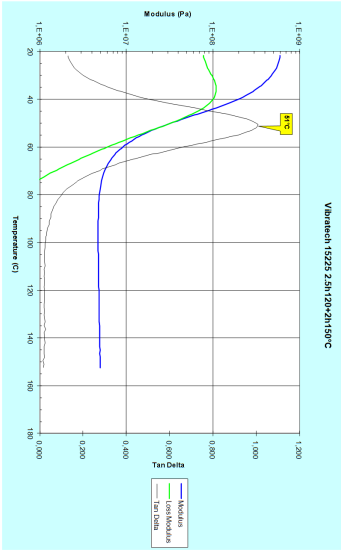

P4 - ref. 15350 FL

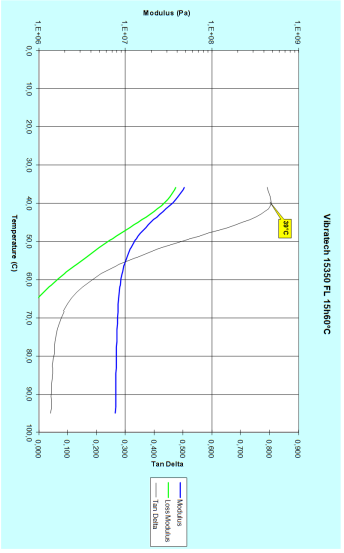

P2 - ref. 15244

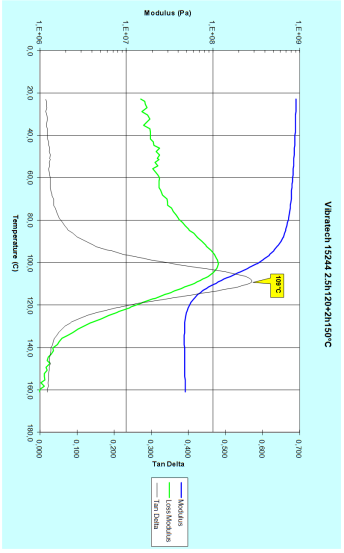

A.3.2/ PROPERTIES OF THE RESINS USED FOR SAMPLES P5 TO P7

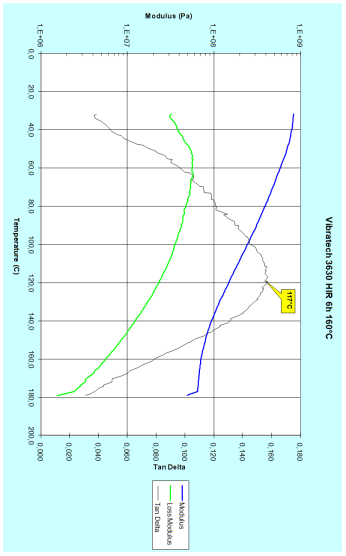

P7 - ref. 3630 HIR

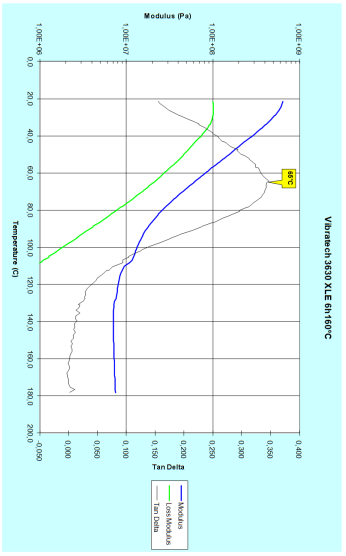

P5 - ref. 3630 XLE

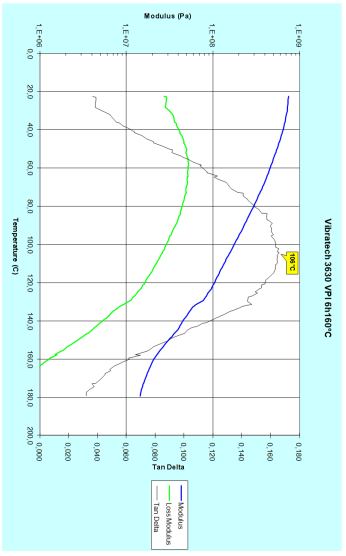

P6 - ref. 3630 VPI

A.4/ Mode shapes of core samples with windings and resin

For the core samples P3 and P6 introduced in Chapter 4, the deformed shapes of lowest-frequency modes are computed with optimised material properties, and illustrated in Subsections A.4.1 and A.4.2, respectively.

A.4.1/ Mode shapes of sample P3

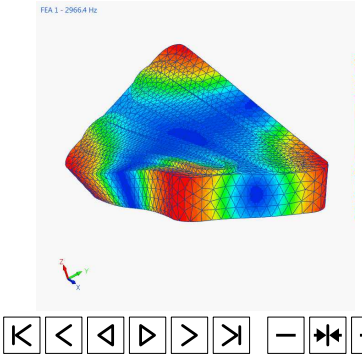

P3 - mode 1 (2,966 Hz)

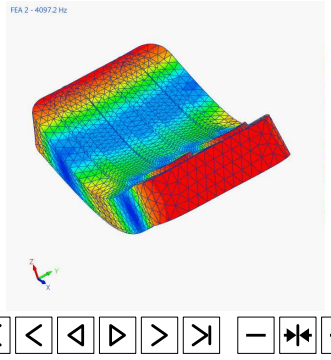

P3 - mode 2 (4,097 Hz)

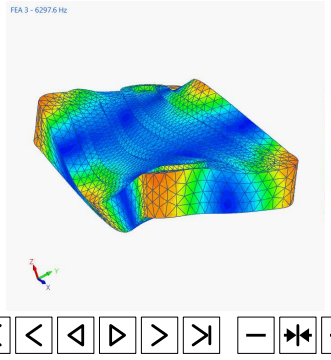

P3 - mode 3 (6,298 Hz)

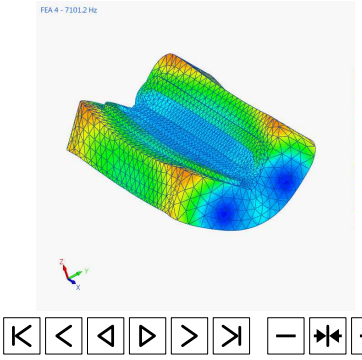

P3 - mode 4 (7,101 Hz)

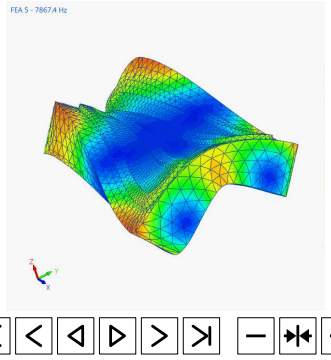

P3 - mode 5 (7,867 Hz)

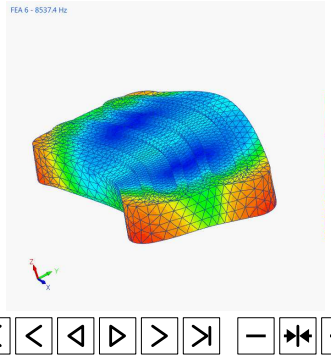

P3 - mode 6 (8,537 Hz)

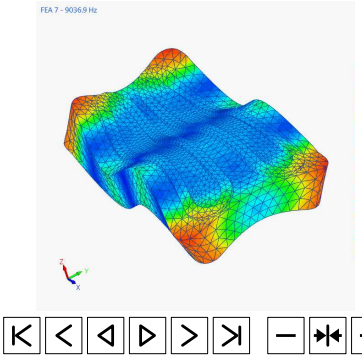

P3 - mode 7 (9,037 Hz)

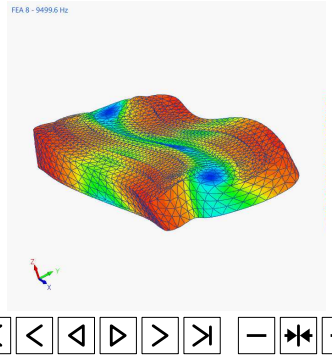

P3 - mode 8 (9,500 Hz)

A.4.2/ MODE SHAPES OF SAMPLE P6

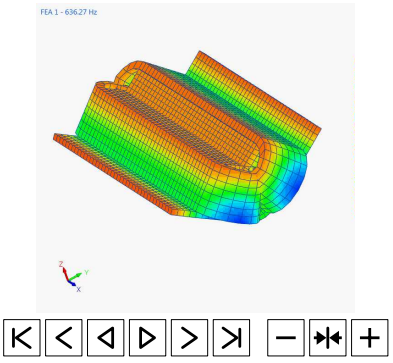

P6 - mode 1 (636 Hz)

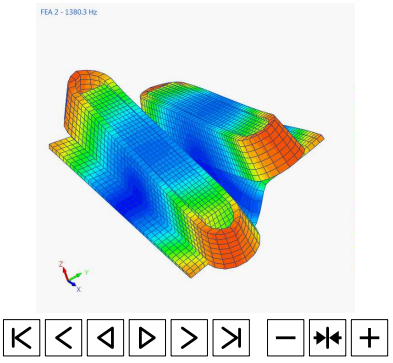

P6 - mode 2 (1,380 Hz)

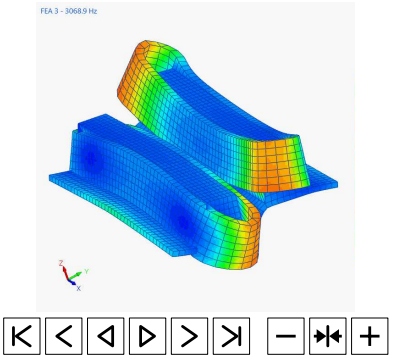

P6 - mode 3 (3,069 Hz)

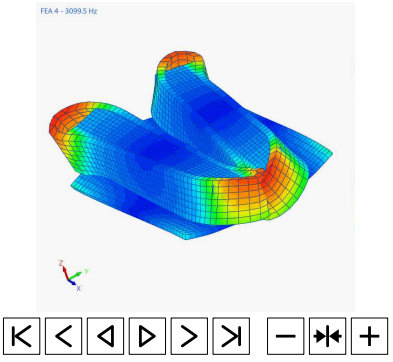

P6 - mode 4 (3,100 Hz)

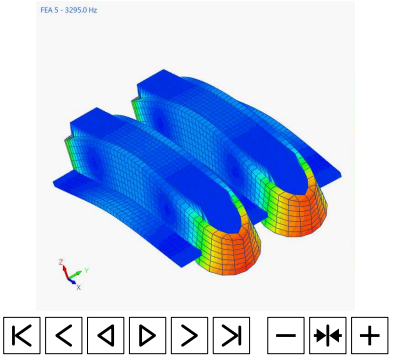

P6 - mode 5 (3,295 Hz)

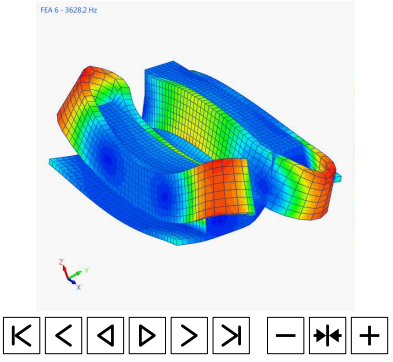

P6 - mode 6 (3,628 Hz)

A.5/ UPDATED MODELS FOR CORE SAMPLES WITH WINDINGS AND RESIN

The updated FE models for the core samples introduced in Chapter 4 have been compared in Subsection 4.3.2, where only the most accurate for recreating the modal behaviour measured on the real samples have been selected. This section gathers all of the tested modelling possibilities throughout pages 170 to 176, where labels "G" and "T" refer to the "potted" and "impregnated" families, respectively. The available updating parameters are listed in white on a green background in the figures, where **TK** is the thickness, **NSM** the non-structural mass and **RHO** the density. The labels **ISO** and **ORTHO** refer to the respective elastic parameter sets $\{E, \nu\}$ and $\{E_x, E_y, E_z, G_{yz}, G_{zx}, G_{xy}\}$, and **KXYZ** to the values $\{K_x, K_y, K_z\}$ of stiffness elements. Note that the structure is meshed with either tetrahedral or cuboid elements, which has negligible influence on the dynamic behaviour. A case specifying "all" updating parameters actually considers only the parameters defined in the corresponding figure. Also, a 2-D coating mesh shares the associated solid body's nodes.

Specificities:

- volumes of both windings and resin are replaced by a 2-D coating

Updating parameters:

- ***NSM*** only

Results:

- $N_{mp} = 3$ and $\overline{|\Delta f|} = 50.4\%$

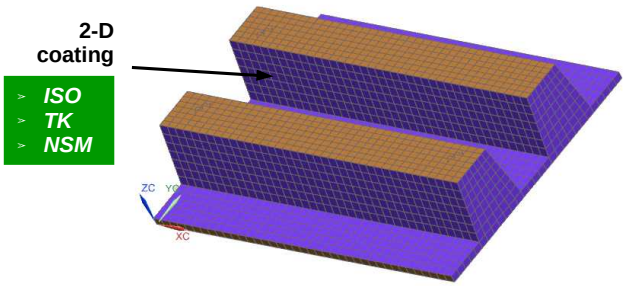

Figure A.1 – FEM T1 - “potted” family

Specificities:

- same as FEM T1

Updating parameters:

- all

Results:

- $N_{mp} = 3$ and $\overline{|\Delta f|} = 35.8\%$

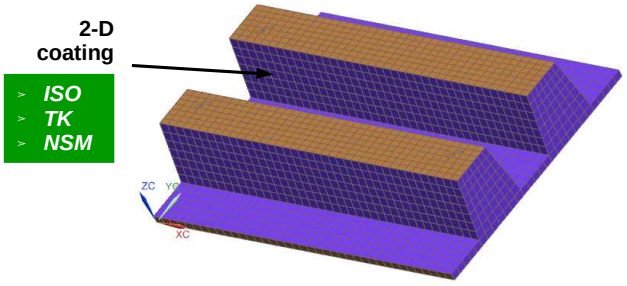

Figure A.2 – FEM T2

Specificities:

- total mass represented by adapted tooth density
- inspired from the method in [86]

Updating parameters:

- all

Results:

- $N_{mp} = 3$ and $\overline{|\Delta f|} = 57.7\%$

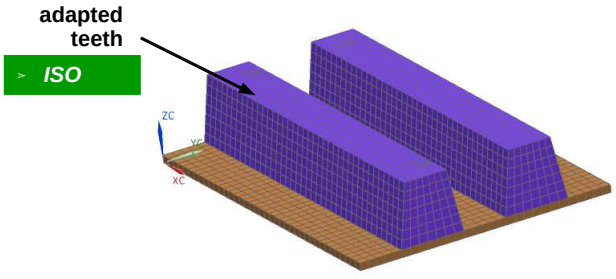

Figure A.3 – FEM T3

Specificities:

- same as FEM T3

Updating parameters:

- all

Results:

- $N_{mp} = 3$ and $\overline{|\Delta f|} = 56.5\%$

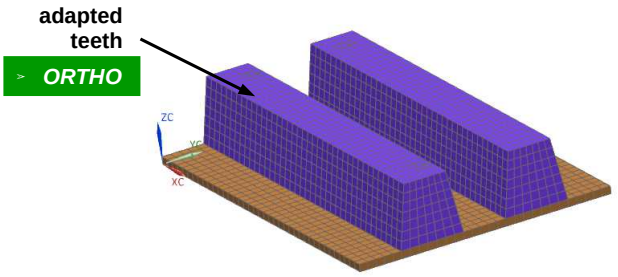

Figure A.4 – FEM T4

Specificities:

- 3-D windings
- the resin is replaced by 3-D elements between the teeth and the winding edges and 2-D coating over the windings

Updating parameters:

- all

Results:

- $N_{mp} = 2$ and $\overline{|\Delta f|} = 29.2\%$

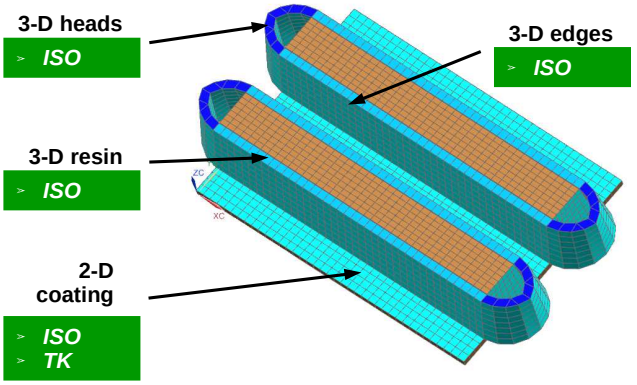

Figure A.5 – FEM T5

Specificities:

- all 3D
- teeth adjacent to the winding edges (no resin between them)

Updating parameters:

- all

Results:

- $N_{mp} = 3$ and $\overline{|\Delta f|} = 1.35\%$

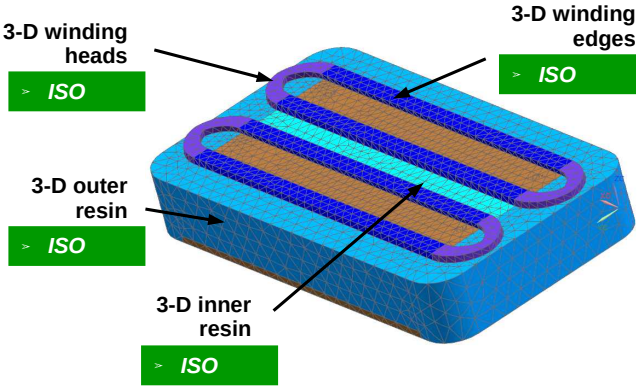

Figure A.6 – FEM T6

Specificities:

- same as FEM T6, with orthotropic inner resin

Updating parameters:

- all

Results:

- $N_{mp} = 3$ and $\overline{|\Delta f|} = 1.20\%$

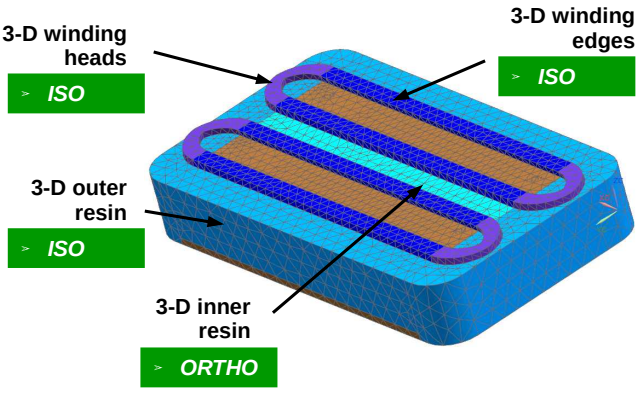

Figure A.7 – FEM T7

Specificities:

- same as FEM T7, with orthotropic winding heads and edges

Updating parameters:

- all

Results:

- $N_{mp} = 3$ and $\overline{|\Delta f|} = 0.22\%$

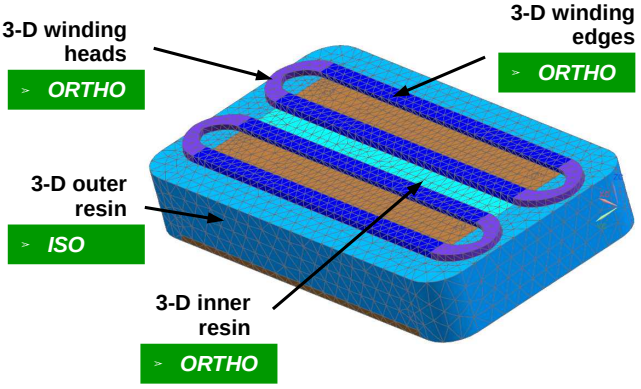

Figure A.8 – FEM T8

Specificities:

- same as FEM T8, with orthotropic outer resin (i.e. all orthotropic)

Updating parameters:

- all

Results:

- $N_{mp} = 3$ and $\overline{|\Delta f|} = 0.12\%$

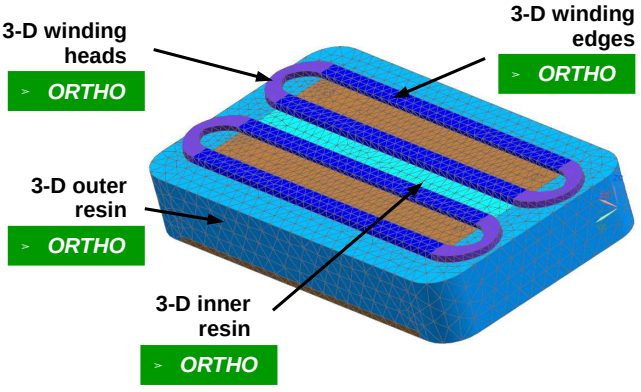

Figure A.9 – FEM T9

Specificities:

- each zone is characterised by a single set of elastic properties (e.g. winding heads and neighbouring resin)
- representative densities conserved as in FEM T9 (not updated)

Updating parameters:

- all

Results:

- $N_{mp} = 3$ and $\overline{|\Delta f|} = 0.4\%$

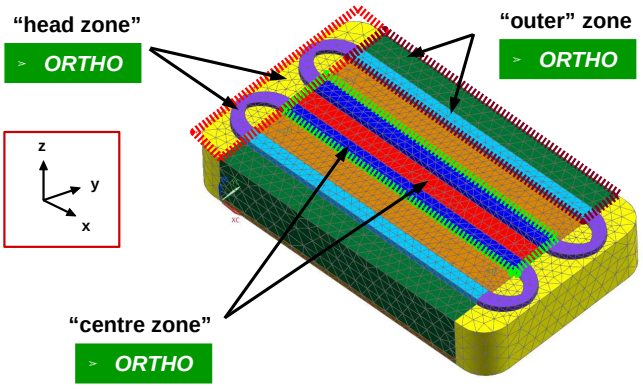

Figure A.10 – FEM T10

Specificities:

- total mass represented by adapted tooth density
- inspired from the method in [86]

Updating parameters:

- all

Results:

- $N_{mp} = 3$ and $\overline{|\Delta f|} = 12.0\%$

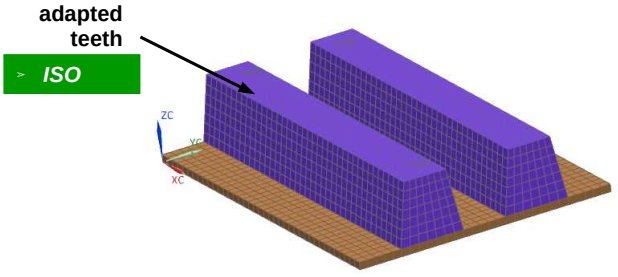

Figure A.11 – FEM G1 - "impregnated" family

Specificities:

- same as FEM G1

Updating parameters:

- all

Results:

- $N_{mp} = 3$ and $\overline{|\Delta f|} = 1.19\%$

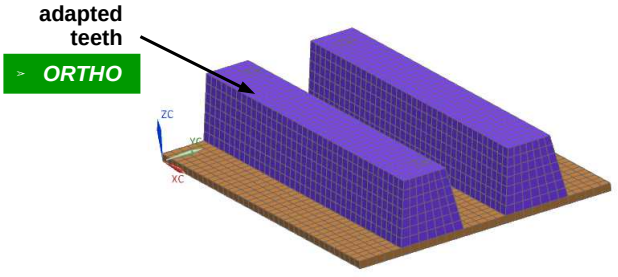

Figure A.12 – FEM G2

Specificities:

- winding edges coated on the teeth (common interface nodes)

Updating parameters:

- all

Results:

- $N_{mp} = 3$ and $\overline{|\Delta f|} = 14.5\%$
- very low final E values (reduced by 99.5% after updating)

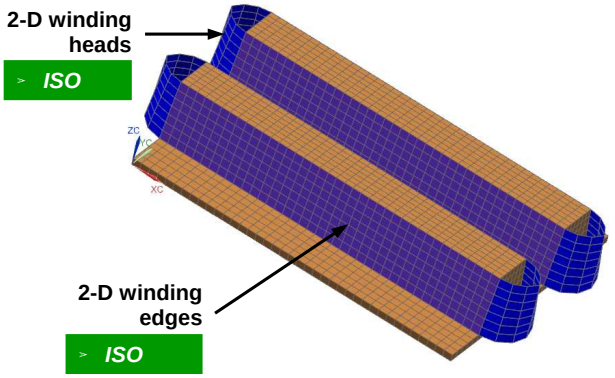

Figure A.13 – FEM G3

Specificities:

- winding edges coated on the teeth (common interface nodes)
- no heads
- inspired from the suggestions in [46]

Updating parameters:

- ***TK*** and ***NSM*** only

Results:

- $N_{mp} = 3$ and $\overline{|\Delta f|} = 7.02\%$

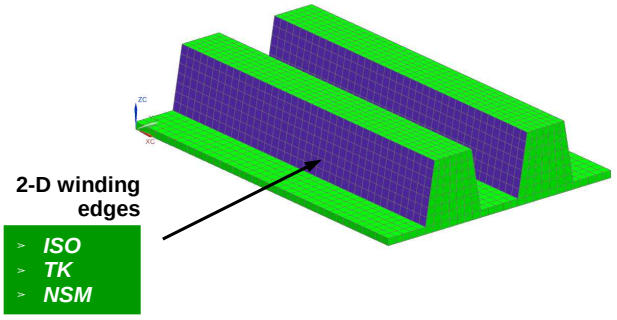

Figure A.14 – FEM G4

Specificities:

- the meshes of winding edges and teeth are separated, with geometrically-coincident nodes
- each node pair is linked by 3-D stiffness elements (each direction can be updated independently)

Updating parameters:

- all

Results:

- $N_{mp} = 3$ and $\overline{|\Delta f|} = 2.65\%$

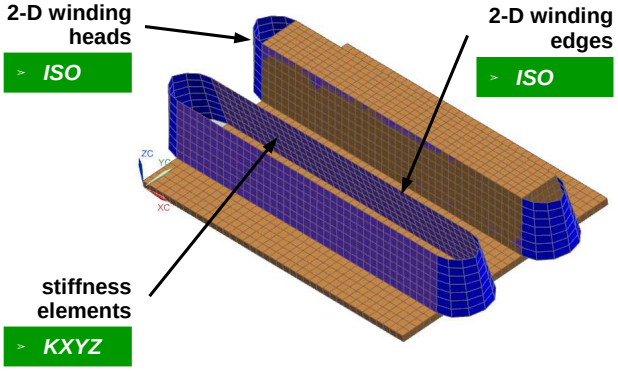

Figure A.15 – FEM G5 (adapted view)

Specificities:

- same as FEM G5, with 2-mm shell offset

Updating parameters:

- all

Results:

- $N_{mp} = 3$ and $\overline{|\Delta f|} = 4.39\%$

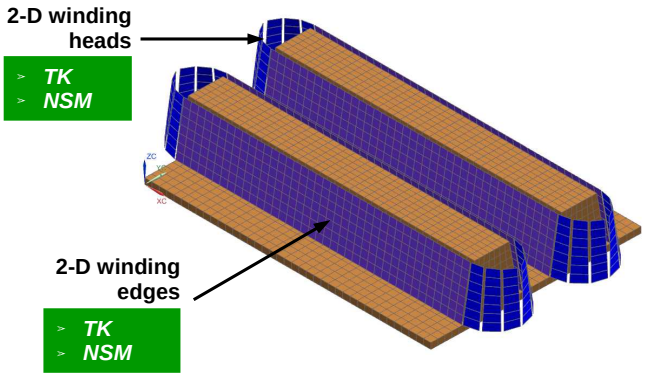

Figure A.16 – FEM G6

Specificities:

- the meshes of winding edges and teeth share the same interface nodes with a 2-D intermediate mesh (instead of stiffness elements)
- the winding heads are modelled by 2-D coating meshes

Updating parameters:

- all

Results:

- $N_{mp} = 3$ and $\overline{|\Delta f|} = 3.51\%$
- very low final E value in the winding edges (reduced by 99.9% after updating)

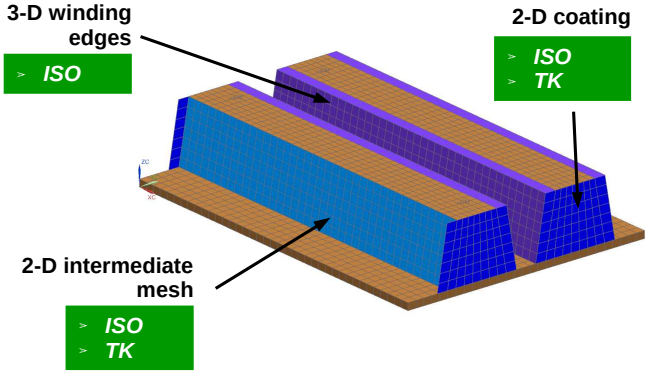

Figure A.17 – FEM G7 (adapted view)

Specificities:

- same as FEM G5, with 3-D orthotropic windings instead

Updating parameters:

- all

Results:

- $N_{mp} = 3$ and $\overline{|\Delta f|} = 0.69\%$

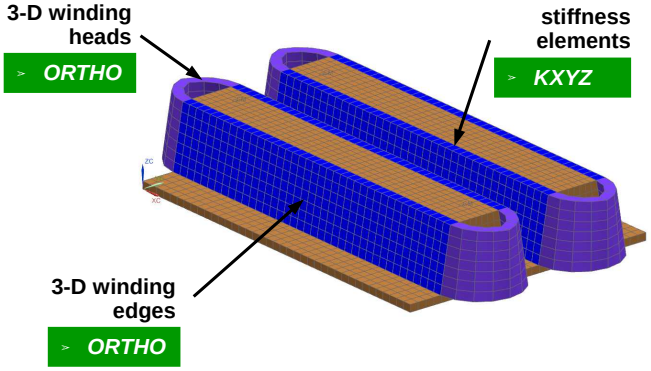

Figure A.18 – FEM G8

Specificities:

- same as FEM G8, with a 3-D mesh instead of the stiffness elements

Updating parameters:

- all

Results:

- $N_{mp} = 3$ and $\overline{|\Delta f|} = 0.39\%$

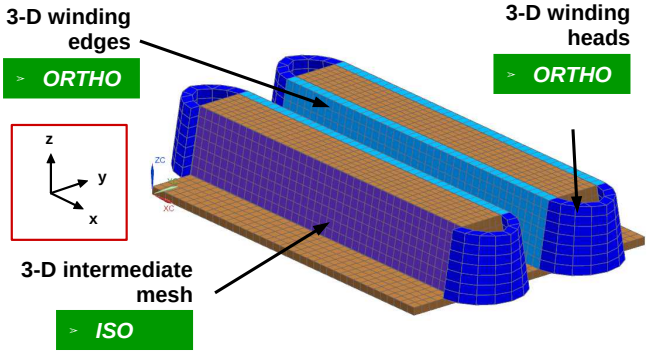

Figure A.19 – FEM G9 (adapted view)

Specificities:

- same as FEM G9

Updating parameters:

- all
- constraint: constant total winding mass

Results:

- $N_{mp} = 3$ and $\overline{|\Delta f|} = 0.10\%$

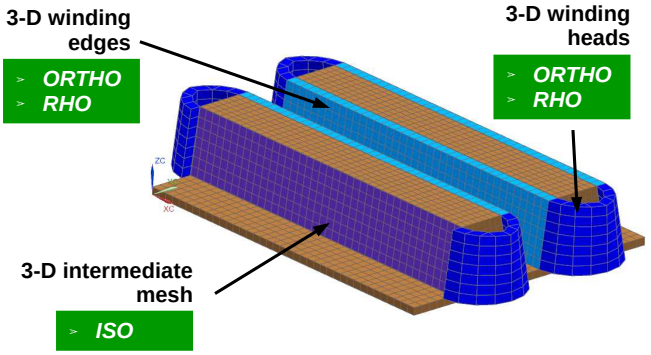

Figure A.20 – FEM G10 (adapted view)

Specificities:

- same as FEM G9, with merged nodes at the tooth edges

Updating parameters:

- all

Results:

- $N_{mp} = 3$ and $\overline{|\Delta f|} = 1.74\%$

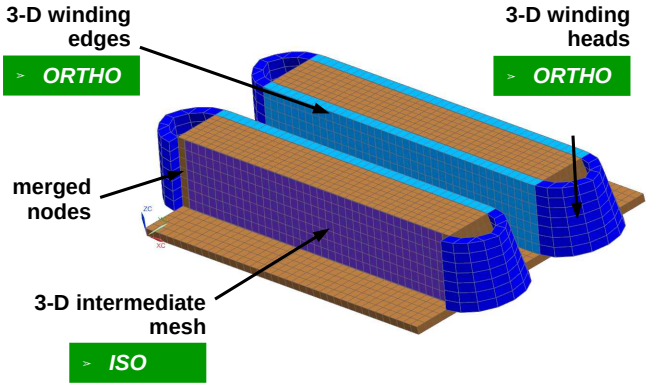

Figure A.21 – FEM G11 (adapted view)

B

NOMENCLATURE

B.1/ ABBREVIATIONS

DMA	dynamic mechanical analysis/analyser
DOE	design of experiments
DOF	degree of freedom
FE	finite element
FRF	frequency response function
INRIA	property identification method detailed in Paragraph 3.2.1.2
KPC	property identification method detailed in Paragraph 3.2.1.4
MAC	Modal Assurance Criterion
NSM	non-structural mass
NVH	noise, vibration and harshness
PEMAT	property identification method detailed in Paragraph 3.2.1.3
PG	mode pair - "potted family"
PT	mode pair - "impregnated family"
PWM	pulse-width modulation
S/N	serial number
WA	property identification method detailed in Paragraph 3.2.1.1
2D, 3D	two-dimension, three-dimension

B.2/ PHYSICAL SYMBOLS

B	magnetic induction or flux density $\left[\mathrm{T} \text{ or } \mathrm{Wb} \cdot \mathrm{m}^{-2} \text{ or } \mathrm{H} \cdot \mathrm{A} \cdot \mathrm{m}^{-2}\right]$
$\mathcal{B}_{uN}$	number of nodes on face $u = N$ $[-]$
$[C]$	elasticity matrix $\left[\mathrm{N} \cdot \mathrm{m}^{-2}\right]$
$[\mathcal{D}]$	viscous damping matrix $\left[\mathrm{kg} \cdot \mathrm{s}^{-1}\right]$
f^{mm}	magnetomotive force $[\mathrm{A}]$
$F_{d,i}$	reaction force on node i, direction d $[\mathrm{N}]$
$\{\mathcal{F}\}$	harmonic force vector $[\mathrm{N}]$
$\vec{H}$	magnetic field $\left[\mathrm{A} \cdot \mathrm{m}^{-1}\right]$
I	electric current $[\mathrm{A}]$

K_x, K_y, K_z	value of stiffness element about translational DOFs Tx, Ty and Tz $\left[\mathrm{N}\cdot\mathrm{m}^{-1}\right]$
$[\mathcal{K}]$	stiffness matrix $\left[\mathrm{N}\cdot\mathrm{m}^{-1}\right]$
$\mathcal{K}_{row:col}$	component of stiffness matrix $\left[\mathrm{N}\cdot\mathrm{m}^{-1}\right]$
$[\mathcal{M}]$	mass matrix [kg]
$\mathcal{N}_r$	rotor speed [rpm]
Rx, Ry, Rz	rotational DOFs about directions x, y and z
$[S]$	compliance matrix $\left[\mathrm{m}^2\cdot\mathrm{N}^{-1}\right]$
$[\mathcal{S}]$	sensitivity matrix $[-]$
$\mathfrak{s}_\mathfrak{f}$	stacking factor $[-]$
Tx, Ty, Tz	translational DOFs about directions x, y and z
t_{MAC}	MAC-value threshold below which mode pairs are discarded from the correlation process $[-]$
$\mathcal{U}_{hN}$	set of nodes on face $h = N$
$\Delta l_{d,i}$	displacement of node i, direction d [m]
$\{\varepsilon\}$	strain tensor (column vector form) $[-]$
ζ	damping ratio ($\zeta = {}^{c}/_{c_{\mathrm{crit}}}$) $[-]$
η	loss factor ($\eta = 2\cdot\zeta$) $[-]$
Λ	magnetic permeance [H]
μ	magnetic permeability $\left[\mathrm{N}\cdot\mathrm{A}^{-2}\text{ or }\mathrm{H}\cdot\mathrm{m}^{-1}\right]$
ρ	mass density $\left[\mathrm{kg}\cdot\mathrm{m}^{-3}\right]$
$\{\sigma\}$	stress tensor (column vector form) $\left[\mathrm{N}\cdot\mathrm{m}^{-2}\right]$
$\{\phi\}$	mode (deformed) shape [m]

B.3/ MATHEMATICAL SYMBOLS, NOTATIONS AND CONVENTIONS

$[\mathcal{B}]$	deformation interpolation matrix
$a\mathrm{E}b$	$a\cdot 10^b$
$\mathbf{i}$	imaginary symbol ($\mathbf{i} = \sqrt{-1}$)
$\Im(c)$	imaginary part of complex number c
$\mathfrak{N}(x,y,z)$	three-dimensional interpolation function
$\Re(c)$	real part of complex number c
$[\mathcal{T}_d(\theta_d)]$	matrix of rotation of angle θ_d about axis d
δ_{ij}	Kronecker symbol (equals 1 if $i = j$ and 0 if $i \neq j$)
$[\Lambda]$	spectral matrix
$[\mathbf{0}_{u,v}]$	$u \times v$ matrix filled with 0 (applies for vectors also)
$[\mathbf{1}_{u,v}]$	$u \times v$ matrix filled with 1 (applies for vectors also)

$[\mathbf{I}_{u,v}]$	$u \times v$ matrix filled with δ_{ij} (identity if $u = v$)
$[-]$	matrix or physical units
$\{-\}$	vector
$\log(x)$	common logarithm (base 10) of x
$\ln(x)$	natural logarithm (base e) of x
$\exp(x)$	exponential function of x, equivalent to e^x
a^b	a power b
$a^{\{b\}}$	b-th term of set a
$\tilde{\psi}$	global/equivalent property ψ
$\vec{a} \cdot \vec{b}$	dot-product of vectors $\vec{a}$ and $\vec{b}$ (scalar)
$\vec{a} \times \vec{b}$	cross-product of vectors $\vec{a}$ and $\vec{b}$ (vector)
$[R]^\intercal$	transposed matrix (or vector) of $[R]$

B.4/ USUAL MAGNETIC CORE MODE SHAPES

The notations used in this document to describe mode shapes of cylinders, magnetic core structures or entire stators are presented on pages 180 to 182. The model used is the magnetic core presented in Sections 2.3, 3.2 and 3.3.

When applicable, mode shapes are defined with an order set (n, m), where n stands for the *spatial order* (i.e. number of lobes along the circular section) and m for the number of *nodal circles* along the length (i.e. circles of nodes having null displacement).

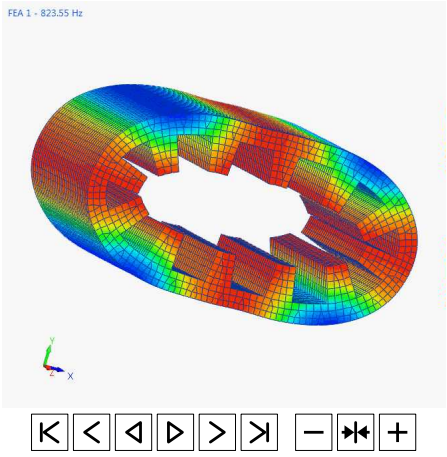

mode (2,0) - 824 Hz

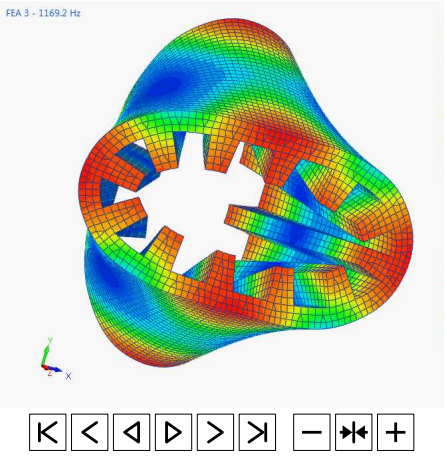

mode (2,1) - 1,169 Hz

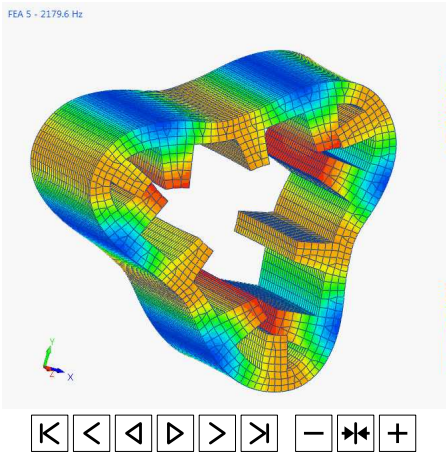

mode (3,0) - 2,180 Hz

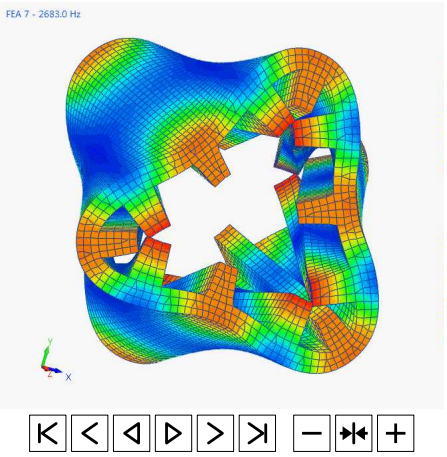

mode (3,1) - 2,683 Hz

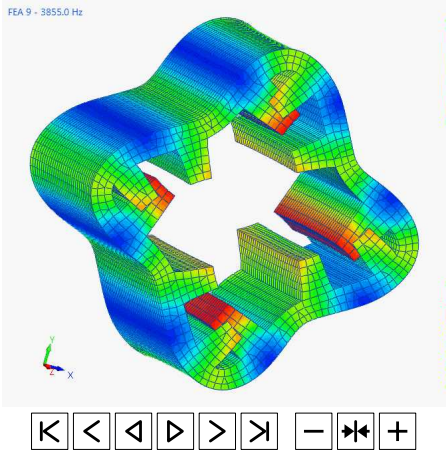

mode (4,0) - 3,855 Hz

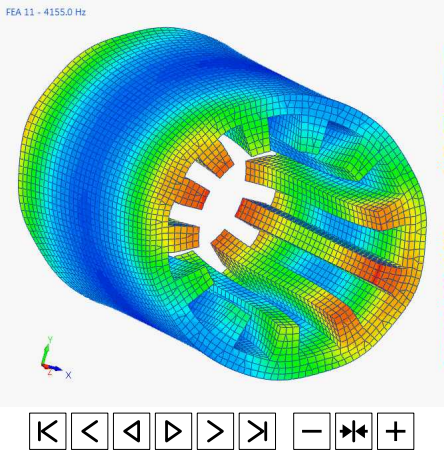

"parallelogram" bending mode - 4,155 Hz

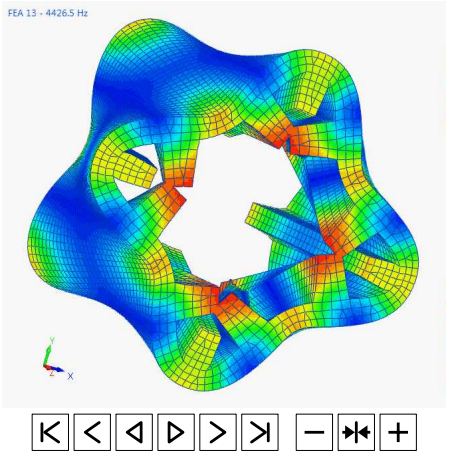

mode (4,1) - 4,427 Hz

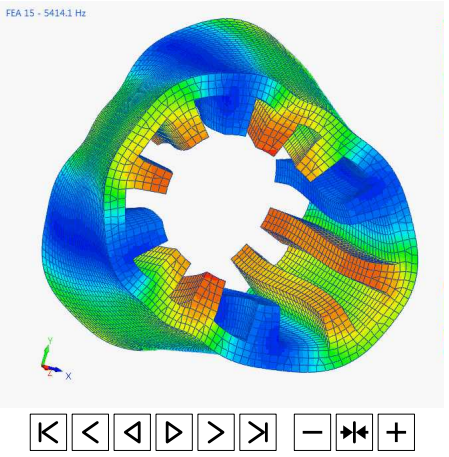

ovalisation 2 + longitudinal coupled mode - 5,414 Hz

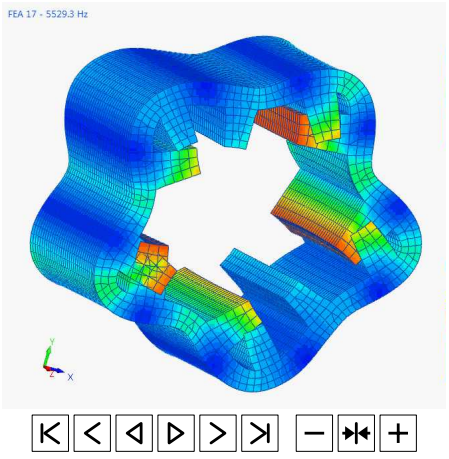

mode (5,0) - 5,529 Hz

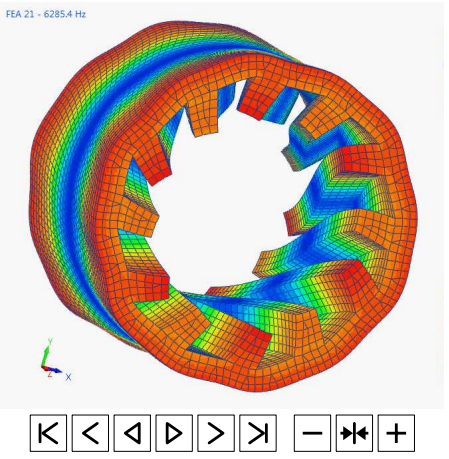

torsion mode - 6,285 Hz

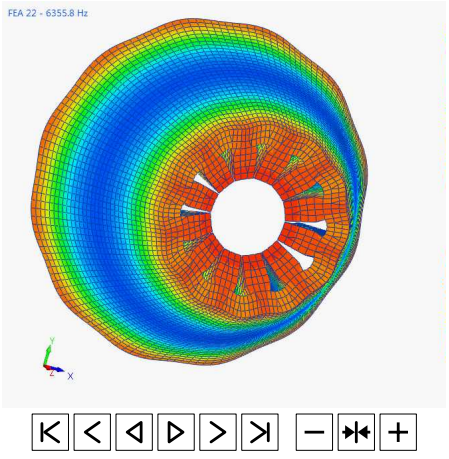

mode (0,1) - 6,356 Hz

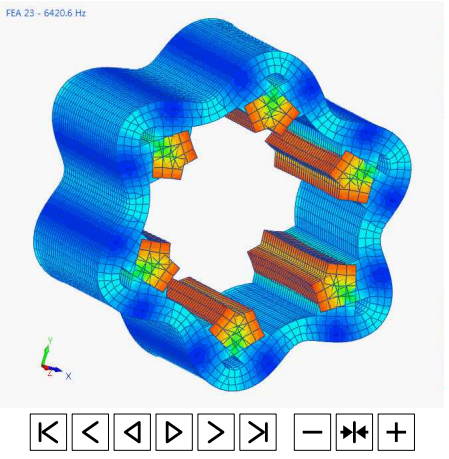

mode (6,0) - 6,421 Hz

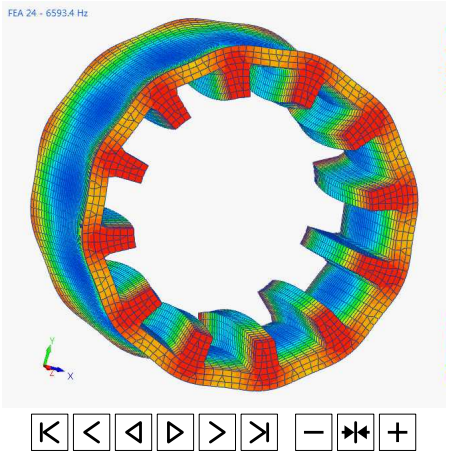

"breathing" mode (0,0) - 6,593 Hz

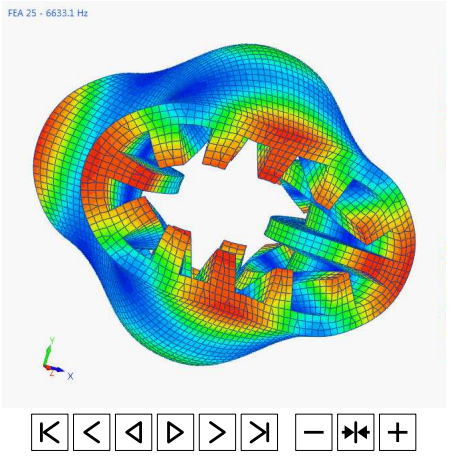

mode (2,2) - 6,633 Hz

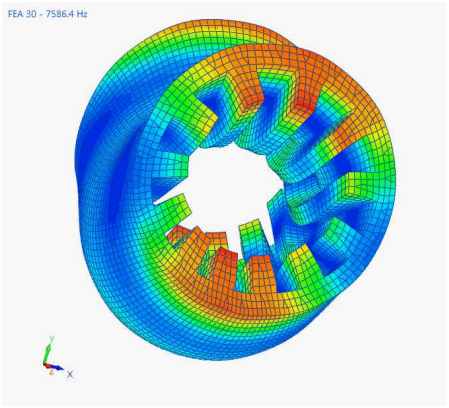

bending mode - 7,586 Hz

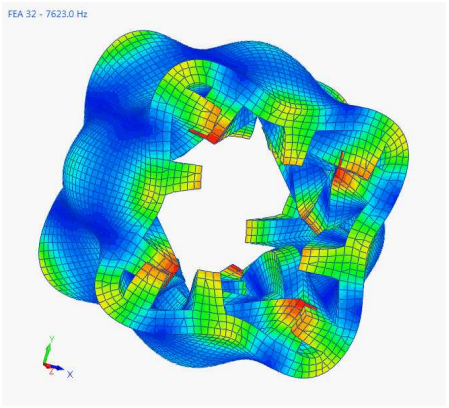

mode (4,2) - 7,623 Hz

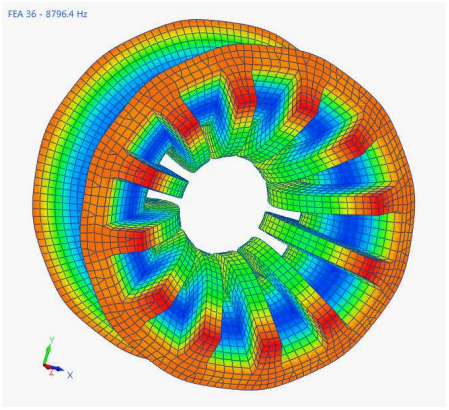

mode (0,2) - 8,796 Hz

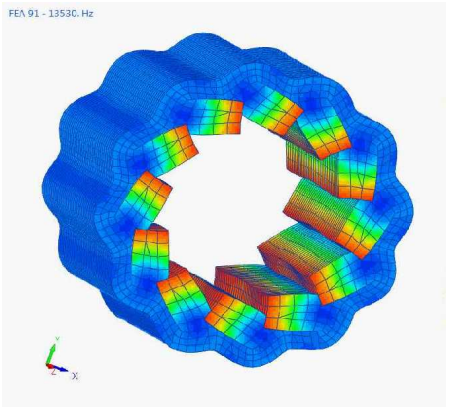

"tooth rocking" mode - 13,530 Hz

Bibliography

[1] Hearmon, R. F. S. **The elastic constants of anisotropic materials**. *Reviews of Modern Physics 18*, 3 (1946), p. 409.

[2] Haut, F. J. G. **The Early History of the Electric Locomotive**. Richard Tilling for the author, 1952.

[3] Kaye, G. W. C., and Laby, T. H. **Physical and Chemical Constants - Some Mathematical Functions**. Longmans, Green, 1957.

[4] Guyan, R. **Reduction of stiffness and mass matrices**. *AIAA journal 3*, 2 (1965), 380–380.

[5] Puck, A. **Grundlagen der Spannungs und Verformungs Analyse [basic notions of tension and distorsion analysis]**. *Dipl. Ing. Kunststoffe, Bd 57*, 4 (1967).

[6] Bampton, M., and Craig, R. **Coupling of substructures for dynamic analyses.** *AIAA Journal 6*, 7 (1968), 1313–1319.

[7] Tsai, S. W., Halpin, J. C., Pagano, N. J., and Schwartz, R. T. **Composite materials workshop**. Technomic, 1968.

[8] Hayes, M. **A simple statical approach to the measurement of the elastic constants in anisotropic media**. *Journal of Materials Science 4*, 1 (1969), pp. 10–14.

[9] Barker, R. M., Fu-Tien, L., and Dana, J. R. **Three-dimensional finite-element analysis of laminated composites**. *Computers & Structures 2*, 5 (1972), pp. 1013–1029.

[10] Watt, J. P., Davies, G. F., and O'Connell, R. J. **The elastic properties of composite materials**. *Reviews of Geophysics 14*, 4 (1976), pp. 541–563.

[11] Zienkiewicz, O., and Taylor, R. **The finite element method**, vol. 3. McGraw-hill London, 1977.

[12] Blevins, R. D. **Formulas for natural frequency and mode shape**. Van Nostrand Reinhold New York, 1979.

[13] Ferry, J. **Viscoelastic Properties of Polymers, 3rd edition**. John Wiley and Sons, 1980.

[14] Begis, D., Duvaut, G., and Hassim, A. **Homogénéisation par éléments finis des modules de comportements élastiques de matériaux composites [finite-element homogenisation of composite materials' elastic constants]**. Tech. Rep. 101, Institut National de Recherche en Informatique et Automatique, 1981.

[15] Craig, R. **Structural dynamics: an introduction to computer methods**, vol. 40. Wiley New York, 1981.

[16] Begis, D., Bestagno, A., Duvaut, G., Hassim, A., and Nuc, M. **A new method of computing global elastic moduli for composite materials**. Tech. Rep. 195, Institut National de Recherche en Informatique et Automatique, 1983.

[17] WATANABE, S., KENJO, S., IDE, K., SATO, F., AND YAMAMOTO, M. **Natural frequencies and vibration behaviour of motor stators**. *IEEE Transactions on Power Apparatus and Systems*, 4 (1983), 949–956.

[18] HEARN, E. J. **Mechanics of Materials**, vol. 1 - 2. Pergamon Press, 1985.

[19] SINGAL, R. K., WILLIAMS, K., AND VERMA, S. P. **Vibration behaviour of stators of electrical machines, part 2, experimental study**. *Journal of sound and vibration 115*, 1 (1987), 13–23.

[20] VERMA, S., SINGAL, R., AND WILLIAMS, K. **Vibration behaviour of stators of electrical machines, part 1, theoretical study**. *Journal of Sound and Vibration 115*, 1 (1987), 1–12.

[21] CHEVALIER, Y. **Comportements élastique et viscoélastique des composites [Elastic viscoelastic behaviours of composite materials]**, vol. 5. Techniques de l'Ingénieur, 1988.

[22] SINGAL, R., VERMA, S., AND WILLIAMS, K. **Vibrations of long and short laminated stators of electrical machines part 3, results for short stators and validity of simplified frequency equation**. *Journal of sound and vibration 129*, 1 (1989), 31–44.

[23] VERMA, S. P., WILLIAMS, K., AND SINGAL, R. K. **Vibrations of long and short laminated stators of electrical machines part 1, theory, experimental models, procedure and set-up**. *Journal of sound and vibration 129*, 1 (1989), 1–13.

[24] WILLIAMS, K., SINGAL, R., AND VERMA, S. **Vibrations of long and short laminated stators of electrical machines part 2, results for long stators**. *Journal of Sound and Vibration 129*, 1 (1989), 15–29.

[25] SADOWSKI, N., LEFÈVRE, Y., LAJOIE-MAZENC, M., AND BASTOS, J. P. A. **Sur le calcul des forces magnétiques**. *Journal de physique III 2*, 5 (1992), 859–870.

[26] MOTTERSHEAD, J., AND FRISWELL, M. **Model updating in structural dynamics, a survey**. *Journal of Sound and Vibration 167*, 2 (1993), 347–375.

[27] LUCIANO, R., AND BARBERO, E. **Formulas for the stiffness of composites with periodic microstructure**. *International Journal of Solids and Structures 31*, 21 (1994), pp. 2933–2944.

[28] BESBES, M. **Contribution à la modélisation numérique des phénomènes couplés magnétoélastiques. Application à l'étude des vibrations d'origine magnétique dans les MRV. [Numerical modelling of magnetoelastic coupled phenomena. Analysis of magnetic-borne vibrations in SRMs]**. PhD thesis, Université de Paris 06, 1995.

[29] LUKKASSEN, D., PERSSON, L.-E., AND WALL, P. **Some engineering and mathematical aspects on the homogenization method**. *Composites Engineering 5*, 5 (1995), pp. 519–531.

[30] CASSORET, B. **Réduction active du bruit magnétique des machines asynchrones directement connectées au réseau [Active reduction of magnetic noise of grid-connected asynchronous machines]**. PhD thesis, Université d'Artois, 1996.

[31] ARKKIO, A. **Unbalanced magnetic pull in cage induction motors with asymmetry in rotor structures**. In *Eighth International Conference on Electrical Machines and Drives* (1997), IET, pp. 36–40.

[32] BRUDNY, J. F. **Modélisation de la denture des machines asynchrones. phénomène de résonance [models of asynchronous machine teeth, resonance phenomena]**. *Journal de Physique III 7*, 5 (1997), 1009–1023.

[33] GARVEY, S., PENNY, J., FRISWELL, M., AND GLEW, C. **Modelling the vibrational behaviour of stator cores of electrical machines with a view to successfully predicting machine noise**. In *IEE Colloquium on Modeling the Performance of Electrical Machines* (April 1997), pp. 3/1–313.

[34] KOISHI, M., SHIRATORI, M., MIYOSHI, T., AND KABE, K. **Homogenization method for dynamic viscoelastic analysis of composite materials**. *JSME International Journal-Series A-Mechanics and Material Engineering 40*, 3 (1997), pp. 306–312.

[35] WANG, H., AND WILLIAMS, K. **Effects of laminations on the vibrational behaviour of electrical machine stators**. *Journal of Sound and Vibration 202*, 5 (1997), 703–715.

[36] KIKUCHI, T., AND KENJO, T. **In-depth learning of cogging/detenting torque through experiments and simulations**. *IEEE Transactions on Education 41*, 4 (1998), 16–pp.

[37] LÅFTMAN, L. **Magnetostriction and its contribution to noise in a pwm inverter fed induction machine**. *Le Journal de Physique IV 8*, PR2 (1998).

[38] RICHARD, N. **Calculation of electromagnetic forces on large generator end-windings under fault conditions using a three-dimensional finite element method**. *Mathematics and computers in simulation 46*, 3 (1998), 257–263.

[39] SMIT, R., BREKELMANS, W., AND MEIJER, H. **Prediction of the mechanical behavior of nonlinear heterogeneous systems by multi-level finite element modeling**. *Computer Methods in Applied Mechanics and Engineering 155*, 1 (1998), pp. 181–192.

[40] VIJAYRAGHAVAN, P., AND KRISHNAN, R. **Noise in electric machines: A review**. In *IEEE Industry Applications Conference* (1998), vol. 1, IEEE, pp. 251–258.

[41] BERTHELOT, J.-M. **Composite materials, mechanical behavior and structural analysis**. Springer, 1999.

[42] DELAERE, K., BELMANS, R., HAMEYER, K., HEYLEN, W., AND SAS, P. **Coupling of magnetic analysis and vibrational modal analysis using local forces**. In X^{th} *International Symposium on Theoretical Electrical Engineering ISTET* (1999), vol. 99, pp. 417–422.

[43] DIAS, M. J. **The effect of the clamping force on the dynamic behavior of a stator core**. In *Proceedings of the 17th International Modal Analysis Conference* (1999), vol. 3727, Society for Experimental Mechanics, p. p. 201.

[44] PILLAY, P., AND CAI, W. **An investigation into vibration in switched reluctance motors**. *IEEE Transactions on Industry Applications 35*, 3 (1999), 589–596.

[45] RIKARDS, R., CHATE, A., STEINCHEN, W., KESSLER, A., AND BLEDZKI, A. K. **Method for identification of elastic properties of laminates based on experiment design**. *Composites Part B: Engineering 30*, 3 (1999), pp. 279–289.

[46] WANG, C., AND LAI, J. **Vibration analysis of an induction motor**. *Journal of sound and vibration 224*, 4 (1999), 733–756.

[47] WU, T., AND THOMPSON, D. **The effects of local preload on the foundation stiffness and vertical vibration of railway track**. *Journal of Sound and Vibration 219*, 5 (1999), pp. 881–904.

[48] ANWAR, M. N., AND HUSAIN, O. **Radial force calculation and acoustic noise prediction in switched reluctance machines**. *IEEE Transactions on Industry Applications 36*, 6 (2000), 1589–1597.

[49] ARAÚJO, A. L., SOARES, M., MOREIRA DE FREITAS, M. J., PEDERSEN, P., AND HERSKOVITS, J. **Combined numerical-experimental model for the identification of mechanical properties of laminated structures**. *Composite Structures 50*, 4 (2000), pp. 363–372.

[50] DELAERE, K., HEYLEN, E., BELMANS, R., AND HAMEYER, K. **Finite element based expressions for lorentz, maxwell and magnetostriction forces**. In *Proceedings of* 5th *International Symposium on Electric and Magnetic Fields* (2000), vol. 5, pp. 17–19.

[51] KAMIŃSKI, M., AND KLEIBER, M. **Perturbation based stochastic finite element method for homogenization of two-phase elastic composites**. *Computers & Structures 78*, 6 (2000), pp. 811–826.

[52] PIERRON, F., ZHAVORONOK, S., AND GRÉDIAC, M. **Identification of the through-thickness properties of thick laminated tubes using the virtual fields method**. *International Journal of Solids and Structures 37*, 32 (2000), pp. 4437–4453.

[53] TRINDADE, M., BENJEDDOU, A., AND OHAYON, R. **Modeling of frequency-dependent viscoelastic materials for active-passive vibration damping**. *Journal of Vibration and Acoustics 122*, 2 (2000), 169–174.

[54] ANWAR, M., HUSAIN, I., AND KELLY, S. **Effects of end-shields on the stator mode frequencies of electric machines**. In *Thirty-Sixth IAS Annual Meeting, Industry Applications Conference* (September 2001), vol. 1, pp. 26–32.

[55] CAI, W., AND PILLAY, P. **Resonant frequencies and mode shapes of switched reluctance motors**. *IEEE Transactions on Energy Conversion 16*, 1 (2001), 43.

[56] CAI, W., PILLAY, P., AND OMEKANDA, A. **Analytical formulae for calculating srm modal frequencies for reduced vibration and acoustic noise design**. In *IEEE International Electric Machines and Drives Conference* (2001), IEEE, pp. 203–207.

[57] CAI, W., PILLAY, P., AND OMEKANDA, A. **Low vibration design of srms for automotive applications using modal analysis**. In *IEEE International Electric Machines and Drives Conference* (2001), IEEE, pp. 261–266.

[58] CHUNG, P. W., TAMMA, K. K., AND NAMBURU, R. R. **Asymptotic expansion homogenization for heterogeneous media - computational issues and applications**. *Composites Part A - Applied Science and Manufacturing 32*, 9 (2001), pp. 1291–1301.

[59] HA, K., AND HONG, J. **Dynamic rotor eccentricity analysis by coupling electromagnetic and structural time stepping fem**. *IEEE Transactions on Magnetics 37*, 5 (2001), 3452–3455.

[60] RIKARDS, R., CHATE, A., AND GAILIS, G. **Identification of elastic properties of laminates based on experiment design**. *International Journal of Solids and Structures 38*, 30 (2001), pp. 5097–5115.

[61] SAINT-MICHEL, J. **Bobinage des machines tournantes à courant alternatif [Winding processes of AC rotating machines]**. Techniques de l'Ingénieur, 2001.

[62] TSAI, M.-H., AND CHANG, K.-C. **A study of the modal strain energy method for viscoelastically damped structures**. *Journal of the Chinese Institute of Engineers 24*, 3 (2001), 311–320.

[63] CAI, W., PILLAY, P., AND TANG, Z. **Impact of stator windings and end-bells on resonant frequencies and mode shapes of switched reluctance motors**. *IEEE Transactions on Industry Applications 38*, 4 (August 2002), 1027–1036.

[64] DELAERE, K., HEYLEN, W., BELMANS, R., AND HAMEYER, K. **Comparison of induction machine stator vibration spectra induced by reluctance forces and magnetostriction**. *IEEE Transactions on Magnetics 38*, 2 (2002), 969–972.

[65] FASANELLA, E., JACKSON, K., AND LYLE, K. **Finite element simulation of a full-scale crash test of a composite helicopter**. *Journal of the American Helicopter Society 47*, 3 (2002), pp. 156–168.

[66] HONG, J., HA, K., AND LEE, J. **Stator pole and yoke design for vibration reduction of switched reluctance motor**. *IEEE Transactions on Magnetics 38*, 2 (2002), 1.

[67] LEE, J. H., LEE, Y. H., KIM, D. H., LEE, K. S., AND PARK, I. H. **Dynamic vibration analysis of switched reluctance motor using magnetic charge force density and mechanical analysis**. *IEEE Transactions On Applied Superconductivity 12*, 1 (2002), 1511.

[68] MILTON, G. **The theory of composites**, vol. 6. Cambridge University Press, 2002.

[69] ALLEMANG, R. **The modal assurance criterion - twenty years of use and abuse**. *Journal of Sound and Vibration 37*, 8 (2003), 14–23.

[70] DE GERSEM, H., HAMEYER, K., AND WEILAND, T. **Skew interface conditions in 2-d finite-element machine models**. *IEEE Transactions on Magnetics 39*, 3 (2003), 1452–1455.

[71] SELLGREN, U. **Component mode synthesis. a method for efficient dynamic simulation of complex technical systems**. Tech. rep., Department of Machine Design, The Royal Institute of Technology (KTH), 2003.

[72] TANG, Z., PILLAY, P., OMEKANDA, A., LI, C., AND CETINKAYA, C. **Effects of material properties on switched reluctance motor vibration determination**. In *Conference Record of the Industry Applications Conference* (2003), vol. 1, IEEE, pp. 235–241.

[73] TANG, Z., PILLAY, P., AND OMEKANDA, A. M. **Analysis of mounting effects on vibrations of switched reluctance motors**. In *IEEE International Electric Machines and Drives Conference* (2003), vol. 1, IEEE, pp. 97–103.

[74] TENHUNEN, A., BENEDETTI, T., HOLOPAINEN, T., AND ARKKIO, A. **Electromagnetic forces in cage induction motors with rotor eccentricity**. In *IEEE International Electric Machines and Drives Conference* (2003), vol. 3, IEEE, pp. 1616–1622.

[75] BELHACEN, A. **Magnetoelasticity, Magnetic Forces and Magnetostriction in Electrical Machines**. PhD thesis, Helsinki Univ. Tech., 2004.

[76] GALUCIO, A., DEÜ, J.-F., AND OHAYON, R. **Finite element formulation of viscoelastic sandwich beams using fractional derivative operators**. *Computational Mechanics 33*, 4 (2004), 282–291.

[77] GARVEY, S., PENNY, J., FRISWELL, M., AND LEES, A. **The stiffening effect of laminated rotor cores on flexible rotor electrical machines**. *IMechE Event publications* (2004).

[78] KUHLMANN, G., AND ROLFES, R. **A hierarchic 3d finite element for laminated composites**. *International journal for numerical methods in engineering 61*, 1 (2004), pp. 96–116.

[79] LOVELACE, E., JAHNS, T., KEIM, T., AND LANG, J. **Mechanical design considerations for conventionally laminated, high-speed, interior pm synchronous machine rotors**. *IEEE Transactions on Industry Applications 40*, 3 (2004), 806–812.

[80] MAGALHÃES DOURADO, N., CARDOSO XAVIER, J., AND LOPES MORAIS, J. **On the identification of linear elastic mechanical behaviour of orthotropic materials using evolutionary algorithms**. In *IUTAM Symposium on Evolutionary Methods in Mechanics* (2004), Springer, pp. pp. 251–264.

[81] REDDY, J. N. **Mechanics of Laminated Composite Plates and Shells, Theory and Analysis, 2nd Edition**. CRC Press, 2004.

[82] RIKARDS, R. **Identification of mechanical properties of laminates**. *Modern Trends in Composite Laminates Mechanics*, 448 (2004), p. 181.

[83] SALTELLI, A., TARANTOLA, S., CAMPOLONGO, F., AND RATTO, M. **Sensitivity analysis in practice: a guide to assessing scientific models**. John Wiley & Sons, 2004.

[84] SHETH, N., AND RAJAGOPAL, K. **Effects of nonuniform airgap on the torque characteristics of a switched reluctance motor**. *IEEE Transactions on Magnetics 40*, 4 (2004), 2032–2034.

[85] TABATABAEI, I., FAIZ, J., LESANI, H., AND NABAVI-RAZAVI, M. **Modeling and simulation of a salient-pole synchronous generator with dynamic eccentricity using modified winding function theory**. *IEEE Transactions on Magnetics 40*, 3 (2004), 1550–1555.

[86] TANG, Z., PILLAY, P., OMEKANDA, A. M., LI, C., AND CETINKAYA, C. **Young's modulus for laminated machine structures with particular reference to switched reluctance motor vibrations**. *IEEE Transactions on Industry Applications 40*, 3 (2004), 748–754.

[87] VEL, S., AND BATRA, R. **Three-dimensional exact solution for the vibration of functionally graded rectangular plates**. *Journal of Sound and Vibration 272*, 3 (2004), pp. 703–730.

[88] BRISO-MONTIANO, J., KARRELMEYER, R., AND DILGER, E. **Simulation of faults by means of finite element analysis in a switched reluctance motor**. In *Multiphysics Conference* (2005), pp. 1–6.

[89] DORRELL, D., CHINDURZA, I., AND COSSAR, C. **Effects of rotor eccentricity on torque in switched reluctance machines**. *IEEE transactions on magnetics 41*, 10 (2005), 3961–3963.

[90] GIERAS, J. F., WANG, C., AND LAI, J. C. **Noise of polyphase electric motors**. CRC press, 2005.

[91] SHETH, N., AND RAJAGOPAL, K. **Variations in overall developed torque of a switched reluctance motor with airgap nonuniformity**. *IEEE Transactions on Magnetics 41*, 10 (2005), 3973–3975.

[92] FAIZ, J., AND PAKDELIAN, S. **Finite-element analysis of a switched reluctance motor under static eccentricity fault**. *IEEE Transactions on Magnetics 42*, 8 (2006), 2004–2008.

[93] FIEDLER, J. **Design of Low-Noise Switched Reluctance Drives**. PhD thesis, Fakultät für Elektrotechnik und Informationstechnik der Rheinisch-Westfälischen Technischen Hochschule Aachen, 2006.

[94] KAEWUNRUEN, S., AND REMENNIKOV, A. **Laboratory measurements of dynamic properties of rail pads under incremental preload**. In *19th Australasian Conference on the Mechanics of Structures and Materials* (2006), p. 378.

[95] KIM, Y.-C., AND KIM, K.-W. **Influence of lamination pressure upon the stiffness of laminated rotor**. *JSME International Journal Series C 49*, 2 (2006), pp. 426–431.

[96] SCHLENSOK, C., AND HENNEBERGER, G. **Comparison of stator- and rotor-force excitation for the acoustic simulation of an induction machine with squirrel-cage rotor**. *International Journal for Computation and Maths in Electrical and Electronic Engineering 25*, 2 (2006), 475–486.

[97] SCHLENSOK, C., SCHMÜLLING, B., VAN DER GIET, M., AND HAMEYER, K. **Electromagnetically excited audible noise-evaluation and optimization of electrical machines by numerical simulation**. *Journal of Electrical Power Quality and Utilisation 26*, 3 (2006), 727–742.

[98] CECCHI, A., AND SAB, K. **A homogenized reissner-mindlin model for orthotropic periodic plates - application to brickwork panels**. *International journal of solids and structures 44*, 18 (2007), pp. 6055–6079.

[99] HERRANZ GRACIA, M., AND HAMEYER, K. **Influence of the magnetic anisotropy on electrical machines**. In 13th *International Symposium on Electromagnetic Fields in Mechatronics* (Prague, September 2007).

[100] KALIAPPAN, S. **Characterization of physical properties of polymers using AFM force-distance curves**. PhD thesis, Chemie-Biologie Fachbereich der Universität Siegen, 2007.

[101] LE BESNERAIS, J. **Reduction of magnetic noise in PWM-supplied induction machines, low-noise design rules and multi-objective optimisation**. PhD thesis, Laboratoire d'Électricité et d'Électronique de Puissance de Lille, École Centrale de Lille, 2008.

[102] LE BESNERAIS, J., LANFRANCHI, V., HECQUET, M., AND BROCHET, P. **Bruit audible d'origine magnétique dans les machines asynchrones [audible electromagnetic noise in asynchronous machines]**. *Techniques de l'Ingénieur, Génie Électrique 6*, D3580 (2008).

[103] LIN, R., AND ARKKIO, A. **3-d finite element analysis of magnetic forces on stator end-windings of an induction machine**. *IEEE Transactions on Magnetics 44*, 11 (2008), 4045–4048.

[104] PEILLEX, G., BAILLET, L., AND BERTHIER, Y. **Homogenization in non-linear dynamics due to frictional contact**. *International Journal of Solids and Structures 45*, 9 (2008), pp. 2451–2469.

[105] SCHLENSOK, C., VAN DER GIET, M., HERRANZ GRACIA, M., VAN RIESEN, D., AND HAMEYER, K. **Structure-dynamic analysis of an induction machine depending on stator-housing coupling**. *IEEE Transactions on Industry Applications 44*, 3 (May 2008), 753–759.

[106] SCHLENSOK, C., VAN RIESEN, D., VAN DER GIET, M., AND HAMEYER, K. **Deformation analysis of induction machines by means of analytical and numerical methods**. *IEEE Transactions On Magnetics 44*, 6 (June 2008).

[107] VAN DER GIET, M., AND HAMEYER, K. **Identification of homogenized equivalent materials for the modal analysis of composite structures in electrical machines**. In *IMechE* (2008), IMechE, pp. 437–448.

[108] VAN DER GIET, M., ROTHE, R., HERRANZ GRACIA, M., AND HAMEYER, K. **Analysis of noise exciting magnetic force waves by means of numerical simulation and a space vector definition**. In 18th *International Conference on Electrical Machines* (2008), IEEE, pp. 1–6.

[109] BERTHELOT, J.-M. **Basic Concepts of the Mechanical Behaviour of Materials and Structures**. Institute for Advanced Materials and Mechanics, 2009.

[110] KALAMKAROV, A., ANDRIANOV, I. V., AND DANISHEVS'KYY, V. V. **Asymptotic homogenization of composite materials and structures**. *Applied Mechanics Reviews 62* (2009).

[111] KALAMKAROV, A. L., HASSAN, E. M., GEORGIADES, A. V., AND SAVI, M. A. **Asymptotic homogenization model for 3d grid-reinforced composite structures with generally orthotropic reinforcements**. *Composite structures 89*, 2 (2009), pp. 186–196.

[112] LE BESNERAIS, J., LANFRANCHI, V., HECQUET, M., AND BROCHET, P. **Optimal slot numbers for magnetic noise reduction in variable-speed induction motors**. *IEEE Transactions on Magnetics 45*, 8 (2009), 3131–3136.

[113] OUISSE, M. **Vibrations des systèmes discrets [Vibrations of discrete systems]**. École Nationale Supérieure de Mécanique et des Microtechniques, 2009.

[114] TORKAMAN, H., AND AFJEI, E. **Magnetostatic field analysis regarding the effects of dynamic eccentricity in switched reluctance motor**. *Progress In Electromagnetics Research 8* (2009), 163–180.

[115] TRIVAUDEY, F. **Mécanique des structures (structural dynamics)**. École Nationale Supérieure de Mécanique et des Microtechniques, 2009.

[116] VAN DER GIET, M., ROTHE, R., AND HAMEYER, K. **Asymptotic fourier decomposition of tooth forces in terms of convolved air gap field harmonics for noise diagnosis of electrical machines**. *The International Journal for Computation and Mathematics in Electrical and Electronic Engineering 28*, 4 (2009), 804–818.

[117] YVONNET, J., GONZALEZ, D., AND HE, Q.-C. **Numerically explicit potentials for the homogenization of nonlinear elastic heterogeneous materials**. *Computer Methods in Applied Mechanics and Engineering 198*, 33 (2009), pp. 2723–2737.

[118] BOESING, M., SCHOENEN, T., KASPER, K. A., AND DE DONCKER, R. W. **Vibration synthesis for electrical machines based on force response superposition**. *IEEE Transactions on Magnetics 46*, 8 (2010), 2986–2989.

[119] CHEVALIER, Y., AND TUONG, J. V. **Mechanics of viscoelastic materials and wave dispersion**. Iste/Wiley, 2010.

[120] DE LIMA, A., RADE, D., AND BOUHADDI, N. **Optimization of viscoelastic systems combining robust condensation and metamodeling**. *Journal of the Brazilian Society of Mechanical Sciences and Engineering 32*, SPE (2010), 485–495.

[121] FONTEYN, K., BELAHCEN, A., KOUHIA, R., RASILO, P., AND ARKKIO, A. **Fem for directly coupled magneto-mechanical phenomena in electrical machines**. *IEEE Transactions on Magnetics 46*, 8 (2010), 2923–2926.

[122] GOVERS, Y., AND LINK, M. **Stochastic model updating - covariance matrix adjustment from uncertain experimental modal data**. *Mechanical Systems and Signal Processing 24*, 3 (2010), 696–706.

[123] LE BESNERAIS, J., LANFRANCHI, V., HECQUET, M., BROCHET, P., AND FRIEDRICH, G. **Prediction of audible magnetic noise radiated by adjustable-speed drive induction machines**. *IEEE Transactions on Industry Applications 46*, 4 (2010), 1367–1373.

[124] LIN, R., LAIHO, A. N., HAAVISTO, A., AND ARKKIO, A. **End-winding vibrations caused by steady-state magnetic forces in an induction machine**. *IEEE Transactions on Magnetics 46*, 7 (2010), 2665–2674.

[125] MATHAN, G., AND SIVA PRASAD, N. **Evaluation of effective material properties of spiral wound gasket through homogenization**. *International Journal of Pressure Vessels and Piping 87*, 12 (2010), pp. 704–713.

[126] RAINER, S., BÍRÓ, O., WEILHARTER, B., AND STERMECKI, A. **Weak coupling between electromagnetic and structural models for electrical machines**. *IEEE Transactions on Magnetics 46*, 8 (2010), 2807–2810.

[127] TORKAMAN, H., AFJEI, E., AND AMIRI, H. **Dynamic eccentricity fault diagnosis in switched reluctance motor**. In *International Symposium on Power Electronics Electrical Drives Automation and Motion (SPEEDAM)* (2010), IEEE, pp. 519–522.

[128] VASQUES, C., MOREIRA, R., AND RODRIGUES, J. **Viscoelastic damping technologies – part i: Modeling and finite element implementation**. *Mechanical Engineering 1*, 2 (2010), 96–110.

[129] CASSORET, B., LECOINTE, J., AND BRUDNY, J. **Influence of the pole number on the magnetic noise of electrical ac machines**. *Progress In Electromagnetics Research 33* (2011), 83–97.

[130] CHENTOUF, S.-A. **Simulations et essais dynamiques sur stators de moteurs de traction [Simulations and dynamic experimental analyses on traction motor stators]**. PhD thesis, Université de Franche-Comté, 2011.

[131] CHENTOUF, S.-A., RAYNAUD, J.-L., HUANG, S.-J., BOUHADDI, N., AND LAITEM, C. **Modèle dynamique de stators de moteurs ferroviaires [dynamic models of railway motor stators]**. In *Congrès Français de Mécanique* (Besançon, 28 août-2 septembre 2011).

[132] HASSAN, E. M., GEORGIADES, A. V., SAVI, M. A., AND KALAMKAROV, A. L. **Analytical and numerical analysis of 3d grid-reinforced orthotropic composite structures**. *International Journal of Engineering Science 49*, 7 (2011), pp. 589–605.

[133] NICHOLSON, J. **The chemistry of polymers**. Royal Society of Chemistry, 2011.

[134] OUISSE, M. **Dynamique des structures, outils et concepts fondamentaux pour la validation de modèles [Structural dynamics, fundamental tool and concepts for model validation]**. École Nationale Supérieure de Mécanique et des Microtechniques, 2011.

[135] PELLEREY, P., LANFRANCHI, V., AND FRIEDRICH, G. **Vibratory simulation tool for an electromagnetically excited non skewed electrical motor, case of the wound rotor synchronous machine**. *ELECTRIMACS2011, Cergy-Pontoise, France* (2011).

[136] WEILHARTER, B., BÍRÓ, O., LANG, H., AND RAINER, S. **Computation of the noise radiation of an induction machine using 3d fem-bem**. *The International Journal for Computation and Mathematics in Electrical and Electronic Engineering 30*, 6 (2011), 1737–1750.

[137] WITCZAK, P. **Analytical method for calculation of eigenfrequencies and modes of stator cores in ac machines**. *Maszyny Elektryczne: zeszyty problemowe*, 92 (2011), 1–6.

[138] CURÀ, F., MURA, A., AND SCARPA, F. **Modal strain energy based methods for the analysis of complex patterned free layer damped plates**. *Journal of Vibration and Control 18*, 9 (2012), 1291–1302.

[139] DUPONT, J.-B., AND BOUVET, P. **Multiphysics modelling to simulate the noise of an automotive electric motor**. *SAE International* (2012).

[140] DUPONT, J.-B., BOUVET, P., AND HUMBERT, L. **Vibroacoustic simulation of an electric motor: methodology and focus on the structural fem representativity**. In *International Conference on Electrical Machines* (Marseille, September 2012), pp. 1–7.

[141] HUMBERT, L., PELLEREY, P., AND CRISTAUDO, S. **Electromagnetic and structural coupled simulation to investigate nvh behavior of an electrical automotive powertrain**. *SAE International*, 12SNVH-0002 (2012), 1–12.

[142] JI, T., TANG, W., AND WU, Q. **Detection of power transformer winding deformation and variation of measurement connections using a hybrid winding model**. *Electric Power Systems Research 87* (2012), 39–46.

[143] MSC NASTRAN. **Dynamic Analysis User's Guide**. MSC Software, 2012.

[144] PELLEREY, P., LANFRANCHI, V., AND FRIEDRICH, G. **Coupled numerical simulation between electromagnetic and structural models. influence of the supply harmonics for synchronous machine vibrations**. *IEEE Transactions on Magnetics 48*, 2 (2012), 983–986.

[145] SCHLEGL, B., SCHEINECKER, C., MARN, A., NEUMAYER, F., HIMMELREICH, M., AND HEITMEIR, F. **Development of a full parameterized fe-modeling tool for efficient vibration investigations on end windings of turbo- and hydro- generators**. In *International Conference on Electrical Machines* (2012), pp. 1–7.

[146] VAN DER GIET, M., KASPER, K., DE DONCKER, R. W., AND HAMEYER, K. **Material parameters for the structural dynamic simulation of electrical machines**. In *International Conference on Electrical Machines* (2012), pp. 1–7.

[147] CHENG, G.-D., CAI, Y.-W., AND XU, L. **Novel implementation of homogenization method to predict effective properties of periodic materials**. *Acta Mechanica Sinica 29*, 4 (2013), pp. 550–556.

[148] DUPONT, J.-B., BOUVET, P., AND WOJTOWICKI, J.-L. **Simulation of the airborne and structure-borne noise of electric powertrain: Validation of the simulation methodology**. Tech. rep., SAE Technical Paper, 2013.

[149] FEMTOOLS. **FEMtools Model Updating Theoretical Manual, version 3.7**. Dynamic Design Solutions NV, 2013.

[150] FEMTOOLS. **FEMtools Model Updating User's Guide, version 3.7**. Dynamic Design Solutions NV, 2013.

[151] PIRNAT, M., ČEPON, G., AND BOLTEŽAR, M. **Introduction of the linear contact model in the dynamic model of laminated structure dynamics - an experimental and numerical identification**. *Mechanism and Machine Theory 64* (2013), pp. 144–154.

[152] ROULEAU, L. **Modélisation vibro-acoustique de structures sandwich munies de matériaux visco-élastiques [Vibrational-acoustic modelling of sandwich structures with viscoelastic materials]**. PhD thesis, Conservatoire National des Arts et Métiers, 2013.

[153] BODINE ELECTRIC COMPANY. **Cutaway of an electric motor (http://gearmotorblog.wordpress.com/2010/03/04/bodine-motor-windings)**, 2014. Accessed on 2014, April 14th.

[154] BOUAYED, K., MORDILLAT, P., MEBAREK, L., AND HAMDI, M. **Numerical modelling of the vibro-acoustic behavior of a closed vehicle with frequency dependent polymer materials**. In *INTER-NOISE and NOISE-CON Congress and Conference Proceedings* (2014), vol. 249, Institute of Noise Control Engineering, pp. 5685–5693.

[155] BUTAUD, P., OUISSE, M., PLACET, V., AND FOLTÊTE, E. **Experimental investigations on viscoelastic properties of a shape memory polymer**. In *ASME 2014 Conference on Smart Materials, Adaptive Structures and Intelligent Systems* (2014), American Society of Mechanical Engineers, pp. V001T01A029–V001T01A029.

[156] DUPONT, J.-B., AND LANFRANCHI, V. **Noise radiated by a permanent-magnet synchronous motor - simulation methodology and influence of motor defects**. In *International Conference on Electrical Machines* (2014).

[157] HALLAL, J. **Etudes des vibrations d'origine électromagnétique d'une machine électrique - conception optimisée et variabilité du comportement vibratoire**. PhD thesis, Compiègne, 2014.

[158] LEMOINE, D. **Electromagnetic noise, lecture notes, industrial training utc-vibratec**, 2014.

[159] MILLITHALER, P., SADOULET-REBOUL, É., OUISSE, M., DUPONT, J.-B., AND BOUHADDI, N. **3d homogenization: identification of equivalent anisotropic material properties of heterogeneous structures and dynamic application on preloaded finite element models and superelements**. In *ISMA2014, International Conference on Noise and Vibration Engineering* (2014).

[160] MILLITHALER, P., SADOULET-REBOUL, É., OUISSE, M., DUPONT, J.-B., AND BOUHADDI, N. **Equivalent orthotropic material properties for stators of electric cars**. In *CST2014, International Conference on Computational Structures Technology* (2014).

[161] OTHERPOWER. **Side view of a skewed stator (http://www.otherpower.com/images/scimages/5171/awp_1.html)**, 2014. Accessed on 2014, November 28th.

[162] TONG, W. **Mechanical design of electric motors**. Taylor and Francis, 2014.

[163] DUPONT, J.-B., LENEVEU, R., CLERC, C., LOUVIOT, R., AND LALEVEE, D. **Approche multiphysique pour la simulation du bruit rayonné par un transformateur : prise en compte des effets magnétostrictifs [multi-physical approach for suimulating the noise emitted by an electric transformer and accounting for magnetotstrictive effects]**. In *Congrès Français de Mécanique* (2015).

[164] ELECTRICBIKE.COM. **Side view of a laminated stator (https://www.electricbike.com/motor-tech-learn-the-terms-part-1)**, 2015. Accessed on 2015, April 8th.

[165] MILLITHALER, P., SADOULET-REBOUL, É., OUISSE, M., DUPONT, J.-B., AND BOUHADDI, N. **Identification of equivalent anisotropic material properties of 3d-heterogeneous structures**. In *International Conference on Dynamics of Composite Structures* (2015).

[166] MILLITHALER, P., SADOULET-REBOUL, É., OUISSE, M., DUPONT, J.-B., AND BOUHADDI, N. **Structural dynamics of electric machine stators: modelling guidelines and identification of three-dimensional equivalent material properties for multi-layered orthotropic laminates**. *Journal of Sound and Vibration 348* (2015), 185–205.

[167] POLARIS LASER LAMINATIONS. **Individual stator steel sheets (http://www.polarislaserlaminations.com/motor-laminations.html)**, 2015. Accessed on 2015, April 8th.

[168] WILSON PROCESS SYSTEMS. **Resin encapsulation or potting (http://www.wps.co.uk/contract-electronic-manufacturing-services/enviromental-protection/resin-encapsulation-potting/)**, 2015. Accessed on 2015, March 13th.

[169] ELECTRICAL-ENGINEERING PORTAL.COM. **Side view of an ac motor stator (http://electrical-engineering-portal.com/keeping-motor-windings-dry)**. Accessed on 2015, April 1st.

[170] ELECTRICAL KNOWHOW.COM. **Winding process of a srm stator (http://www.electrical-knowhow.com/2012/05/classification-of-electric-motors-part_22.html)**. Accessed on 2015, April 1st.

Examiners' reports — rapports du jury

le cnam
laboratoire de mécanique des structures et des systèmes couplés
lmssc

Rapport sur le mémoire

Dynamic behaviours of electrical machines - Modelling guidelines for efficient finite-element simulations and design specifications for noise reduction

présenté par Pierre MILLITHALER
pour l'obtention du grade de Docteur de l'Université de Franche-Comté

Rapporteur : Jean-François DEÜ,
Professeur des Universités au Conservatoire National des Arts et Métiers

---

Le travail de thèse de Monsieur Pierre MILLITHALER porte sur la modélisation du comportement dynamique de moteurs électriques. De façon plus précise, il s'agit de développer des modélisations numériques efficaces, basées sur la méthode des éléments finis, pour prédire le comportement vibratoire d'un stator de machine électrique. La problématique sous-jacente concerne l'amélioration du design des moteurs électriques avec notamment un objectif de réduction du bruit émis. Cette thèse, financée par un contrat CIFRE, s'inscrit dans le cadre d'une collaboration entre l'entreprise Vibratec et le département de Mécanique Appliqué de l'institut FEMTO-ST à Besançon.

Le mémoire, de plus de 200 pages et rédigé en Anglais, est organisé en cinq chapitres principaux complétés par une courte introduction présentant le contexte scientifique et les objectifs de la thèse ainsi que le plan du manuscrit. Le document se termine par une conclusion générale récapitulant les apports du travail et les perspectives envisagées, quelques annexes, ainsi qu'une liste de 193 références bibliographiques. On peut noter que l'annexe A, qui correspond à un chapitre à part entière, est placée en fin de document pour des raisons de confidentialité. Il est également important de souligner que le manuscrit est très bien structuré et rédigé avec beaucoup de soin, ce qui rend sa lecture très agréable malgré la complexité du problème traité.

Le premier chapitre, de 30 pages, présente tout d'abord un certain nombre de notions de base sur le fonctionnement des machines électriques. L'auteur détaille en particulier diverses architectures de machines électriques existantes. Il présente ensuite quelques généralités sur les excitations d'origine électromagnétique qui sont classiquement considérées comme les plus pénalisantes dans les problématiques de vibration et bruit à basse fréquence. La seconde partie du chapitre expose certaines notions théoriques utilisées dans la suite du travail concernant (i) la dynamique des structures, (ii) le recalage de modèle, et (iii) la modélisation des matériaux viscoélastiques. Ce premier chapitre, bien que très général, donne un bon aperçu du fonctionnement des moteurs électriques aux non-spécialistes. Il permet en outre d'introduire les notions de base utiles pour la construction des modèles prédictifs proposés dans la suite. Même si les deux parties du chapitre n'ont pas vraiment de lien entre elles, elles sont très bien rédigées et permettent d'obtenir un document auto-suffisant.

Le second chapitre, de 26 pages, dresse un état de l'art des connaissances actuelles en matière de comportement dynamique de machines électriques et des techniques de modélisation usuelles. Monsieur MILLITHALER propose également dans ce chapitre une analyse de sensibilité destinée à illustrer quels sont les paramètres qui influent sur la simulation du comportement dynamique d'un stator de moteur électrique. La première partie du chapitre présente quelques généralités sur (i) les pièces qui composent un moteur électrique (en particulier la géométrie du stator) et (ii) la nature des excitations dynamiques à l'origine des phénomènes de vibration. Il s'agit ici d'une analyse de la littérature qui cible en particulier sur la modélisation du couplage magnéto-mécanique, les effets magnétostrictifs, l'influence des excitations harmoniques et les phénomènes d'excentricité du rotor. En complément de cette analyse bibliographique, des simulations éléments finis sont réalisées de façon à analyser la sensibilité de certains paramètres sur le comportement dynamique du stator, à savoir (i) les caractéristiques élastiques du cœur magnétique et du stator complet et (ii) la connexion entre le cœur magnétique et la carcasse du stator. Pour ce dernier point, la conclusion est qu'en première approche, l'utilisation d'une liaison parfaite (en éliminant les nœuds doubles à l'interface dans un modèle éléments finis) peut suffire en l'absence de données complémentaires. Par contre, les premiers modes de vibration du stator (modes d'ovalisation) sont très influencés par les propriétés équivalentes des matériaux constitutifs du stator et en particulier celles de la résine pour l'enrobage du bobinage. Même si aucune modélisation originale n'est proposée dans ce second chapitre, l'étude bibliographique et les analyses de sensibilité sont tout à fait pertinentes et permettent de cibler les ponts à développer dans la suite du travail.

Le troisième chapitre, de plus de 60 pages, porte sur le comportement du cœur magnétique feuilleté d'un stator. Des méthodes d'homogénéisation 3D sont développées pour modéliser cette partie du stator. Après une présentation rapide d'un modèle analytique sur une géométrie simple, Monsieur MILLITHALER s'intéresse à des modélisations numériques par propriétés orthotropes puis par propriétés anisotropes équivalentes. Dans ce cadre, quelques modèles de la littérature sont tout d'abord exposés puis deux approches originales sont développées. La première, basée sur la détermination de propriétés orthotropes équivalentes, est comparée aux autres modèles de la littérature puis à des résultats d'essais issus d'une analyse modale expérimentale sur un stator industriel. Cette comparaison porte sur les premiers modes de vibration du stator et permet de valider l'approche développée. Pour prendre en compte des effets de précontrainte ou de frottement résultant du procédé de fabrication du stator, la méthodologie est étendue au cas de propriétés anisotropes équivalentes (matériau triclinique avec 21 coefficients indépendants). Ce chapitre propose donc une méthodologie numérique originale pour caractériser le comportement dynamique du cœur magnétique feuilleté d'un stator. Cela correspond sans nul doute à un des apports importants du travail. Le travail bibliographique est ici encore très conséquent. Même si la problématique industrielle sous-jacente ne concerne que les premiers modes de vibration d'un stator, il aurait été intéressant d'exposer les limites de l'approche notamment par rapport à la bande de fréquence d'intérêt. Quoi qu'il en soit, l'approche développée est convaincante pour l'application envisagée et permet d'aboutir à un super-élément facilement exploitable dans un cadre éléments finis.

Le quatrième chapitre, de 31 pages, détaille une démarche expérimentale menée chez Vibratec visant à améliorer la modélisation des bobinages et des résines. La première partie présente quelques généralités sur le comportement dynamique des bobinages. La seconde partie porte sur la campagne expérimentale. Enfin, la dernière partie concerne les modèles éléments finis utilisés pour caractériser le comportement du bobinage en prenant en compte le couplage avec la résine. Dans la partie expérimentale, huit structures-test sont étudiées. Il s'agit de structures ayant une géométrie représentative de deux dents d'un stator de moteur électrique. Des bobines en cuivre sont apposées sur les dents puis les structures sont résinées : trois sont imprégnées (trempées puis égouttées) et cinq sont enrobées (englobées dans un bloc de résine) avant cuisson. Chaque résine est caractérisée par des propriétés viscoélastiques distinctes. Des analyses modales expérimentales par excitations

harmoniques sont finalement réalisées sur chaque structure. Les bases modales sont ensuite utilisées pour le recalage des modèles éléments finis. Outre la caractérisation de différentes résines et l'étude de l'influence de la température et du procédé d'élaboration, ce chapitre a pour principal intérêt de dégager des consignes pratiques pour la mise en œuvre de modèles numérique adaptés. Il s'agit donc d'une partie très appliquée du travail dont l'intérêt industriel ne fait pas de doute. Un autre résultat important de chapitre est que le comportement dynamique d'une structure aussi complexe qu'un stator de machine électrique, est influencée par de très nombreux paramètres et notamment par le procédé d'élaboration.

Le dernier chapitre, de 35 pages, placé en annexe du document de thèse, est consacré à la modélisation de la résine et en particulier de ces propriétés viscoélastiques dans un modèle complet de machine électrique. L'objectif recherché est de déterminer les propriétés optimales d'une résine d'enrobage de façon à minimiser la réponse acoustique de la structure. Une analyse mécanique dynamique (DMA) est dans un premier temps effectuée sur des éprouvettes de résine. Les résultats permettent de déterminer la dépendance à la température et à fréquence des modules élastiques et des taux d'amortissement. Des simulations électromagnétiques sont ensuite mises en œuvre puis projetées sur le modèle mécanique du stator. Au moyen de simulations éléments finis, la dépendance en fréquence des propriétés de la résine du stator est modélisée. Finalement, les paramètres viscoélastiques de la résine sont optimisés en réponse aux excitations électromagnétiques. Il est montré, via la simulation, qu'un gain de 10 dB peut être obtenu sur la valeur des pics de la puissance rayonnée. Ce dernier chapitre représente donc une autre contribution majeure du travail. En effet, les modélisations utilisées et les résultats de simulations présentés sont tout à fait originaux et permettent d'envisager de réelles améliorations du design des machines électriques.

Conclusions :

Le travail présenté par Monsieur Pierre MILLITHALER dans son mémoire s'inscrit dans une problématique d'actualité qui concerne le développement de méthodes numériques efficaces pour la prédiction du comportement vibratoire de moteurs électriques. L'objectif sous-jacent concerne l'amélioration du design de ces structures notamment pour réduire les nuisances sonores générées. La diversité des domaines abordés et la façon dont le travail est présenté montrent que le candidat a réussi à s'adapter à une problématique pluridisciplinaire extrêmement complexe et à maîtriser des aspects à la fois théoriques, numériques et expérimentaux en dynamique des structures. Il est important de noter que des approches originales ont été non seulement développées mais également mises en œuvre sur des applications industrielles. Le travail de Monsieur Pierre MILLITHALER représente donc de mon point de vue une contribution remarquable à la problématique de modélisation des machines électriques.

En conclusion, je donne un avis très favorable à la soutenance orale de thèse de Monsieur Pierre MILLITHALER en vue de l'obtention du Doctorat de l'Université de Franche-Comté.

Paris, le 22 septembre 2015
Jean-François DEÜ

Philippe LUTZ
Directeur ED SPIM

Université de Franche-Comté ED SPIM

Rapport sur le mémoire de thèse intitulé

Dynamic behaviour of electric machine stators, modelling guidelines for efficient finite-element simulations and specifications for noise reduction

présenté par

Pierre Millithaler

en vue de la soutenance d'une thèse à l'Université de Franche-Comté
en Sciences pour l'Ingénieur et Microtechniques.

Objectif de la recherche

La thèse de Pierre Millithaler concerne la modélisation vibratoire de moteurs électriques et plus particulièrement de stators de moteurs à courant alternatif. Les difficultés de ce type de structure provient de la nature stratifiée du matériau constituant les circuits magnétiques et de la complexité des bobinages qui correspondent à des sous-structures très hétérogènes. Dans ce travail, l'auteur tente de définir les meilleures stratégies de modélisation de façon à obtenir un outil de calcul du bruit rayonné le plus prédictif possible.

Ce travail est motivé par les problèmes acoustiques rencontrés dans les motorisations électriques de véhicules automobiles. Il est donc en fort lien avec l'industrie liée à ce secteur et a été financé par une Convention Industrielle de Formation par la REcherche (CIFRE) avec la société Vibratec.

Contenu du document

Le mémoire est entièrement rédigé en langue anglaise. Il est constitué d'une introduction générale, de quatre chapitres, d'une conclusion et de deux annexes dont l'une correspond à un cinquième chapitre confidentiel. L'**introduction** rappelle brièvement l'importance que peut avoir la motorisation électrique dans les transports terrestres, plus particulièrement pour l'automobile où de nouvelles solutions énergétiques sont activement recherchées. L'auteur énonce alors le besoin de mieux maîtriser la modélisation des moteurs électriques qui peuvent engendrer des nuisances sonores non négligeables. Ce besoin concerne la modélisation des circuits magnétiques et des bobinages.

Le **premier chapitre** décrit l'architecture et le fonctionnement des moteurs électriques, ainsi que les aspects mécaniques responsables des sollicitations vibratoires qu'ils peuvent entraîner. L'auteur présente d'abord les technologies de moteurs à courant continu, à courant alternatif synchrones et asynchrones et les moteurs pas à pas à réluctance variable. Il s'intéresse ensuite aux efforts électromagnétiques qui s'exercent sur les stators de moteurs à courant alternatif. L'expression du champ magnétique est alors donné en fonction des forces magnétomotrices et de la perméance dans l'entrefer. Parmi les deux effets de sources vibratoires, l'auteur se réfère à la littérature pour dénoncer l'aspect négligeable des effets de magnétostriction dans les matériaux ferromagnétiques devant ceux des pressions de Maxwell appliquées aux interfaces. Ensuite, l'auteur expose brillamment les notions de base sur le calcul dynamique de structures en décrivant : l'élasticité linéaire, la mise en équation et la résolution de systèmes mécaniques par Éléments Finis, les méthodes de réduction de modèles, ainsi que les étapes de recalage de modèles par approches déterministes. En fin de chapitre, l'auteur rappelle également quelques notions sur la viscoélasticité qui vont en particulier concerner la modélisation des résines utilisées dans la fabrication des bobines.

Le **deuxième chapitre** est également de type bibliographique où l'auteur donne une revue précise des études liées aux comportements vibro-acoustiques de moteurs électriques. En terme de conception, Pierre Millithaler décrit les travaux cherchant à fixer quelques règles permettant de réduire le bruit harmonique généré par les moteurs. La forme des stators, le nombre d'encoches, le nombre de pairs de pôles, la présence d'encoches obliques et de flasques constituent des exemples de sujets étudiés dans la littérature. En ce qui concerne les excitations dynamiques, l'auteur reprend plus en détail les différentes causes possibles : la pression de Maxwell qui est la composante principale du couplage magnéto-mécanique, les effets de magnétostriction qui sont encore discutés dans la littérature et les effets d'excentricités qui contribuent à des déséquilibrages mécaniques et magnétiques pouvant introduire des harmoniques importantes dans la vibration du moteur. A l'aide de simulations numériques qu'il a réalisées, l'auteur s'intéresse ensuite à la sensibilité des propriétés élastiques de matériaux sur le comportement vibratoire d'un circuit magnétique seul et d'un stator complet. Il met en particulier en évidence l'importance des propriétés élastiques tangentielles sur les modes d'ovalisation et des propriétés de la carcasse sur l'ensemble des modes propres du stator complet. La dernière partie de ce chapitre est consacrée au problème de la modélisation de la liaison entre le circuit magnétique et la carcasse du stator. Quelques études sont citées par l'auteur, elles s'avèrent insuffisantes pour avoir une idée de l'importance du modèle de ces liaisons. L'auteur propose alors une nouvelle étude de sensibilité basée sur un modèle numérique où la liaison est réalisée par des éléments élastiques tridimensionnels. Les résultats de simulation démontrent : une sensibilité moindre que celle des propriétés de matériaux, une sensibilité non négligeable de la raideur tangentielle, une sensibilité faible pour la raideur radiale et aucune sensibilité pour la raideur axiale. La prise en compte d'une raideur tangentielle et sa variabilité spatiale peut être prise en compte pour raffiner le modèle, mais l'auteur souligne la difficulté d'obtenir ces valeurs de raideur et considère que la liaison rigide devrait donner des résultats assez satisfaisants.

Le **troisième chapitre** est dédié à la modélisation du circuit magnétique de stators de machines à courant alternatif. Pour réduire les courants de Foucault et donc l'échauffement de la machine, les circuits magnétiques sont fabriqués en un feuilletage de tôles en fer doux isolées électriquement. La complexité de modélisation provient de la propriété élastique du feuilletage qui doit être abordé sous la forme d'une homogénéisation. Parmi les méthodes d'homogénéisation sous forme de matériaux orthotropes, l'auteur énumère plus précisément :

- l'approche des moyennes pondérées qui consiste à définir une loi de mélange entre propriétés élastiques ;
- l'approche PEMAT qui propose une homogénéisation à l'aide d'une permutation astucieuse des matrices d'élasticités ;
- l'approche INRIA qui se base sur le calcul des modules de comportements élastiques par une homogénéisation d'un milieu périodique ;
- la méthode « KPC » dont le principe repose sur l'extraction d'une matrice de raideur équivalente à partir de la condensation d'un modèle éléments finis de plusieurs couches.

Dans la suite du chapitre, l'auteur propose sa propre approche d'homogénéisation. Elle consiste à calculer les contraintes et déformations statiques d'un empilement de couches modélisé par éléments finis. Les coefficients élastiques peuvent alors être déduits à partir de tractions et cisaillements imposés à la structure, mais deux scénarios de cisaillements longitudinaux et transversaux sont possibles et proposés dans l'étude. Les résultats d'homogénéisation obtenus sur une structure cubique avec toutes les méthodes exposées montrent des différences notables. Une analyse modale fine comparant les modes calculés par homogénéisation avec un modèle de référence permet alors de conclure sur la pertinence de l'approche proposée avec le scénario du cisaillement longitudinal. L'auteur démontre ensuite d'excellents résultats dans le cas de poutres lorsque le nombre de couches est grand et que l'épaisseur de chaque couche est petite devant celle de la structure. Concernant la

modélisation d'un circuit magnétique de moteur asynchrone, l'auteur préconise de définir plusieurs zones en fonction de la distance avec les soudures. Avec des propriétés différentes dans chaque zone, les comparaisons calculs-essais donnent de très bons résultats et valident l'approche proposée.

La dernière grande partie du chapitre est focalisée sur développement d'une approche plus générale où le matériau homogénéisé est considéré triclinique. La matrice de souplesse contient alors 21 coefficients qui sont déterminés à partir de 27 scénarios numériques de chargements et conditions aux limites sur un échantillon possédant très peu d'éléments finis. Certaines hypothèses de symétries sont prises en compte *a priori* alors que d'autres sont vérifiées *a posteriori*. Les scénarios de cisaillement longitudinaux ou transversaux sont également proposés comme deux alternatives possibles. L'auteur valide les scénarios proposés sur un matériau homogène, dévoile les effets de précontraintes sur la matrice de raideur identifiée (couplages tractions-compressions et cisaillements). Concernant le choix du type de scénario de cisaillement, l'auteur démontre que l'utilisation de scénarios de cisaillements transversaux donne de meilleurs résultats pour le matériau homogène précontraint alors que c'est l'inverse pour un matériau multicouches. Cette conclusion est issue d'exemples où les précontraintes n'ont pas la même orientation, une comparaison avec mêmes précontraintes aurait pu être menée. Pour la modélisation du circuit magnétique étudié dans cette thèse, l'auteur montre finalement de meilleurs résultats lorsque les zones éloignées des soudures sont modélisées par une approche d'homogénéisation triclinique, alors que l'utilisation de l'approche orthotrope semble suffisante pour les encoches et zones proches des cordons de soudure.

Le **quatrième chapitre** est consacré à la modélisation des bobinages. Ils sont constitués de boucles de fils de cuivre imprégnées de résines isolantes. La revue bibliographique sur les différentes approches de modélisation numérique du comportement dynamique de bobines révèle beaucoup d'approximations à cause de la complexité de ce type de structure. Pierre Millithaler propose de commencer par une analyse modale expérimentale de bobines électriques. Les structures tests étudiées possèdent deux bobines entourant deux encoches en acier dans le même plan. La provenance des bobines, la nature de la résine et la manière de l'appliquer diffèrent pour chaque structure test. Le comportement dynamique des structures obtenues avec l'application de la résine en pot comprend quatre types de modes principaux alors qu'il n'y en a que trois pour les structures imprégnées de résine. Quatre modèles éléments finis ont été ensuite proposés où l'auteur décrit la stratégie de recalage choisie. Les modèles les plus pertinents sont alors établis selon la manière d'appliquer la résine. Pierre Millithaler étudie également l'effet de la température sur un modèle par famille de structure test. Les résultats sont très intéressants, ils permettent de montrer l'importance du changement de comportement en fonction de celui de la résine utilisée. En fin de chapitre, l'auteur focalise son étude sur l'échantillon comprenant des bobines fabriquées industriellement où la résine est appliquée en pot. L'intérêt de cet échantillon est que les bobines sont disjointes, il s'agit alors d'un concept de structure plus proche de stators fabriqués dans l'industrie. Le modèle numérique peut aussi être simplifié en considérant que toutes les zones de résine peuvent être modélisées par un matériau isotrope. Après recalage, l'auteur montre alors clairement que la dépendance thermique du comportement dynamique de la structure complexe ne dépend que de celui de la résine seule.

Pour des raisons de confidentialités, le **cinquième chapitre** proposé en annexe n'est pas commenté ici, mais le rapporteur tient à souligner la grande qualité d'un travail de modélisation très complet, prenant en compte l'ensemble des résultats issus des chapitres précédents.

Dans la **conclusion générale** du mémoire, l'auteur résume les points importants de la thèse et donne une liste de règles générales à retenir pour la conception de modèles de stators de moteurs électriques. Les perspectives énoncées sont à court terme. Elles concernent les applications industrielles directes : mise en place de la stratégie de modélisation proposée pour moteurs de véhicules automobiles électriques, travail sur l'optimisation de la résine pour réduire le bruit émis et extension à d'autres architectures de stators de moteurs électriques. Des perspectives plus à long

terme auraient pu être proposées, en particulier sur des applications autres que les stators de moteurs électriques.

Avis sur le travail présenté

Le travail de thèse présenté dans ce mémoire correspond à une étude très complète, d'excellente qualité et apporte une réelle avancée dans la modélisation des moteurs électriques. L'étude bibliographique est exhaustive et donne une synthèse très claire sur les difficultés et verrous technologiques rencontrés par les industriels. Les approches de modélisation proposées sont très pertinentes et seront certainement utilisées dans les futurs travaux d'ingénierie.

Dans son ensemble, le document est très bien rédigé. Les cheminements présentés, la clarté des formulations utilisées, la précision des hypothèses réalisées, les interprétations des résultats obtenus démontrent clairement que le candidat possède une grande rigueur scientifique. Par ailleurs, la présence de listes de règles synthétiques est très utile, elles permettront aux futurs ingénieurs d'utiliser le mémoire comme un document de référence. Le choix d'une rédaction en anglais est un véritable atout, il offre un accès à l'international qui sera fortement apprécié par la société porteuse de ce travail. Le nombre de publications et de communications montrent également une volonté de diffuser la connaissance malgré le caractère confidentiel d'une partie des travaux (1 publication dans un journal international, 1 publication en attente de soumission, 3 conférences internationales avec actes).

En conclusion, la quantité et la qualité de ce travail est tout à fait en accord avec celui attendu pour une thèse, je donne un avis très favorable à la soutenance de Monsieur Millithaler.

Fait au Mans, le 15 août 2015

Charles PEZERAT - Professeur des Universités

Laboratoire d'Acoustique de l'Université du Maine (UMR CNRS 6613)
ENSIM
Rue Aristote
72085 LE MANS Cedex 09
tel: 02 43 83 39 53 - fax : 02 43 83 37 94
email : charles.pezerat@univ-lemans.fr

Philippe LUTZ
Directeur Ed SPIM

Document generated with LaTeX and:
the LaTeX style for PhD Thesis created by S. Galland — http://www.multiagent.fr/ThesisStyle
the tex-upmethodology package suite — http://www.arakhne.org/tex-upmethodology/

Abstract:

Boosted by the increasing interest of industries such as automotive, 100% electric engine technologies power more and more affordable vehicles for the general public. In spite of a rather favourable common opinion about the low noise emitted by electric motors, controlling the vibratory and acoustic performances of such machines remains a very costly challenge to take up. Associating the expertise of the company Vibratec and the institute Femto-ST Applied Mechanics Department, this industry-oriented Ph.D. thesis aims at improving the current knowledge about the mechanical behaviour of electric machines. New finite-element modelling methods are proposed from homogenisation approaches, experimental analyses, model updating procedures and variability studies in temperature and frequency, in order to predict the behaviour of an electric motor more efficiently.

Keywords: finite elements, electric machine stator, magnetic core, laminated composites, heterogeneous structures, homogenisation method, windings, resin, experimental modal analysis, polymer, viscoelasticity, electromagnetic simulation, dynamic response

Résumé :

Dopées par un intérêt croissant des industries telles que l'automobile, les technologies de motorisation 100% électriques équippent de plus en plus de véhicules à la portée du grand public. En dépit d'une opinion commune favorable sur les faibles émissions sonores des moteurs électriques, la maîtrise des performances vibratoires et acoustiques d'une telle machine reste un challenge très coûteux à relever. Associant l'expertise de l'entreprise Vibratec et du département Mécanique Appliquée de l'institut Femto-ST, cette thèse CIFRE vise à améliorer les connaissances actuelles sur le comportement mécanique de machines électriques. De nouvelles méthodes de modélisation par éléments finis sont proposées à partir d'approches d'homogénéisation, analyses expérimentales, recalage de modèles et études de variabilité en température et en fréquence, pour permettre une prédiction plus performante du comportement vibratoire d'un moteur électrique.

Mots-clés : éléments finis, stator de machine électrique, cœur magnétique, matériaux composites stratifiés, structures hétérogènes, méthode d'homogénéisation, bobinages, résine, analyse modale expérimentale, polymère, viscoélasticité, simulation électromagnétique, réponse dynamique

SPIM

■ École doctorale SPIM 16 route de Gray F - 25030 Besançon cedex

■ tél. +33 (0)3 81 66 66 02 ■ ed-spim@univ-fcomte.fr ■ www.ed-spim.univ-fcomte.fr

UFC
UNIVERSITÉ
DE FRANCHE-COMTÉ